

## **INFORMATION TO USERS**

The most advanced technology has been used to photograph and reproduce this manuscript from the microfilm master. UMI films the original text directly from the copy submitted. Thus, some dissertation copies are in typewriter face, while others may be from a computer printer.

In the unlikely event that the author did not send UMI a complete manuscript and there are missing pages, these will be noted. Also, if unauthorized copyrighted material had to be removed, a note will indicate the deletion.

Oversize materials (e.g., maps, drawings, charts) are reproduced by sectioning the original, beginning at the upper left-hand corner and continuing from left to right in equal sections with small overlaps. Each oversize page is available as one exposure on a standard 35 mm slide or as a 17" x 23" black and white photographic print for an additional charge.

Photographs included in the original manuscript have been reproduced xerographically in this copy. 35 mm slides or 6" x 9" black and white photographic prints are available for any photographs or illustrations appearing in this copy for an additional charge. Contact UMI directly to order.



300 North Zeeb Road, Ann Arbor, MI 48106-1346 USA



**Order Number 8727382**

**Calculations of viscous flows with a multigrid method**

**Martinelli, Luigi, Ph.D.**

**Princeton University, 1987**

**U·M·I**  
300 N. Zeeb Rd.  
Ann Arbor, MI 48106



**PLEASE NOTE:**

In all cases this material has been filmed in the best possible way from the available copy.  
Problems encountered with this document have been identified here with a check mark ✓.

1. Glossy photographs or pages ✓
2. Colored illustrations, paper or print ✓
3. Photographs with dark background ✓
4. Illustrations are poor copy \_\_\_\_\_
5. Pages with black marks, not original copy \_\_\_\_\_
6. Print shows through as there is text on both sides of page \_\_\_\_\_
7. Indistinct, broken or small print on several pages ✓
8. Print exceeds margin requirements ✓
9. Tightly bound copy with print lost in spine ✓
10. Computer printout pages with indistinct print \_\_\_\_\_
11. Page(s) \_\_\_\_\_ lacking when material received, and not available from school or author.
12. Page(s) \_\_\_\_\_ seem to be missing in numbering only as text follows.
13. Two pages numbered \_\_\_\_\_. Text follows.
14. Curling and wrinkled pages \_\_\_\_\_
15. Dissertation contains pages with print at a slant, filmed as received ✓
16. Other \_\_\_\_\_  
\_\_\_\_\_  
\_\_\_\_\_

**University  
Microfilms  
International**



**CALCULATIONS OF VISCOUS FLOWS WITH  
A MULTIGRID METHOD**

**Luigi Martinelli**

A DISSERTATION  
PRESENTED TO THE  
FACULTY OF PRINCETON UNIVERSITY  
IN CANDIDACY FOR THE DEGREE  
OF DOCTOR OF PHILOSOPHY

RECOMMENDED FOR ACCEPTANCE BY THE  
DEPARTMENT OF  
MECHANICAL AND AEROSPACE ENGINEERING

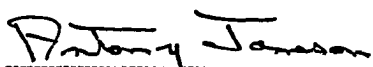
OCTOBER, 1987

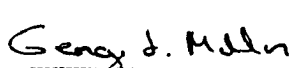
**CALCULATIONS OF VISCOUS FLOWS WITH  
A MULTIGRID METHOD**

Prepared by:

  
Luigi Martinelli

Approved by:

  
Professor A. Jameson  
Dissertation Advisor

  
Professor G.L. Mellor  
Dissertation Reader

  
Professor F.A. Williams  
Dissertation Reader

*Per Luisa e Micol T.*

## ACKNOWLEDGMENTS

I would never have been able to bring this work to a conclusion without the patience and incomparable guidance of Professor Antony Jameson. I have greatly benefited from his teaching not only professionally but also personally. His teaching made my stay in Princeton a fruitful and pleasant one, and it has been an important part of my overall education.

I would like to sincerely thank both Dr. Timothy Baker for our many discussions and for his continued encouragement and help during the entire course of this project, and Professor Francesco Grasso with whom I had the pleasure of collaborating in the preliminary stages of this study. I am also thankful to Dr. Paul Rubbert and Dr. Larry Wigton of the Boeing Company for putting at my disposal an excellent grid generation code, and for providing me with access to the CRAY-XMP computer at the Boeing facility when I most needed it.

I would like to thank Professor George L. Mellor and Professor Forman A. Williams for reading this dissertation. Their suggestions were instrumental in developing a clearer presentation of the subject.

Finally I would like to thank Professor Frediano V. Bracco for having given me the opportunity to join the graduate program at Princeton and for having patiently guided and supported me during the first lap of my course of study.

*1782*  
This thesis carries T-1754 in the records of the Department of Mechanical and Aerospace Engineering.

## ABSTRACT

The continuing evolution of supercomputers is shifting the optimal trade off between computational costs and completeness of the mathematical model toward the solution of the full set of nonlinear conservation laws. During the last decade the development of effective methods for solving the inviscid form of the conservation laws has provided the necessary framework for attempting the analysis of viscous flows by solving the compressible Navier Stokes and Reynolds averaged equations. The present work carries out this extension for 2-D transonic viscous flows past airfoils.

Two multigrid schemes for the solution of the 2-D viscous compressible conservation equations are developed and validated. The unknown variables are stored at the cell centers in the first approach and at the cell vertices in the second. A finite volume formulation is used to discretize the spatial operators, and several discretization formulas for the viscous terms are studied.

Validation of the schemes is carried out in several steps. Firstly, the accuracy of the schemes for the solution of the inviscid form of the equations with high aspect ratio cells is demonstrated. The schemes are then validated by comparisons with experimental observations and other computations for laminar flows in the transonic and supersonic regimes. Finally, several examples of applications to the Reynolds averaged equations in the transonic regime are presented and discussed. For these computations, closure is achieved by using a simple algebraic turbulence model widely accepted in computational aerodynamics.

The validation of two efficient, robust, and accurate multigrid methods brings numerical simulation of the Navier Stokes and Reynolds averaged equations to a new plateau. The combination of accuracy and speed provides a necessary tool for the study of turbulence modeling for aerodynamic flows, by making it possible to obtain a rapid and reliable assessment of the effects of substituting alternative models.

### List of Symbols

Symbol	Legenda
$a$	Speed of sound
$c$	Airfoil chord
$e$	Internal energy per unit mass
$f$	Scalar amplification factor
$\mathbf{f}_c$	Convective flux vector
$\mathbf{f}_v$	Viscous flux vector
$\mathbf{g}_c$	Convective flux vector
$\mathbf{g}_v$	Viscous flux vector
$h$	Jacobian determinant
$k$	Thermal conductivity coefficient
$\mathbf{n}$	Normal unit vector
$p$	Pressure
$\mathbf{q}$	Heat flux
$q$	Velocity component (computational plane)
$r$	Velocity component (computational plane)
$\mathbf{u}$	Velocity vector
$u$	Cartesian x-component of the velocity vector
$v$	Cartesian y-component of the velocity vector
$w$	Conservative variables
$t$	Time
$\mathbf{t}$	Tangential unit vector
$(x,y)$	Cartesian coordinates
$C_d$	Drag coefficient
$C_l$	Lift coefficient
$C_m$	Moment coefficient
$C_p$	Pressure coefficient
$D\Omega$	Diffusion operator
$E$	Total energy per unit mass (thermal plus kinetic )

$G(p,q)$	.....	Amplification factor
$I_{k,k-1}$	.....	Multigrid interpolation operator
$M_\infty$	.....	Free stream Mach number
$Pr$	.....	Prandtl number
$Q_0$	.....	Convection operator
$Q_{k,k-1}$	.....	Multigrid transfer operator
$R_0$	.....	Residual operator
$Re_\infty$	.....	Reynolds number based on the chord and free stream conditions
$S$	.....	Scaling factor for adaptive dissipation
$T$	.....	Temperature
$T_{k,k-1}$	.....	Multigrid transfer operator
$\mathbf{U}$	.....	Non-conservative variables
$\alpha$	.....	Angle of attack
$\gamma$	.....	Specific heat ratio
$\delta$	.....	Difference operator
$\delta_{ij}$	.....	Kronecker delta
$\epsilon$	.....	Turbulent energy mean dissipation rate , also smoothing coefficient.
$\kappa$	.....	Turbulent kinetic energy
$\lambda$	.....	Wave speed
$\mu$	.....	Viscosity coefficient
$\nu$	.....	Eddy diffusivity
$(\xi,\eta)$	.....	Generalized curvilinear coordinate system, also Computational plane coordinate system.
$\rho$	.....	Density
$\sigma$	.....	Stress tensor component
$\tau$	.....	Stress tensor component
$\Delta$	.....	Increment operator
$\Omega$	.....	Control volume area

## List of Figures

Figure	Caption
<i>Fig. 3.1</i>	Metric singularity of a typical H mesh
<i>Fig. 3.1.1</i>	Computational cell for the cell centered schemes
<i>Fig. 3.1.2a</i>	Auxiliary control volume for the discretization of the viscous terms for the CCS-A scheme.
<i>Fig. 3.1.2b</i>	Auxiliary control volume for the discretization of the viscous terms for the CCS-B scheme.
<i>Fig. 3.2.1</i>	Computational cell for the vertex based scheme.
<i>Fig. 3.2.2</i>	Auxiliary control volume for the discretization of the viscous terms for the vertex based scheme.
<i>Fig. 3.2.3</i>	Nodal distribution for the 1-D vertex scheme.
<i>Fig. 3.4.1</i>	Solid Boundary for the cell centered scheme.
<i>Fig. 3.4.2</i>	Solid Boundary for the vertex based scheme.
<i>Fig. 3.4.3</i>	C - mesh topology.
<i>Fig. 3.5.1</i>	Stability region of the three stage scheme.
<i>Fig. 3.5.2</i>	Stability region of the five stage scheme with three evaluation of the dissipation.
<i>Fig. 3.7.1</i>	NACA 0012 airfoil - 256×64 C-mesh for Euler computations.
<i>Fig. 3.7.2a</i>	NACA 0012 airfoil - Pressure coefficient along the surface. (Adaptive dissipation)
<i>Fig. 3.7.2b</i>	NACA 0012 airfoil - Pressure coefficient along the surface. (Flux Limited dissipation)
<i>Fig. 3.7.3a</i>	NACA 0012 airfoil - Pressure coefficient along the surface. (Adaptive dissipation)
<i>Fig. 3.7.3b</i>	NACA 0012 airfoil - Pressure coefficient along the surface. (Flux Limited dissipation)
<i>Fig. 3.7.4</i>	KORN airfoil - 256×64 C-mesh
<i>Fig. 3.7.5</i>	KORN airfoil - Pressure coefficient along the surface. (Adaptive dissipation)

<i>Fig. 3.7.6</i>	....	KORN airfoil - 256x64 C-mesh
<i>Fig. 3.7.7</i>	....	KORN airfoil - Pressure coefficient along the surface. (Adaptive dissipation)
<i>Fig. 3.7.8a</i>	....	RAE 2822 airfoil - Pressure coefficient along the surface. (Adaptive dissipation)
<i>Fig. 3.7.8b</i>	....	RAE 2822 airfoil - Pressure coefficient along the surface. (Adaptive dissipation)
<i>Fig. 4.3.1</i>	....	Saw shoot multigrid cycle.
<i>Fig. 4.3.2</i>	....	W - multigrid cycle.
<i>Fig. 5.1.1</i>	....	NACA 0012 airfoil - 256x64 C-mesh for laminar computations.
<i>Fig. 5.1.2</i>	....	NACA 0012 airfoil - Pressure Contours ( $DP = .05$ )
<i>Fig. 5.1.3</i>	....	NACA 0012 airfoil - Mach Contours ( $DM = .05$ )
<i>Fig. 5.1.4</i>	....	NACA 0012 airfoil - Density Contours ( $D\rho = .05$ )
<i>Fig. 5.1.5</i>	....	NACA 0012 airfoil - Pressure coefficient along the surface.
<i>Fig. 5.1.6</i>	....	NACA 0012 airfoil - Pressure Contours ( $DP = .05$ )
<i>Fig. 5.1.7</i>	....	NACA 0012 airfoil - Mach Contours ( $DM = .05$ )
<i>Fig. 5.1.8</i>	....	NACA 0012 airfoil - Density Contours ( $D\rho = .05$ )
<i>Fig. 5.1.9</i>	....	NACA 0012 airfoil - Pressure coefficient along the surface.
<i>Fig. 5.1.10</i>	....	NACA 0012 airfoil - Pressure Contours ( $DP = .05$ )
<i>Fig. 5.1.11</i>	....	NACA 0012 airfoil - Mach Contours ( $DM = .05$ )
<i>Fig. 5.1.12</i>	....	NACA 0012 airfoil - Density Contours ( $D\rho = .05$ )
<i>Fig. 5.1.13</i>	....	NACA 0012 airfoil - Pressure coefficient along the surface.
<i>Fig. 5.1.14</i>	....	NACA 0012 airfoil - Pressure Contours ( $DP = .05$ )
<i>Fig. 5.1.15</i>	....	NACA 0012 airfoil - Mach Contours ( $DM = .05$ )
<i>Fig. 5.1.16</i>	....	NACA 0012 airfoil - Density Contours ( $D\rho = .05$ )
<i>Fig. 5.1.17</i>	....	NACA 0012 airfoil - Pressure coefficient along the surface.
<i>Fig. 5.1.18</i>	....	NACA 0012 airfoil - Pressure Contours ( $DP = .05$ )
<i>Fig. 5.1.19</i>	....	NACA 0012 airfoil - Mach Contours ( $DM = .05$ )

<i>Fig. 5.1.20</i>	....	NACA 0012 airfoil - Density Contours ( $D\rho = .05$ )
<i>Fig. 5.1.21</i>	....	NACA 0012 airfoil - Pressure coefficient along the surface.
<i>Fig. 5.1.22</i>	....	NACA 0012 airfoil - Pressure Contours ( $DP = .05$ )
<i>Fig. 5.1.23</i>	....	NACA 0012 airfoil - Mach Contours ( $DM = .05$ )
<i>Fig. 5.1.24</i>	....	NACA 0012 airfoil - Density Contours ( $D\rho = .05$ )
<i>Fig. 5.1.25</i>	....	NACA 0012 airfoil - Pressure coefficient along the surface.
<i>Fig. 5.1.26</i>	....	NACA 0012 airfoil - Pressure Contours ( $DP = .05$ )
<i>Fig. 5.1.27</i>	....	NACA 0012 airfoil - Mach Contours ( $DM = .05$ )
<i>Fig. 5.1.28</i>	....	NACA 0012 airfoil - Density Contours ( $D\rho = .05$ )
<i>Fig. 5.1.29</i>	....	NACA 0012 airfoil - Pressure coefficient along the surface.
<i>Fig. 5.2.1</i>	....	NACA 0012 airfoil - 320×64 C-mesh for laminar computations.
<i>Fig. 5.2.2</i>	....	NACA 0012 airfoil - Top CCS - A Bottom CCS - B Density Contours
<i>Fig. 5.2.3</i>	....	NACA 0012 airfoil - Top CCS - A Bottom CCS - B Pressure Contours
<i>Fig. 5.2.4</i>	....	NACA 0012 airfoil - Top CCS - A Bottom CCS - B Mach Contours
<i>Fig. 5.2.5</i>	....	NACA 0012 airfoil - Top CCS - A Bottom CCS - B Entropy Contours
<i>Fig. 5.2.6</i>	....	NACA 0012 airfoil - Pressure coefficient along the surface.
<i>Fig. 5.2.7</i>	....	NACA 0012 airfoil - Pressure coefficient along the surface.
<i>Fig. 5.2.8</i>	....	NACA 0012 airfoil - Convergence history.
<i>Fig. 5.2.9</i>	....	NACA 0012 airfoil - Convergence history.
<i>Fig. 5.2.10</i>	....	NACA 0012 airfoil - CCS - A Density Contours
<i>Fig. 5.2.11</i>	....	NACA 0012 airfoil - CCS - A Pressure Contours
<i>Fig. 5.2.12</i>	....	NACA 0012 airfoil - CCS - A

		Mach Contours
<i>Fig. 5.2.13</i>	....	NACA 0012 airfoil -
		Top CCS - A
		Bottom CCS - B
		Entropy Contours
<i>Fig. 5.2.14</i>	....	NACA 0012 airfoil -
		Pressure coefficient along the surface.
<i>Fig. 5.2.15</i>	....	NACA 0012 airfoil -
		Convergence history.
<i>Fig. 5.2.16</i>	....	NACA 0012 airfoil -
		Pressure coefficient along the surface.
<i>Fig. 5.2.17</i>	....	NACA 0012 airfoil -
		Convergence history.
<i>Fig. 5.2.18</i>	....	NACA 0012 airfoil -
		Experimental Density Contours
<i>Fig. 5.2.19</i>	....	NACA 0012 airfoil -
		Computed Density Contours
<i>Fig. 5.2.20</i>	....	NACA 0012 airfoil -
		Experimental Density Contours
<i>Fig. 5.2.21</i>	....	NACA 0012 airfoil -
		Computed Density Contours
<i>Fig. 5.2.22</i>	....	NACA 0012 airfoil - CCS - A
		Pressure Contours
<i>Fig. 5.2.23</i>	....	NACA 0012 airfoil - CCS - A
		Mach Contours
<i>Fig. 5.2.24</i>	....	NACA 0012 airfoil - CCS - A
		Computed Density Contours
<i>Fig. 5.2.25</i>	....	NACA 0012 airfoil - CCS - A
		Experimental Density Contours
<i>Fig. 6.2.1</i>	....	NACA 0012 airfoil -
		320x64 C-mesh for turbulent computations.
<i>Fig. 6.2.2</i>	....	NACA 0012 airfoil - $C_l-\alpha$ plot
		$M_\infty = .7$
		$Re_\infty = 9 \times 10^6$
<i>Fig. 6.2.3</i>	....	NACA 0012 airfoil - $C_l-C_d$ plot
		$M_\infty = .7$
		$Re_\infty = 9 \times 10^6$
<i>Fig. 6.2.4a</i>	....	NACA 0012 case (1) - CCS - A
		Pressure coefficient along the surface.
<i>Fig. 6.2.4b</i>	....	NACA 0012 case (2) - CCS - A
		Pressure coefficient along the surface.
<i>Fig. 6.2.4c</i>	....	NACA 0012 case (3) - CCS - A
		Pressure coefficient along the surface.
<i>Fig. 6.2.4d</i>	....	NACA 0012 case (4) - CCS - A
		Pressure coefficient along the surface.
<i>Fig. 6.2.5a</i>	....	NACA 0012 case (1) - CCS - A
		Convergence History.
<i>Fig. 6.2.5b</i>	....	NACA 0012 case (2) - CCS - A
		Convergence History.
<i>Fig. 6.2.5c</i>	....	NACA 0012 case (3) - CCS - A
		Convergence History.

- Fig. 6.2.6* .... NACA 0012 case (5) - CCS - A  
 Pressure coefficient along the surface.
- Fig. 6.2.7* .... NACA 0012 case (5) - CCS - A  
 Convergence History.
- Fig. 6.2.8* .... RAE 2822 airfoil - CCS - A  
 320x64 grid for turbulent calculations.
- Fig. 6.2.9* .... RAE 2822 airfoil - CCS - A  
 512x64 grid for turbulent calculations.
- Fig. 6.2.10* .... RAE 2822 airfoil case (1) - CCS - A  
 Pressure coefficient along the surface.  
 Comparison with Experiments.
- Fig. 6.2.11* .... RAE 2822 airfoil case (1) - CCS - A  
 Convergence History.
- Fig. 6.2.12* .... RAE 2822 airfoil case (10) - CCS - A  
 Pressure coefficient along the surface.  
 Comparison with Experiments.
- Fig. 6.2.13* .... RAE 2822 airfoil case (10) - CCS - A  
 Convergence History.
- Fig. 6.2.14* .... RAE 2822 airfoil case (6) - CCS - A  
 Pressure coefficient along the surface.  
 Comparison with Experiments.
- Fig. 6.2.15* .... RAE 2822 airfoil case (6) - CCS - A  
 Convergence History.
- Fig. 6.2.16* .... RAE 2822 airfoil case (9) - CCS - A  
 Pressure coefficient along the surface.  
 Comparison with Experiments.
- Fig. 6.2.17* .... RAE 2822 airfoil case (9) - CCS - A  
 Convergence History.
- Fig. 6.2.18* .... RAE 2822 airfoil case (9) - CCS - A  
 Pressure coefficient along the surface.  
 Comparison with Experiments.
- Fig. 6.2.19* .... RAE 2822 airfoil case (6) - CCS - A  
 Convergence History.
- Fig. 6.2.20* .... JONES airfoil - CCS - A  
 512x64 grid for turbulent calculations.
- Fig. 6.2.21* .... JONES airfoil - CCS - A  
 Pressure coefficient along the surface.
- Fig. 6.2.22* .... JONES airfoil - CCS - A  
 Convergence History.
- Fig. 6.3.1* .... RAE 2822 airfoil - CCS - A  
 320x64 grid for turbulent calculations.
- Fig. 6.3.2* .... RAE 2822 airfoil case (9) - CCS - A  
 Pressure coefficient along the surface.
- Fig. 6.3.3* .... RAE 2822 airfoil case (9) - CCS - A  
 Convergence History.
- Fig. 6.3.4* .... RAE 2822 airfoil case (9) - CCS - A  
 Density Contours
- Fig. 6.3.5* .... RAE 2822 airfoil case (9) - CCS - A  
 Pressure Contours
- Fig. 6.3.6* .... RAE 2822 airfoil case (9) - CCS - A  
 Mach Contours

- Fig. 6.3.7* .... RAE 2822 airfoil case (9) - CCS - A  
     Entropy Contours
- Fig. 6.3.8* .... RAE 2822 airfoil case (9) - CCS - A  
     Mach Contours - close up
- Fig. 6.3.9* .... RAE 2822 airfoil case (9) - CCS - A  
     Velocity vector field - close up
- Fig. 6.3.10* .... NACA 0012 airfoil - CCS - A  
     Pressure coefficient along the surface.
- Fig. 6.3.11* .... NACA 0012 airfoil - CCS - A  
     Convergence history.
- Fig. 6.3.12* .... NACA 0012 airfoil - CCS - A  
     Density Contours
- Fig. 6.3.13* .... NACA 0012 airfoil - CCS - A  
     Pressure Contours
- Fig. 6.3.14* .... NACA 0012 airfoil - CCS - A  
     Mach Contours
- Fig. 6.3.15* .... NACA 0012 airfoil - CCS - A  
     Velocity vector field - close up
- Fig. 6.3.16* .... NACA 0012 airfoil - CCS - A  
     Pressure Contours - close up
- Fig. 6.3.17* .... NACA 0012 airfoil - CCS - A  
     Velocity vector field - close up
- Fig. 6.3.18* .... NACA 0012 airfoil - CCS - A  
     Velocity vector field - close up
- Fig. 6.3.19* .... NACA 0012 airfoil - CCS - A  
     Velocity vector field - close up
- Fig. 7.1* .... RAE 2822 Embedded Grid system.
- Fig. 7.2* .... RAE 2822 airfoil case (9) - CCS - A  
     Pressure coefficient along the surface.  
     (Flux Limited dissipation model)

--

## Table of Contents

<b>Acknowledgments .....</b>	<b>i</b>
<b>Abstract .....</b>	<b>ii</b>
<b>List of Symbols .....</b>	<b>iii</b>
<b>List of Figures .....</b>	<b>iv</b>
<b>CHAPTER 1 - INTRODUCTION .....</b>	<b>1</b>
1.1 Computational Fluid Dynamics .....	1
1.2 Importance of Viscous Effects .....	2
1.3 Computations with Viscous Effects .....	3
1.4 Difficulties in Viscous Effects .....	5
1.5 Directions of the Research .....	6
1.6 Outline of the Presentation .....	7
<b>CHAPTER 2 - MATHEMATICAL MODEL .....</b>	<b>9</b>
2.1 Integral form of the Navier Stokes Equations .....	9
2.2 Differential form of the Navier Stokes Equations .....	10
2.3 Boundary Conditions .....	12
2.4 Compressible Reynolds Averaged Equations .....	13
<b>CHAPTER 3 - NUMERICAL DISCRETIZATION .....</b>	<b>17</b>
3.1 Cell Centered Scheme .....	18

3.2 Vertex Scheme .....	20
3.3 Artificial Dissipation .....	23
3.4 Discrete Boundary Conditions .....	26
3.5 Time Stepping Scheme .....	28
3.6 Analysis of the Time step limit .....	30
3.7 Verification of The Basic Scheme for The Euler Equations .....	33
<b>CHAPTER 4 - CONVERGENCE ACCELERATION TECHNIQUES .....</b>	<b>52</b>
4.1 Local Time Stepping .....	52
4.2 Residual Averaging .....	54
4.3 Multigrid Strategy .....	56
<b>CHAPTER 5 - RESULTS FOR LAMINAR FLOWS OVER A NACA 0012 WING SECTION .....</b>	<b>62</b>
5.1 Laminar Flows With the Vertex Scheme .....	63
5.2 Laminar Flows With the Cell Centered Scheme .....	66
5.3 Comparisons With Experiments .....	68
<b>CHAPTER 6 - NUMERICAL SIMULATION OF TURBULENT TRANSONIC AIRFOIL FLOWS .....</b>	<b>96</b>
6.1 Preliminary Assessment of the Schemes for the Reynolds Averaged Equations .....	97
6.2 Computed Aerodynamics Characteristics of Airfoils in the Transonic Regime .....	98
6.3 Detailed Analysis of Turbulent Flow Fields .....	104

<b>CHAPTER 7 - CONCLUSIONS AND FUTURE WORK .....</b>	<b>148</b>
<b>REFERENCES .....</b>	<b>153</b>
<b>APPENDIX A - Baldwin &amp; Lomax Turbulence Model .....</b>	<b>157</b>
<b>APPENDIX B - Discrete Gauss Theorem .....</b>	<b>161</b>
<b>APPENDIX C - Computations of Internal</b>	
<b>Laminar Flows .....</b>	<b>163</b>

## CHAPTER 1

### INTRODUCTION

#### 1. Computational Fluid Dynamics

In the past two decades, the discipline of Computational Fluid Dynamics (CFD) has grown to become an important tool for the analysis of aerodynamic problems. Following the early developments of panel methods that made possible, in the sixties, the analysis of subsonic flows around complex geometries, the battleground of CFD has shifted, in the seventies, toward the analysis of problems in the transonic regime. This regime of flight is not only the most profitable for commercial transport but it is also of particular interest for military aircraft in maneuvering flight. Nowadays, CFD is routinely used in the early stages of new projects, complementing wind tunnel tests as an integral part of the aerodynamic design process [1].

Parallel to general the acceptance of CFD by the aeronautical industry, the rapid improvements in algorithms and also in both speed and memory of computers have boosted the widespread use and development of numerical methods for computing aerodynamic flows. CFD has evolved by steps to the solution of problems of increased mathematical complexity [2]. In the seventies, major advances were made in the simulation of transonic flows by small-disturbance and potential-flow equations. More recently, the continuing evolution of supercomputers has moved the optimal trade off between cost and feasibility of computations and completeness of the mathematical model toward the solution of the full set of non linear conservation laws. Indeed,

the first half of the eighties has seen much of the interest shift toward the solution of the Euler equations. As a result of widespread efforts to devise improved methods of solving the inviscid conservation laws, the principles underlying the construction of accurate numerical approximation of the convective operators are now fairly well understood. We are at a point where the solution of the compressible Navier Stokes and Reynolds averaged equations for aerodynamic configurations can be attempted.

## 2. Importance of Viscous Effects

Although it is true that the viscous effects are unimportant outside the boundary layer , wake , and shock regions, the presence of the boundary layer can have a drastic influence on the global pattern of the flow field in many practical aeronautical applications. In the transonic regime, even on single 2-D airfoils at moderate angle of attack, the viscous effects can cause the location of the shock to shift by as much as 20% of the chord. Depending on the strength of the shock wave, the interaction between the shock and boundary layer can cause separation of the flow at the shock foot with a subsequent rise in drag , or even an unsteady oscillation of the shock itself ( known as buffeting). Massive separation regions could be present on airfoils as consequence of ice formation and, furthermore, the characteristics of a wing at stall are entirely determined by viscous phenomena. On more complex geometries, such as multi-element airfoils at take off and landing conditions, the complex interaction of wakes and boundary layers determines the flow pattern and eventually the aerodynamic characteristics of the lifting device. Some of the viscous effects, such as the displacement effect of the boundary layer over the airfoil, the displacement effect of the wake, and the wake curvature effect , can be effectively approximated by incorporating boundary layer corrections coupled with the inviscid solution from the potential or Euler equations [3,4,5]. In a region of strong interaction, however, such as the shock foot or the trailing edge, the boundary layer approximation breaks down, leading to the necessity of resolving the complete set of the governing equations. Inviscid models with boundary layer corrections have

proved successful for attached flows and have contributed to improved wing designs for transport aircraft. However, flows corresponding to higher angles of attack (e. g. military aircraft stall) are less amenable to this approach [1].

### 3. Computations with Viscous Effects

Even with the new generation of computers the resolution and the accuracy attainable in the solution of the Navier Stokes equations are still severely limited by the disparate length scales present in the viscous region and the external flow. At high Reynolds numbers the problem is complicated further by the onset and development of turbulence that fills up the spectrum of possible length and time scales. While there is the possibility of attacking the Navier Stokes equations for laminar flow problems, the solution of the complete set of equations for Reynolds numbers of practical interest in aeronautics is still beyond the reach of currently available computers and any computer in the foreseeable future [2]. The problem of describing turbulent flows must still be approached by the solution of the Reynolds averaged equations that require a suitable turbulence model for closure. While the development of a fairly general and reliable turbulence model is still an open problem and represents a research effort by itself [6], improvements in the speed and accuracy of numerical schemes are still needed before complete viscous computations can be routinely performed [7].

The considerable attention given to the development of efficient solution techniques for the Euler equations has produced very accurate and robust algorithms in recent years. Both explicit and implicit finite difference methods have reached a mature stage enabling the solution of 2-D and 3-D inviscid equations. Traditionally, implicit methods have been praised for their stability properties and criticized for their high operation count and poor performance on vector machines; on the other hand explicit schemes offer advantages in storage requirements and good performance on vector computers at the price of stricter constraints on the maximum admissible time step.

Most of the available schemes have been extended to the treatment of the viscous equations. McCormack extended both his explicit and implicit schemes [8,9], while Beam and Warming [10] included the treatment of viscous terms in their celebrated alternating direction implicit scheme. ADI schemes for the Navier Stokes equations were also employed by Steger and Pulliam [11,12,13,14] in the development of their ARC2D and ARC3D computer codes, and Shang and Hankey have recently used a similar approach for calculating the flow field on a hypersonic cruiser [15]. However, up to now neither implicit nor explicit algorithms have reached their full potential capability.

Looking at the literature of the past 20 years (the Peyret and Viviand survey [16] thoroughly covers the period 1965-75 while Metha and Lomax [17] review the current state of the art), it would appear that implicit schemes could be better suited for dealing with the solution of the extremely stiff non-linear system resulting from the discretization of the time dependent gas-dynamics equations. One might expect that the time step constraint would heavily penalize the convergence properties of an explicit scheme, giving a definite edge to the implicit method. This would certainly be the case if a fully implicit solution of the system of discretized Navier Stokes equations by a Newton method were practicable. However, until now, the only direct method that has been successfully developed for the solution of the inviscid equations [18] uses a particular formulation that does not appear to be amenable to the Navier Stokes equations. All the available implicit schemes solve a factorized form of the discretized equations that drastically reduces their capability of completely bypassing the time step limit constraint.

Among the explicit methods, the finite volume approach of Jameson, Schmidt and Turkel [19], which uses a multistage time marching scheme, has been successfully applied to compute the inviscid flow field on geometries of increasing complexity. Indeed, solutions for a complete aircraft were recently obtained [20]. Moreover, development of acceleration techniques, such as the multigrid scheme of Jameson [21], has drastically reduced the cost of computing the steady state solution for inviscid flow over simpler 2-D and 3-D configurations. This impressive

success with the Euler equations has recently stimulated new interest in the application of explicit methods to the solution of the Navier Stokes equations [22,23].

#### 4. Difficulties in Viscous Computations

Some of the principal difficulties of the problem derive from the treatment of the convective terms and therefore they are already encountered in the solution of the Euler equations, namely:

- (1) The conservation equations are non-linear.
- (2) The solution in the transonic regime will generally contain shock waves.
- (3) The presence of regions, such as stagnation points and trailing edges where large derivatives occur, leads to large discretization errors.
- (4) The solution is required in unbounded domains.

Other problems are specifically related to the nature of the viscous phenomena bounded in extremely thin regions such as boundary layers and wakes.

- (1) Computations have to be performed on highly stretched meshes to provide the clustering of points needed to resolve the high gradients in the viscous regions. To provide a constant resolution of boundary layers and wakes, the degree of stretching should be, ideally, a function of the Reynolds number based on the streamwise distance.
- (2) The small dimensions of the computational cells (typically of order  $2/Re^{1/4}$ ) leads to extremely small allowable time steps for both implicit and explicit schemes, drastically degrading the convergence rate.

An additional problem is encountered in the simulation of turbulent flows by using the Reynolds averaged equations. A sufficient number of closure approximations is needed in order to equate the number of unknowns to the number of equations available. There must be provided by the introduction of a turbulence model.

##### 5. Directions of the Research

This work is concerned with the development of accurate and efficient explicit schemes for the solution of 2-D viscous flow problems in aerodynamics. Besides the fact that the analysis of 2-D configurations is of practical interest in the early stages of a design, a systematic study of the accuracy of numerical methods in 3-D is severely limited by the memory of currently available computers. Nevertheless the numerical schemes of the present study can be generally carried over to the full 3-D viscous conservation laws.

The principal requirement for a satisfactory solution of the viscous equations of gasdynamics is the reduction of the discretization error to a level such that any numerical dissipative phenomena, introduced by the scheme, should not interfere with the effects of physical transport phenomena. This problem is particularly severe in regions of strong interaction where, depending on the scale of the problem (the Reynolds number), an accurate solution is still impeded by the lack of powerful enough computers. In the approach followed in the present study the discretization of the spatial operators is entirely separated from the time marching scheme. The conservation equations are first discretized by a finite volume technique using either a vertex or a cell centered formulation (i. e. the flow variables are stored respectively at the corners or centers of the computational cell). Then, a class of multistage schemes is used to perform time integration. This procedure makes it possible to address independently specific problems related to different parts of the numerical scheme. For example spatial discretization errors, artificial dissipation and shock capturing properties (upwind biasing) are totally independent of the problem of time marching stability and convergence acceleration. Following this approach, several alternative discretization formulas for the viscous terms have been studied and evaluated while carefully monitoring the effects of artificial dissipation and, for the first time, the goal of obtaining accurate Euler solutions on highly stretched grids has been achieved in the present work.

For steady state computations, efficiency has also been enhanced by the use of multiple grids, locally varying time steps and implicit smoothing of the residuals. Although the idea of

using multiple grid techniques for accelerating the convergence to a steady state of the compressible Navier Stokes and Reynolds averaged equations has been subject to other investigations [24,25], reports of success are rare. In most cases the results have been encouraging but the convergence rate obtained fell far short of those obtained by similar multigrid schemes when applied to the inviscid equations [26]. In this thesis, stemming from the work of Jameson [27], two highly efficient multigrid schemes have been developed for the full set of viscous conservation laws, allowing convergence to be achieved in 5 times fewer cycles than any other method yet developed.

#### 6. Outline of the Presentation

The following chapters discuss the implementation of these ideas in some detail. In Chapter 2 the mathematical formulation of the problem is discussed. The compressible Navier Stokes equations and their Reynolds averaged form are reviewed together with the appropriate boundary conditions. Chapter 3 reviews the alternative discretization procedures using both vertex and cell centered formulations ,as well as the time integration schemes. In Chapter 4 the multigrid procedure that has been employed is discussed together with the other convergence acceleration techniques.

When assessing the validity of a computational method, in the absence of analytic results, it is extremely important to compare the computed results with available experimental data and/or other computed results. In the present study , in order to avoid uncertainties that arise from turbulence modeling ,the proposed algorithm has been extensively tested for laminar flows over 2-D airfoils over a fairly wide range of Mach and Reynolds numbers. These results are reported and discussed in Chapter 5.

Applications to the solution of the Reynolds averaged equations are also presented in Chapter 6. For these computations a simple algebraic turbulence model originally developed by Baldwin and Lomax [28] and discussed in Appendix A has been used for closure. The choice of

this turbulence model was made exclusively for sake of comparison with other computed results in the literature.

As a result of the present work, two efficient, robust, and accurate multigrid methods have been devised for the Navier Stokes and Reynolds averaged equations. The combination of accuracy and speed provides an essential tool for studies of turbulence modeling for aerodynamic flows, by making it possible to obtain a rapid and reliable assessment of the effects of substituting alternative models.

## CHAPTER 2

### MATHEMATICAL FORMULATION

#### 1. Integral form of the Navier Stokes Equations

Within the continuum limit, the motion of a compressible fluid is governed by the equations that derive from the principles of classical mechanics and thermodynamics applied to a finite control volume [29]. Let  $\rho$ ,  $\mathbf{u}$ ,  $E$  be respectively the density, velocity vector and total absolute enthalpy per unit mass (thermal plus kinetic energy), then for a domain  $\Omega$ , fixed with respect to a cartesian frame of reference, bounded by the surface  $\partial\Omega$ , the integral form of the conservation equations can be written, neglecting the body forces, as:

$$\begin{aligned} \frac{d}{dt} \int_{\Omega} \rho d\Omega + \int_{\partial\Omega} \rho \mathbf{u} \cdot \mathbf{n} d(\partial\Omega) &= 0 \\ \frac{d}{dt} \int_{\Omega} \rho u_i u_i d\Omega + \int_{\partial\Omega} \rho \mathbf{u} \mathbf{u} \cdot \mathbf{n} d(\partial\Omega) &= - \int_{\Omega} p \mathbf{n} d\Omega + \int_{\partial\Omega} \underline{\sigma} \mathbf{n} d(\partial\Omega) \\ \frac{d}{dt} \int_{\Omega} \rho \frac{d}{dt} \int_{\Omega} \rho E d\Omega + \int_{\partial\Omega} \rho E \mathbf{u} \cdot \mathbf{n} d(\partial\Omega) &= - \int_{\Omega} p \mathbf{u} \cdot \mathbf{n} d(\partial\Omega) + \int_{\partial\Omega} \mathbf{u} \cdot \underline{\sigma} \mathbf{n} d(\partial\Omega) \end{aligned} \quad (2.1.1)$$

where  $\underline{\sigma}$  is the viscous stress tensor and  $\mathbf{q}$  is the heat flux vector.

The pressure  $p$  is related to the conservative variables by the equation of state. For a calorically and thermally perfect gas this is:

$$p = (\gamma - 1) \rho [E - \frac{1}{2}(\mathbf{u} \cdot \mathbf{u})] \quad (2.1.2)$$

For a Newtonian fluid it is assumed that the stress  $\underline{\sigma}$  is proportional to the rate of strain and, making use of the Stokes postulate (neglecting the bulk viscosity), the constitutive equation

for the stress tensor can be written as:

$$\underline{\sigma} = \mu [(\nabla \underline{u} + \nabla \underline{u}^T) - \frac{2}{3} \nabla \cdot \underline{u} \underline{I}] \quad (2.1.3)$$

The Fourier postulate is used to obtain the constitutive equation for the heat flux vector

$$\underline{q} = -k \nabla T \quad . \quad (2.1.4)$$

For a compressible fluid additional relations are used to account for the variation of the molecular transport coefficients with the local thermodynamic state of the fluid. In the present study we assume that the molecular viscosity is a function of the temperature alone, and that its dependence on the temperature can be properly modeled by either the Sutherland law

$$\mu = \frac{1.461 \cdot 10^{-6} T^{3/2}}{T + 110.3} \quad (2.1.5)$$

or the Chapman-Rubesin approximation

$$\mu = const \times T^n \quad (2.1.6)$$

The assumption of constant Prandtl number gives the additional relation for the thermal conductivity:

$$k = \frac{c_p \mu}{Pr} \quad (2.1.7)$$

## 2. Differential form of the Navier Stokes Equations

While the finite volume formulation used to discretize the conservation equations makes use of the integral form presented in the previous section, it is also convenient to introduce the differential form in order to analyze some of the properties of the numerical scheme, and to derive the Reynolds averaged equations for turbulent flows.

With the following definition of the non dimensional variables:

$$(x^*, y^*) = (x/c, y/c)$$

$$t^* = t(p_\infty/\rho_\infty)^{1/2}/c$$

$$\rho^* = \frac{\rho}{\rho_\infty}$$

$$u^* = \frac{u}{(p_\infty/\rho_\infty)^{1/2}}$$

$$\begin{aligned} v^* &= \frac{v}{(\rho/\rho_\infty)^{1/2}} \\ E^* &= \frac{E}{(\rho/\rho_\infty)} \\ p^* &= \frac{p}{p_\infty} \\ \mu^* &= \frac{\mu}{\mu_\infty} \\ k^* &= \frac{k}{k_\infty} = \frac{c_p \mu^*}{Pr} \end{aligned}$$

where  $c$  is the chord length and the subscript  $\infty$  refers to the free stream condition, and dropping the superscript \* from here on for sake of brevity, the Navier Stokes equations in two dimensions and a cartesian coordinate system can be written as:

$$\frac{\partial w}{\partial t} + \frac{\partial f_c}{\partial x} + \frac{\partial g_c}{\partial y} = \frac{\sqrt{M_\infty}}{Re_\infty} \left[ \frac{\partial f_v}{\partial x} + \frac{\partial g_v}{\partial y} \right] \quad (2.2.1)$$

where the vector of the dependent variables  $w$ , the convective flux vectors  $f_c$  and  $g_c$ , and the flux vectors for the viscous terms  $f_v$  and  $g_v$  are defined by the following relations:

$$w = \begin{bmatrix} \rho \\ \rho u \\ \rho v \\ \rho E \end{bmatrix} \quad f_c = \begin{bmatrix} \rho u \\ \rho u^2 + p \\ \rho uv \\ \rho uE + up \end{bmatrix} \quad g_c = \begin{bmatrix} \rho v \\ \rho uv \\ \rho v^2 + p \\ \rho vE + vp \end{bmatrix} \quad (2.2.2)$$

$$f_v = \begin{bmatrix} 0 \\ \sigma_{xx} \\ \sigma_{xy} \\ u\sigma_{xx} + v\sigma_{xy} - q_x \end{bmatrix} \quad g_v = \begin{bmatrix} 0 \\ \sigma_{xy} \\ \sigma_{yy} \\ u\sigma_{yx} + v\sigma_{yy} - q_y \end{bmatrix} \quad (2.2.3)$$

The pressure  $p$  is related to the dependent variables by the equation of state:

$$p = (\gamma - 1) \rho [E - \frac{1}{2}(u^2 + v^2)]. \quad (2.2.4)$$

Finally the following relations :

$$\begin{aligned} \sigma_{xx} &= 2\mu u_x - \frac{2}{3}\mu(u_x + v_y) \\ \sigma_{yy} &= 2\mu v_y - \frac{2}{3}\mu(u_x + v_y) \\ \sigma_{xy} &= \sigma_{yx} = \mu(u_y + v_x) \\ q_x &= -k \frac{\partial T}{\partial x} = -\frac{\gamma}{\gamma - 1} \frac{\mu}{Pr} \frac{\partial p}{\partial x} \\ q_y &= -k \frac{\partial T}{\partial y} = -\frac{\gamma}{\gamma - 1} \frac{\mu}{Pr} \frac{\partial p}{\partial y} \end{aligned} \quad (2.2.5)$$

represent the constitutive equations of the stress tensor  $\sigma_{ij}$  and of the heat flux vector  $q$ .

### 3. Boundary Conditions

Appropriate conditions at the fluid boundary are needed to complete the definition of the mathematical problem posed by the solution of the system of conservation laws (2.1.1). The dependence of the solution of the compressible Navier Stokes equations on the formulation of the boundary conditions has not been extensively investigated. In general the boundary conditions are set on the basis of phenomenological arguments.

At a solid boundary the following conditions are imposed for the momentum equation:

$$\begin{aligned} (\mathbf{u} \cdot \mathbf{n})_w &= 0 \\ (\mathbf{u} \cdot \mathbf{t})_w &= 0 \end{aligned} \quad (2.3.1)$$

where  $n$  and  $t$  are, respectively, the unit normal and the unit tangent vectors. These correspond, respectively, to no-injection and no-slip conditions along the material surface. The validity of the adherence condition at a fluid-solid interface is verified for a flow under normal conditions. However, for some of the laminar solutions computed in this study, which correspond to low density flow conditions, the validity of such an assumption can be questioned.

An additional boundary condition is also required for the energy equation. In this study, both adiabatic

$$(\mathbf{q} \cdot \mathbf{n})_w = 0 , \quad (2.3.2)$$

and isothermal

$$T_w = const \quad (2.3.3)$$

conditions are considered.

The value of the pressure along the solid boundary is derived from the conservation at the wall of the normal component of the momentum. In dimensionless form this relation is given by:

$$(\nabla p \cdot \mathbf{n})_w = \frac{\sqrt{\gamma} M}{Re_\infty} (\underline{\sigma} \cdot \mathbf{n})_w . \quad (2.3.4)$$

#### 4. Compressible Reynolds Averaged equations

While it is generally accepted that the Navier Stokes equations presented in the previous sections are in principle capable of describing the behaviour of all kind of flows, at high Reynolds numbers the onset of turbulence makes it impracticable to solve them. Even if one could, the problems of existence, uniqueness, and stability of the solution still remain to be answered.

The most common approach to overcome this difficulty is to use a statistical averaging procedure (Reynolds decomposition) of the variables [30]. The generic variable  $g$  is replaced into the Navier Stokes equations by the sum of a mean value  $\bar{g}$  and a local instantaneous fluctuation  $g'$ . Then, an average of the conservation laws is taken yielding the equations for the mean motion. There remains some latitude in the definition of the averaging operators. The form of the averaged equations used in the present study is discussed next.

Following Rubesin and Rose [31], the density  $\rho$ , the pressure  $p$ , the shear stress tensor  $\sigma_{ij}$ , and the components of the heat flux vector  $q_i$  are decomposed in a time averaged mean ( $\bar{g}$ ), and a fluctuation ( $g' = g - \bar{g}$ ). The time average operator is defined as:

$$\bar{g} = \frac{1}{T} \int_0^T g dt \quad (2.4.1)$$

where the time interval  $T$  is assumed to be longer than the characteristic time scale of the turbulence. The velocity components  $u_i$ , the internal energy per unit mass  $e$ , the molecular viscosity coefficient  $\mu$ , and the thermal conductivity  $k$  are decomposed into a mass-weighted averaged ( $\bar{g}$ ) and a local instantaneous fluctuation ( $g'' = g - \bar{g}$ ). The mass-weighted average operator is defined as :

$$\bar{g} = \frac{\rho \bar{g}}{\rho} \quad . \quad (2.4.2)$$

When the expansion of the dependent variables is carried out in the differential conservation laws and a time average of the equations is taken, the following equations are obtained:

$$\frac{\partial \bar{p}}{\partial t} + \frac{\partial}{\partial x_j} (\bar{\rho} \bar{u}_j) = 0 \quad (2.4.3)$$

$$\frac{\partial \bar{\rho} \bar{u}_i}{\partial t} + \frac{\partial}{\partial x_j} \left[ \bar{\rho} \bar{u}_j \bar{u}_i + \bar{p} \delta_{ij} - (\bar{\sigma}_{ij} - \bar{\rho} \bar{u}''_i \bar{u}''_j) \right] = 0 \quad (2.4.4)$$

$$\begin{aligned} \frac{\partial \bar{\rho} \bar{E}}{\partial t} + \frac{\partial}{\partial x_j} \left[ \bar{\rho} \bar{u}_j \bar{E} - \bar{u}_i (-\bar{p} \delta_{ij} + \bar{\sigma}_{ij} - \bar{\rho} \bar{u}''_i \bar{u}''_j) - \right. \\ \left. \bar{u}''_i (-\bar{p} \delta_{ij} + \bar{\sigma}_{ij} - \frac{1}{2} \bar{\rho} \bar{u}''_i \bar{u}''_j) + \bar{q}_j + \bar{\rho} \bar{u}''_j \bar{e}'' \right] = 0 \end{aligned} \quad (2.4.5)$$

Because of the Reynolds decomposition and averaging, extra terms (the correlation tensors) arise in the equations. Physically those terms represent the turbulent transport of momentum and energy due to velocity and pressure fluctuations. The mean energy dissipation  $\bar{u}''_i (-\bar{p} \delta_{ij} + \bar{\sigma}_{ij} - \frac{1}{2} \bar{\rho} \bar{u}''_i \bar{u}''_j)$  is generally neglected on the basis of an order of magnitude consideration. One can also observe that by defining

$$\sigma_{ij\text{tot}} = \bar{\sigma}_{ij} - \bar{\rho} \bar{u}''_i \bar{u}''_j \quad (2.4.6)$$

$$q_{j\text{tot}} = \bar{q}_j + \bar{\rho} \bar{u}''_j \bar{e}'' \quad (2.4.7)$$

the equations are reduced to the same form as the instantaneous Navier Stokes equations. However one is faced with the closure problem of defining new appropriate constitutive relations for the unknown terms.

Owing to the non-linearity of the Navier-Stokes equations, it is not possible to give rigorous constitutive equations for the correlations, because the process of propagation of the correlations is an infinite one, and equations for the correlations of a certain order will contain higher order correlations. The result is that the process must be truncated by introducing submodels that relate the higher order correlations to lower order ones as well as the mean properties of the flow. Although an extensive review of possible turbulence models goes beyond the intent of the present study, it seems appropriate to summarize the possible approaches that have been proposed to achieve closure of the Reynolds averaged equations for aerodynamic flows.

Following the Bussinesq hypothesis, the procedure for evaluating the eddy diffusivity  $v_{urb}$  is generally employed to classify the currently used turbulence models. The eddy diffusivity  $v_{urb}$  can be generally written as:

$$v_{urb} = C_v L V \quad (2.4.8)$$

where  $C_v$  is an empirical constant,  $V$  is a characteristic velocity scale, and  $L$  is a characteristic

length scale. The simplest eddy viscosity models belong to the class of the so called algebraic or zero - equation models. In these models the velocity and length scales are correlated to the mean flow properties through algebraic laws. The Cebeci - Smith model [32] and the subsequent reformulation of it by Baldwin and Lomax [28] belong to this class. In these models a two layer formulation is assumed, with different definitions of the length and velocity scales in the inner and outer part of the boundary layer. One principal drawback common to all algebraic models is that the history of the flow is completely neglected.

More sophisticated models make use of additional partial differential equations. In the so called one-equation models it is generally assumed that the velocity scale  $V$  is proportional to the square root of the mean turbulent kinetic energy  $\kappa$ , whereas the length scale  $L$  is specified by an algebraic relation of the form  $L=L(y)$ . In this case the solution an additional conservation law for the mean turbulent kinetic energy is required. In the one-equation models the length scale is not related to the properties of the mean flow. To overcome this deficiency an additional field equation is introduced in the so called two-equation models. For example the  $k-\epsilon$  formulation [33] requires the solution of additional differential equations for the mean turbulent kinetic energy  $\kappa$  and for the mean rate of dissipation  $\epsilon$ . It is then assumed that  $V$  is proportional to  $\sqrt{\kappa}$ , and  $L = L(\kappa, \epsilon)$ .

Whenever additional transport equations are specified, a choice must be made about their treatment in the region very close to the wall. Either the integration of the additional laws is carried out directly to the wall, or the values at the solid surfaces are extrapolated by using wall functions. The first approach can be severely complicated by the appropriate modeling required in the near wall region; on the other hand, by using the wall function approach, detailed knowledge of the wall region is lost. Both formulations have merits, but a final assessment of their respective capabilities and limitations for treating aerodynamics flows is still needed [34].

In a different class of models, rather then rely on the Boussinesq hypothesis, the solution of the transport equation for the Reynolds stress is directly attempted. This approach requires

closure of higher order correlation tensors and increases the number of additional field equations required. In the case of a second order closure, for example, seven additional field equations must be solved [6]. The increased amount of work required by a Reynolds stress model severely limits the application of this approach to the simulation of flows on complex geometries.

A particularly interesting model recently developed by Johnson and King [35] should also be mentioned. Following the approach originally suggested by Bradshaw, Ferris and Atwell [36], the mean turbulent kinetic energy equation is reduced to an ordinary differential equation for the Reynolds stress along the path of its maximum. Additional algebraic relations correlate the values of the eddy viscosity to the computed Reynolds stress values. The model seems perhaps less accurate than the algebraic models for the simulation of attached flows, but the success obtained for separated flows [37] strongly indicates the merits and potential advantages of this hybrid formulation.

In the present study the Reynolds stress tensor is modeled as being proportional to the rate of deformation tensor of the mean flow. Therefore the expression for the total stress tensor is assumed to be:

$$(\sigma_{ij})_{tot} = \mu_{tot} (\nabla \bar{u} + \nabla \bar{u}^T - \frac{2}{3} \nabla \cdot \bar{u}) \quad (2.4.9)$$

where  $\mu_{tot} = \mu_{lam} + \mu_{turb}$ , and  $\mu_{turb}$  is the eddy viscosity coefficient. Similarly, the total heat flux vector results :

$$\mathbf{q} = -\gamma \left[ \frac{\mu_{lam}}{P_r} + \frac{\mu_{turb}}{P_{r,turb}} \right] \nabla \bar{\epsilon} \quad (2.4.10)$$

The eddy viscosity is computed by using the algebraic model of Baldwin and Lomax [28] which is detailed in Appendix A.

## CHAPTER 3

### NUMERICAL DISCRETIZATION

A finite volume technique is used to discretize the spatial operators appearing in eq (2.1.1).

Following this approach the computational domain is divided in subregions (the computational cells) and a discrete approximation of the analytical form of the equations is recovered by using the integral form of the conservation laws. Although the shape of the subdomains can in general be arbitrary [38], in this work we make use of quadrilateral cells. The use of the finite volume formulation offers several advantages over the classical finite difference form. First of all this procedure allows the average rate of change of the unknown vector  $w$  to be estimated in each subdomain while strictly preserving the conservation form. This property is of particular importance for shock capturing schemes. Moreover, since no metric derivatives are required, the finite volume formulation can handle without any problems mesh singularities such the singular point at the leading edge of a typical 2-D H-mesh (fig. 3.1) or, in 3-D, singular lines such as the axis in an axisymmetric case.

Two main alternative formulations are considered and discussed in the following sections. The variables are stored at the cell centers in the first approach and at the cell vertices in the second one. With either formulation one is then left with the problem of integrating in time a system of ordinary differential equations of the general form:

$$\frac{d(w\Omega)_{ij}}{dt} + R(w)_{ij} = 0 \quad (3.1)$$

where  $R(w)_{ij}$  represents the net contributions from the approximation of the convective ( $C(w)_{ij}$ )

and diffusion ( $D(w)_{ij}$ ) operators at the  $ij$ -th location, and  $\Omega_{ij}$  is the area of the control volume surrounding the  $ij$ -th point. This task is accomplished by making use of explicit multistage schemes of a particular class [39] that is reviewed in the closing section of this chapter.

Keeping the space and time discretization separate allows additional flexibility in the choice of the integration scheme which can be tailored for the solution of specific problems, such as the use of a scheme with a high order of accuracy in time for unsteady computations. Moreover, for steady state computations, it ensures recovery of a stationary solution that does not depend on the time step. This is a definite advantage over other explicit schemes such as the MacCormack scheme.

### 1. Cell Centered scheme

Let the unknown vectors  $w$  be stored at the center of the computational cell (fig. 3.1.1): then an approximation of the convective operator can be obtained as follows [39]. First the flux velocity  $Q_l$  is evaluated on each side of the  $l$ -th edge as :

$$Q_l^+ = \frac{\Delta y_l (\rho u)_l^+ - \Delta x_l (\rho v)_l^+}{\rho_l^+} \quad (3.1.1)$$
$$Q_l^- = \frac{\Delta y_l (\rho u)_l^- - \Delta x_l (\rho v)_l^-}{\rho_l^-}$$

where  $\Delta y_l$  and  $\Delta x_l$  are the increments of  $x$  and  $y$  along the  $l$ -th edge with the appropriate sign.

Then the net flux across the  $l$ -th edge can be evaluated as

$$\mathbf{F}_l = \frac{1}{2} (Q_l^+ w^+ + Q_l^- w^-) \quad (3.1.2)$$

Finally the net contribution of convection to the balance in the  $ij$  cell is computed as

$$C(w)_{ij} = \sum_{l=1}^4 \mathbf{F}_l \quad (3.1.3)$$

This discretization reduces to central differencing on a cartesian grid and is second order accurate on a mesh with a smooth variation in the cell distribution.

In constructing an approximation to the viscous terms, we wish to retain all the advantages of the finite volume formulation which are a consequence of its derivation from the integral form

of the equations. Thus a similar flux balance is formed for the viscous terms also using the cell as a control volume. The numerical estimate of the viscous terms, however, needs an approximation of the first partial derivatives of the velocity and temperature to evaluate the shear stress and heat flux components. For computing these derivatives we make use of a discrete form of the Gauss theorem [Appendix B]. Two different approximation methods have been considered.

In the first method (CCS-A) the theorem is applied on the path joining the centers of two adjacent cells with the end points of their dividing side (fig. 3.1.2a). This requires averaging of the flow variables at the cell vertices but gives an estimate of the derivatives directly at the midpoint of the edges. For the  $i$ -th edge we have:

$$\Phi_i = (\mathbf{f}_v \Delta y_i - \mathbf{g}_v \Delta x_i) \quad (3.1.4)$$

The net viscous flux contribution out of the computational cell is then obtained by summing over the four sides as:

$$D(\mathbf{w})_{ij} = \sum_{i=1}^4 \Phi_i. \quad (3.1.5)$$

The second discretization procedure (CCS-B) does not require averaging of the flow variables. Instead the shear stress and heat flux components are computed at the cell vertices by application of the discrete Gauss theorem to the quadrilateral region formed by joining the centers of four cells surrounding the vertex (fig. 3.1.2b). Then a second application of the Gauss theorem gives directly the total volume contribution of the viscous terms in the computational cell. Alternatively this procedure can be seen as an average of the components of  $\mathbf{f}_v$ ,  $\mathbf{g}_v$  at the midpoint of the  $i$ -th edge :

$$\begin{aligned} \mathbf{f}_{v_i} &= \frac{1}{2}(\mathbf{f}_{v_1} + \mathbf{f}_{v_2}) \\ \mathbf{g}_{v_i} &= \frac{1}{2}(\mathbf{g}_{v_1} + \mathbf{g}_{v_2}) \end{aligned} \quad (3.1.6)$$

followed by the evaluation of the fluxes (3.1.4) and the sum (3.1.5) over the four sides of the cell.

In this study we employ an algebraic turbulence model that eliminates the need for additional discretization procedure. However the discretization formulas developed for the convective

and diffusive operators can be used to discretize the additional conservation equations required by multi-equation turbulence models.

The two formulations (CCS-A) and (CCS-B) are clearly equivalent on a regular cartesian mesh. However, the same is not generally true on body fitted curvilinear grids because of the different averaging procedures utilized by the two schemes. It turns out, in practice, that there are no substantial differences and both schemes perform equally well on body fitted grids. Another potential difference between the two formulations could arise in the application to the Reynolds averaged equations, since it has been noted that improper averaging of the eddy viscosity can degrade the accuracy [40]. The first formulation is better suited for computing the eddy viscosity at the cell centers. In doing so, however, additional averaging of the eddy viscosity is needed to compute a value at the cell edges. In the second formulation it is convenient to evaluate the eddy viscosity at the vertices, and no additional averaging of the eddy viscosity is required to compute the Reynolds stress terms. It turns out in practice that there are no noticeable differences between the two formulations also in this respect.

## 2. Vertex Scheme

One of the main difficulties of solving the viscous conservation laws is caused by the high aspect ratio of the computational cells in the vicinity of the body surface and wake regions. The accuracy of the discretization formulas on the highly stretched meshes designed to resolve the viscous effects is of particular concern in this study. In principle, none of the averaging procedures required by the two cell centered schemes discussed in the previous section should degrade on high aspect ratio cells. However, an alternative formulation where the flow variables are defined at the corners of the computational cell has also been considered, and will be discussed next.

The derivation of the finite volume formulation for a scheme where the variables are stored at the vertices of the computational cell follows the same principles underlined in the previous

section. Here a control volume is formed for each vertex by taking the union of the four cells meeting at that vertex. Eq. (3.1) then takes the form

$$\frac{d}{dt} (\sum_k \Omega_k) w_{ij} + \sum_k C_k (w)_{ij} - \sum_k D_k (w)_{ij} = 0 \quad (3.2.1)$$

where  $\Omega_k$ ,  $C_k$ ,  $D_k$  are respectively the cell area, convective flux balance and viscous contribution for the  $k$ -th cell in the control volume surrounding the vertex  $ij$ .

For the convection contribution the mean flux across an edge can be conveniently approximated as the average of the values at its two end points (fig. 3.2.1).

$$F_{12} = \frac{1}{2} (F_1 + F_2) \quad (3.2.2)$$

The sum  $\sum_k C_k$  in eq (3.2.1), which then amounts to a trapezoidal integration rule around the boundary of the control surface, should remain fairly accurate even on an irregular mesh. This is an advantage of the vertex formulation over the cell centered scheme, in which the midpoint of the line joining the centers does not necessarily coincide with the midpoint of the corresponding edge.

This could yield a reduction of accuracy on a distorted or kinked mesh [41].

In order to estimate the viscous terms, an auxiliary control volume is formed by connecting the cell centers  $c_1$ ,  $c_2$ ,  $c_3$ , and  $c_4$  (fig. 3.2.2). The discrete Gauss theorem is applied once on the computational cell to obtain a numerical approximation to the stress tensor and heat flux at the cell centers. The divergence of the stress tensor and of the heat flux vector is then obtained directly at the enclosed vertex by a second application of the theorem to the auxiliary control volume which is scaled, for consistency, to the sum of the four computational cells used in the convective balance. The net viscous contribution is then recovered in the following form:

$$\begin{aligned} D(\rho u)_{ij} &= [[(\sigma_{xx_i} - \sigma_{xx_s}) \cdot (y_{c_s} - y_{c_i}) - (\sigma_{xx_i} - \sigma_{xx_s}) \cdot (y_{c_i} - y_{c_s})] \\ &\quad - [(\sigma_{xy_i} - \sigma_{xy_s}) \cdot (x_{c_s} - x_{c_i}) - (\sigma_{xy_i} - \sigma_{xy_s}) \cdot (x_{c_i} - x_{c_s})]] / \\ &\quad [(x_{c_i} - x_{c_s}) \cdot (y_{c_s} - y_{c_i}) - (y_{c_i} - y_{c_s}) \cdot (x_{c_i} - x_{c_s})] \\ D(\rho v)_{ij} &= [[(\sigma_{xy_i} - \sigma_{xy_s}) \cdot (y_{c_s} - y_{c_i}) - (\sigma_{xy_i} - \sigma_{xy_s}) \cdot (y_{c_i} - y_{c_s})] \\ &\quad - [(\sigma_{yy_i} - \sigma_{yy_s}) \cdot (x_{c_s} - x_{c_i}) - (\sigma_{yy_i} - \sigma_{yy_s}) \cdot (x_{c_i} - x_{c_s})]] / \\ &\quad [(x_{c_i} - x_{c_s}) \cdot (y_{c_s} - y_{c_i}) - (y_{c_i} - y_{c_s}) \cdot (x_{c_i} - x_{c_s})] \end{aligned} \quad (3.2.3)$$

$$\begin{aligned}
 D(\rho E)_{ij} = & [[[(u\sigma_{xx} + v\sigma_{xy} - q_x)_c, -(u\sigma_{xx} + v\sigma_{xy} - q_x)_c], (y_{c_1} - y_{c_2})] \\
 & - [(u\sigma_{xx} + v\sigma_{xy} - q_x)_c, -(u\sigma_{xx} + v\sigma_{xy} - q_x)_c], (y_{c_1} - y_{c_2})] \\
 & - [[(u\sigma_{xy} + v\sigma_{yy} - q_y)_c, -(u\sigma_{xy} + v\sigma_{yy} - q_y)_c], (x_{c_1} - x_{c_2})] \\
 & - [(u\sigma_{xy} + v\sigma_{yy} - q_y)_c, -(u\sigma_{xy} + v\sigma_{yy} - q_y)_c], (x_{c_1} - x_{c_2})]] / \\
 & [(x_{c_1} - x_{c_2})(y_{c_1} - y_{c_2}) - (y_{c_1} - y_{c_2})(x_{c_1} - x_{c_2})]
 \end{aligned}$$

The above procedure has been devised with the objective of keeping the support as small as possible. Also, the discretization formulas derived reduce to the standard second differences formulas on regular cartesian grids. The reasoning that suggested the above discretization can be better illustrated with the help of the one dimensional analogue (fig. 3.2.3). It is straightforward to see that the one dimensional form of the proposed discretization reduces to :

$$u_{xx}(x_{i+1/2} - x_{i-1/2}) = \left[ \frac{\delta u}{\delta x} \right]_{i+1/2} - \left[ \frac{\delta u}{\delta x} \right]_{i-1/2} \quad (3.2.4)$$

that is a three point formula involving only the values at the nodes  $i, i-1, i+1$ . Also in the limit of constant  $\delta x$  the above expression reduces to the standard second difference approximation. However, if the same control volume used for the convective balance is also used for discretizing the viscous terms, the following five point formula would be recovered:

$$2u_{xx}(x_{i+1/2} - x_{i-1/2}) = \left[ \left[ \frac{\delta u}{\delta x} \right]_{i+3/2} + \left[ \frac{\delta u}{\delta x} \right]_{i+1/2} \right] - \left[ \left[ \frac{\delta u}{\delta x} \right]_{i-1/2} + \left[ \frac{\delta u}{\delta x} \right]_{i-3/2} \right] \quad (3.2.5)$$

Note also that in the limit of constant  $\delta x$  the above formula becomes:

$$u_{xx} = \frac{u_{i+2} - 2u_{i+1} + u_{i-2}}{4\delta x^2} \quad (3.2.6)$$

causing the decoupling of odd and even points.

The discretization procedure developed here could be easily extended to treat additional field equations required by more complex turbulence models. If an algebraic model is used, however, it is more convenient to compute the eddy viscosity at the center of the computational cell. The vertex formulation guarantees conservation, is computationally efficient and yields second order accuracy on a grid with a smooth variation in the distribution of points.

### 3. Artificial Dissipation

The finite volume scheme defined by eq. (3.1) is intrinsically dissipative in regions where the physical viscous terms dominate. However, moving away from the solid boundaries and the wake regions, the convective operator starts to play a major role. This is partly due to the fact that the physical effects of transport die out, and it is partly caused by the stretching of the computational mesh that contributes to a loss of resolution in the approximation of the viscous terms. In both cases the possibility of undamped oscillatory modes common to the treatment of the Euler equations arises. Therefore in order to avoid decoupling of even and odd points [39] the addition of artificial dissipative terms is needed.

A second reason for introducing additional dissipative terms is to allow the clean capture of shock waves. Although the Navier Stokes equations should give in principle an accurate description of the structure of a weak shock wave [42], the thickness of the shock which is of the order of the mean free path, would require an extremely fine resolution that cannot be attained even with the new generation of computers. For this reason it pays off to trade some of the accuracy in the neighborhood of the shock wave in favor of damping undesirable oscillations.

Several formulations of artificial damping terms have been proposed for the inviscid equations. Stemming from the early work of Godunov [43] a variety of dissipative and upwind schemes designed to have good shock capturing properties have been proposed in the past. However the objective of combining high accuracy, resolution of shock waves and contact discontinuities with the elimination of spurious oscillations continues to be one of the main areas in which contributions are needed. This is particularly true on the highly stretched meshes designed to resolve the viscous phenomena. One approach to this problem is flux difference splitting in conjunction with flux limited dissipation [49]. It turns out in practice, however, that shock waves can be effectively captured with a simple formulation by making use of adaptive coefficients [39].

A low background level of dissipation is introduced and it is increased in the neighborhood

of the shock wave to a peak value proportional to the local wave speed. The dissipative terms are constructed in a similar manner for every equation by using a flux balance formulation that preserves the original conservation form. Namely, for a rectilinear mesh these terms have the following form:

$$d_{i+\frac{1}{2},j} - d_{i-\frac{1}{2},j} + d_{i,j+\frac{1}{2}} - d_{i,j-\frac{1}{2}} \quad (3.3.1)$$

where the fluxes are constructed by blending first and third differences of the dependent variables.

For example the dissipative flux in the  $i$ -direction for the continuity equation is given by:

$$d_{i+\frac{1}{2},j} = S (\epsilon^{(2)} - \epsilon^{(4)} \delta_x^2) (p_{i+1,j} - p_{i,j}) \quad (3.3.2)$$

where  $\delta_x^2$  is the second difference operator;  $\epsilon^{(2)}$  and  $\epsilon^{(4)}$  are adaptive coefficients, and  $S$  is a scaling factor proportional to an estimate of the maximum local wave speed.

The coefficient  $\epsilon^{(4)}$  provides a background dissipation in smooth regions of the flow field, while shock capturing is controlled by the coefficient  $\epsilon^{(2)}$  which is made proportional to the normalized second difference of some relevant flow quantity. Generally this can be taken as the normalized second difference of the pressure

$$\epsilon^{(2)} \propto \left| \frac{p_{i+1,j} - 2p_{i,j} + p_{i-1,j}}{p_{i+1,j} + 2p_{i,j} + p_{i-1,j}} \right| \quad (3.3.3)$$

Alternatively, the normalized second difference of the entropy can be particularly effective for viscous computations.

In order to obtain a proper solution of the Navier Stokes equations the artificial dissipation terms should be of a smaller order than the real viscous terms, and care must be taken in order to avoid the interference of the artificial damping terms with the physical transport phenomena. Moreover the formulation of the extra dissipative terms must be consistent with the original form of the conservation equations. For these reasons the formulation with adaptive coefficients is particularly attractive, since it allows the precise monitoring of the magnitude of the artificial dissipation terms and their relative weight with respect to the physical terms. In an upwind scheme the dissipation is built into the discretization itself and therefore its size cannot be easily controlled.

In this work several different scaling factors have been studied for use in (3.3.2). In its original form [19] it has been proposed that :

$$S = \lambda_i + \lambda_j \quad (3.3.4)$$

where:

$$\begin{aligned} \lambda_i &= |uy_\eta - vx_\eta| + a(x_\eta^2 + y_\eta^2)^{1/2} \\ \lambda_j &= |vx_\xi - uy_\xi| + a(x_\xi^2 + y_\xi^2)^{1/2} \end{aligned} \quad (3.3.5)$$

where  $\xi$  and  $\eta$  are the coordinate directions in the computational plane.

This scaling has been found to be appropriate on grids with an aspect ratio close to 1. By analogy with the formulation of flux splitting [44,45] in which the flux itself is decomposed into components corresponding to different wave speeds the scaling factor could be chosen to be decomposed into the two coordinate directions as

$$\begin{aligned} S_i &= \lambda_i \\ S_j &= \lambda_j \end{aligned} \quad (3.3.6)$$

This again leads to good shock capturing properties and it has been found to be adequate for computational meshes of moderately high aspect ratio (up to 10). However from the expression (3.3.6) it is clear that a further increase in the aspect ratio of the mesh will cause an imbalance of the coefficients in the  $i$  and  $j$  directions.

Instead of (3.3.4) or (3.3.6), in order to redistribute the artificial dissipation between the two coordinate directions, it is here proposed to adjust the scaling factors in the following form:

$$\begin{aligned} S_i &= \Phi(r)\lambda_i \\ S_j &= \Phi(\frac{1}{r})\lambda_j \end{aligned} \quad (3.3.7)$$

where

$$r = \frac{\lambda_j}{\lambda_i} \quad (3.3.8)$$

and

$$\Phi(r) = 1 + r^\alpha$$

where  $\alpha < 1$ . This formulation has been found to be satisfactory in computations where the aspect

ratio on the airfoil was increased to a maximum of 500.

#### 4. Discrete Boundary Conditions

The selection of appropriate discrete boundary conditions represents one of the major tasks in the development of a code for flow prediction. Not only the physical definition of the problem must be satisfied (for example inviscid flows require tangency of the velocity vector at solid walls whereas non slip conditions must be imposed for viscous flows), but also the discretization formula of the interior scheme could dictate the need of adjoining additional boundary conditions that are not necessarily required by the mathematical definition of the problem. Moreover the need to reduce unbounded domains to finite computational regions imposes the additional constraint of setting appropriate boundary conditions in the far field.

For the cell centered scheme at solid boundaries, the boundary conditions are set by adding an extra row of cells inside the walls (fig. 3.4.1). Then the non slip conditions are imposed by reflection of the velocity components:

$$\begin{aligned} u_1 &= -u_2 \\ v_1 &= -v_2 \end{aligned} \tag{3.4.1}$$

Adiabatic wall conditions are imposed by setting:

$$T_1 = T_2 \tag{3.4.2}$$

and the pressure at the wall is recovered by requiring:

$$p_1 = p_2 \tag{3.4.3}$$

corresponding to the high Reynolds number approximation of eq (2.3.4).

For the vertex scheme (fig. 3.4.2) the velocity components at the wall are set to be :

$$u_1 = v_1 = 0 \tag{3.4.5}$$

A constant value of the temperature is assigned at the wall:

$$T_1 = T_w. \tag{3.4.6}$$

Since the value of the density at the wall  $\rho_1$  can be computed by the interior scheme the value of

the pressure at the wall is then recovered from the equation of state

$$P_1 = (\gamma - 1) \rho_1 E_1 \quad (3.4.7)$$

For the treatment of the far field boundaries, care must be taken to avoid the reflection of outgoing disturbances. In the present study we make use of a C type (fig. 3.4.3) topology in which the inflow and outflow boundaries are well defined.

Provided that the boundary is placed far from the body (typically 20 chords) The inflow boundary  $\Sigma_{in}$  can be treated effectively by making use of the inviscid approximation [39]. Assuming that the flow is subsonic at infinity, fixed and extrapolated Riemann invariants for the one dimensional flow normal to the boundary, are introduced:

$$\begin{aligned} Ri_{\infty} &= q_{\infty} - \frac{2a_{\infty}}{\gamma - 1} \\ Ri_e &= q_{\infty} + \frac{2a_e}{\gamma - 1}. \end{aligned} \quad (3.4.8)$$

These correspond respectively to incoming and outgoing characteristics. By matching the values at the boundary the relations (3.4.8) give :

$$\begin{aligned} q_{\infty} &= \frac{1}{2}(Ri_e + Ri_{\infty}) \\ a_{\infty} &= \frac{(\gamma - 1)}{4}(Ri_e - Ri_{\infty}) \end{aligned} \quad (3.4.9)$$

These are the actual normal velocity component and speed of sound to be specified in the far field. The values of the tangential components of the velocity and of the entropy can then be specified by free stream values. This set of 4 variables fully defines the flow conditions at the inflow.

At the outflow boundary  $\Sigma_{out}$ , provided that fully developed conditions are reached in the wake region, the tangential component of the velocity and the entropy can be extrapolated from the inside.

For supersonic flows at the inflow all the quantities are set to the free stream values while at the outflow they are extrapolated from the interior.

Along the wake cut  $\Sigma_{wake}$  averaging is used ,in the vertex scheme, to provide continuity of the flow variables.

### 5. Time stepping scheme

The discretization procedure described in the previous sections lead to a set of coupled ordinary differential equations which can be written in the form:

$$\frac{d(\mathbf{w}\Omega)}{dt} + \mathbf{R}(\mathbf{w}) = 0 \quad (3.5.1)$$

where  $\mathbf{w}$  is the vector of the flow variables at the discrete set of points where they are stored,  $S$  the control volume, and  $\mathbf{R}(\mathbf{w})$  is the vector of the residuals consisting of the flux balance from the convective and diffusive terms as well as the artificial dissipative terms.

The time integration is performed by using schemes from a class of explicit one step multistage schemes derived from a generalization of the Runge Kutta formulation. These schemes have the advantage that they do not require a special start-up procedure, and moreover they can be tailored to give the desired stability properties [39]. Schemes of this class have been proved to be extremely effective in practice as a method of solving the Euler equations for unsteady problems [46] as well as for steady state computations.

Let  $\mathbf{w}^n$  be the result after  $n$  steps. Then the general form of an  $m$  stage scheme can be written as:

$$\begin{aligned} \mathbf{w}^{(0)} &= \mathbf{w}^n \\ \mathbf{w}^{(1)} &= \mathbf{w}^{(0)} - \alpha_1 \Delta t \mathbf{R}^{(0)} \\ &\dots \\ \mathbf{w}^{(m-1)} &= \mathbf{w}^{(0)} - \alpha_{m-1} \Delta t \mathbf{R}^{(m-2)} \\ \mathbf{w}^{(m)} &= \mathbf{w}^{(0)} - \Delta t \mathbf{R}^{(m-1)} \\ \mathbf{w}^{n+1} &= \mathbf{w}^{(m)} \end{aligned} \quad (3.5.1)$$

The residual of the  $q+1-st$  stage may be evaluated as:

$$\mathbf{R}^{(q)} = \sum_{r=1}^q \beta_{qr} \mathbf{R}(\mathbf{w}^{(r)}) \quad (3.5.2)$$

where

$$\sum_{r=0}^q \beta_{qr} = 1 \quad (3.5.3)$$

Schemes of this class have been extensively studied and analyzed in the literature [39]. It has been

proved that for an hyperbolic problem the maximum stability bound on the CFL number that can be obtained with an  $m$  stage scheme is  $(m-1)$  along the imaginary axis.

However the characteristics of the compressible Navier Stokes equations are mixed in the sense that there are regions within the flow field where they are hyperbolic and regions (i.e. near solid boundaries) where they present a parabolic problem. Therefore stability along the real axis is also needed. Moreover the computation of the viscous terms is expensive, and an evaluation at every stage of these terms would heavily penalize the operation count of the integration scheme. For these reasons we make use of an hybrid formulation in which the residual at the  $q+1st$  stage is taken as:

$$R^{(q)} = \sum_{r=0}^q [\beta_{qr} C(w^{(r)}) - \gamma_{qr} D(w^{(r)})] \quad (3.5.4)$$

where

$$\sum_{r=0}^q \beta_{qr} = 1 \quad , \quad \sum_{r=0}^q \gamma_{qr} = 1 \quad (3.5.5)$$

The optimal choice of the scheme depends on a trade-off between the extent of the stability region and the cost of the integration. A very effective three stage scheme with coefficients :

$$\alpha_1 = \alpha_2 = .6$$

and with a single evaluation of the dissipation has been employed for many of the calculations in the present work. The stability region of this scheme, obtained by Fourier analysis of the linear one-dimensional model problem  $u_t + u_x + \mu \Delta x^3 u_{xxx} = 0$  [39], is shown in fig.( 3.5.1). If a multistage scheme is used to solve such a model problem, the amplification factor  $f(z)$  can be recursively computed as a function of the Fourier symbol of the residual  $z = -i\lambda \sin \xi - 4\mu(1-\cos \xi)^2$ , where  $\lambda = \Delta t / \Delta x$  is the CFL number. The stability region is then given in the complex  $z$ -plane by those values of  $z$  for which  $f(z) < 1$ . We have also used a five stage scheme with coefficients,

$$\alpha_1 = \frac{1}{4} \quad , \quad \alpha_2 = \frac{1}{6} \quad , \quad \alpha_3 = \frac{3}{8} \quad , \quad \alpha_4 = \frac{1}{2}$$

and three evaluations of the dissipative operators at the first, third, and fifth stage. The stability region of this scheme is much larger, extending to a value of the CFL of 4 along the imaginary

axis and about 9 along the real axis (fig. 3.5.2).

#### 6. Analysis of the time step limit

The exact computation of the time step limit for a multistage scheme of the class just described would require the numerical analysis of the eigenvalues of the amplification matrix. However useful bounds can also be obtained by approximate analysis. This section addresses the problem of evaluating the constraint that has to be imposed on the time step to guarantee the stability of a multistage scheme applied to the solution of the full set of conservation laws (eq. 2.2.1). Although the analysis that follows is only approximate, nevertheless it provides useful stability criteria for the explicit schemes that are used in the present study. For the sake of simplicity, the amplification operator of a single stage scheme is considered here, although in practice a multistage scheme is needed to assure stability. Also, the convective and diffusion operators are treated separately. The stability for the convective operator is analyzed first.

The LHS of eq. (2.2.1) can be rewritten in a generalized curvilinear coordinate system  $\xi, \eta$  as :

$$\frac{\partial}{\partial t} h w + \frac{\partial}{\partial \xi} F + \frac{\partial}{\partial \eta} G = 0 \quad (3.6.1)$$

where:

$$F = y_\eta f_c - x_\eta g_c \quad (3.6.2)$$

$$G = x_\xi g_c - y_\xi f_c,$$

and  $h$  is the Jacobian of the transformation  $x(\xi, \eta), y(\xi, \eta)$ , that is the cell volume. Linearizing around a reference state, eq. (3.6.1) can be written in matrix form as :

$$\frac{\partial}{\partial t} h w = A_o \frac{\partial}{\partial \xi} w + B_o \frac{\partial}{\partial \eta} w, \quad (3.6.3)$$

where  $A_o$  and  $B_o$  are the Jacobian flux matrices. By approximating  $\frac{\partial}{\partial \xi} w$  and  $\frac{\partial}{\partial \eta} w$  with central differences ( $\Delta \xi = \Delta \eta = 1$ ), and taking the Fourier transform, the following expression is obtained:

$$\hat{w}^{n+1} = G(p, q) \hat{w}^n \quad (3.6.4)$$

where  $G(p, q)$  is the amplification matrix, and  $p, q$  are the Fourier variables. For a single stage scheme,  $G(p, q)$  has the following form :

$$G(p, q) = I - i \frac{\Delta t}{h} (\mathbf{A}_o \sin p + \mathbf{B}_o \sin q) = I - i \frac{\Delta t}{h} (\hat{\mathbf{A}}_o) . \quad (3.6.5)$$

For stability, the following expression has to be satisfied:

$$G^* G < 1 . \quad (3.6.6)$$

In particular eq. (3.6.6) can be satisfied by a multistage scheme if

$$\frac{\Delta t}{h} < \max(\rho(\hat{\mathbf{A}}_o))^{-1} \quad (3.6.7)$$

where  $\rho(\hat{\mathbf{A}}_o)$  is the spectral radius of the matrix  $\hat{\mathbf{A}}_o$ .

For computational efficiency, however, the time step limit is computed in a slightly different form :

$$\frac{\Delta t}{h} < (\rho(\mathbf{A}_o) + \rho(\mathbf{B}_o))^{-1} \quad (3.6.8)$$

Note also that the above estimate is more conservative than the original one (eq. 3.6.7). Also, with the following definition

$$q = uy_\eta - vx_\eta \quad (3.6.9)$$

the eigenvalues of the Jacobian flux matrix  $\mathbf{A}_o$  are readily computed [47] :

$$\lambda_A = |q|, |q| - \sqrt{(x_\eta^2 + y_\eta^2)a^2}, |q| + \sqrt{(x_\eta^2 + y_\eta^2)a^2}. \quad (3.6.10)$$

From the eigenvalues (3.6.10) an estimate of the spectral radius is then readily computed as:

$$\rho(\mathbf{A}_o) = |q| + \sqrt{(x_\eta^2 + y_\eta^2)a^2}. \quad (3.6.11)$$

Similarly, letting  $r = vx_\xi - uy_\xi$ , the eigenvalues of the Jacobian flux matrix  $\mathbf{B}_o$  are computed as :

$$\lambda_B = |r|, |r| - \sqrt{(x_\xi^2 + y_\xi^2)a^2}, |r| + \sqrt{(x_\xi^2 + y_\xi^2)a^2}; \quad (3.6.12)$$

And, therefore:

$$\Delta t = (|q| + \sqrt{(x_\eta^2 + y_\eta^2)a^2} + |r| + \sqrt{(x_\xi^2 + y_\xi^2)a^2})^{-1} \quad (3.6.13)$$

For a multistage scheme the estimate of the time step limit is modified accordingly to the following expression:

$$\Delta t_{conv} = CFL_{lim} * \Delta t \quad (3.6.14)$$

where  $CFL_{\text{lim}}$  is a constant that depends on the scheme, and it corresponds to the maximum stability limit along the imaginary axis.

A similar approach is used to evaluate a stability criterion for the viscous fluxes. To evaluate the maximum allowable time step, corresponding to the diffusion operator, it is useful to consider the following model problem:

$$\frac{\partial}{\partial t} \mathbf{U} = \mathbf{C} \frac{\partial^2}{\partial \xi^2} \mathbf{U} + \mathbf{D} \frac{\partial^2}{\partial \eta^2} \mathbf{U} + \mathbf{E} \frac{\partial^2}{\partial \eta \partial \xi} \mathbf{U}. \quad (3.6.15)$$

This problem corresponds to the non conservative form of the diffusion operator [ 48 ] in the Navier Stokes equations (2.2.1). In eq (3.6.15)  $\mathbf{U} = [\rho, u, v, p]^T$  is the vector of the independent non conservative variables. Taking the Fourier transform of the above expression , where the second derivatives are approximated by the standard second differences formulas, one obtains:

$$\hat{\mathbf{U}}^{n+1} = G(p, q) \hat{\mathbf{U}}^n \quad (3.6.16)$$

For a single stage scheme, the amplification matrix  $G(p, q)$  has the following form:

$$G(p, q) = I - 2\Delta t \left[ C(1 - \cos p) + D(1 - \cos q) + 2E \sin p \sin q \right]. \quad (3.6.17)$$

From the above form of the amplification factor  $G(p, q)$  it is evident that the parabolic problem (3.6.15) needs stability along the negative imaginary axis.

With only the additional assumption of orthogonality  $\nabla \xi \cdot \nabla \eta$  , and with the help of a considerable amount of algebra, the eigenvalues of the matrix  $\mathbf{C}$  are found to be:

$$\nu_C = \frac{\mu(x_\eta^2 + y_\eta^2)}{h^2 p} \cdot \frac{4\mu(x_\xi^2 + y_\xi^2)}{3h^2 p} \cdot \frac{\gamma\mu(x_\xi^2 + y_\xi^2)}{Pr h^2 p}. \quad (3.6.18)$$

Similarly, the eigenvalues of  $\mathbf{D}$  are given by :

$$\nu_D = \frac{\mu(x_\xi^2 + y_\xi^2)}{h^2 p} \cdot \frac{4\mu(x_\eta^2 + y_\eta^2)}{3h^2 p} \cdot \frac{\gamma\mu(x_\eta^2 + y_\eta^2)}{Pr h^2 p}. \quad (3.6.19)$$

Also, the eigenvalues of  $\mathbf{E}$  are found to be :

$$\nu_E = \pm \frac{\mu}{3h^2 p} \sqrt{(x_\xi^2 + y_\xi^2)(x_\eta^2 + y_\eta^2)} \quad (3.6.20)$$

We can also obtain an estimate of the time step limit for the parabolic problem that is given in the following form:

$$\Delta t_{vis} < (2(\rho(C) + \rho(D) + \rho(E)))^{-1} \quad (3.6.21)$$

where  $\rho(C) = \frac{\gamma\mu(x_\xi^2 + y_\xi^2)}{Prh^2\rho}$ ,  $\rho(D) = \frac{\gamma\mu(x_\eta^2 + y_\eta^2)}{Prh^2\rho}$ , and  $\rho(E)$  is given by the positive value of

eq (3.6.20). For the multistage scheme it is then assumed that:

$$\Delta t_{vis} < K(2(\rho(C) + \rho(D) + \rho(E)))^{-1} \quad (3.6.22)$$

where  $K$  is the stability limit of the scheme along the negative real axis.

When considering the full problem represented by the Navier Stokes equation (2.2.1) the condition

$$\Delta t = \min(\Delta t_{conv}, \Delta t_{vis}) \quad (3.6.23)$$

should be sufficient to guarantee stability. However, a more conservative approach is employed in the present work. Namely the time step is chosen to be :

$$\Delta t = \frac{h}{\rho(A_o) + \rho(B_o) + 2h(\rho(C) + \rho(D)) + 2\rho(E)} \quad (3.6.24)$$

Note that the above expression is consistent with the integral form used.

The expressions (3.6.10-3.6.13) are already in a form consistent with the dimensionless conservation equations (2.2.1). When the estimate of the spectral radii of the viscous Jacobian fluxes are cast in the dimensionless form of the finite volume formulation, one obtains:

$$v_i = \frac{\sqrt{\gamma}M_\infty}{Re\Omega} \left[ \frac{\gamma\mu}{Pr\rho} (x_\xi^2 + y_\xi^2) + \frac{\mu}{3\rho} \sqrt{(x_\xi^2 + y_\xi^2)(x_\eta^2 + y_\eta^2)} \right] \quad (3.6.25)$$

$$v_j = \frac{\sqrt{\gamma}M_\infty}{Re\Omega} \left[ \frac{\gamma\mu}{Pr\rho} (x_\eta^2 + y_\eta^2) + \frac{\mu}{3\rho} \sqrt{(x_\xi^2 + y_\xi^2)(x_\eta^2 + y_\eta^2)} \right]$$

where  $v_i$  and  $v_j$  represent, respectively,  $\rho(C) + \rho(E)$  and  $\rho(D) + \rho(E)$ , and  $\Omega$  is the area of the control volume used in the finite volume formulation.

## 7. Verification of the basic scheme for the Euler equations

The shock capturing capability and accuracy of the basic formulation can be better appreciated with the help of the following examples.

The first is a comparison of the surface pressure plots obtained by computing the Euler solu-

tion on a NACA 0012 airfoil at  $M_\infty = .8$  and  $1.25^\circ$  angle of attack on identical meshes (fig. 3.7.1) using the cell centered scheme augmented by the adaptive dissipation formulation with the scaling described in section 3.3, and a flux limited dissipation [49]. Results for  $128 \times 32$  (fig. 3.7.2) and a  $256 \times 64$  (fig. 3.7.3) grid with  $3/4$  of the points along the innermost C-line fitted on the airfoil show close agreement between the pressure plots obtained with the two methods. Pressure jumps across the shock waves are well computed by the adaptive dissipation scheme and the shock layer is limited to just 3 inner points. The slightly different computed lift and drag coefficients are mainly due to the better resolution of the weakest shock on the bottom surface achieved by the flux limited model. The computational cost of the flux limited dissipation is, however, higher by a factor of two.

The most significant demonstration of the accuracy obtained with the adaptive dissipation method on highly stretched, high aspect ratio meshes is given by the next set of computed results. The cell centered formulation and adaptive dissipation model were used to compute the inviscid flow field on a supercritical Korn airfoil at the design conditions of  $M_\infty = .75$  and  $0^\circ$  angle of attack. Again the mesh (fig. 3.7.4) is a  $256 \times 64$  with  $3/4$  of the points along the innermost C-line located on the airfoil. However the first point away from the wall was placed at a distance of 0.0004 chords. The aspect ratio is dramatically increased with respect to a standard mesh designed for inviscid calculations. This computation is a formidably difficult test for any numerical scheme since Morawetz [50] theorem states that a shock free solution is an isolated point and, therefore any small perturbation in the airfoil geometry or inaccuracy of the numerical scheme will cause the disruption of the correct solution leading to the formation of a shock wave. Fig. 3.7.5 shows the computed shock free surface pressure distribution. No shocks are present, and the computed drag coefficient of just one count ( $0.0001$ ) is a good indication of the accuracy of the computation. The dimensionless entropy error measured by the difference between the computed and free stream entropies was found to be less than  $1 \times 10^{-4}$  everywhere in the flow field except at a discrete number of points near the leading and trailing edges where it was found to be less than

$5 \times 10^{-4}$ .

A second computation of the same case where the distribution of points on the airfoil was deliberately changed (fig. 3.7.6) to give an additional region of abrupt variation in the aspect ratio located on the suction surface at about  $c/4$  from the leading edge, shows the robustness of the proposed scaling and its insensitivity to the mesh point distribution. The computed results (fig. 3.7.7) for this second test are identical to the ones already described.

The last example demonstrates the accuracy of the basic formulation for the computation of inviscid flows with shock waves on a high aspect ratio grid. Fig (3.7.8a) shows the computed inviscid pressure distribution for the RAE 2822 airfoil at  $M_\infty = .73$  and  $2.79^\circ$  angle of attack obtained by using a  $512 \times 64$  grid designed to resolve the boundary layer region at high Reynolds number ( cfr. 6.2). The computed pressure coefficient is almost identical to the one obtained by using a standard Euler grid with an identical distribution of cells in the streamwise direction (Fig 3.7.8b). This comparison demonstrates that the scheme retains its original accuracy on high aspect ratio grids also for a flow containing a fairly strong shock wave. Finally, the discrepancy between the computed inviscid solution and the measurements should be noted. The inviscid model predicts a shock wave located too far downstream and, consequently, overpredicts the lift, drag, and moment coefficients. This indicates that viscous effects are clearly important for the correct determination of the aerodynamic characteristics of airfoils in the transonic regime. Nevertheless, the accurate and grid independent solutions that are obtained with the inviscid model give confidence in the accuracy of the numerical approximation of the convection operator. They also establish a solid starting point for the analysis of viscous flows.

--

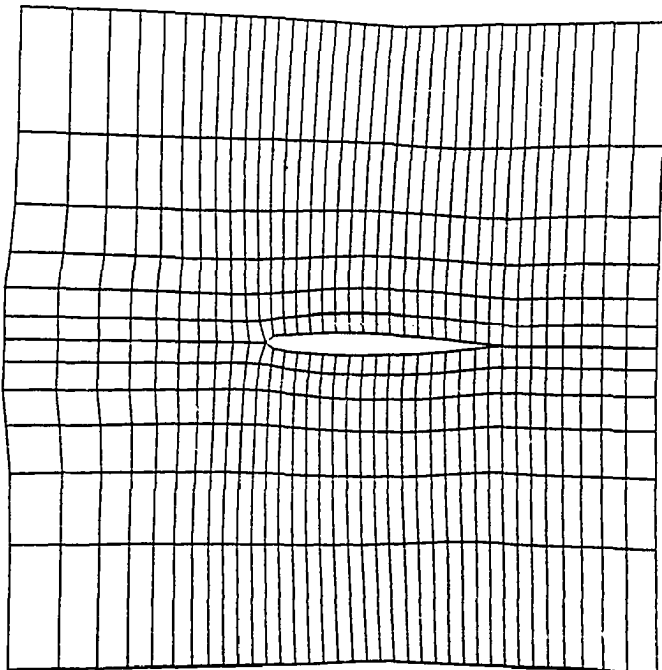


*Fig. 3.1*  
**Metric singularity of a typical H mesh.**

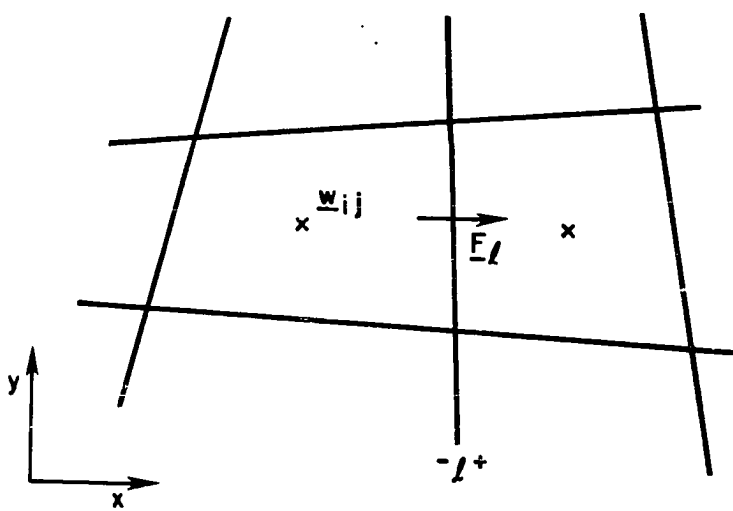


**Fig. 3.1.1**  
Computational cell for the cell centered schemes.

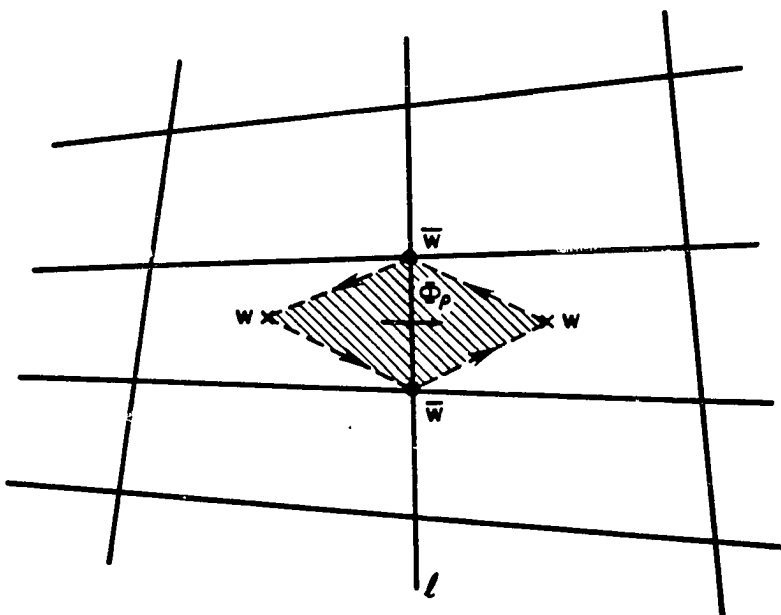


*Fig. 3.1.2a*  
Auxiliary control volume for the discretization  
of the viscous terms for the CCS-A scheme.

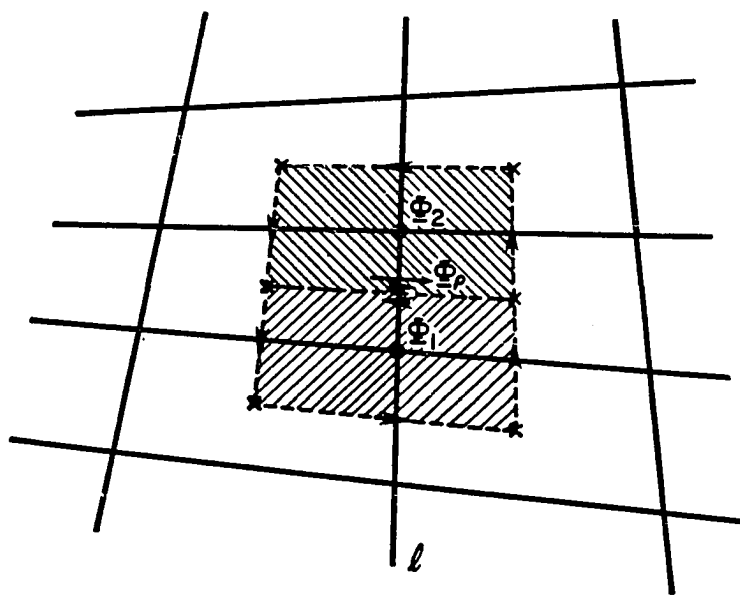


*Fig. 3.1.2b*  
Auxiliary control volume for the discretization  
of the viscous terms for the CCS-B scheme.

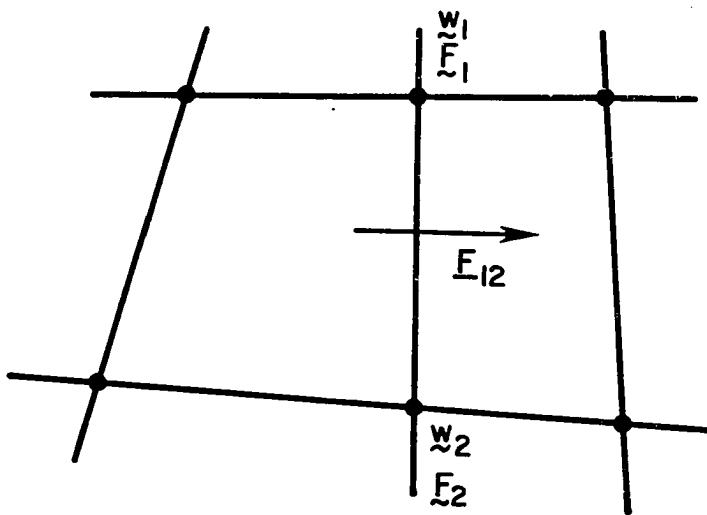


*Fig. 3.2.1*  
Computational cell for the vertex based scheme.

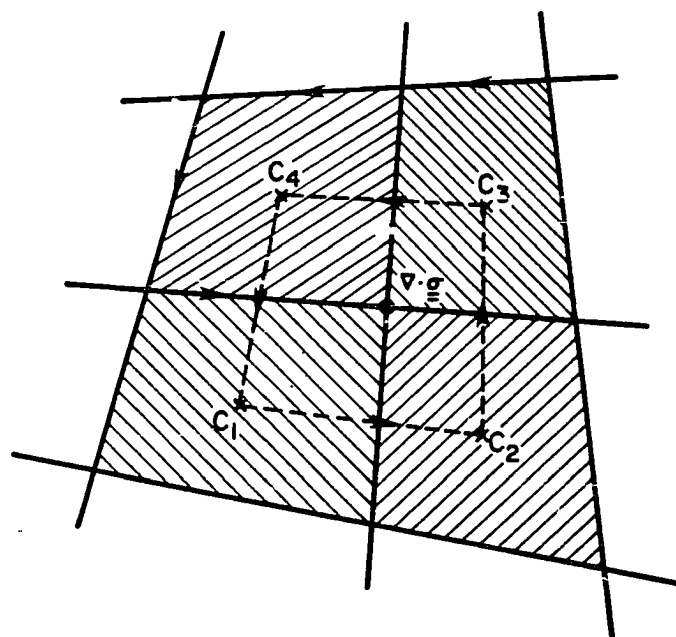


**Fig. 3.2.2**  
Auxiliary control volume for the discretization  
of the viscous terms for the vertex based scheme.



**Fig. 3.2.3**  
Nodal distribution for the 1-D vertex scheme.

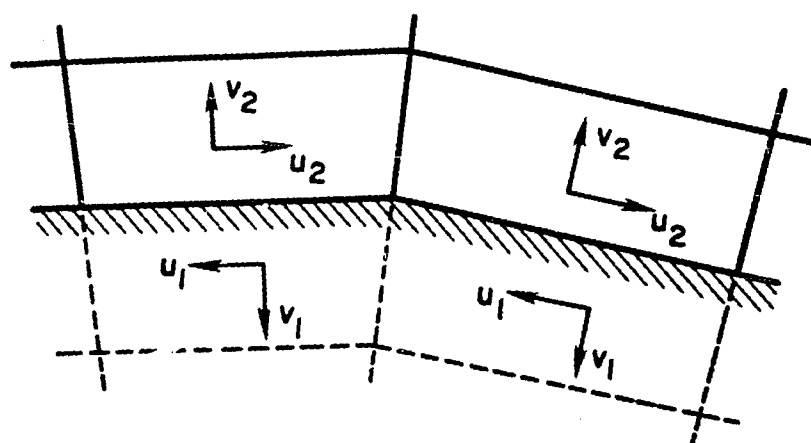


Fig. 3.4.1  
Solid Boundary for the cell centered scheme.

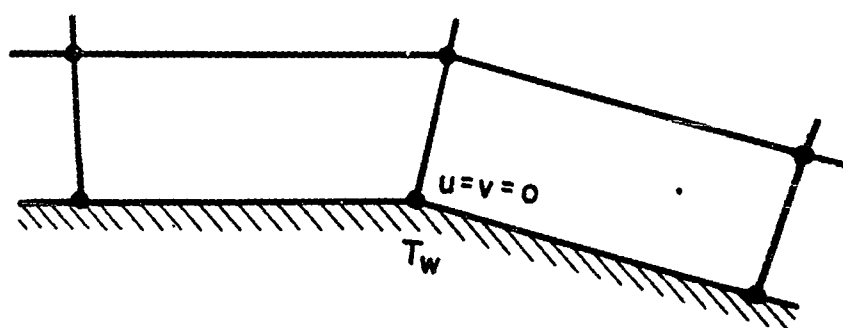
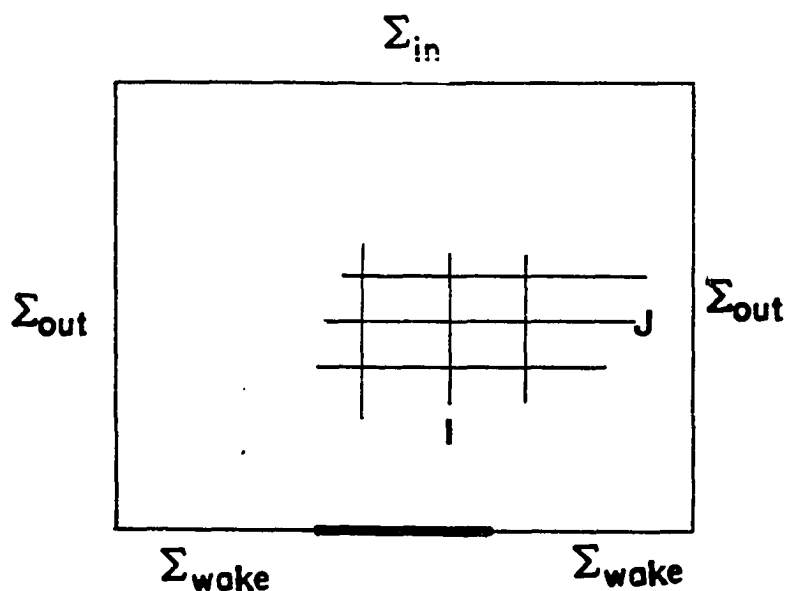
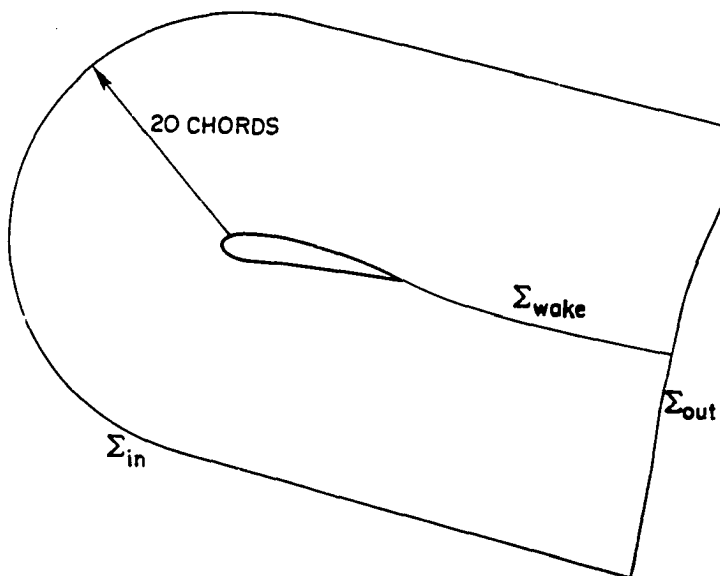
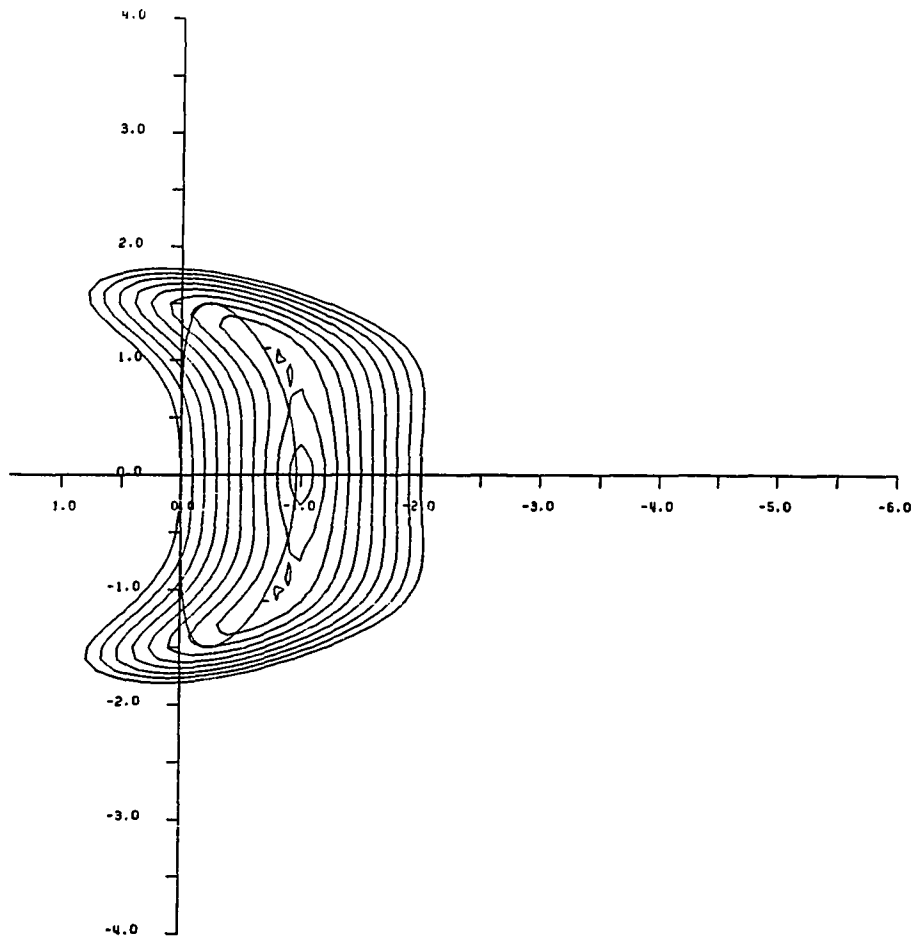


Fig. 3.4.2  
Solid Boundary for the vertex based scheme.

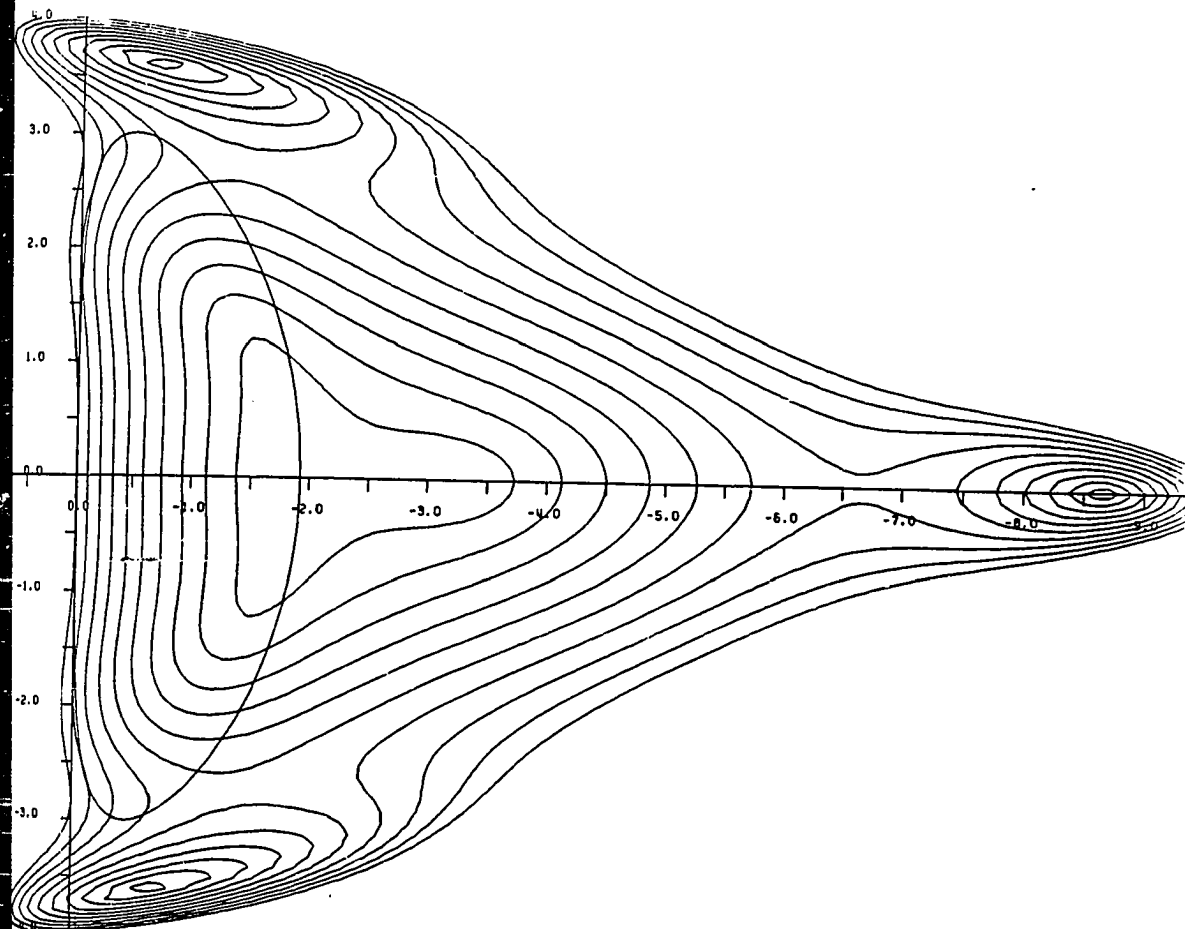


*Fig. 3.4.3  
C - mesh topology.*

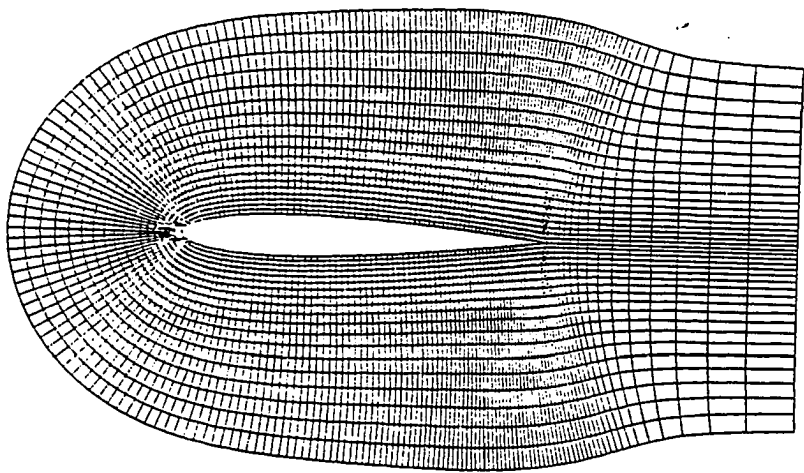
Top - Physical plane ( $x, y$ )  
Bottom - Computational plane ( $\xi = i \Delta \xi$ ,  $\eta = j \Delta \eta$ )  
 $\eta = \text{const}$  lines correspond to C-lines in the physical plane.



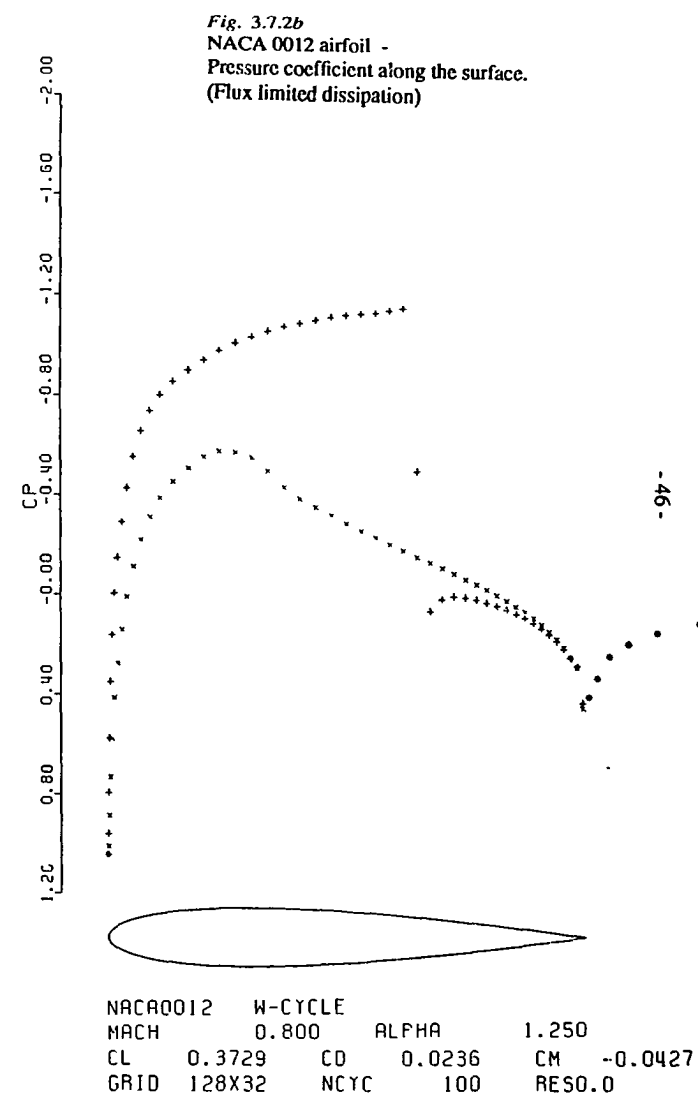
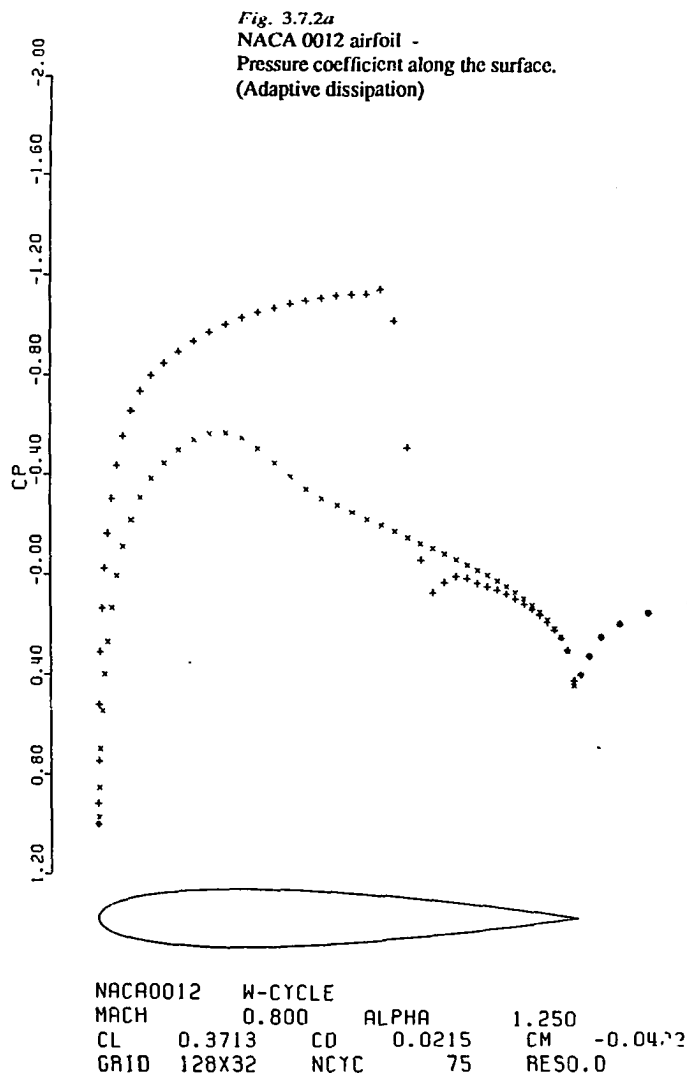
**Fig. 3.5.1**  
Stability region of the three stage scheme  
with single evaluation of dissipation.  
Contour lines  $\Delta |f(z)| = .1$   
and locus of  $z(\xi)$  for  $\lambda = 1.5$ ,  $\mu = 1/32$   
in the complex z-plane ( $z = -i\lambda \sin \xi - 4\lambda \mu (1 - \cos \xi)^2$ ).

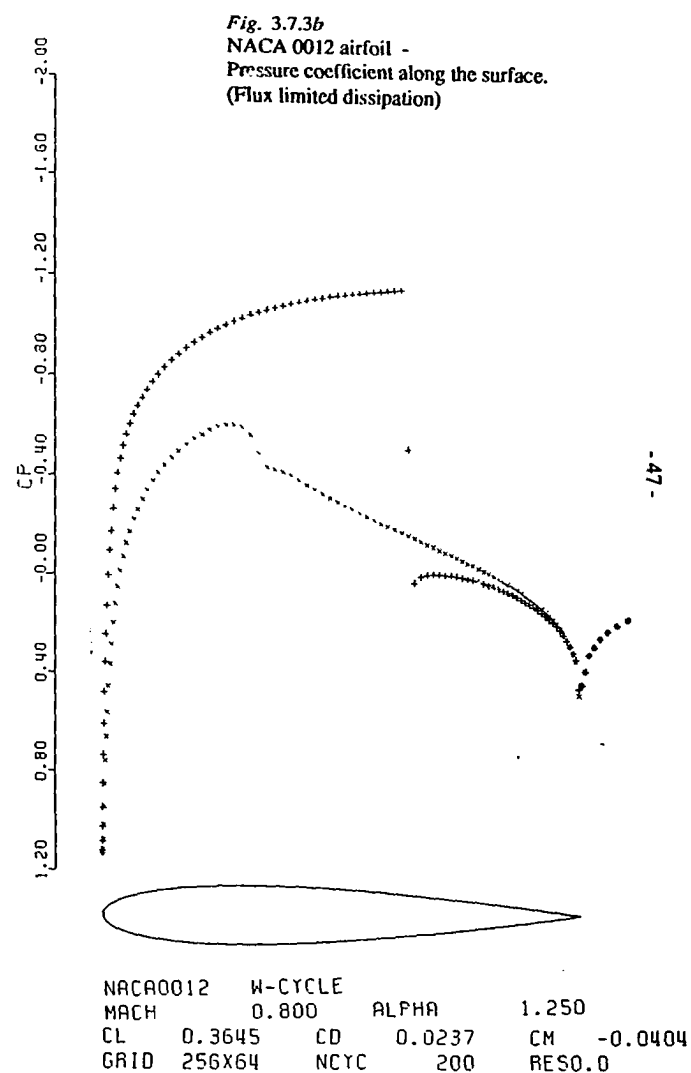
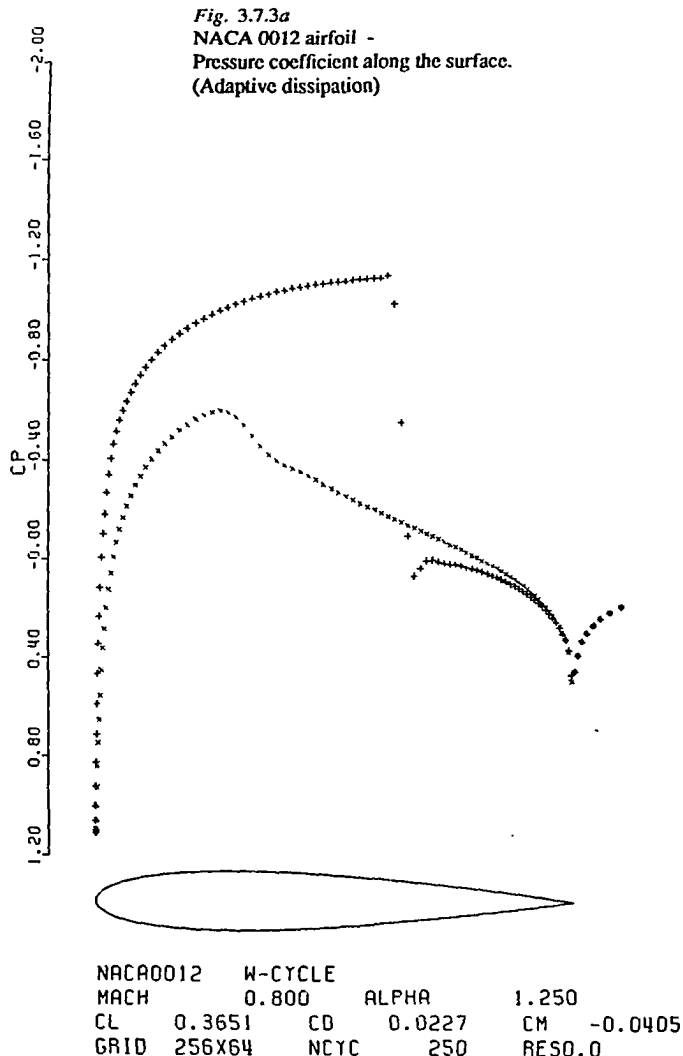


**Fig. 3.5.2**  
Stability region of the five stage scheme  
with three evaluations of dissipation.  
Contour lines  $\Delta f(z) = .1$   
and locus of  $z(\xi)$  for  $\lambda = 3.0, \mu = 1/32$   
in the complex z-plane ( $z = -i\lambda \sin \xi - 4\lambda \mu (1 - \cos \xi)^2$ ).



*Fig. 3.7.1*  
**NACA 0012 airfoil -**  
**256x64 C-mesh for Euler computations.**





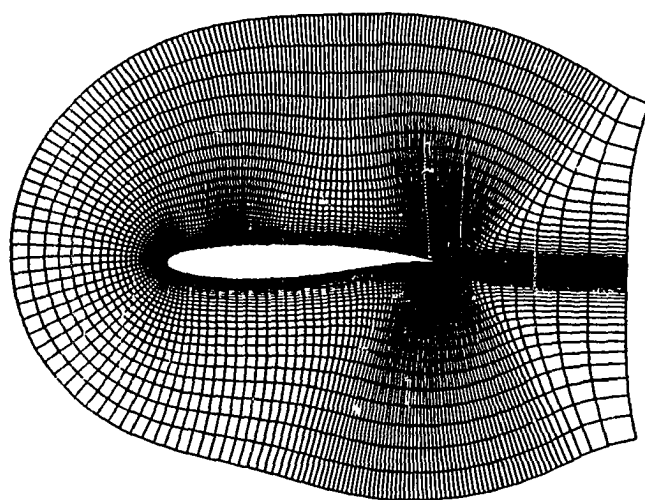


Fig. 3.7.4  
KORN airfoil -  
256x64 C-mesh

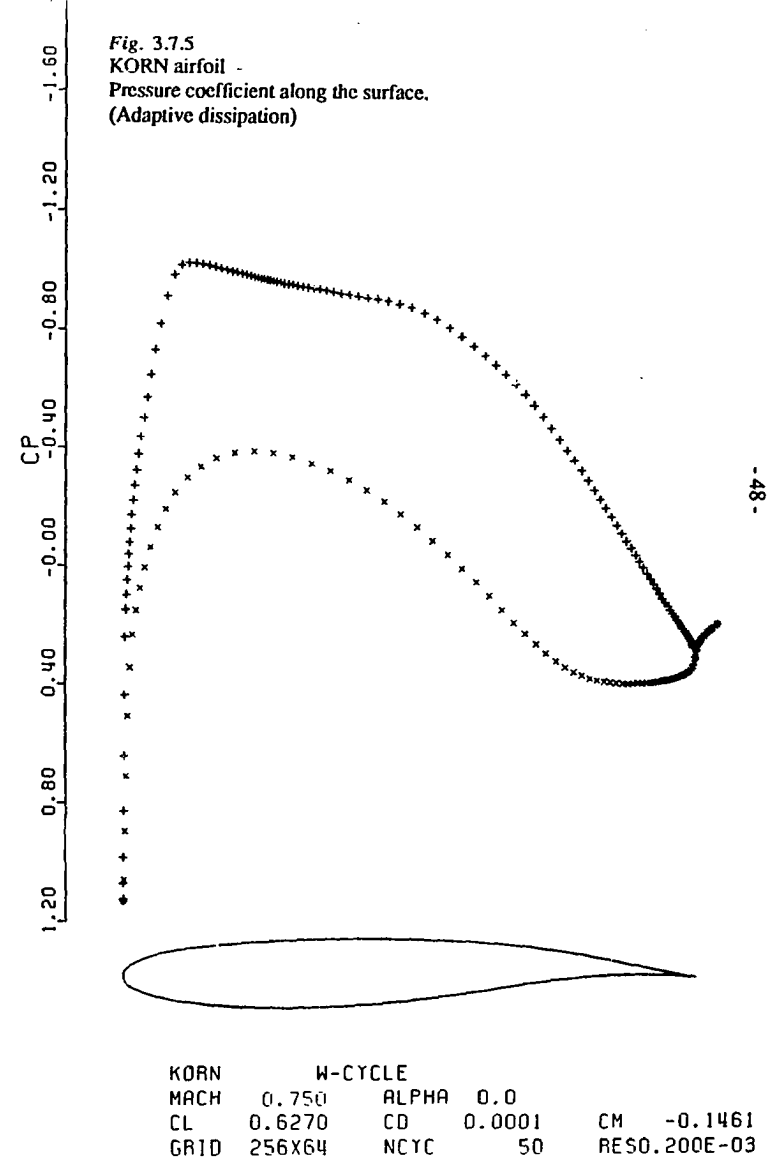


Fig. 3.7.6  
KORN airfoil -  
256x64 C-mesh

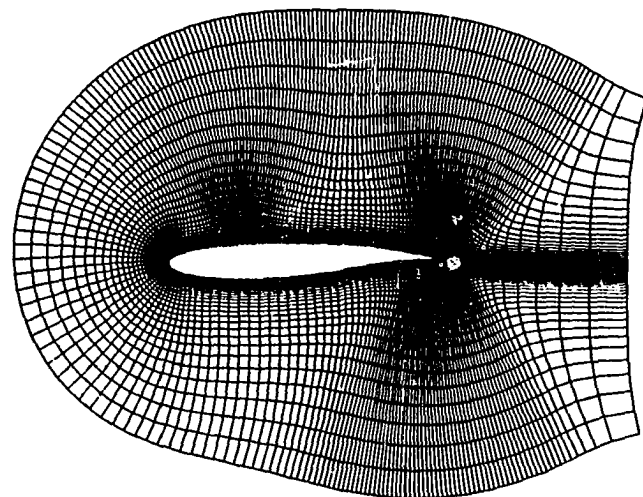
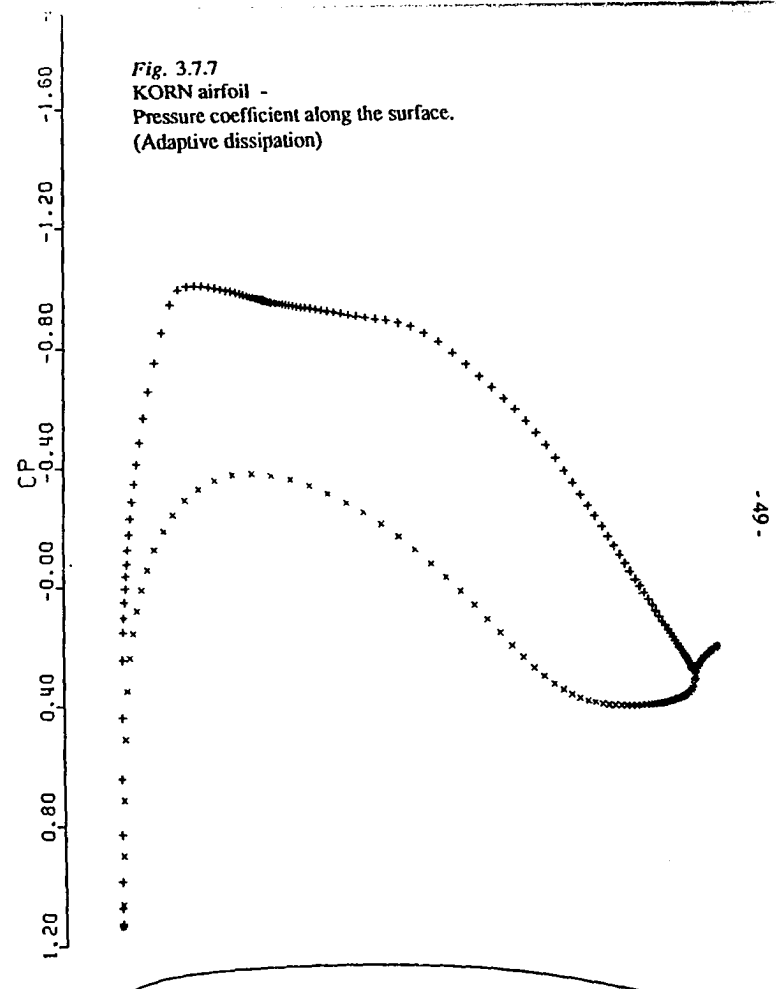
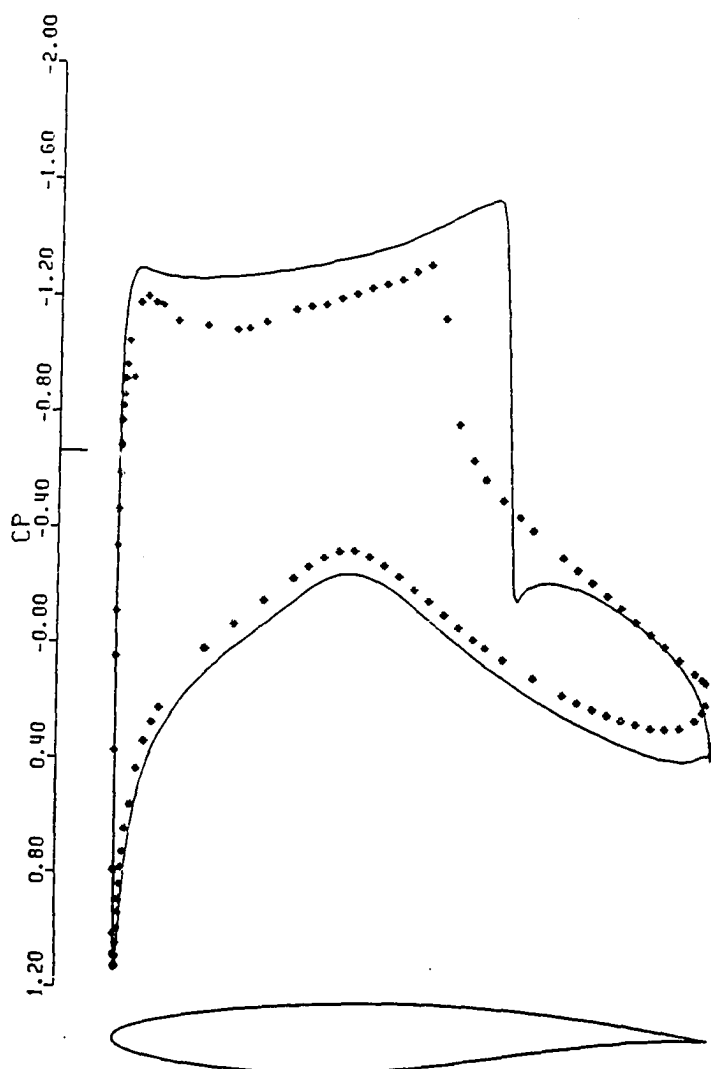


Fig. 3.7.7  
KORN airfoil -  
Pressure coefficient along the surface.  
(Adaptive dissipation)

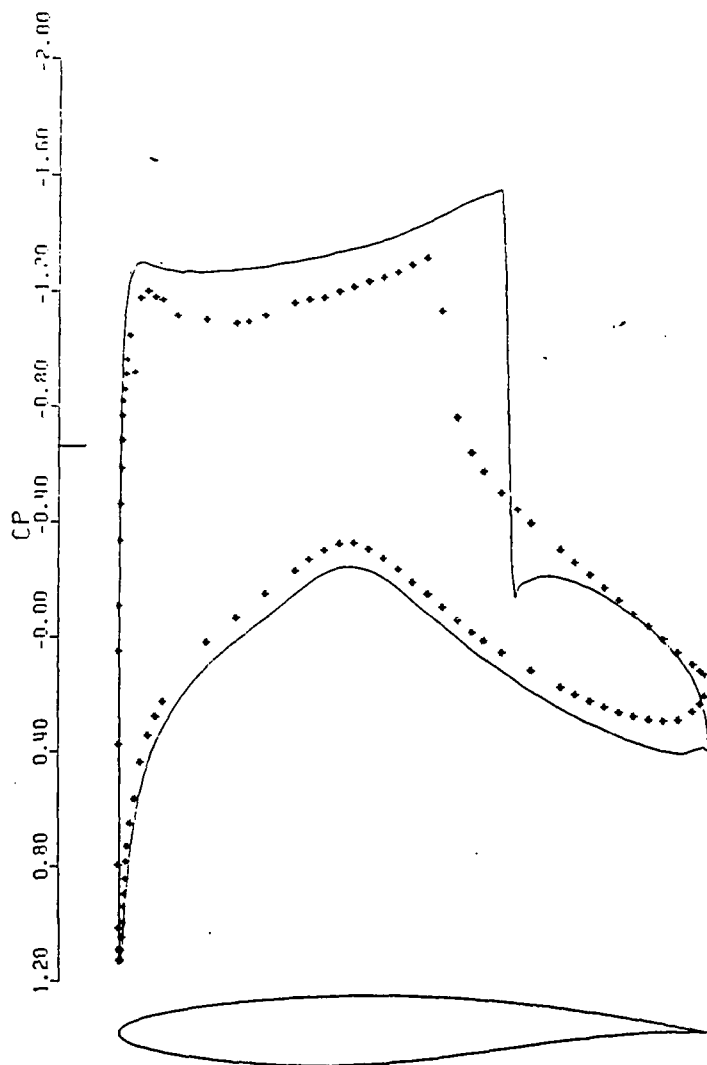


KORN W-CYCLE  
MACH 0.750 ALPHA 0.0  
CL 0.6270 CD 0.0001 CM -0.1463  
GRID 256x64 NCYC 50 RESO.200E-03



RAE2822 W-CYCLE EULER \* 9  
MACH 0.730 ALPHA 2.790  
CL 1.0302 CD 0.0203 CM -0.1420  
GRID 512X64 NCYC 200 RESO.100E-03

Fig. 3.7.8a  
RAE 2822 airfoil - Euler calculation  
Pressure coefficient along the surface.  
(Navier-Stokes grid)  
Solid line - Computed inviscid solution  
\* - Experiments (Ref. 64 )



RAE2822 W-CYCLE EULER \* 9  
MACH 0.730 ALPHA 2.790  
CL 1.0347 CD 0.0207 CM -0.1435  
GRID 512X64 NCYC 200 RESO.0

*Fig. 3.7.8b*  
RAE 2822 airfoil - Euler calculation  
Pressure coefficient along the surface.  
(Standard Euler grid)  
Solid line - Computed inviscid solution  
\* - Experiments (Ref. 64 )

## CHAPTER 4

### CONVERGENCE ACCELERATION TECHNIQUES

In this Chapter the numerical techniques applied to accelerate the convergence to a steady state are presented and discussed. One of the main constraints on the convergence rate of an explicit scheme is represented by the time step limit. For the hyperbolic convection operator the time step is limited by the Courant Friedrich Lewy condition, which requires that the domain of dependence of the numerical scheme must at least contain the region of the dependence of the original differential equation. In the case of the compressible Navier Stokes equations the diffusion operator imposes some additional constraints.

The first two techniques discussed are mainly aimed at relaxing somewhat the time step constraint. The last section is entirely devoted to the discussion of the multigrid technique that has been employed.

#### 1. Local Time Stepping

The most obvious way of accelerating the convergence to a steady state for an explicit as well as an implicit factorized scheme is to increase the time step. In a typical computational mesh used for aerodynamic problems the cell size is not uniform because of the stretching away from solid surfaces. This problem is particularly severe in grids designed to resolve the viscous phenomena in the boundary layer and wake regions where the ratio between the smallest and the biggest cell areas can easily amount to a value of the order of  $10^{-9}$ . Consequently, computations

using the minimum time step in the flow field are not feasible because the cost of the integration becomes unrealistic. On the other hand, if one chooses to advance every computational cell at its own stability limit, the propagation of any disturbances out of the computational domain is accomplished in a finite number of steps which becomes proportional to the number of grid points in the direction of the outer boundary. This is the concept of local time stepping which has been widely used for the solution of the steady Euler and Navier Stokes equations to accelerate the convergence of both explicit and implicit schemes.

The criteria on which the local time step might be chosen is dependent on the particular iteration scheme. In the case of the explicit multistage scheme, a conservative estimate of the local time step limit corresponding to a nominal CFL of unity gives, for the convection operator, the following limit:

$$\Delta t = \frac{\Omega_{ij}}{(\lambda_i + \lambda_j)} \quad (4.1.1)$$

where  $\lambda_i$  and  $\lambda_j$  are estimates of the local maximum wave speed in the two computational directions (cfr eqs. 3.6.13). The appearance of the maximum eigenvalue, which is an estimate of the spectral radius, in the expression for the time step limit is not surprising since the multistage scheme resembles the point Jacobi iteration of an implicit scheme. For this reason "diagonal dominance" of the system of equations to be solved is sought.

Following the same principle for the Navier Stokes computations the time step is augmented by a contribution derived from the local maximum eigenvalues of the diffusion operator, and the local time step becomes :

$$\Delta t = \frac{\Omega_{ij}}{(\lambda_i + \lambda_j + v_i + v_j)} \quad (4.1.2)$$

where  $v_i$  and  $v_j$  are the local estimates of the eigenvalues of the diffusion operator in the computational plane (eq. 3.6.25).

## 2. Residual averaging

The rate of convergence of a multistage scheme can also be enhanced by residual averaging [39]. The general idea behind this technique is to replace the residual at one point in the flow field by a weighted average of the residuals at the neighboring points. The average is calculated implicitly.

In the one dimensional case the vector of the residual  $R_j(w)$  is replaced at  $j$ -th point by  $\bar{R}_j(w)$  using the following expression :

$$-\varepsilon \bar{R}_{j-1} + (1+2\varepsilon) \bar{R}_j - \varepsilon \bar{R}_{j+1} = R_j \quad (4.2.1)$$

It can be easily shown that the multistage scheme can be stabilized for an arbitrarily large value of the time step by choosing an appropriate value of the smoothing parameter  $\varepsilon$ . The analysis for the one dimensional non dissipative case [39] gives the following constraint:

$$\varepsilon > \frac{1}{4} \left[ \left( \frac{\Delta t}{\Delta t^*} \right)^2 - 1 \right] \quad (4.2.2)$$

where  $\Delta t^*$  is the maximum stable time step of the basic scheme and  $\Delta t$  is the actual time step .

The analysis in the 2-D case is more complicated. One simple way of extending the concept of Residual Averaging in 2-D is to consider the factorized form :

$$(1 - \varepsilon_i \delta_{xx}) (1 - \varepsilon_j \delta_{yy}) \bar{R}_j = R_j \quad (4.2.3)$$

This form is particular convenient since it only requires inversion of tridiagonal matrices. It has been proved to be effective for Euler computations, but generally less effective with the Navier-Stokes equations. We will refer to this technique as residual averaging with constant coefficients, meaning that the smoothing parameters  $\varepsilon_i$  and  $\varepsilon_j$  are equal for every point in the flow field. The principal drawback is that the values for the smoothing parameters must be empirically determined and tuned.

To obviate this problem another strategy has been devised in the present work. This second technique will be referred to as residual averaging with locally varying coefficients, and it has been proved to be effective especially on highly stretched meshes. If we consider the model

problem:

$$u_t + u_x + u_y = 0 \quad (4.2.4)$$

and we discretize the equation by central differencing, we have for a simple one stage scheme:

$$u^{n+1} = u^n - (\lambda_x \delta_x u_i + \lambda_y \delta_y u_j) \quad (4.2.5)$$

taking the Fourier transform of eq (4.2.5) we get the following expression for the Fourier symbol:

$$f(\xi, \eta) = (\lambda_x \sin \xi + \lambda_y \sin \eta) \quad (4.2.6)$$

where :

$$\begin{aligned} \xi &= p \Delta x & \eta &= q \Delta y \\ \lambda_x &= \frac{\Delta x}{\Delta t} & \lambda_y &= \frac{\Delta y}{\Delta t} \end{aligned} \quad (4.2.7)$$

and the problem is reduced to :

$$\frac{d\hat{u}}{dt} = f(\xi, \eta) \hat{u} \quad (4.2.8)$$

in the transformed space. Consider now a factorized residual averaging of the form :

$$(1 - \varepsilon_x \delta_{xx})(1 - \varepsilon_y \delta_{yy}) \bar{R}_j = R_j \quad (4.2.9)$$

where  $\delta_{xx}$  and  $\delta_{yy}$  are central second difference operators in the two directions  $x$  and  $y$  and  $\varepsilon_x$  and  $\varepsilon_y$  are locally varying smoothing parameters. Then the Fourier symbol will be replaced by:

$$f(\xi, \eta) = \frac{(\lambda_x \sin \xi + \lambda_y \sin \eta)}{(1 + 2\varepsilon_x(1 - \cos \xi))(1 + 2\varepsilon_y(1 - \cos \eta))} \quad (4.2.10)$$

If  $\xi = 0$  or  $\eta = 0$  this reduces to the one dimensional case. The worst possible case is roughly when  $\lambda_x = \lambda_y$  and  $\xi = \eta$ . Then the Fourier symbol (4.2.10) reduces to :

$$f(\xi) = \frac{2(\lambda \sin \xi)}{(1 + 2\varepsilon(1 - \cos \xi))^2} \quad (4.2.11)$$

Now considering the points at which  $df/d\xi$  vanishes we are able to set an upper bound on the maximum growth factor in term of the smoothing parameter  $\varepsilon$  as

$$f_{\max} < \left\{ \frac{(1 - \frac{4\varepsilon}{1+4\varepsilon})(1 + \frac{4\varepsilon}{1+4\varepsilon})}{(1 + \frac{4\varepsilon}{1+8\varepsilon})^2} \right\}^{1/4} \quad (4.2.12)$$

From this formula smoothing rules for the 2-D case can be established. If we define now the following modified wave speeds in the  $i$  and  $j$  directions of the computational plane:

$$\begin{aligned}\bar{\lambda}_i &= \Phi(r)\lambda_i \\ \bar{\lambda}_j &= \Phi(\frac{1}{r})\lambda_j\end{aligned}\quad (4.2.13)$$

where  $r = \lambda_i/\lambda_j$  and  $\Phi(r) = 1 + r^\alpha$ , then the choice of the smoothing parameters can be taken as:

$$\begin{aligned}\varepsilon_i &= \max \left\{ \frac{1}{4} \left[ \left( \frac{\bar{\lambda}_i}{\lambda} \right)^2 - 1 \right], 0 \right\} \\ \varepsilon_j &= \max \left\{ \frac{1}{4} \left[ \left( \frac{\bar{\lambda}_j}{\lambda} \right)^2 - 1 \right], 0 \right\}\end{aligned}\quad (4.2.14)$$

In practical computations it has been found that the coefficient  $\alpha = 2/3$  gives good results.

### 3. Multigrid Strategy

The most effective way of accelerating the convergence rate is furnished by the multigrid technique. The concept of acceleration by introduction of multiple grids was first devised by Federenko [51]. While by now the theory of the multigrid is well established for elliptic problems [52,53] the same theory does not apply to hyperbolic systems. Nevertheless acceleration via multigrid has been clearly demonstrated for the solution of the Euler equations [21,26,54]. In the present work the use of multiple grids is applied to the solution of the compressible Navier Stokes equations. On the basis of the success of the multigrid methods in dealing with the solution of elliptic as well as hyperbolic problems it seems it ought to be possible to accelerate the evolution of a system of mixed type such as the one that corresponds to the full system of conservation laws.

The general idea behind any multigrid time stepping scheme is to transfer part of the task of tracking the evolution of the original system onto coarser grids by introducing a sequence of grid levels. Besides establishing the equilibrium more rapidly, this procedure has the advantage that the computational effort per time step is dramatically reduced on the coarser grids. In general the multigrid scheme can make use of a sequences of independently generated and unstructured grids, and indeed the effectiveness of the multigrid for the solution of the Euler equations on unstructured triangular meshes has been recently demonstrated [55]. For our purposes, using quadrilateral cells, coarser meshes are generated by elimination of alternate points in each coordinate direction. Therefore each cell on a given grid corresponds to a group of four cells on the next

finer grid.

In order to give a precise description of the multigrid scheme employed in the present work, which follows the lines indicated in [27], several transfer operations must be defined. First the solution vector on the generic  $k$ -th level grid must be initialized as:

$$w_k^{(0)} = T_{k,k-1} w_{k-1} \quad (4.3.1)$$

where  $w_{k-1}$  is the current value on the next finer  $k-1$ th level, and  $T_{k-1,k}$  is a transfer operator.

The second step is to transfer a residual forcing function in such a way that the evolution on the coarser grid  $k$  is driven by the residual collected from the level  $k-1$ . This is accomplished by setting:

$$P_k = Q_{k,k-1} R_{k-1}(w_{k-1} - R_k(w_k^{(0)})) \quad (4.3.2)$$

where  $Q_{k,k-1}$  is a second transfer operator. Then  $R_k(w_k) + P_k$  replace the residual  $R_k(w_k)$  in the driving scheme, and the multistage time stepping scheme is then modified as :

$$\begin{aligned} w_k^{(1)} &= w_k^{(0)} - \alpha_1 \Delta t_k (R_k^{(0)} + P_k) \\ &\dots \\ w_k^{(q+1)} &= w_k^{(q+1)} - \alpha_q \Delta t_k (R_k^{(q)} + P_k) \end{aligned} \quad (4.3.3)$$

The final result of the  $m$ -th stage  $w^{(m)}$  provides the initial data for the next grid level  $k-1$ . This completes the description of the transfer in the direction from the finest to coarser grids.

On the way back up the final value of the unknown vector  $w^+$  on the  $k$ -th grid resulting from both the correction calculated during the time step on grid  $k$  and the correction transferred from the next coarser grid  $k+1$  can be written as:

$$w_{k-1}^+ = w_{k-1} + I_{k-1,k} (w_k^+ - w_k^{(0)}) \quad (4.3.4)$$

where  $w_{k-1}$  is the solution on grid  $k-1$  after the time step and before the transfer from grid  $k$  and  $I_{k-1,k}$  is an interpolation operator.

This general description of the operations in the multigrid scheme is completed by specifying proper forms of the transfer and interpolation operators. In this study the definition of the

transfer operators differs depending on whether the variable are defined at the cell centers or the vertices of the computational mesh. For the cell centered scheme the transfer operator is set to be:

$$T_{k,k-1}w_{k-1} = (\sum_{cells} \Omega_{k-1} w_{k-1}) / \Omega_k \quad (4.3.5)$$

This is a weighted average which conserves mass, momentum, and energy. The residual transfer operation is accomplished by simply summing over the four cells of the next finer grid. Namely:

$$Q_{k,k-1}R_{k-1} = \sum_{cells} R_{k-1} \quad (4.3.6)$$

Since the nodes are coincident on all the grid levels, the solution transfer operator of the vertex scheme reduces to a simple elimination of the values at alternate nodes. The residual transfer rule is a weighted sum over the 9 neighboring points [41]. In both schemes the transfer of information up is accomplished by bilinear interpolation.

There remains some latitude in the ordering of the operations just described in the complete multigrid cycle. Two different cycles have been investigated in the present work. Originally a simple saw-tooth cycle was selected. The ordering of the operations is summarized in fig. (4.3.1). One single iteration of the discrete Navier Stokes is performed on every cycle before the collection step on the way down. Once the coarsest grid is reached simple interpolation without any additional iteration is performed on the way up. In this case the total computational work per multigrid cycle relative to the work on the fine mesh satisfies the bound

$$W_{multigrid} < \frac{4}{3} W_{finest}$$

omitting the cost of the transfer operations themselves, which is generally negligible in comparison with the work in the time step. A second more complicated cycle has also been investigated. This is the W - cycle of fig. (4.3.2). In this case the work per cycle can be estimated by the bound

$$W_{multigrid} < 2W_{finest}$$

The main draw back of the multigrid strategy is that the interpolation introduces additional high frequency errors that cannot be rapidly expelled from the fine grid. It is therefore imperative

that the driving scheme should be designed to damp the high frequency components. Both the three stage and five stage schemes employed in the present work possess this property [27].

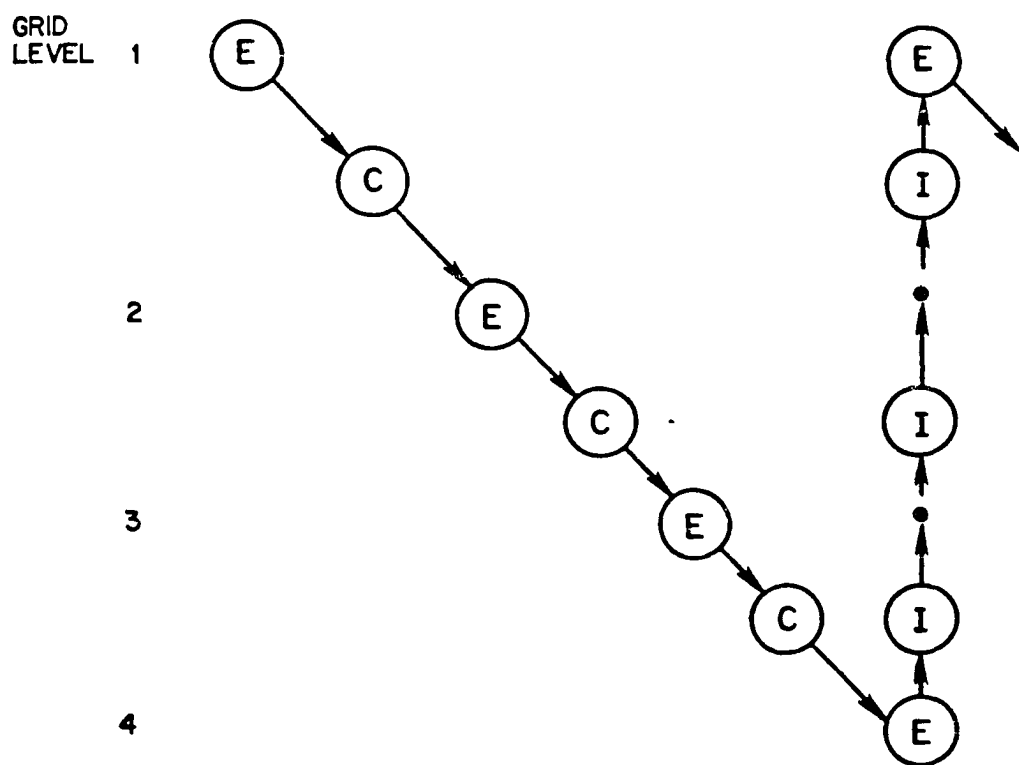


*Fig. 4.3.1*  
Sawtooth multigrid cycle.  
E = multistage time step  
C = Residual collection step  
I = Interpolation step

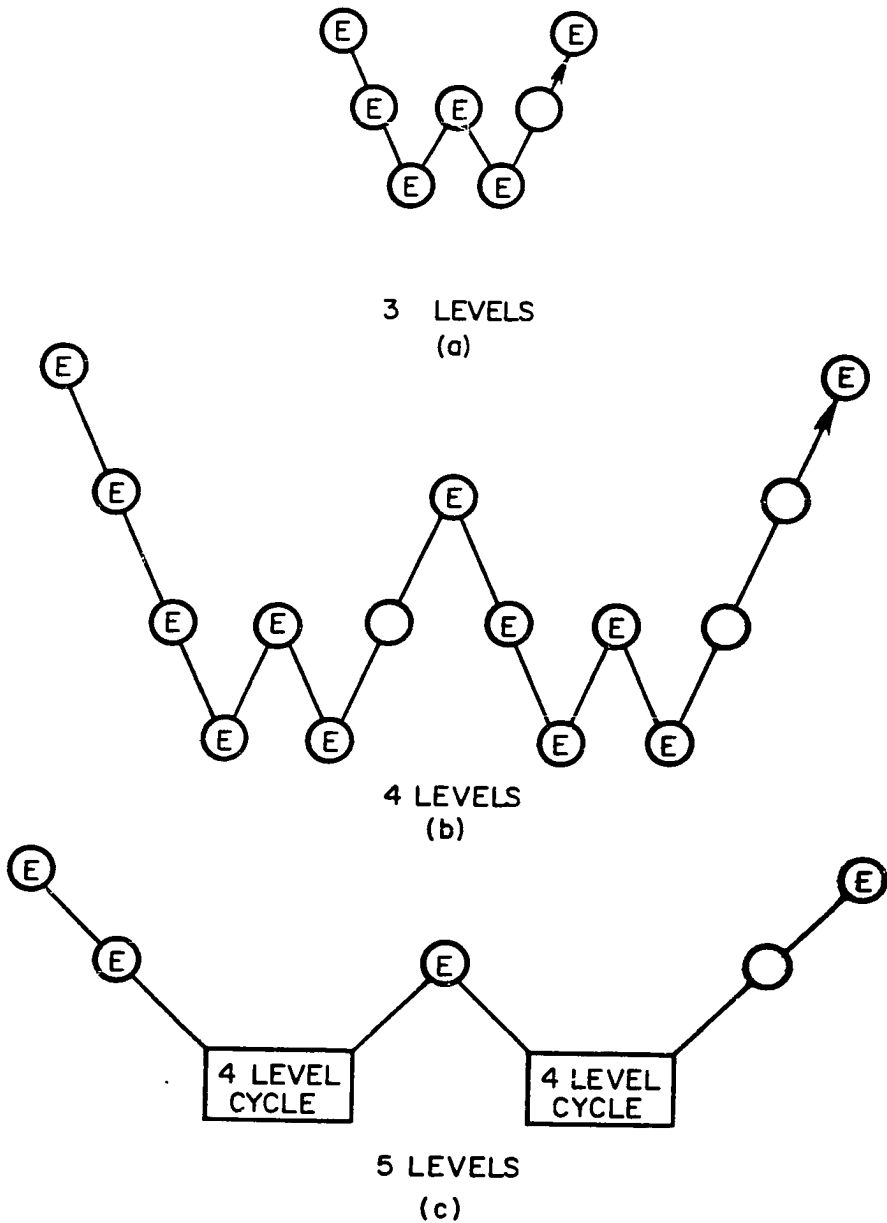


*Fig. 4.3.2*  
W = multigrid cycle.  
E = multistage time step

## CHAPTER 5

### RESULTS FOR LAMINAR FLOWS OVER A NACA 0012

#### WING SECTION

Testing the validity and accuracy of a viscous flow calculation is a difficult task. In the normal regime of flight of an airliner the Reynolds number is of the order of  $10^7$  and the cruising speed is transonic. At such high Reynolds numbers the onset and development of turbulence is certain to occur. We have remarked in the introduction that the problem of turbulence modeling is still an open one, and consequently it becomes extremely difficult to separate the effects of the numerical approximation from those introduced by the model in computations carried out at Reynolds numbers of interest. On the other hand, the accuracy of the numerical scheme may be assessed by putting aside the problem of turbulence, and by comparing the results of calculations of low Reynolds number flows with other computed results and with experimental data, when available. A useful source of comparisons for laminar flows was provided by the GAMM workshop on the solution of The Compressible Navier Stokes Equations [56]. Because the boundary conditions specified for the test cases include a constant wall temperature equal to the adiabatic free stream temperature, the vertex scheme is well suited for a study of those cases. The first section of this chapter will therefore be devoted to the analysis of the results of the mandatory cases of that workshop obtained by the vertex based scheme. Results for some of the same cases computed with the cell centered formulation are reported for comparison. Finally some additional laminar results for the cell centered scheme are also presented to illuminate its properties.

### 1. Laminar flows over a NACA0012 airfoil with the vertex scheme

For most of the calculations the computational domain is discretized in  $256 \times 64$  cells on the finest grid (fig.5.1.1). However, for some of the test cases computations have also been performed on a coarser grid ( $128 \times 32$ ), obtained by eliminating alternate points from the finest one. The first point in the boundary layer is located at .002 chords away from the wall, and  $5/8$  of the total number of points along the innermost C-line are fitted on the airfoil. The far field is located at a distance of 18 chords. Transonic and supersonic flow regimes are considered. For these computations the dependence of the molecular viscosity on the temperature is modeled by the Chapman Rubesin formula (eq. 2.1.6). Also the artificial dissipation terms were carefully monitored. The physical viscous terms were found to be between two and three order of magnitude greater than the artificial damping terms for all the equations with the minimum difference appearing in the energy equation. The flow conditions and the computed integral quantities ( lift coefficient  $C_l$  and pressure drag  $C_d$  ) are summarized in the table I. All these computations have been carried out on a IBM 3081 scalar machine; the cpu time for a typical run on the  $256 \times 64$  grid with 3 levels of the multigrid and 500 multigrid cycles is 149 minutes.

The three stage time stepping scheme was used in these calculations. Convergence was enhanced by residual smoothing with constant coefficients, together with a simple saw-tooth multigrid strategy. The CFL number is between 2.4/3.0 for all the steady computations. For most of the cases convergence is quite satisfactory. A steady state is reached within 300-500 cycles and the RMS of the density residuals on the finest grid is reduced to  $O(10^{-4}-10^{-5})$ .

#### 1.1. Case (1.1) Transonic Laminar Flow at $Re = 73$ and $10^0$ Angle of attack.

Figs. (5.1.2 - 5.1.4) show , respectively , the computed pressure, Mach and density field for this flow condition. From the drawing of the iso-Mach contours it is evident that for this case the viscous effects dominate in a large portion of the flow field. For this reason the leading edge suction is strongly limited by the rapid growth of the boundary layer. This causes the increase of the velocity to be limited , with the result that locally supersonic conditions are reached only in a

small pocket outside the edge of the viscous layer. This can also be seen from the relatively flat surface pressure distribution of fig. (5.1.5). This low Reynolds number computation tests our scheme near the Stokes limit of extremely viscous flows. Nevertheless, the numerical scheme predicts the flow field quantities consistently and the results are in good agreement with other computations [57,58], and experimental measurements [cfr. 5.3].

### 1.2. Case (1.2) Transonic Laminar Flow at $Re = 500$ and $10^0$ Angle of attack.

For this case a small supersonic pocket is present in the flow field. Although the boundary layer extends into a large portion of the flow field, the leading edge expansion is strong enough to accelerate the stream to supersonic conditions. The recompression to subsonic flow seems to take place gradually through the edge of the viscous region. For this case, the contours of the flow quantities are shown in figs. (5.1.6 - 5.1.8), and the surface pressure distribution is shown in fig. (5.1.9). From the iso-Mach contours it can be noted that separation occurs and a very wide separated wake is formed downstream. The magnitude of the velocity vector in the separated region is very small, and accuracy is therefore of special concern. However, the location of the separation point as well as the extent of the separated region compare well with computation performed on a coarser grid, as well as other computations [42,43], indicating that these features are well reproduced by the scheme.

### 1.3. Case (1.3) Supersonic Laminar Flow at $Re = 106$ and $10^0$ Angle of attack.

This is a standard test case that has been received wide attention in the literature [59,60]. At supersonic free stream conditions a strong bow shock wave forms in front of the airfoil. Toward the far field the shock tends to weaken due to the curvature. The position and the strength of the computed shock are well predicted by the scheme as shown by the iso-line plots (figs. 5.1.10 - 5.1.12), and by a direct comparison with the experiments [cfr. 5.3]. This computation once again proves the robustness of the scheme in handling very different flow conditions. The overall comparison between the three test cases so far presented is also a demonstration of the ability of the scheme to correctly predict physical scaling properties of the flow.

**1.4. Case (1.4) Transonic Laminar Flow at  $Re = 500$  and  $0^\circ$  Angle of attack.**

This symmetric case was computed over the entire flow field. Again the computed iso-lines (figs. 5.1.14 - 5.1.16) as well as the surface pressure plot ( fig. 5.1.17) are reported. From the latter it is evident that the flow is separated and that a small recirculation bubble is present. Note, however, that the symmetric solution obtained indicates that the laminar separated region is fairly stable and confined by the thick boundary layer. Supersonic pockets are also present, but they are confined in the outer portion of the flow field by the rapid growth of the viscous layer.

**1.5. Case (1.5) Transonic Laminar Flow at  $Re = 2,000$  and  $0^\circ$  Angle of attack.**

This case has the same flow parameters of the previous one except that the Reynolds number is increased to a value of 2,000. The comparison of the iso-lines of the flow field quantities (figs. 5.1.18 - 5.1.20) to those corresponding to case 1.4 (figs. 5.1.14 - 5.1.16) confirms the physical expectation of a thinner boundary layer, and again verifies the physical scaling of the extent of the viscous region proportional to  $1 / \sqrt{Re}$ . Correspondingly a 40% decrease of the drag coefficient ( Tab. 1) is also computed. Again a perfectly symmetric solution is computed as can be seen from the surface pressure plot of fig. (5.1.21), indicating stability of the physical phenomena.

**1.6. Case (1.6) Transonic Laminar Flow at  $Re = 10,000$  and  $0^\circ$  Angle of attack.**

This is the most interesting and critical test case. At these flow conditions an unsteady behaviour of the flow is observed and vortices are shed from the trailing edge as indicated in figs. (5.1.22 - 5.1.24). These show the flow field pattern at a particular time chosen in order to capture the shedding of vortices at the trailing edge. On account of the unsteady nature of the flow field pattern, the numerical scheme has been run with a constant time step and without implicit smoothing on a single 256x64 grid. The symmetry of the flow field is broken by the vortex shedding phenomena and fairly large pressure oscillations are observed on the surface (fig. 5.1.25).

However on the coarser grid 128x32 almost all the details of the flow are missing. No vortices are shed from the trailing edge, and a symmetric (fig. 5.1.29) pseudo converged solution is

obtained (figs. 5.1.26 - 5.1.29). The completely different results obtained when using two different levels of mesh refinement indicate that higher temporal and spatial accuracy are required to treat cases with such disparate length and time scales.

## 2. Laminar flows over a NACA0012 airfoil with the cell centered scheme.

Some of the test cases presented in the previous paragraph were also computed by the cell centered scheme. The results presented in this section were obtained by driving the  $W$  multigrid cycle with the 5 stage scheme described in (3.5). Smoothing with locally varying coefficients was also employed. The dependence of the molecular viscosity coefficient on the temperature was modeled by using the Sutherland law (eq. 2.1.5). Also, adiabatic boundary conditions were imposed at the wall.

The grid employed is a  $320 \times 64$  (fig. 5.2.1) with the first point on the normal to the airfoil direction placed at a distance of .002 chords away from the wall. Again  $5/8$  of the total number of points along the innermost C-line are fitted on the airfoil. Computations were also performed on a coarser  $160 \times 32$  grid obtained again by eliminating alternate points from the finest one.

The CFL number is increased to a value of 8, and the coarsest grid employed in the multigrid cycle has just 2 computational cells in the  $j$  direction.

### 2.1. Transonic Laminar Flow at $Re = 500$ and $0^{\circ}$ Angle of attack.

The free stream flow conditions for this case are identical to those of case (1.4). For this case a comparison of the flow field quantities computed by the CCS-A and CCS-B schemes shows complete agreement between the two formulations. The comparison of the density (fig. 5.2.2), pressure (fig. 5.2.3), Mach number (fig. 5.2.4) and entropy (fig. 5.2.5) computed by the two schemes on the finest  $320 \times 64$  grid indicate perfect agreement. Moreover the flow pattern is also in good agreement with the one computed by the vertex scheme (figs. 5.1.14 - 5.1.16).

A comparison of the accuracy of the surface pressure plots on a  $160 \times 32$  (fig. 5.2.6) and  $320 \times 64$  (fig. 5.2.7) grid between the results obtained with the two cell centered formulations indicates that no significant difference exists. The slightly different drag coefficient computed by the

vertex scheme (Tab. 1) and the cell centered formulations reflects the differences in the treatment of the boundary conditions at the wall for the energy equation as well as the different modeling of the molecular viscosity coefficient.

A comparison of the convergence history measured by the RMS reduction of the residual of the density indicate that the two cell centered schemes behaves equally well for both the coarser (fig. 5.2.8) and finest (fig. 5.2.9) grids. Note , however, that for these computations the convergence to a steady state within engineering accuracy ( $RMSO(10^{-4})$ ) is obtained with only 75 multigrid cycles.

## 2.2. Transonic Laminar Flow at $Re = 500$ and $10^0$ Angle of attack.

The flow conditions for this case correspond to case (1.2). Again The comparison between the two cell centered formulations is found to be excellent. Since no differences were noted in the flow fields computed by the two cell centered formulations only the density (fig. 5.2.10), pressure (fig. 5.2.11) and Mach number (fig. 5.2.12) iso-lines obtained with the CCS-A formulation are reported. However a direct comparison of the entropy fields computed by the CCS-A and CCS-B formulations is reported in fig. (5.2.13). The choice of a direct comparison of the entropy fields computed with the two formulations is motivated by the observation that this quantity is the most sensitive indicator of the level of accuracy. Again the computed surface pressure distributions computed by the two schemes show very good agreement (fig. 5.2.14) with minimal differences in the prediction of the lift and drag coefficients. Also the convergence plots for the two schemes show similar behaviour with a reduction of the density RMS of  $O(10^{-6})$  achieved in 75 multigrid cycles (fig. 5.2.15).

For this case computations with the CCS-A scheme to the machine accuracy were performed for the coarser  $128 \times 32$  grid. The computed surface pressure is presented in fig. (5.2.16) and the convergence plot is reported in fig. (5.2.17). Machine accurate results are obtained in about 200 multigrid cycles. The lift and drag coefficients were fixed to the fourth decimal place in about 75 cycles. In a recent paper [58], Hollander and Ravalason reported calculation of the same

case to machine accuracy using an implicit factorized scheme. They reported convergence to machine accuracy in about 3,000 iterations for a computation performed on a grid with a total number of points equivalent to our  $160 \times 32$  grid. This comparison is a good indication of the efficiency that our multigrid explicit scheme has achieved for steady state laminar computations.

### 3. Comparisons with experiments

For two of the test cases (1.1 and 1.3) the availability of experimental information [61] about the measured density field allows a direct test of the accuracy of the computed solutions.

From the direct comparisons of the measured density contours and the density contours computed by the vertex scheme (figs. 5.2.18 - 5.2.21) one observes that the overall agreement is quite satisfactory. Especially for the supersonic case the location and strength of the shock wave is well predicted by the computations. In both cases there is, however, some disagreement in the trailing edge region. Similar behaviour at the trailing edge has also been computed by other authors using completely different numerical schemes [59,60]. The origin of this disagreement is not clear.

In the report of the experimental results [61] it is suggested that at these particular flow conditions no-slip boundary conditions might not be appropriate. It was also noted, in the same report, that for computer simulations which were performed allowing slip at the surface the agreement could be indeed be improved. However, no clear conclusion can be drawn. For these reasons we decided to investigate the influence of changing the boundary condition on the energy equation by performing the computations with the cell centered scheme (CCS-A) with adiabatic wall conditions for the supersonic case. The computed flow pattern is very similar to the one computed by the vertex scheme as indicated by the iso-plot of the pressure (fig. 5.2.22) and Mach number (fig. 5.2.23). However the comparison of the computed density field with the experimental data (fig. 5.2.24), while preserving overall agreement, still shows differences at the trailing edge.

Table 1 - Integral Values of Computed Test Cases

Case	Grid Points	$M_\infty$	Re	$\alpha$	$c_L$	$c_D$	$\log(dp/dt)$
1	256x64	.8	73	10°	.6657	.2522	-2.34
2	256x64	.8	500	10°	.4797	.1597	-3.50
3	256x64	2.0	106	10°	.3716	.1851	-1.74
4	256x64	.85	500	0°	.0	.0964	-3.75
5	256x64	.85	2000	0°	.0	.068	-3.62
6.1	128x32	.85	10000	0°	.0	.046	-2.59
6.2	256x64				.1386	.0723	-0.10

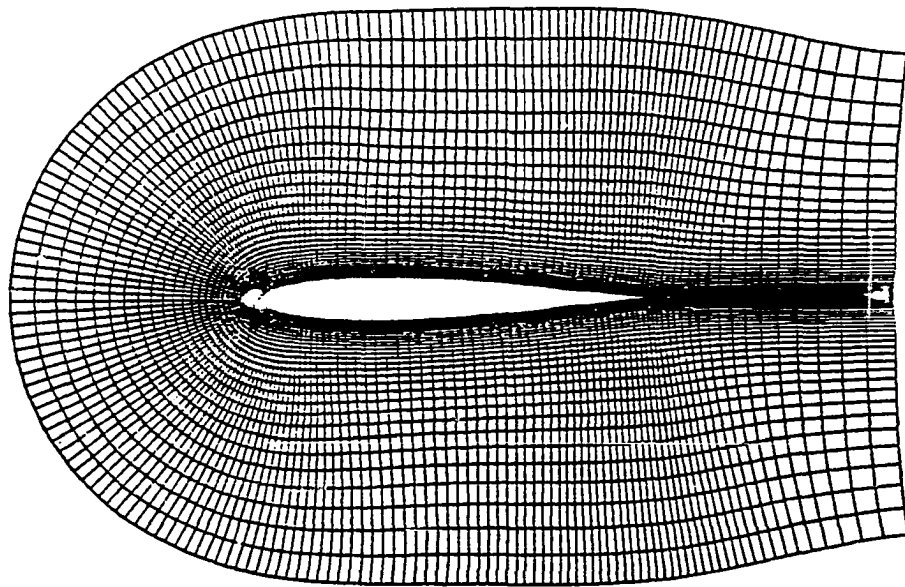


Fig. 5.1.1  
NACA 0012 airfoil -  
256x64 C-mesh for laminar computations.

CASE 1 (256x64)

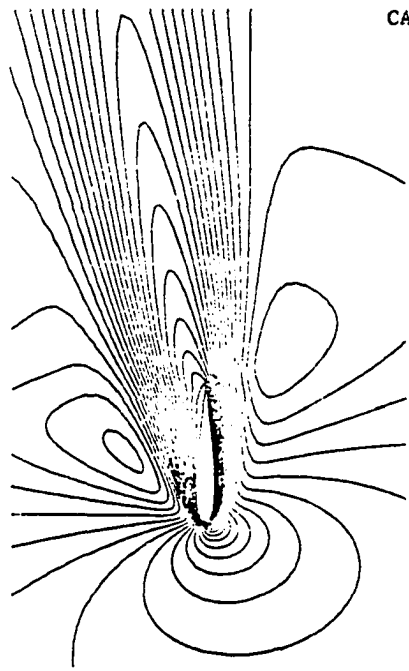


Fig. 5.1.3  
NACA 0012 airfoil -  
Mach Contours ( $D M = .05$ )

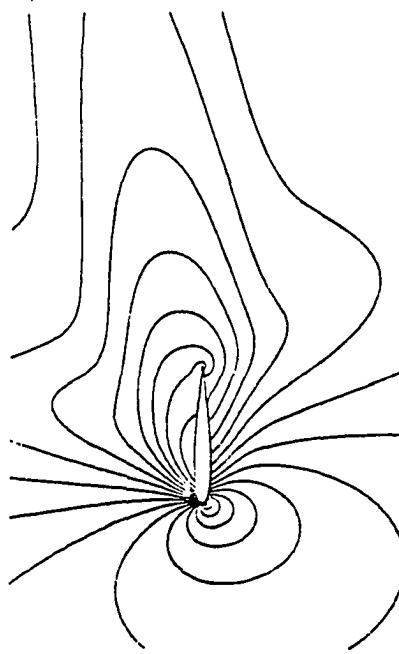


Fig. 5.1.4  
NACA 0012 airfoil -  
Density Contours ( $D p = .05$ )

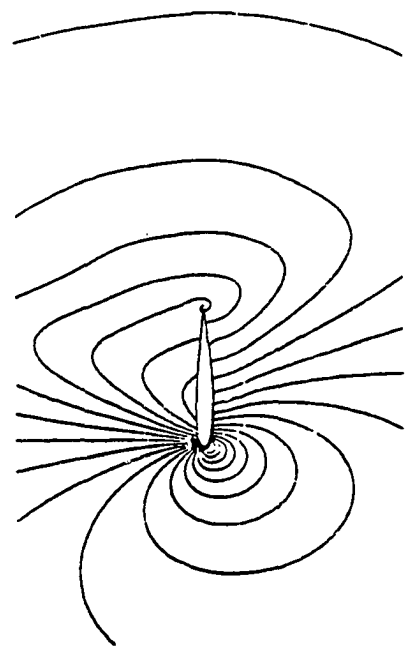


Fig. 5.1.2  
NACA 0012 airfoil -  
Pressure Contours ( $D P = .05$ )

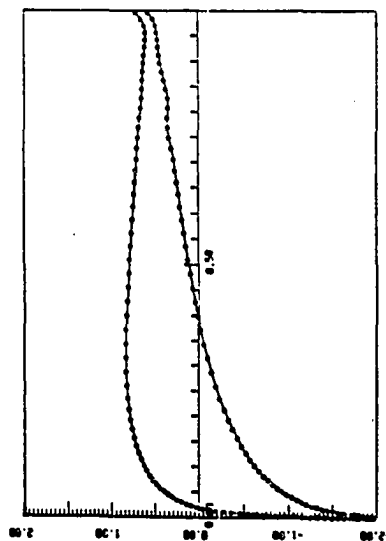


Fig. 5.1.5  
NACA 0012 airfoil -  
Pressure coefficient along the surface.

- 71 -

CASE 2 (256x64)

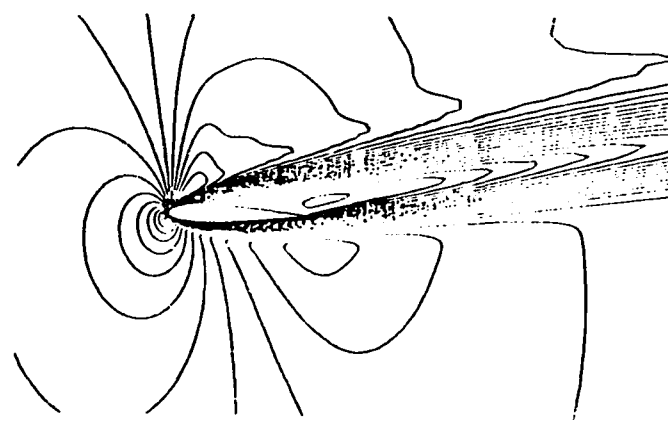


Fig. 5.1.7  
NACA 0012 airfoil -  
Mach Contours ( $D\mu = .05$ )

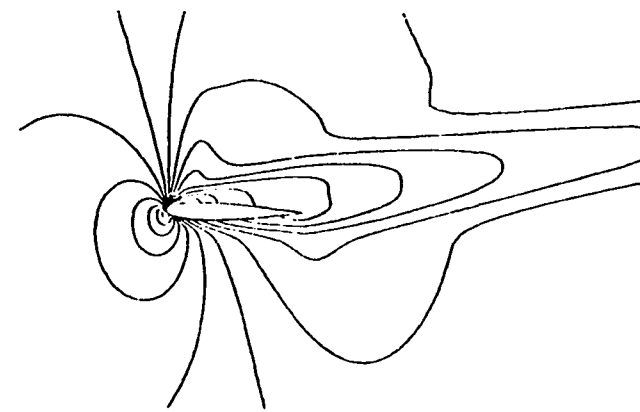


Fig. 5.1.8  
NACA 0012 airfoil -  
Density Contours ( $D\mu = .05$ )

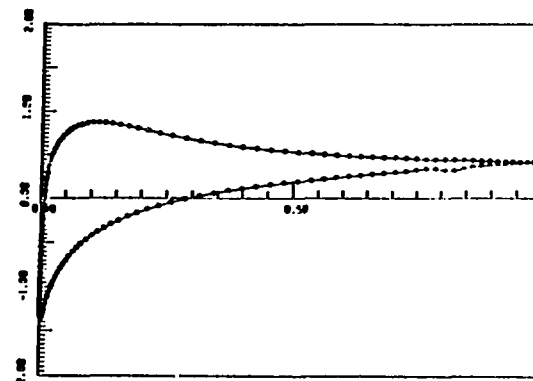


Fig. 5.1.9  
NACA 0012 airfoil -  
Pressure coefficient along the surface.

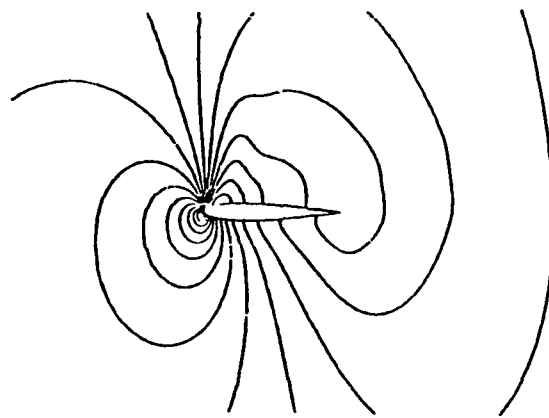


Fig. 5.1.6  
NACA 0012 airfoil -  
Pressure Contours ( $D\mu = .05$ )

CASE 3 (256x64)

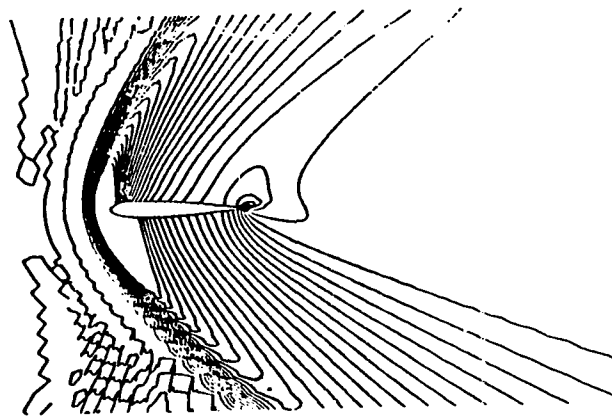


Fig. 5.1.10  
NACA 0012 airfoil -  
Pressure Contours ( $D\bar{P} = .05$ )

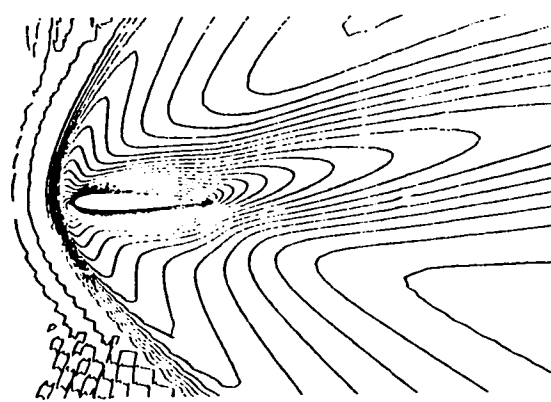


Fig. 5.1.11  
NACA 0012 airfoil -  
Mach Contours ( $D\bar{M} = .05$ )

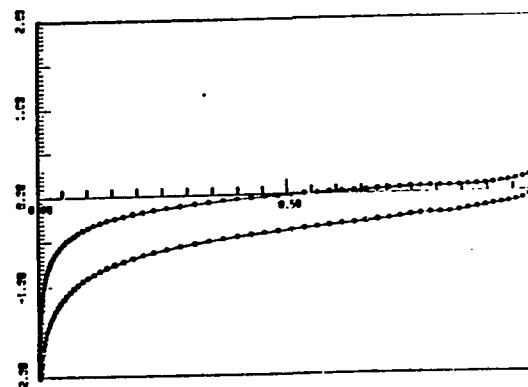


Fig. 5.1.13  
NACA 0012 airfoil -  
Pressure coefficient along the surface.

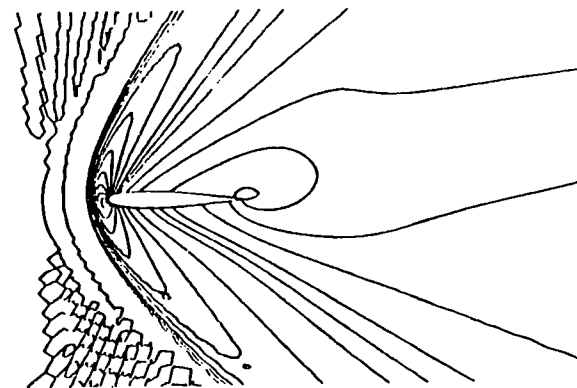


Fig. 5.1.12  
NACA 0012 airfoil -  
Density Contours ( $D\rho = .05$ )

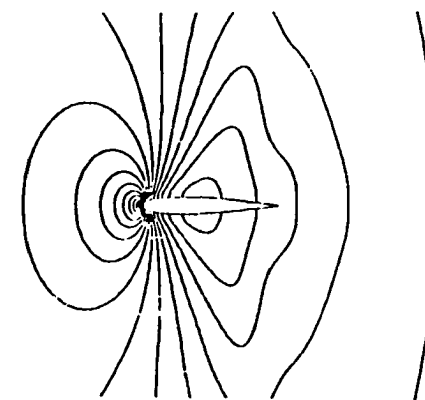


Fig. 5.1.14  
NACA 0012 airfoil -  
Pressure Contours ( $DP = .05$ )

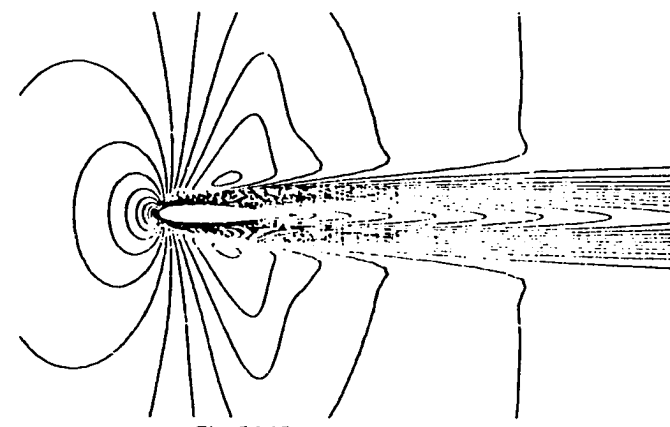


Fig. 5.1.15  
NACA 0012 airfoil -  
Mach Contours ( $DM = .05$ )

- 73 -

CASE 4 (256x64)

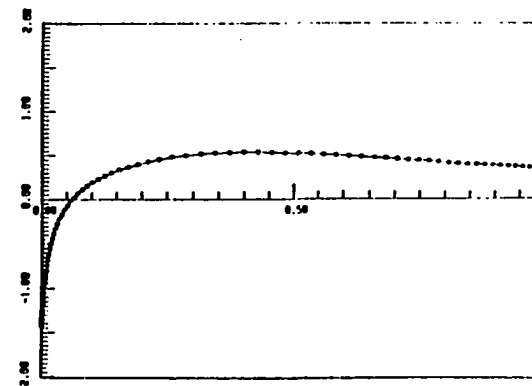


Fig. 5.1.17  
NACA 0012 airfoil -  
Pressure coefficient along the surface.

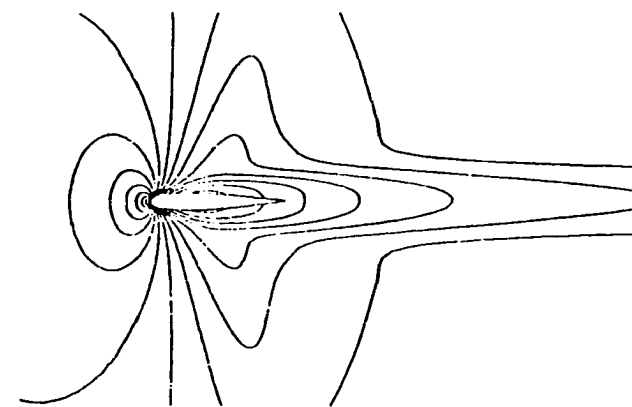


Fig. 5.1.16  
NACA 0012 airfoil -  
Density Contours ( $D\rho = .05$ )

-74-

CASE 5 (256x64)

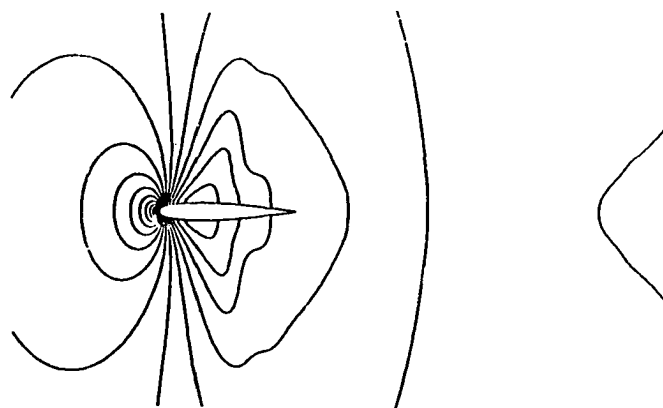


Fig. 5.1.18  
NACA 0012 airfoil -  
Pressure Contours ( $D\rho = .05$ )

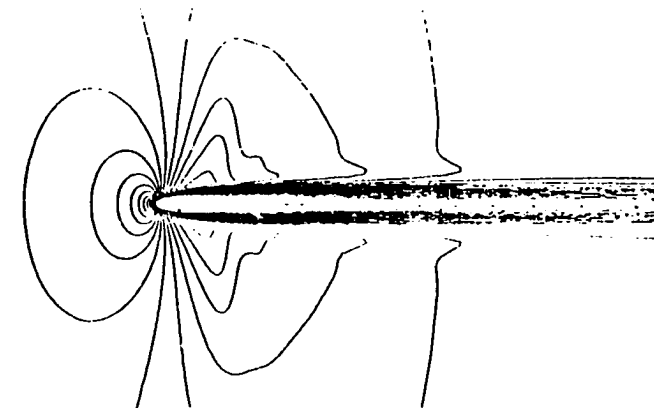


Fig. 5.1.19  
NACA 0012 airfoil -  
Mach Contours ( $DM = .05$ )

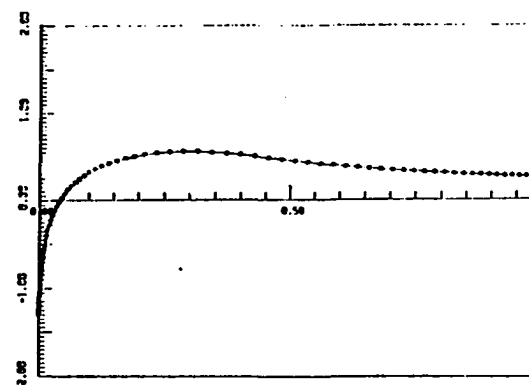


Fig. 5.1.21  
NACA 0012 airfoil -  
Pressure coefficient along the surface.

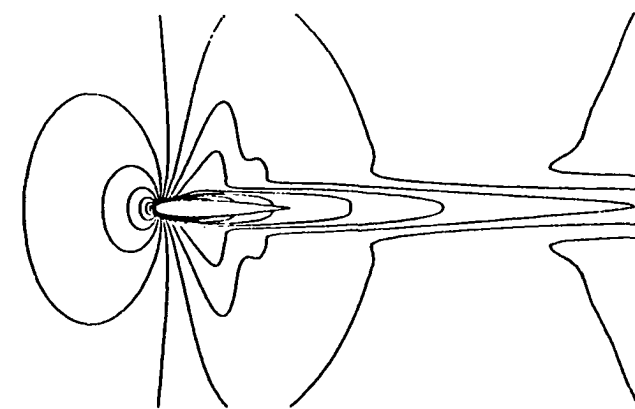


Fig. 5.1.20  
NACA 0012 airfoil -  
Density Contours ( $D\rho = .05$ )

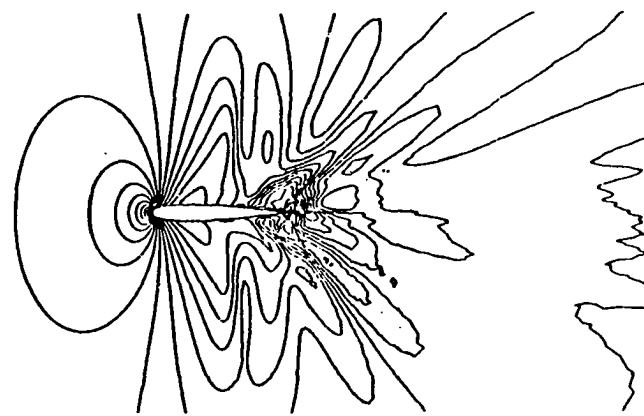


Fig. 5.1.22  
NACA 0012 airfoil -  
Pressure Contours ( $DP = .05$ )

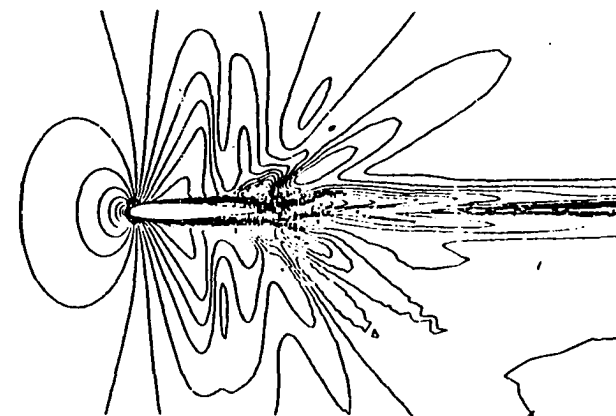


Fig. 5.1.23  
NACA 0012 airfoil -  
Mach Contours ( $DM = .05$ )

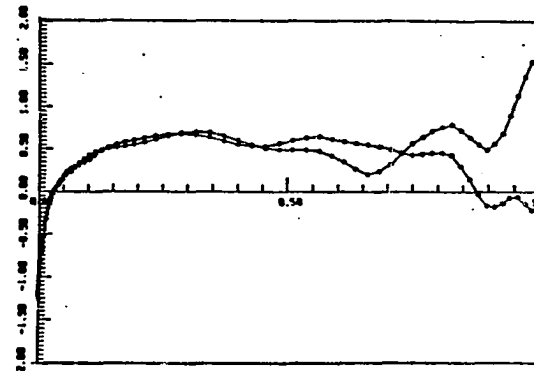


Fig. 5.1.25  
NACA 0012 airfoil -  
Pressure coefficient along the surface.

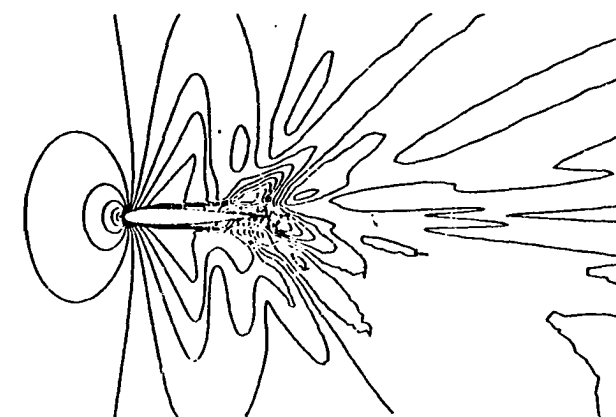


Fig. 5.1.24  
NACA 0012 airfoil -  
Density Contours ( $D\rho = .05$ )

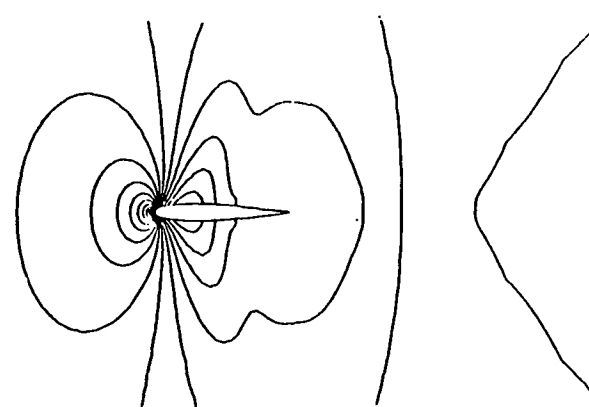


Fig. 5.1.26  
NACA 0012 airfoil -  
Pressure Contours ( $D\rho = .05$ )

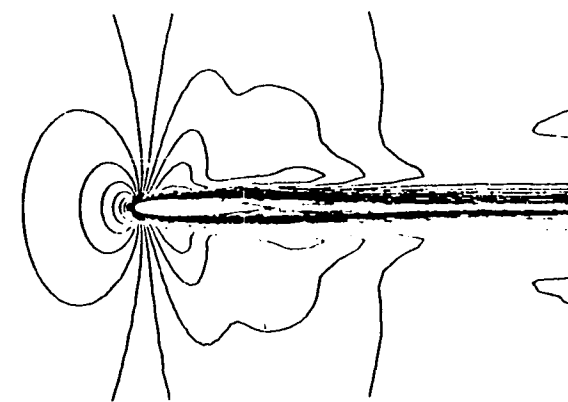


Fig. 5.1.27  
NACA 0012 airfoil -  
Mach Contours ( $D\rho = .05$ )

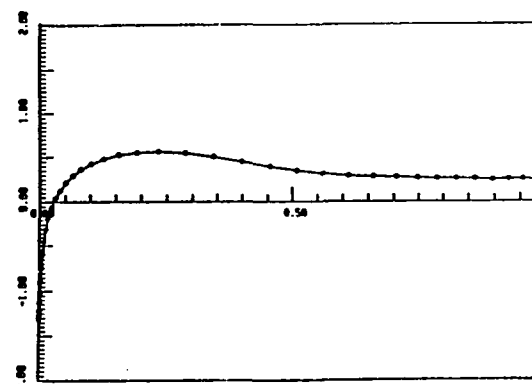


Fig. 5.1.29  
NACA 0012 airfoil -  
Pressure coefficient along the surface.

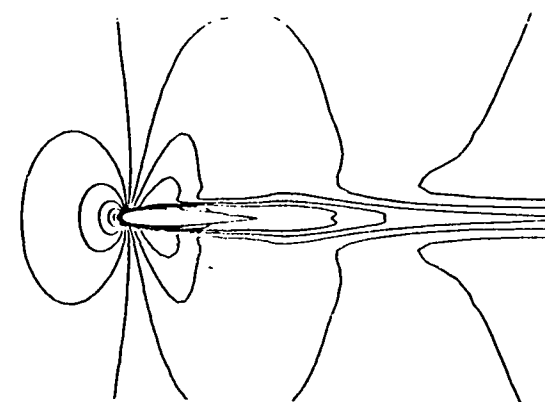
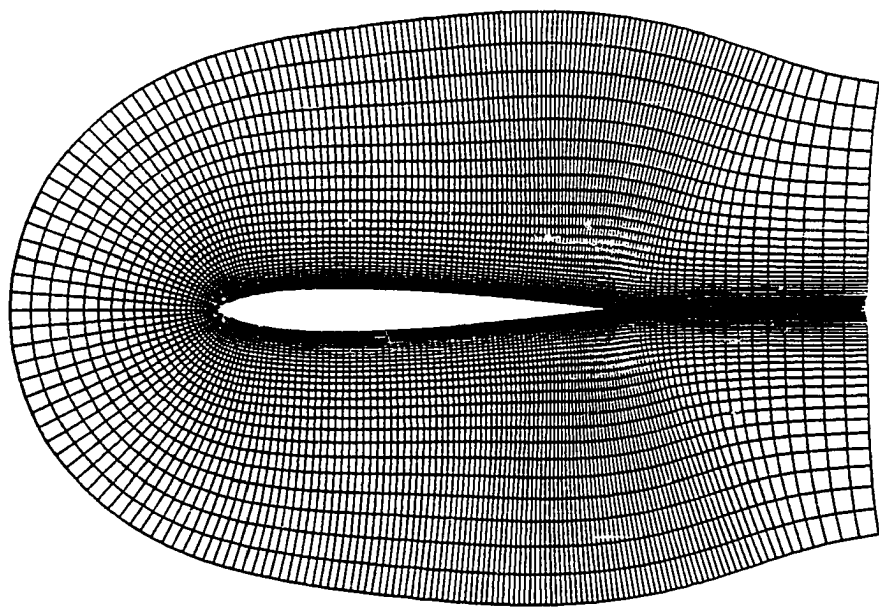
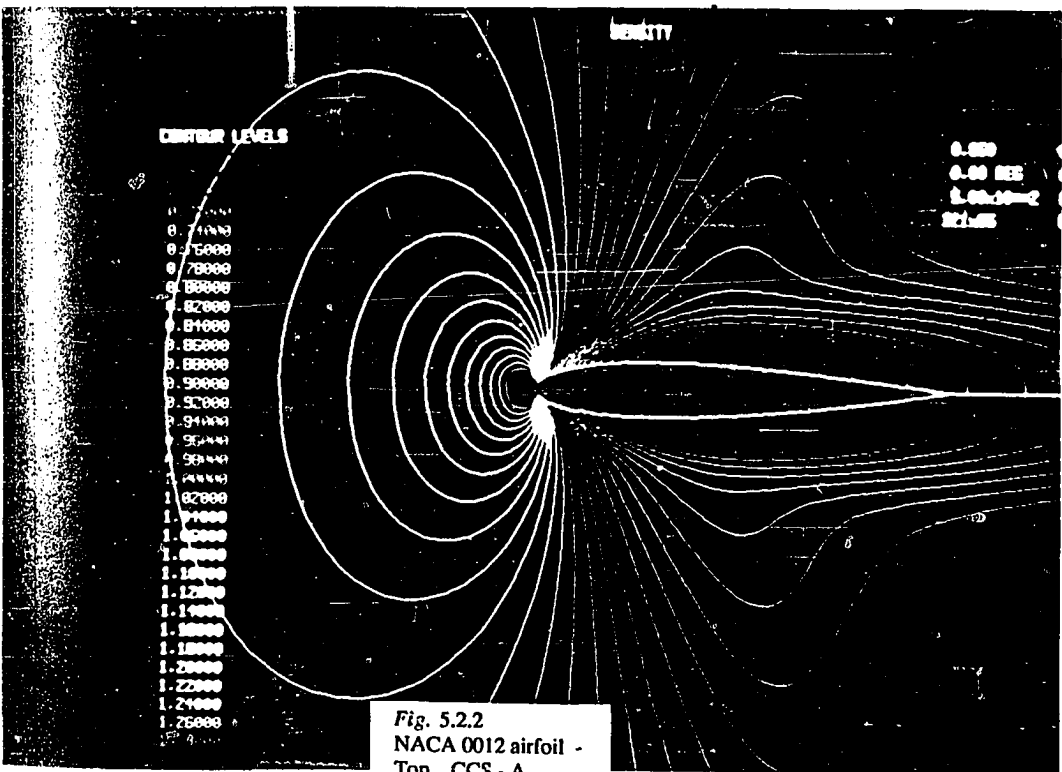
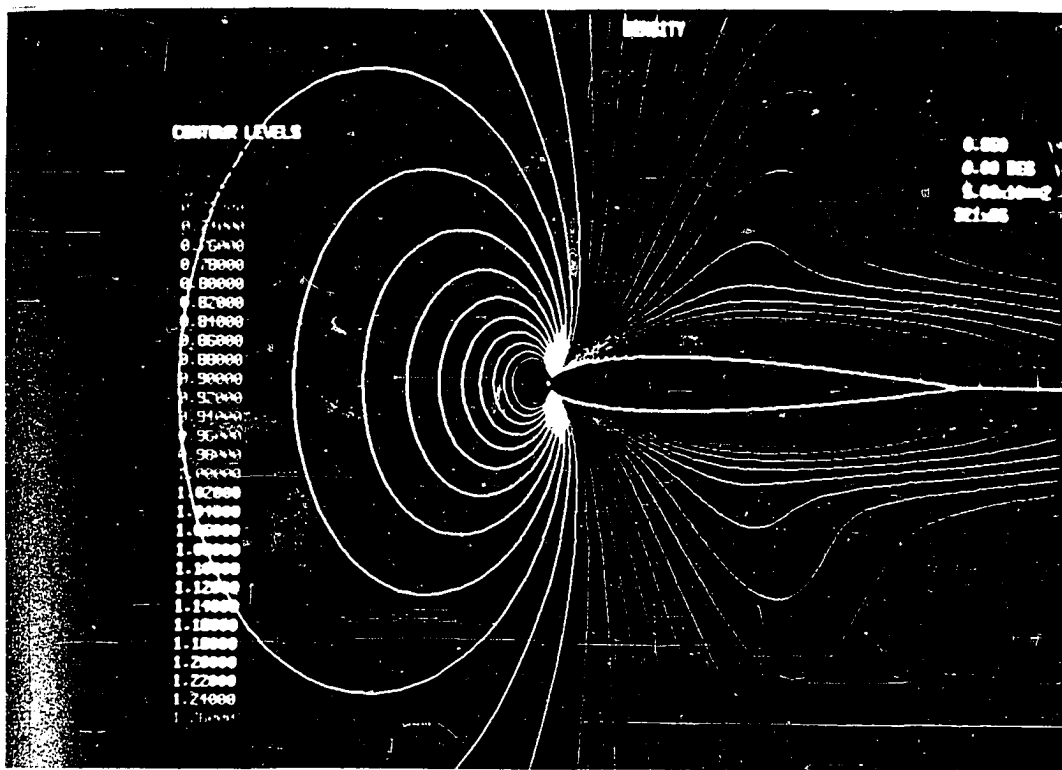


Fig. 5.1.28  
NACA 0012 airfoil -  
Density Contours ( $D\rho = .05$ )



*Fig. 5.2.1*  
NACA 0012 airfoil -  
320×64 C-mesh for laminar computations.



**Fig. 5.2.2**  
NACA 0012 airfoil -  
Top CCS - A  
Bottom CCS - B  
Density Contours

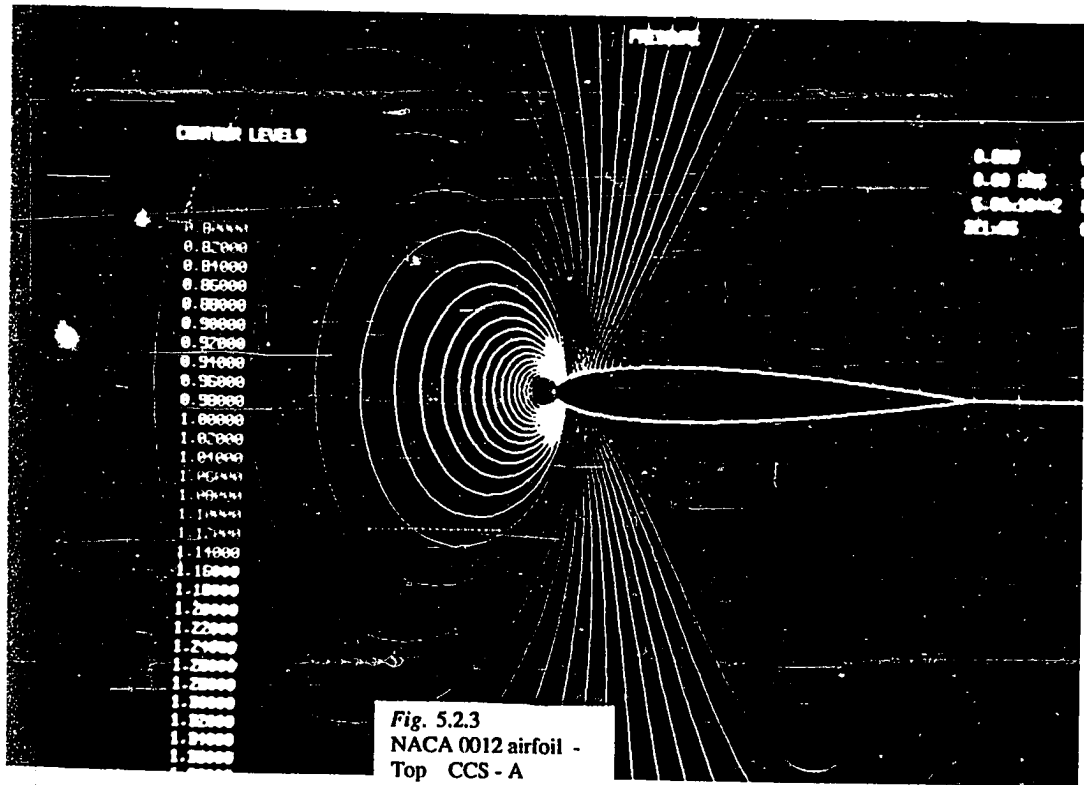
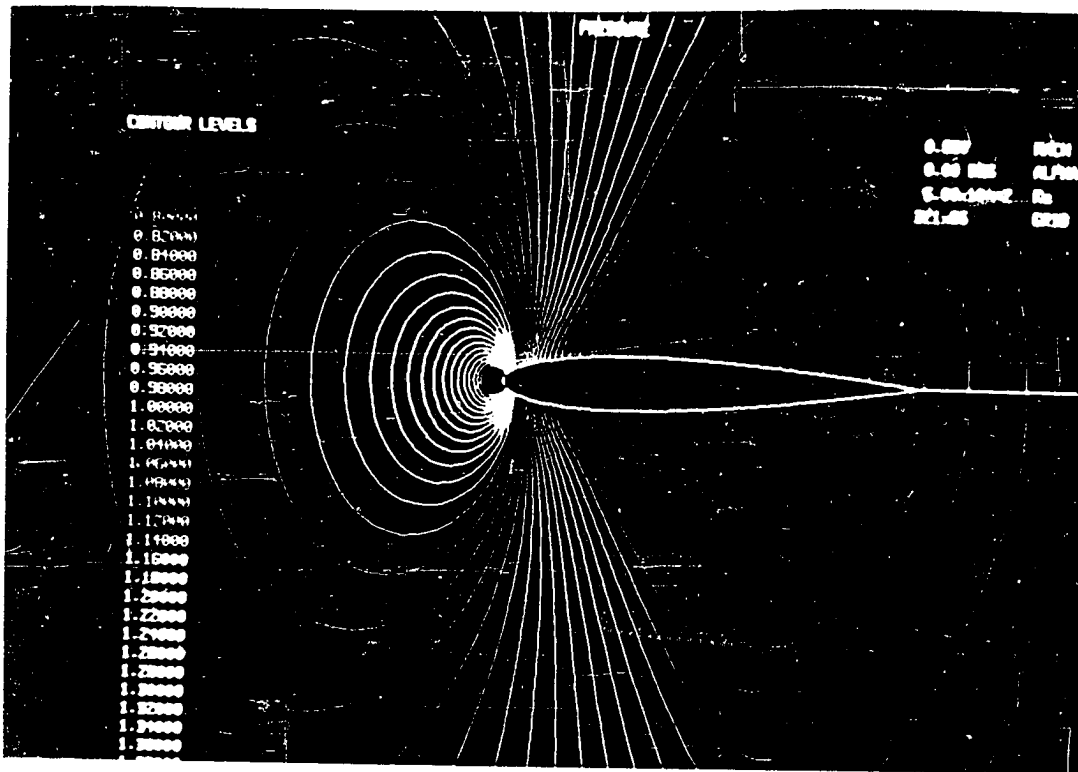


**Fig. 5.2.3**  
**NACA 0012 airfoil -**  
**Top CCS - A**  
**Bottom CCS - B**  
**Pressure Contours**

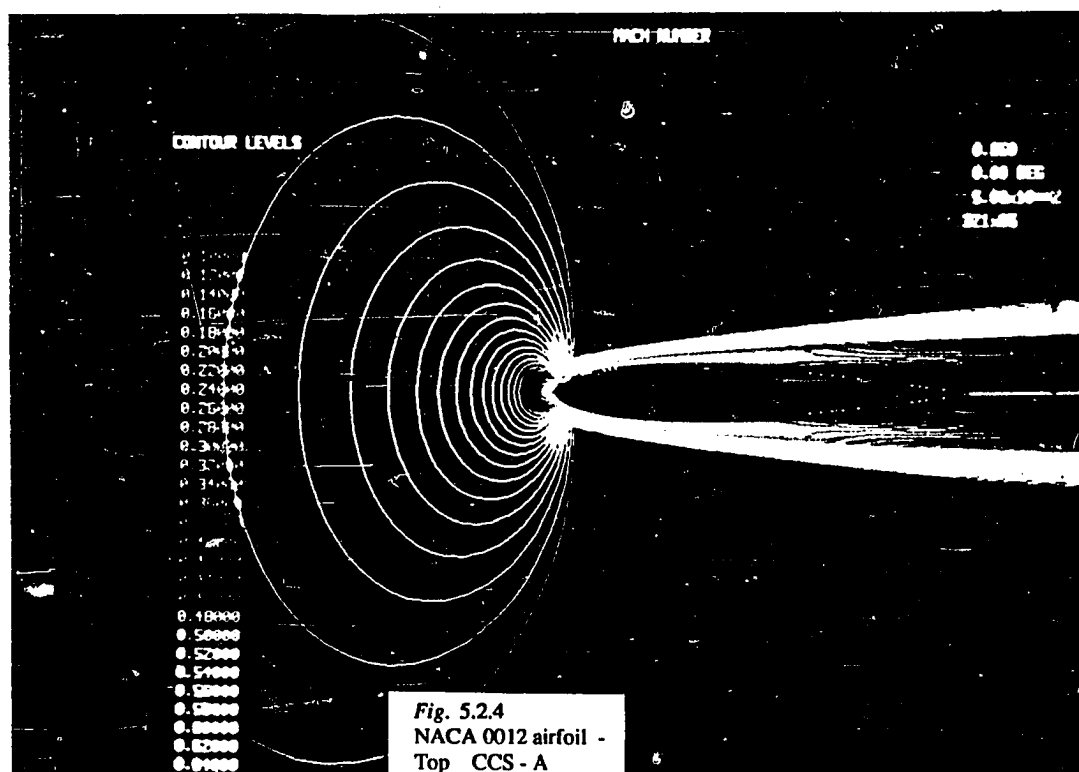
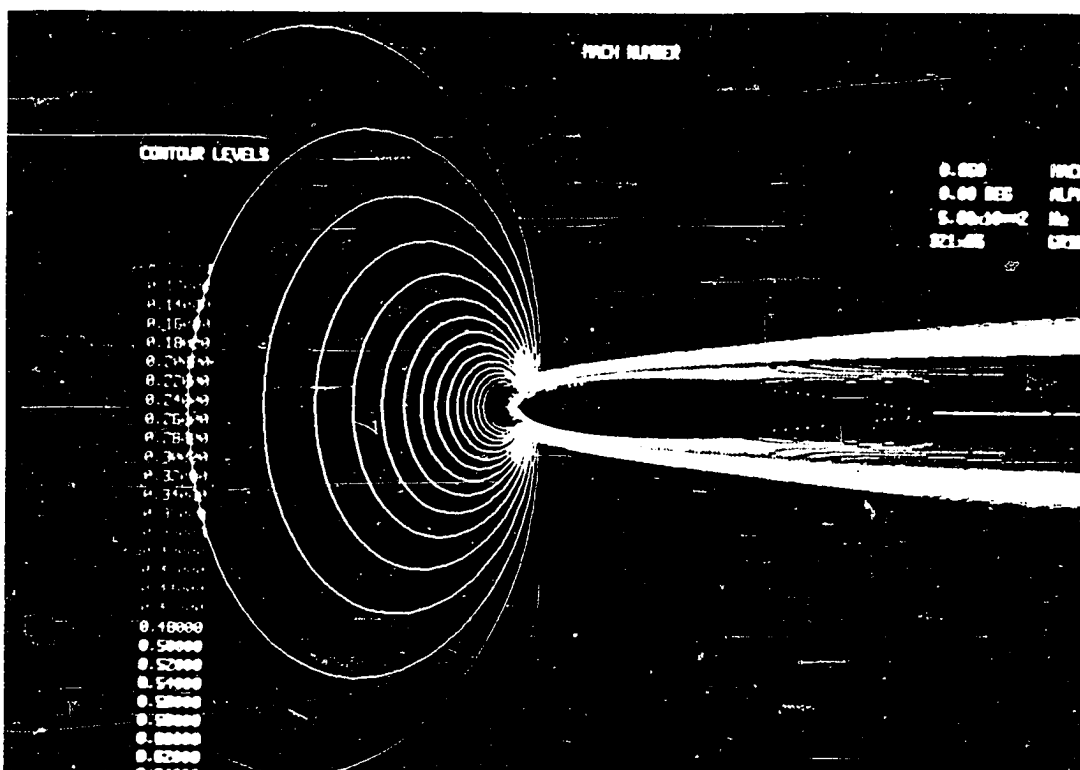


*Fig. 5.2.4*  
NACA 0012 airfoil -  
Top CCS - A  
Bottom CCS - B  
Mach Contours

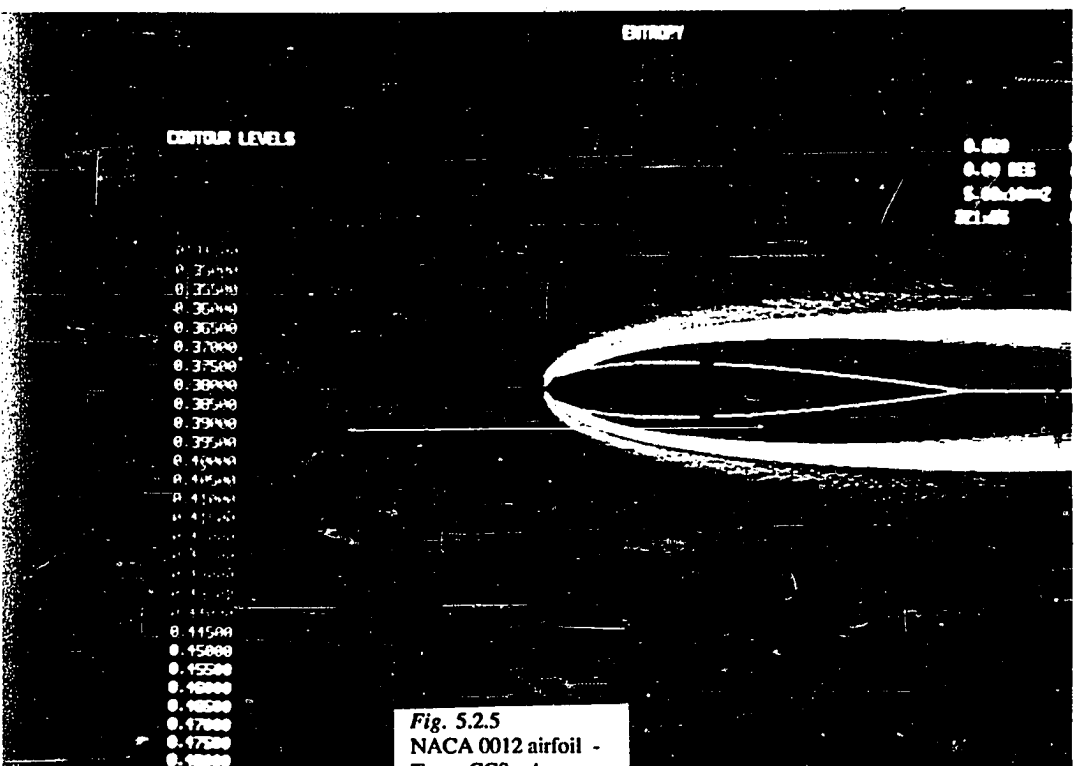
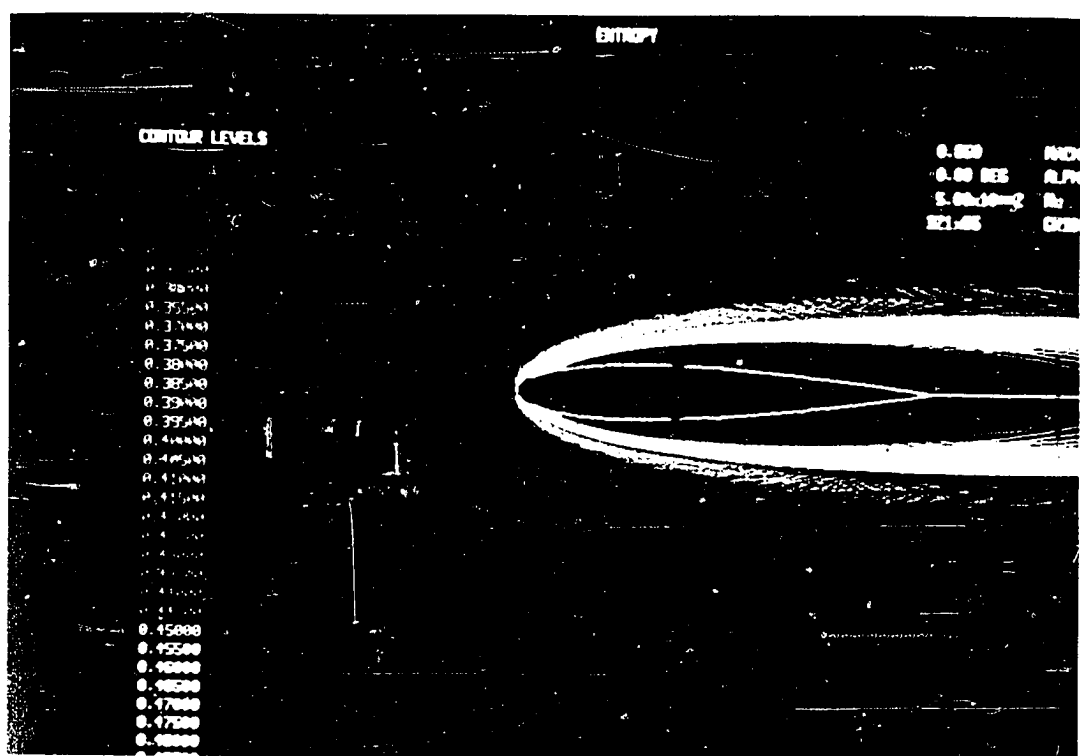


*Fig. 5.2.5*  
NACA 0012 airfoil -  
Top CCS - A  
Bottom CCS - B  
Entropy Contours

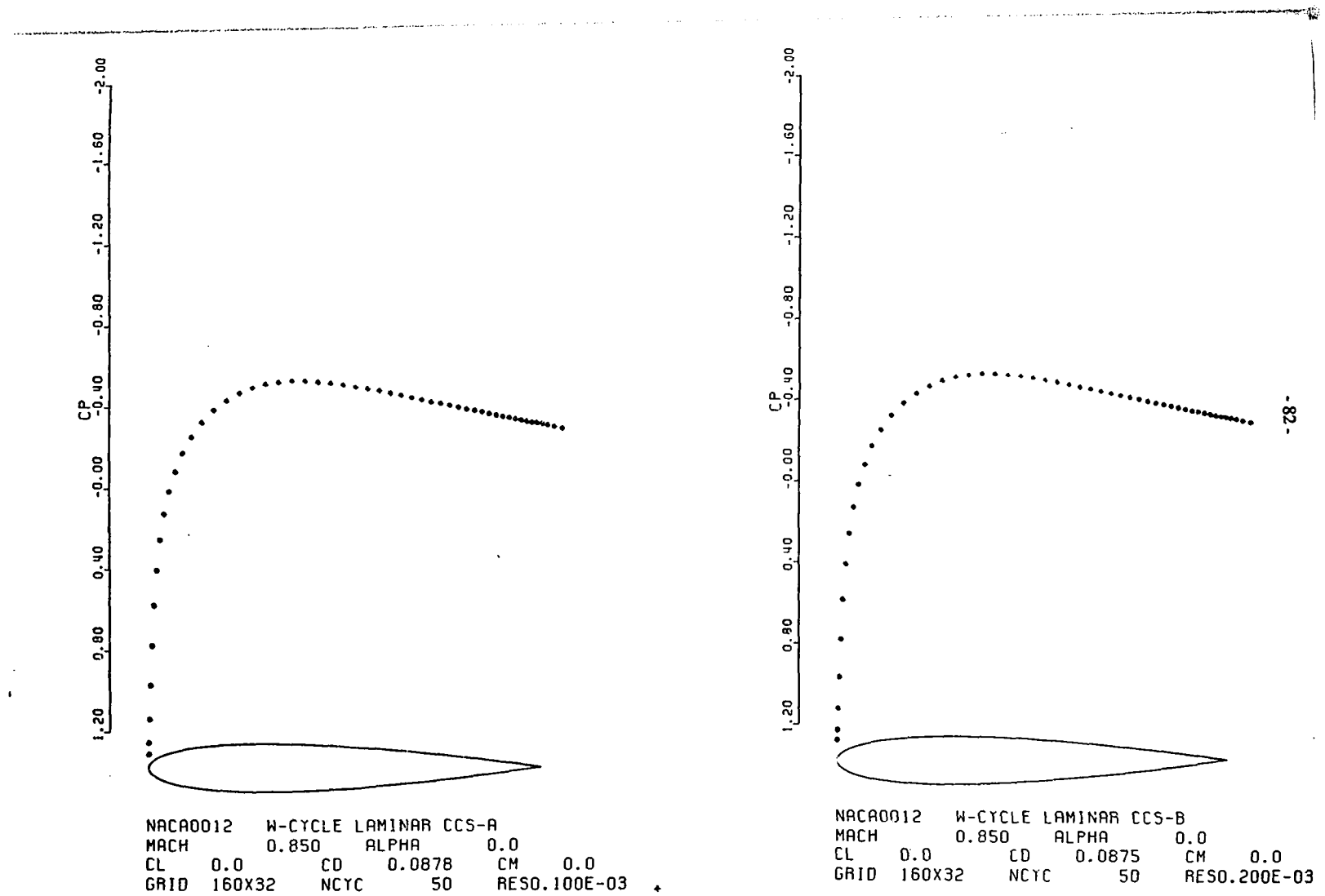


*Fig. 5.2.6*  
NACA 0012 airfoil -  
Pressure coefficient along the surface.

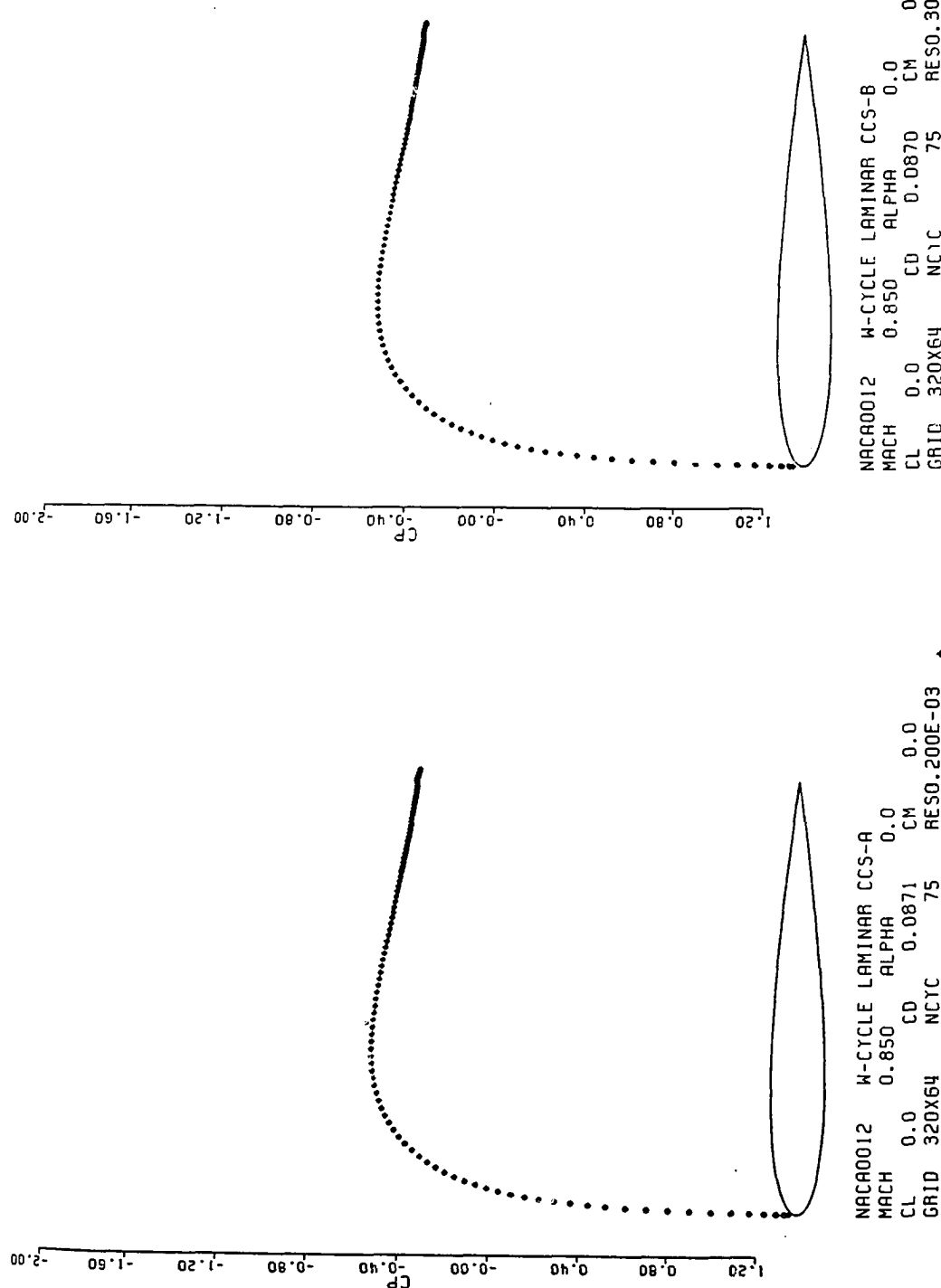
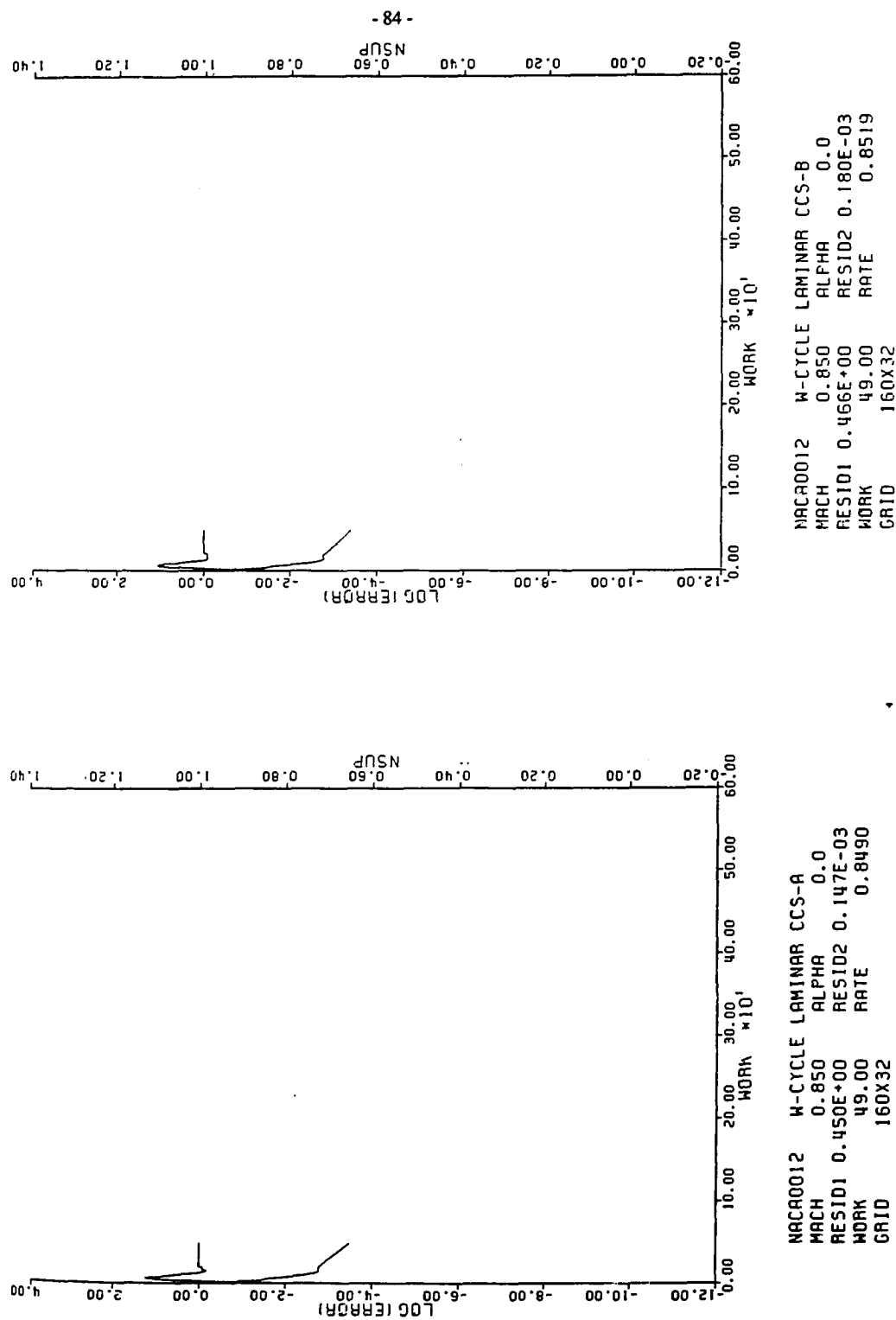
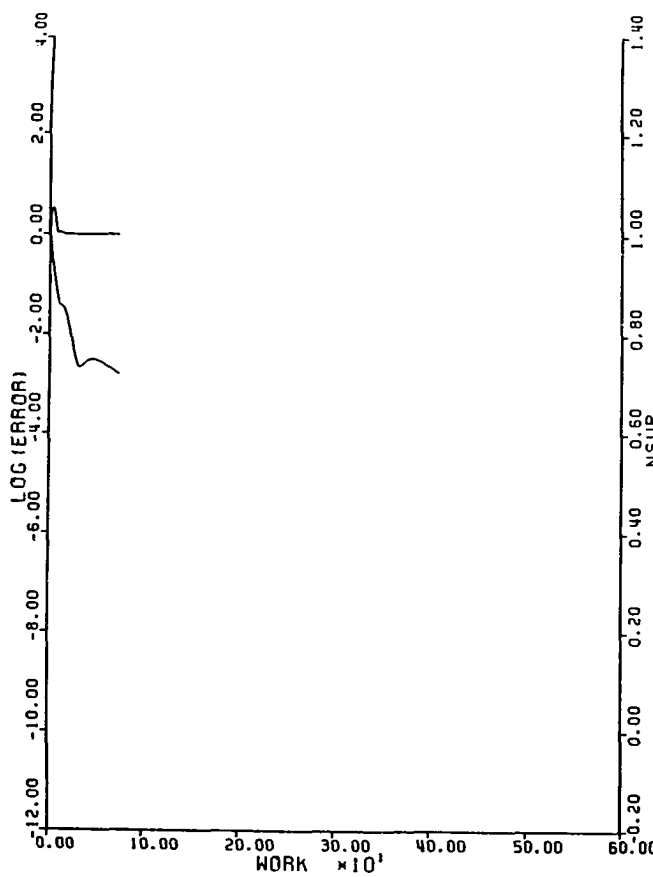


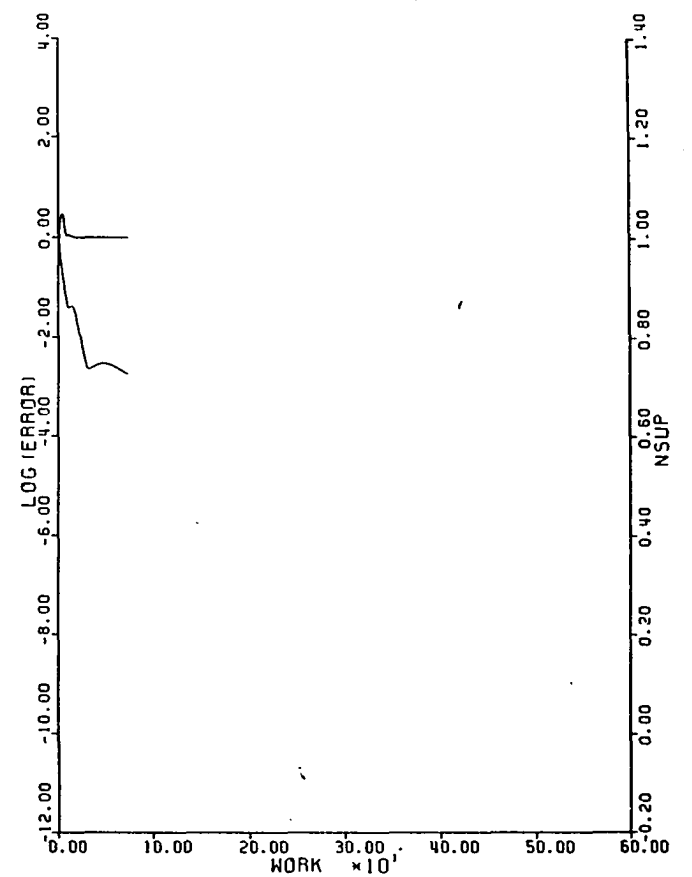
Fig. 5.2.7  
NACA 0012 airfoil -  
Pressure coefficient along the surface.



*Fig. 5.2.8  
NACA 0012 airfoil -  
Convergence history.*



NACA0012    W-CYCLE LAMINAR CCS-A  
MACH        0.850    ALPHA        0.0  
RESID1 0.153E+00    RESID2 0.240E-03  
WORK        74.00    RATE        0.9165  
GRID        320X64



NACA0012    W-CYCLE LAMINAR CCS-B  
MACH        0.850    ALPHA        0.0  
RESID1 0.154E+00    RESID2 0.277E-03  
WORK        74.00    RATE        0.9181  
GRID        320X64

*Fig. 5.2.9*  
NACA 0012 airfoil -  
Convergence history.

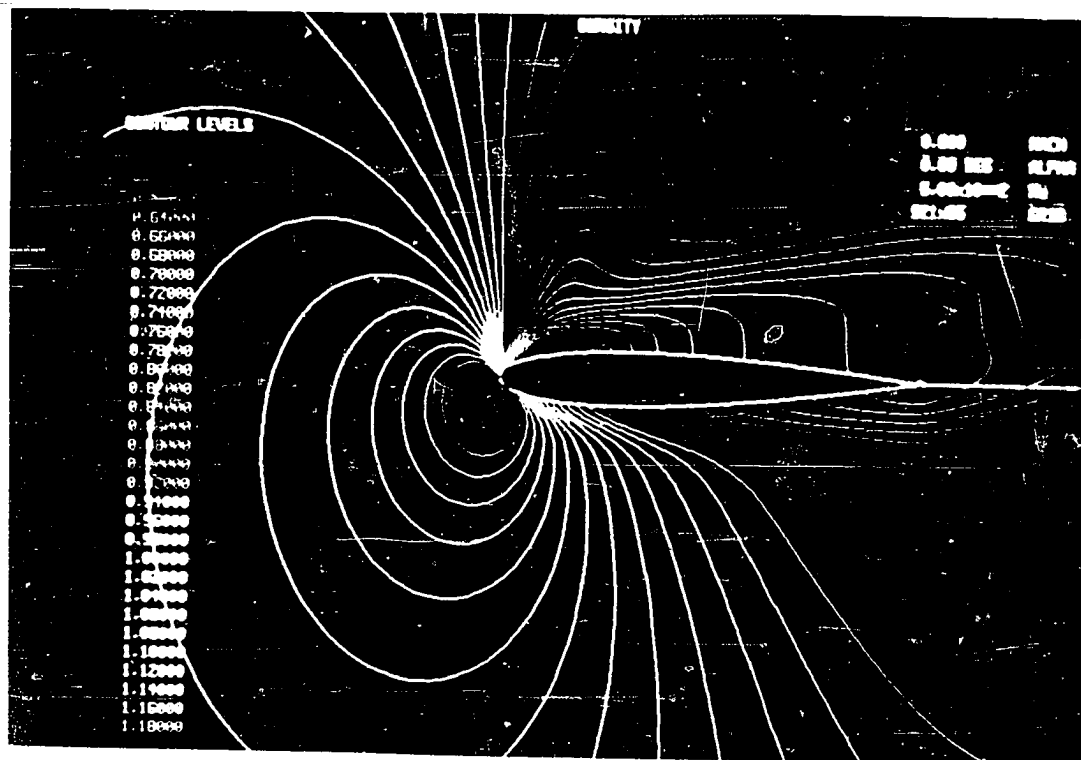


*Fig. 5.2.10*  
NACA 0012 airfoil - CCS - A  
Density Contours

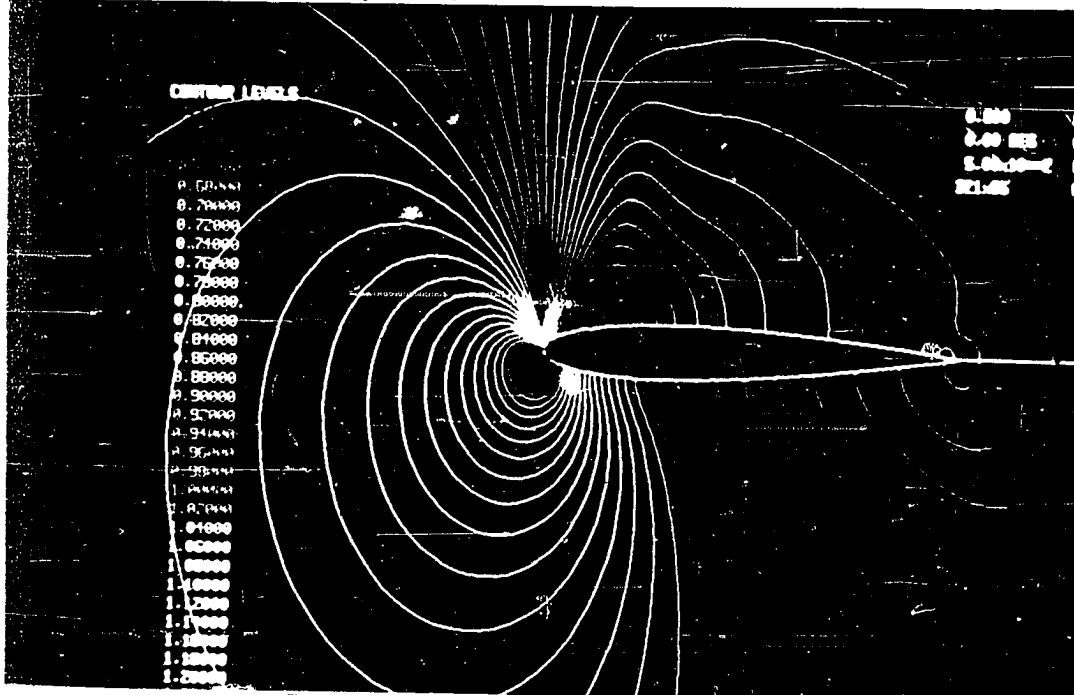


*Fig. 5.2.11*  
NACA 0012 airfoil - CCS - A  
Pressure Contours

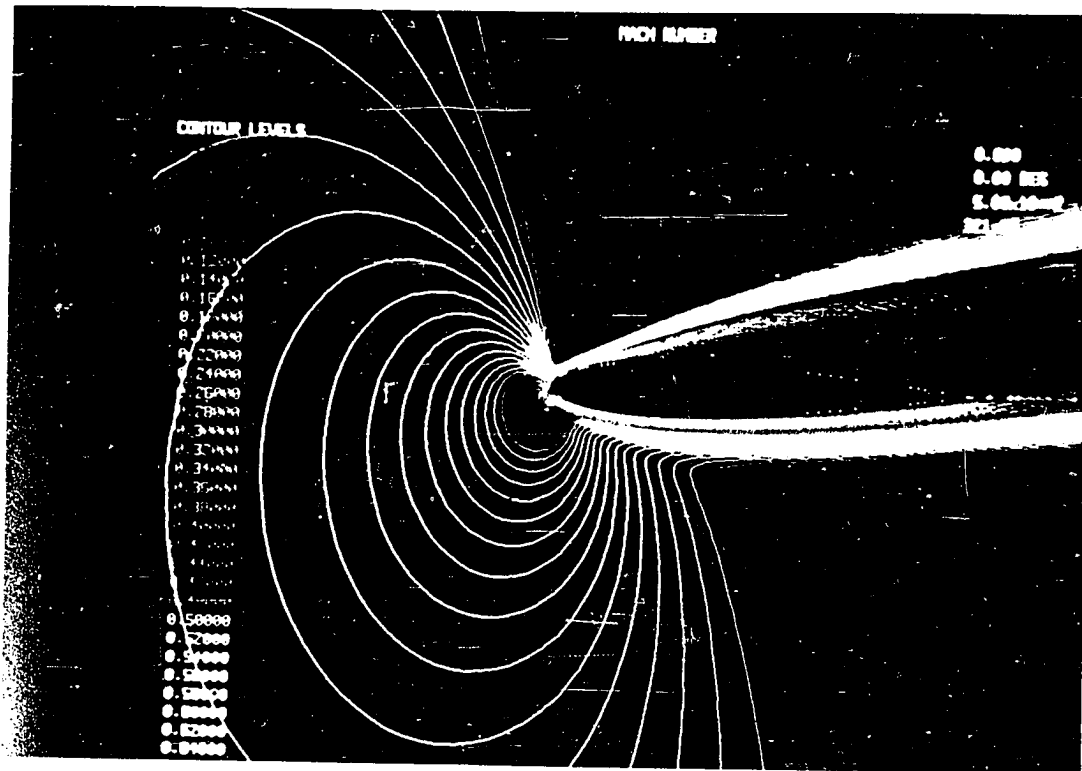


*Fig. 5.2.12*  
NACA 0012 airfoil - CCS - /  
Mach Contours

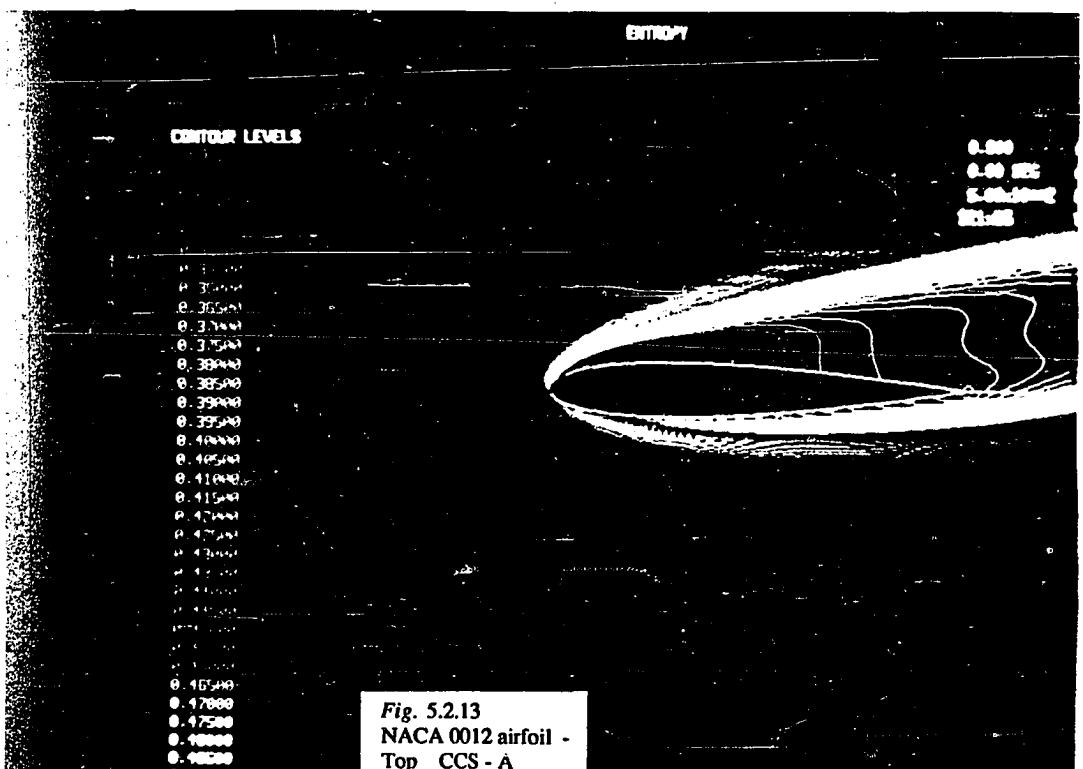
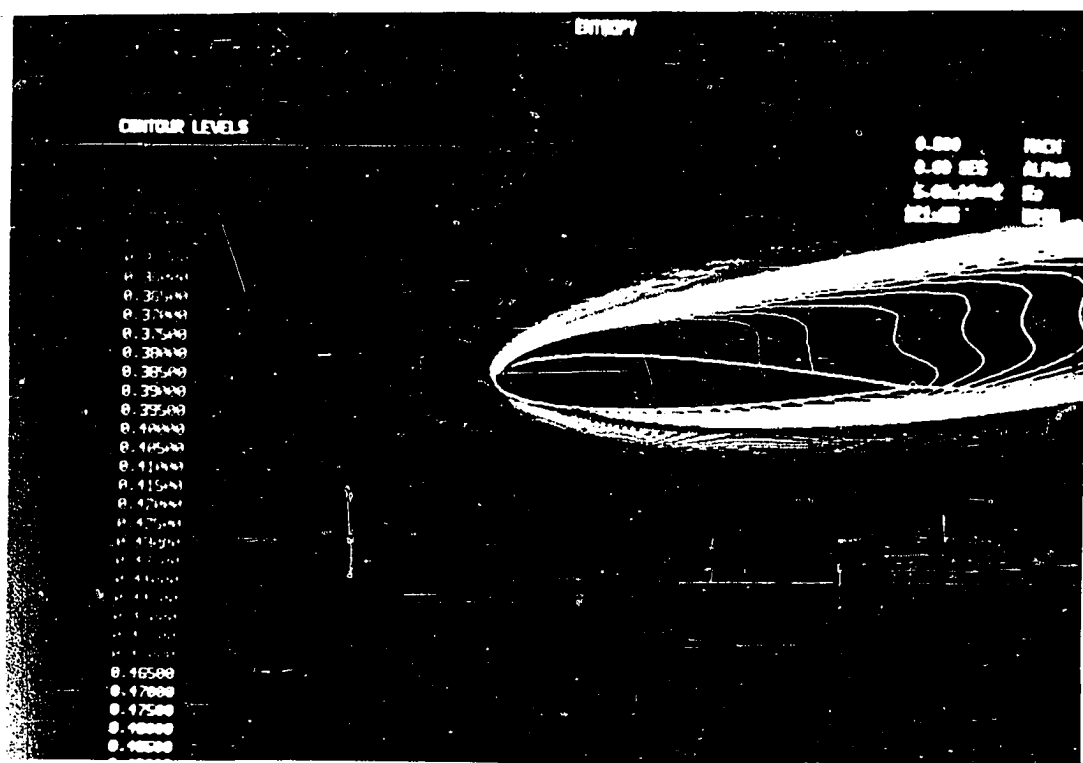


**Fig. 5.2.13**  
**NACA 0012 airfoil -**  
**Top CCS - A**  
**Bottom CCS - B**  
**Entropy Contours**

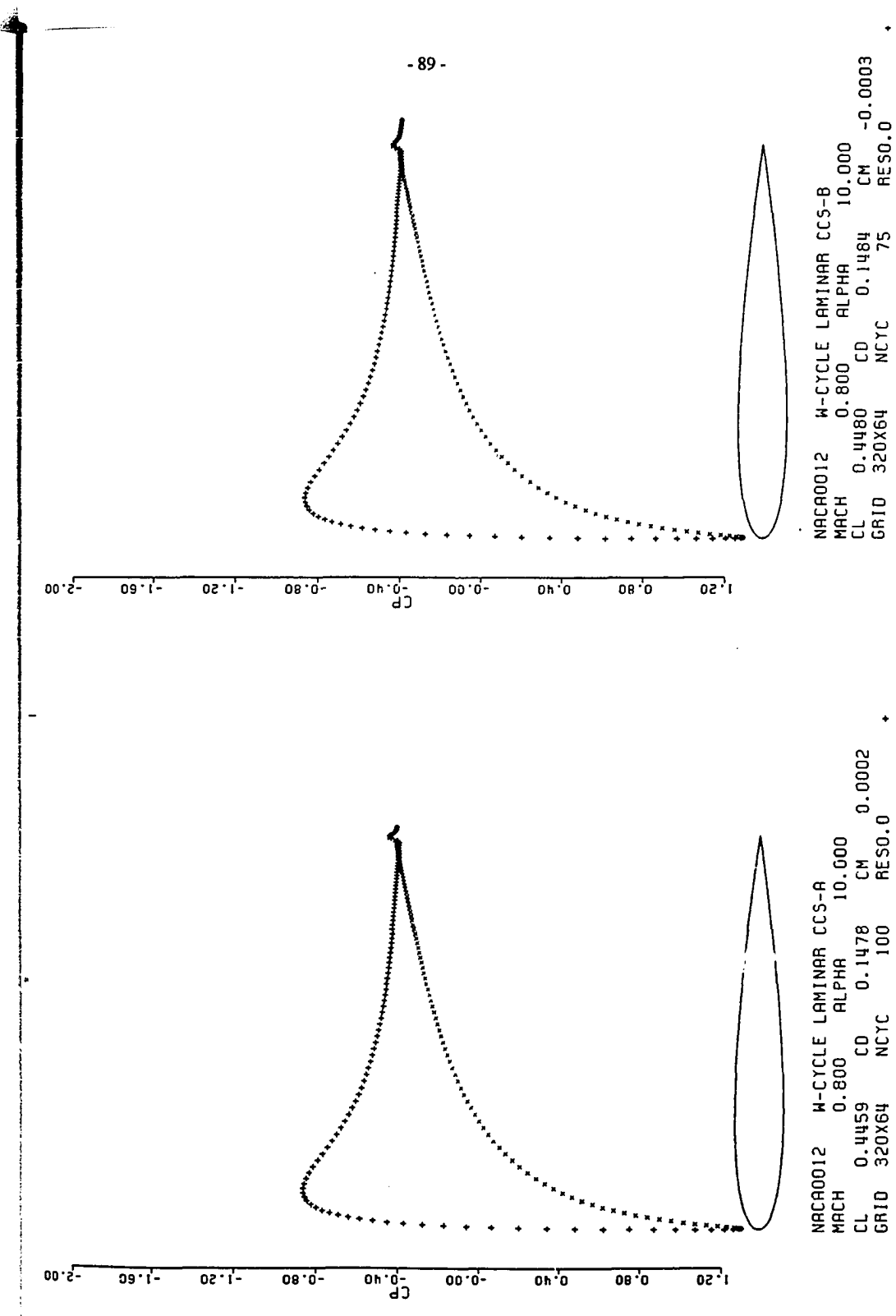


Fig. 5.2.14  
NACA0012 airfoil -  
Pressure coefficient along the surface.

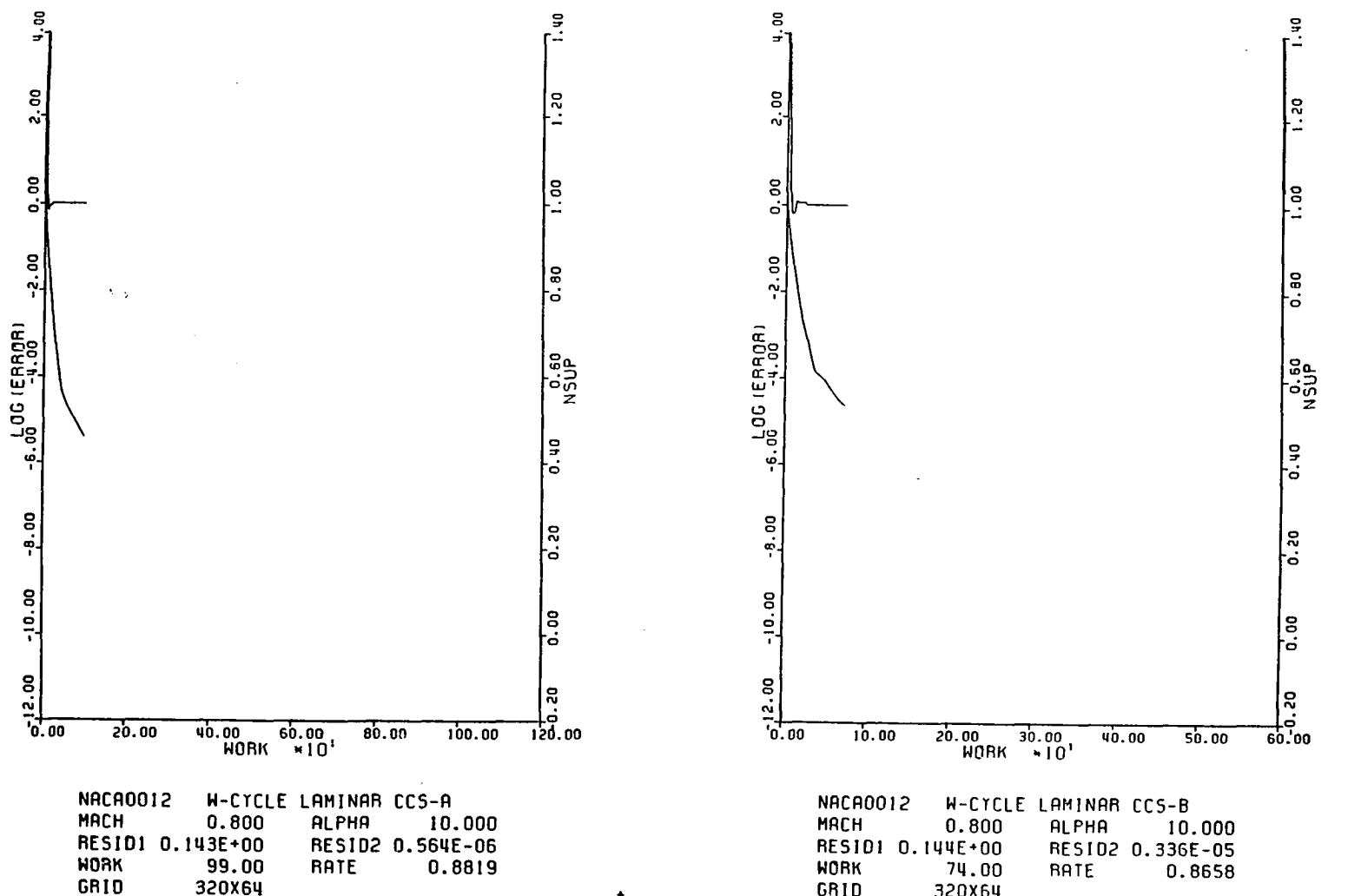
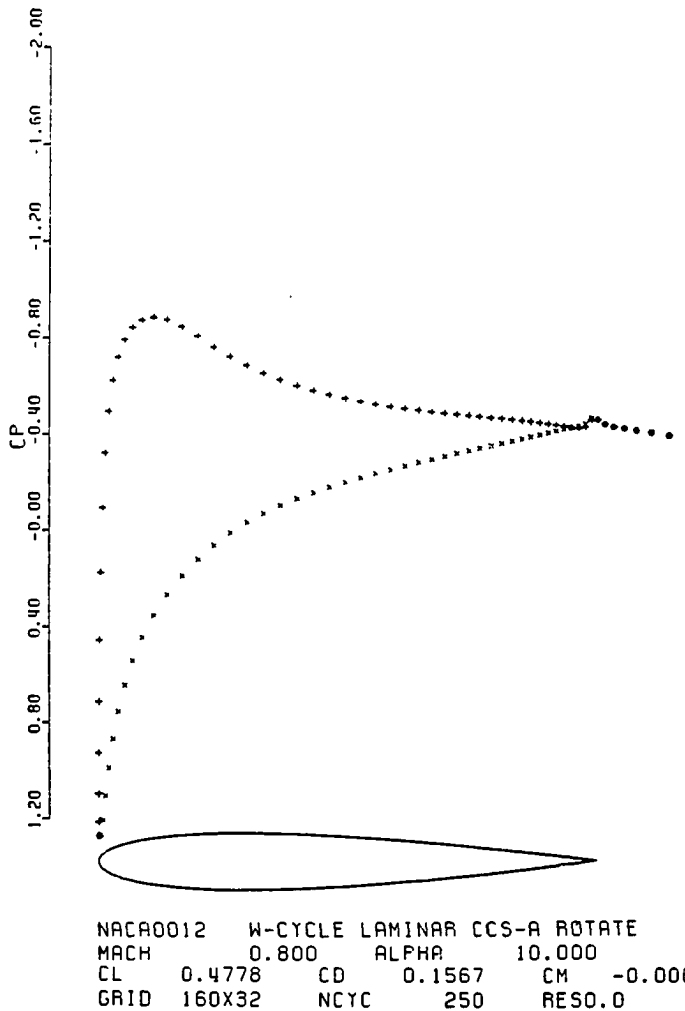
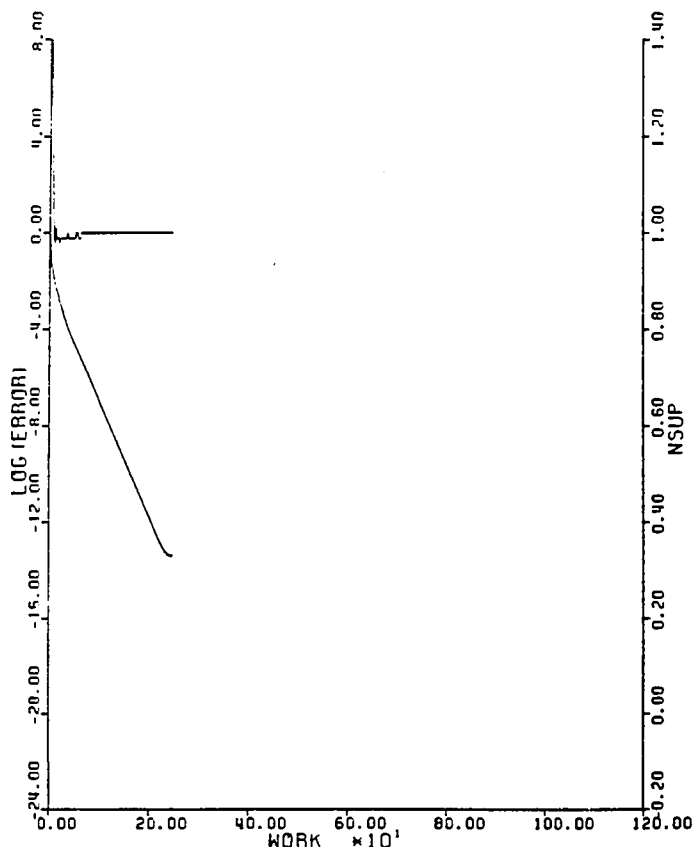


Fig. 5.2.15  
NACA 0012 airfoil -  
Convergence history.



*Fig. 5.2.16*  
**NACA 0012 airfoil -**  
**Pressure coefficient along the surface.**



NACA0012 W-CYCLE LAMINAR CCS-A ROTATE  
MACH 0.600 ALPHA 10.000  
RESID1 0.366E+00 RESID2 0.132E-13  
WORK 249.00 RATE 0.8831  
GRID 160X32

*Fig. 5.2.17*  
NACA 0012 airfoil -  
Convergence history.

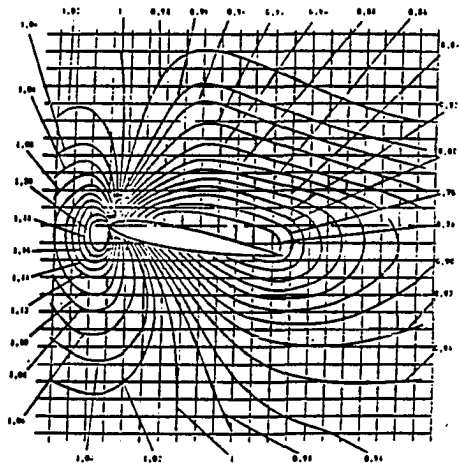


Fig. 5.2.18  
NACA 0012 airfoil -  
Experimental Density Contours

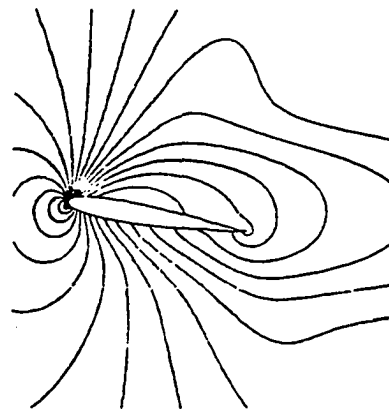


Fig. 5.2.19  
NACA 0012 airfoil -  
Computed Density Contours ( $D \rho = .05$ )

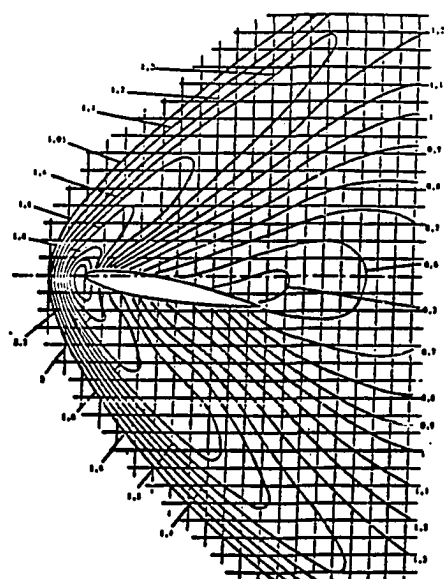


Fig. 5.2.20  
NACA 0012 airfoil -  
Experimental Density Contours

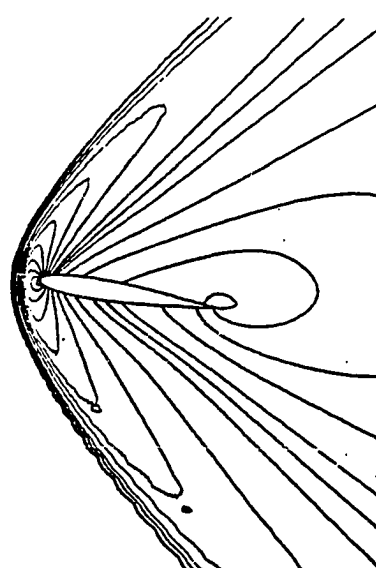
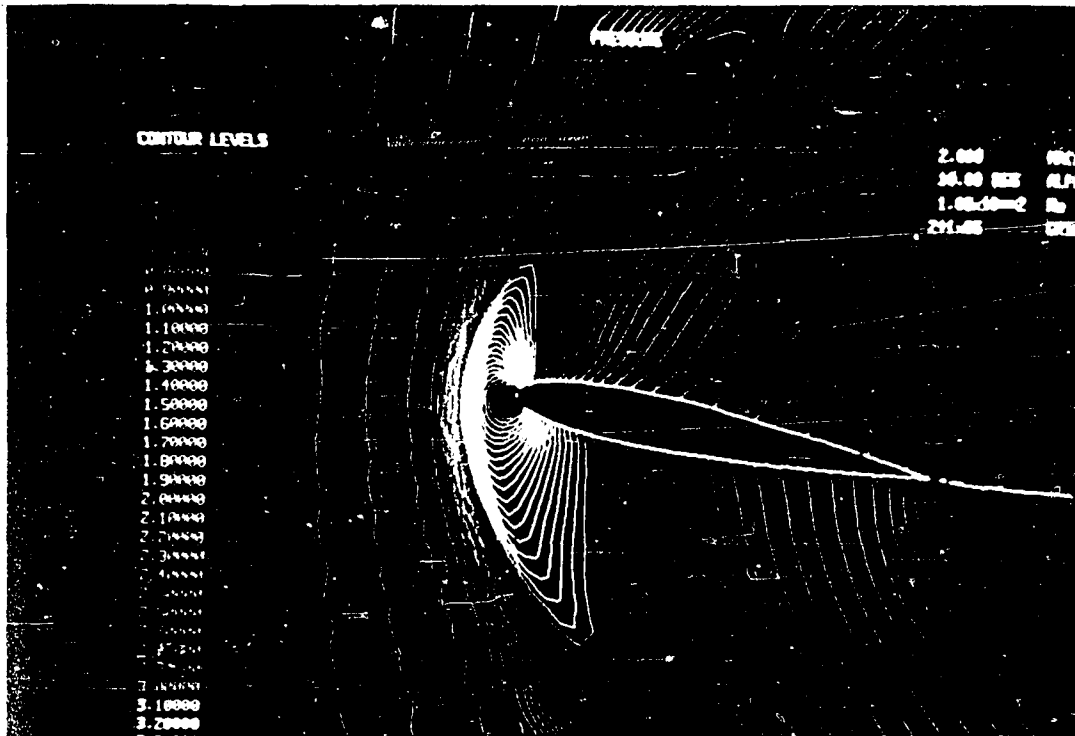
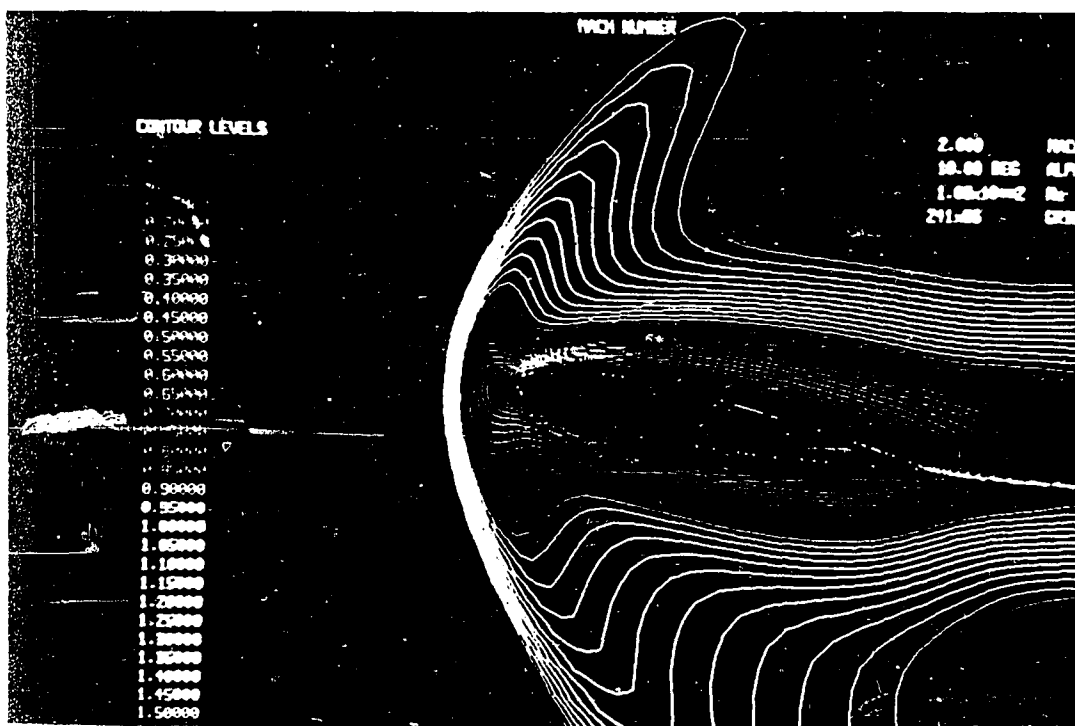


Fig. 5.2.21  
NACA 0012 airfoil -  
Computed Density Contours ( $D \rho = .2$ )



*Fig. 5.2.22  
NACA 0012 airfoil - CCS - A  
Pressure Contours*



*Fig. 5.2.23  
NACA 0012 airfoil - CCS - A  
Mach Contours*

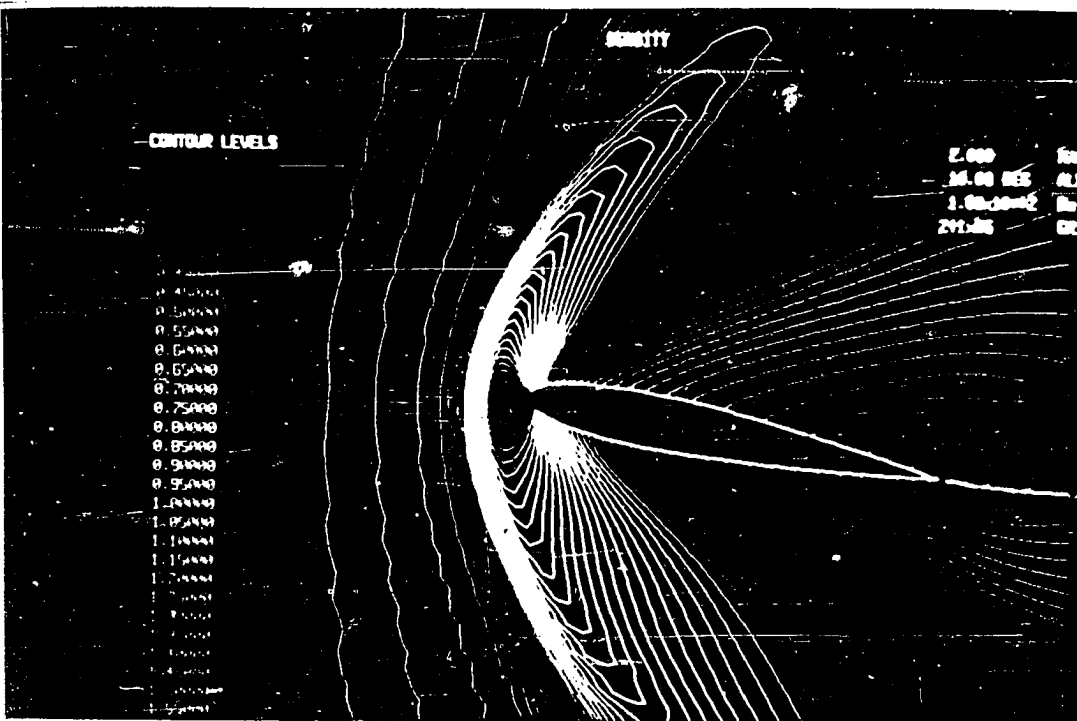


*Fig. 5.2.24*  
NACA 0012 airfoil - CCS - A  
Computed Density Contours

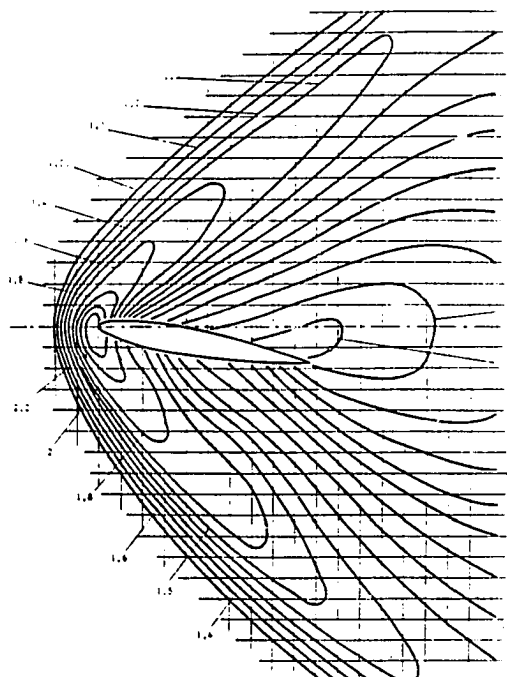


*Fig. 5.2.25*  
NACA 0012 airfoil -  
Experimental Density Contours

## CHAPTER 6

### NUMERICAL SIMULATION OF TURBULENT TRANSONIC AIRFOIL FLOWS

Applications of the proposed numerical schemes to the solution of the Reynolds Averaged equations are presented in this Chapter. For these computations closure was achieved by using a simple algebraic turbulence model due to Baldwin and Lomax [28]. A discussion of the model in the form in which it was used in this work is presented in Appendix A.

Due to the uncertainty caused by turbulence modeling, a preliminary assessment of both cell centered and vertex schemes was performed by comparing the computed results with the results obtained by using a well established Navier-Stokes solver that employs the same turbulence model [14]. These comparisons are described in the next section.

In the following section, results for three different airfoils, obtained with the cell centered scheme, are presented and compared with other computations found in the literature. In the closing section , a detailed analysis of the computed transonic flow fields for typical aeronautical applications is presented with the aim of illuminating the properties of the numerical schemes developed in the present work , and also the effects of turbulence modeling.

### 1. Preliminary Assessment of the Schemes for the Reynolds Averaged Equations.

A preliminary verification [62] of the proposed scheme has been carried out by comparing the solutions computed by using both the cell centered scheme and the vertex scheme with the results from the ARC2D program [14]. The three schemes have been used to compute two typical transonic flow fields for the RAE2822 on an identical mesh 256×64 grid. The height of the first cell was reduced to  $2 \times 10^{-5}$  chords in order to provide the clustering of points needed to resolve the thin boundary layer characteristic of high Reynolds number flows. Therefore the first two points in the outer direction are placed within a distance of  $y^+ < 5$  in walls units. The cell aspect ratio for this grid is therefore very high (up to 1000 on the airfoil).

The simple saw tooth cycle driven by the three stage scheme was used together with residual smoothing with constant coefficients, and the computations with both the cell centered scheme and vertex scheme were performed with a  $CFL = 2.8$ . Transition to turbulence was modeled as suggested in ref. [28], however, no correction for intermittency was accounted for. As in the case of laminar flow computations, it was found that 300 multigrid cycle were sufficient to reach a steady state solution.

The conditions of the free stream , and the angles of attack are summarized in Tables 1 and 2. The solutions computed by the two schemes of this work were found to be in agreement with the prediction of ARC2D. For the subcritical case (i), a comparison of the computed pressure and skin friction distributions shows very good agreement between the results obtained for the cell centered scheme and the vertex based scheme. The computed value for the skin friction , however, appears to be slightly higher than the measured one. The good agreement of the computed pressure distributions is verified also by the comparison of the computed aerodynamic coefficients as indicated in Table 1, where the experimental values [64] are also reported.

For the second case the computed aerodynamic parameters were found, again, to be in reasonable agreement with the results from the ARC2D code (Table 2). An interesting common

feature of our results and those reported by Pulliam [14], is the prediction of small regions of separation at the shock foot and at the upper trailing edge that are not present in the experiments. However, the shock location and strength compare well with the measurements. For this case the skin friction distribution is in good agreement with the experiments in the region behind the shock wave on the top surface, while the computed value of this quantity is found to be higher than the measured one in the fore half of the airfoil. The tendency to overpredict separation in regions of strong interaction seems to be a typical characteristic of algebraic turbulence models. Coakley [63] reported the same kind of behaviour using the Cebeci-Smith formulation. This is not surprising, since with any algebraic model the trace of the Reynolds stress is not accounted for. This can lead to inaccuracy, especially in regions of strong interaction such as the shock foot and the trailing edge.

This preliminary study indicates that the cell centered and the vertex schemes perform equally well on smooth grids. In view of the high degree of agreement between the two schemes, it was felt that either scheme could be used for further detailed comparisons with experimental data. In order to avoid unnecessary repetition, it was decided to use only one scheme for the several remaining cases reported in the following sections.

## 2. Computed Aerodynamic Characteristics of Airfoils in the Transonic Regime.

The ultimate goal of numerical computation is the prediction of the loads on aerodynamic bodies. The parameters of interest for the designer are the coefficients of lift, drag and moment. The computed aerodynamic characteristics of three airfoils ( NACA 0012, RAE 2822, JONES - SUPERCRITICAL) are presented in this section. For this computation the cell centered formulation (CCS-A) was used. The five stage scheme with three evaluations of the dissipation was also employed to drive the W - multigrid cycle. Also implicit smoothing with locally varying coefficients was used. The CFL number was fixed at 7.5. For each of the cases presented the effect of mesh refinement was monitored by performing computations on a sequence of grids.

The free stream flow conditions , and angles of attack cover a wide range in the transonic regime. The results presented correspond to some of the mandatory and suggested cases of a recent Workshop on the simulation of viscous flows, and comparisons are made with the results obtained by two other authors [65,66], and with experimental data, when available. these comparisons are summarized in Tables 3,4,5. Table 3 shows the comparison with experimental data, while Tables 4 and 5 show the comparisons with the results calculated by Coakley [65], and Maksymuk and Pulliam [66]. In the Tables, the computed values of the pressure drag coefficient  $C_d_p$ , friction drag coefficient  $C_d_f$ , and total drag coefficient  $C_d_t$  are reported separately. In the figures only the value of the pressure drag coefficient is reported.

A NACA 0012.

The typical mesh used for the computations on the NACA 0012 airfoil is shown in fig. (6.2.1). It consists of a total of  $320 \times 64$  mesh cells. The number of points that are fitted on the airfoil is either 193 or 257. The minimum distance from the airfoil surface of the first coordinate line is  $4 \times 10^{-6}$  chords, and it correspond to a value of  $y^+ < 5$  for the assigned  $Re_\infty$  of  $9 \times 10^6$ . Transition is fixed at .05 chords. Also the outer boundary is placed at a distance of 20 chords

The first set of computations is designed to recover the  $C_d - \alpha$  curve, as well as the drag polar, corresponding to a free stream speed of  $M_\infty = .7$ . The computed  $C_d - \alpha$  curve , and drag polar are shown, respectively, in fig. (6.2.2) and fig. (6.2.3), in which the experimental values obtained by Harris [68] are also marked for comparison. The computed data correlates extremely well with the experimental values corrected , using the criterion suggested by Harris, for wind tunnel interference. The linear region is recovered, and the computed results show a departure from linearity between  $\alpha = 4-5^\circ$ . This behaviour is caused by the growth of the shock induced separation region. The pressure plots corresponding to the four angles of attack are also shown in figs. (6.2.4). As the angle of attack is increased, the position of the shock wave is progressively shifted upstream while its strength is increased considerably. At about  $3^\circ$  angle of attack, the shock is already strong enough to cause the formation of a separated region right at the wave

foot. The results obtained in the present study compare quite well both with the experiments and with the results computed by other schemes, as summarized in Tables 3,4,5. The convergence histories measured by the decay of the *RMS* of the density residuals corresponding to these computations are also shown in figs (6.2.5) Although it was found that the values of the aerodynamic coefficients are converged to the fourth decimal place in about 125 multigrid cycles, the computations were carried on further to 200 cycles to check the convergence properties of the scheme. A monotone reduction of the density residuals is observed in all the cases considered. This shows that the convergence of the scheme is fairly independent on the physical pattern of the flow field. For the case corresponding to  $5^{\circ}$  angle of attack convergence was found to be somewhat slower. When the stall conditions are approached, it is not certain that the flow will remain steady. However, in this case also, converged values (to the fourth decimal place) of the aerodynamic coefficients were obtained in about 120 multigrid cycles.

Qualitative and quantitative agreement with other computed results as well as with the experiment of Harris is also obtained for the next case presented, corresponding to a free stream speed of  $M_{\infty} = .55$  and at  $8.34^{\circ}$  angle of attack. The presence of a large separation bubble is revealed by the computed pressure plot of fig. (6.2.6). Also for this case the convergence history is quite satisfactory (fig. 6.2.7), and convergence within engineering accuracy is achieved in about 120 multigrid cycles.

#### B RAE 2822

Four cases were computed for the RAE 2822 airfoil. These cases correspond to the experimental conditions 1,6,9, and 10 of ref. [64]. Angle of attack corrections are extremely important for this airfoil. The most widely used method of determining an appropriate correction is to tune the geometrical angle of attack [65,66,67] in such a way that the computed lift matches the experimental one. This criterion has been used for the computation of case 1. However, since the main purpose of this study is the validation of the numerical scheme, the remaining cases were computed with the angle of attack matching that which was used by other authors in the

computations of the same test cases. The free stream conditions and the geometrical angles of attack that correspond to the four cases on this airfoil are again summarized in Tables 3,4,5. Also transition was fixed at the experimental locations. The calculations for cases 1 and 10 were performed on a  $320 \times 64$  grid with 193 points fitted on the airfoil (fig. 6.2.8), while for cases 6 and 9 a finer  $512 \times 64$  grid was employed ( fig. 6.2.9). The distance from the airfoil of the first grid line was chosen in such a way as to provide the necessary clustering of points in the boundary layer region. Again, the distance of the first mesh point was taken to satisfy the condition  $y^+ < 5$ .

Fig. (6.2.10) shows the computed pressure coefficient along the airfoil surface corresponding to case 1. The computed results are in fairly good agreement with the measurements. Note also that the computed aerodynamic coefficients are in excellent agreement with the experimental values (cfr. Tab 3). For this case the angle of attack correction that has been introduced is in close agreement with the correction computed using the criterion suggested by the experimental investigation. The flow remains fully attached, and the resolution provided by the  $320 \times 64$  grid is sufficient for an adequate representation of the physical phenomena. The convergence history is shown in fig. (6.2.11). Again, the convergence rate is quite satisfactory, and a reduction of four orders of magnitude of the density residuals is achieved in 100 multigrid cycles. Also, a converged value of the lift coefficient is recovered in about 75 cycles.

The second computation corresponds to the experimental conditions of case 10. A  $320 \times 64$  grid was again used. The geometrical angle of attack of the computation corresponds to the value used by Coakley [65]. The computed solution for this case is less satisfactory. The comparison of the surface pressure plot in fig. (6.2.12) with the experimental data reveals that the computed shock is too far downstream, and also that its strength is too great. A more detailed analysis of the computed flow field reveals that the flow is separated by the interaction of the shock and the boundary layer. Nevertheless the solution computed with the present method compares favorably with other solutions computed with the same turbulence model [65,66,67]. The source of the disagreement must be therefore attributed to the poor reproduction of the shock boundary layer

interaction with this turbulence model. Indeed, better agreement with the experiments has been obtained by Coakley using the Johnson and King model [65]. We have already mentioned that the main purpose of this study was to compare the characteristics of the numerical scheme developed in the present work with other available results obtained by using the Baldwin Lomax model. The performance of the multigrid scheme continues to be superior to other schemes even for this particular case. The convergence history plot for the computation of this case (fig. 6.2.13) confirms, once again, that the convergence properties of the scheme developed in this work are independent of the complexity of the flow pattern.

With the help of the first two cases presented, we have been able to show that while the Baldwin Lomax turbulence model gives a good reproduction of the flow field for attached flows (case 1), it fails to give an appropriate representation of a strong shock boundary layer interaction (case 10). Also we have proved that the numerical scheme developed in the present work is robust enough to handle complex flow fields. The next logical step is therefore to study the behaviour of the numerical scheme for shocked flows where the turbulence model is able to give a reasonably good representation of the physics. The next two cases belong to this category. For these the finer  $512 \times 64$  grid of fig. (6.2.9), with 385 points fitted on the airfoil has been used.

The surface pressure coefficient distribution for case 6 is shown in fig. (6.2.14). The agreement with the experiments is satisfactory. At the geometrical angle of attack of  $2.4^\circ$  the shock position is found to be slightly upstream than the experimental one, but its strength compares favorably with the measurements. This suggests that the upstream location of the computed shock is attributable to the angle of attack correction used. For this case the convergence history is again quite satisfactory (fig. 6.2.15), and the computed results are also in agreement with other computations (Tables 4,5).

For the last case considered here (case 9), the location of the shock and the qualitative behaviour of the surface pressure coefficient compares well with the experimental values (fig. 6.2.16). The computed aerodynamic coefficients are in good agreement with other computations

as summarized in the Tables, and the convergence history remains satisfactory fig. (6.2.17). A steady state solution , converged within engineering accuracy , is obtained in about 120 multigrid cycles.

In the course of this study we have been particularly concerned with the effect of the dissipation added in the scheme by second differencing. It turns out that the artificial dissipation does not interfere at all with the physical diffusion process. To prove this point case 9 was also run without any such dissipation. Fig. (6.2.18) shows that the pressure distribution computed for case 9 with the second differencing filter turned off is almost identical to the previous solution (fig. 6.2.16). This seems to indicate that the distribution of the eddy viscosity predicted by the turbulence model is qualitatively accurate , and allows, by itself , the clean capture of the shock wave.

All the computations presented so far have been made using the theoretical coordinate definitions of the RAE 2822 airfoil. However, the wind tunnel experiments were performed with a physical model of the airfoil. As one would expect, therefore, the coordinates of the experimental section differ slightly from the coordinates used in the computations. The next example will help to clarify the importance of the surface definition for comparisons between calculations and experimental data. Fig (6.2.19) shows the surface pressure plot obtained by using the physical coordinates of the wind tunnel model in the computation. Since in this case the surface definition is no longer smooth, several bumps in the computed solution are noticeable. The most interesting feature of these results , however, is that the leading edge suction is noticeably increased . This suggests that part of the disagreement between computed solutions and experimental values, in the leading edge region, may be attributable to the coordinate definition of the airfoil.

#### C JONES SUPERCRITICAL AIRFOIL

This airfoil is a supercritical wing section designed by R.T. Jones. No experimental data for this section are available for comparison. However, since other computed solutions are avail-

able, it was decided to test the performance of our numerical method for this airfoil also. The free stream conditions and the values of the computed aerodynamic coefficients are summarized in Tab. 3,4,5. The mesh is made up by  $512 \times 64$  cells with 385 points fitted on the airfoil (fig. 6.2.20). The computed pressure coefficient along the surface is plotted in fig. (6.2.21). The results obtained are in good agreement with other computations [65,66,67]. The convergence for this case is, once again, satisfactory (fig 6.2.22), and a steady state solution is obtained in about 120 multigrid cycles.

These results for three different wing sections validate the numerical scheme developed in the present work in comparison with other computed results and experimental measurements. Throughout the study the method has been proved robust, and to be capable of handling different flow patterns corresponding to a wide range of free stream conditions, and the rate of convergence has been shown to be fairly independent from the complexity of the flow.

### 3. Detailed Analysis of Turbulent Flow Fields

The amount of information that can be extracted from a numerical simulation is much greater than the available experimental data. In a single run it is possible to gather information about the behaviour of all the physical quantities at once. This is a definite advantage of a computer simulation over an experimental investigation. Thus it seems worthwhile to present detailed turbulent flow field patterns. Such an analysis provides an opportunity to check that the computed results correspond to physical expectation. Two cases were selected. These correspond to two different airfoils at different Reynolds number in the transonic regime.

The first is again a computation of the flow field on the RAE2822 airfoil with free stream parameters corresponding to case 9 of the previous section. This computation was carried out on the  $320 \times 64$  grid of fig. (6.3.1) with 193 mesh points fitted on the airfoil. The mesh spacing in the streamwise direction is adjusted to provide ad hoc clustering of points in critical regions of the flow field such as the shock foot and the trailing edge. Again the first point away from the

wall was taken inside the viscous sublayer ( $y^+ < 5$ ) in wall units. Here, however, transition to turbulence is simulated by the model. The scheme used is, again, the cell centered formulation CCS-A. The five stage scheme with three evaluations of the dissipation and locally varying smoothing is used to drive the W multigrid cycle. A modified switch for the second difference dissipation based on the entropy gradient is also employed. This allows the CFL number to be raised to 7.5. Fig. (6.3.2) shows the convergence history measured by the RMS of the density residuals. For this case convergence is quite satisfactory and results within engineering accuracy are obtained in only 120 multigrid cycles. Also the pressure distribution of fig (6.3.3) compares well with the experiments. The slightly higher value of the lift coefficients is due to the discrepancy between the computed and measured pressure distributions just after the leading edge suction peak. However both the pressure drag and moment coefficients compare extremely well with experimental data. The isolines of the density (fig. 6.3.4), pressure (fig. 6.3.5) and Mach number (fig. 6.2.6) show the typical pattern for this airfoil [3]. The drawing of the entropy field (fig. 6.3.7) shows that entropy production and diffusion is concentrated within the thin viscous region. The most interesting (and difficult) feature of this computation is the modeling of the shock boundary layer interaction region. A close up of this portion of the flow field reveals that the physical elements of the phenomena are correctly modeled. The boundary layer thickness increases drastically with the interaction between the shock and the boundary layer. This rapid growth is indicated by the plot of the isomach lines (fig. 6.3.8) as well as by the velocity vector plot of fig. (6.3.9). A mildly separated region is present downstream the interaction region as a consequence of the relatively strong shock. The loss of monotonicity in the convergence history of fig. (6.3.2) corresponds to the discontinuous prediction by the turbulence model of the eddy diffusivity in this small separated region.

The second case is a computation of the transonic turbulent flow field on a NACA0012 airfoil at 0 angle of attack,  $M_\infty = .799$  and  $Re_\infty = 910^6$ . Again a  $320 \times 64$  mesh with 193 points fitted on the airfoil is employed. However, because of the higher Reynolds number the first point in the

boundary layer is moved closer to the wall at a distance of  $2.5 \cdot 10^{-6}$  chords. Again for this computation the cell centered CCS-A scheme is employed, and the 5/3 scheme with implicit smoothing drives the W multigrid cycle. Figs. (6.3.10) show a comparison of the computed pressure distribution for this case on a coarser  $160 \times 32$  and the finest  $320 \times 64$  grid. In both cases a perfectly symmetric solution is obtained, indicating the steady nature of the flow field. The computed pressure distribution on the finest grid and the computed pressure drag coefficient compares very well with the experiments of Harris [68].

On account of the highly stretched mesh of this computation ,the convergence rate measured by the reduction of the RMS of the density residuals (figs. 6.3.11) is considerably slower on both coarse and fine grids than it was for the previous case. However a steady state within engineering accuracy is reached in about 200 multigrid cycles. Again for this case the flow field pattern corresponds to physical expectation as indicated by the drawing of the density (fig. 6.3.12), pressure (fig. 6.3.13) and Mach number (fig. 6.3.14) contours. Since in this case a weaker shock is formed, the interaction of the shock with the boundary layer is milder as indicated by the moderate growth of the viscous region (fig. 6.3.15) at the shock foc' and the flow remains , therefore, attached. This is also evident from the close up view of the shock indicated by the iso-pressure lines (fig.6.3.16) and the velocity profile of fig. (6.3.17). For this symmetric case an interesting check of the behaviour of the computed flow field at the stagnation point (fig.6.3.18) reveals a pattern that very closely resembles the pattern of the analytical solution. Finally, a close up of the trailing edge region (fig.6.3.19) captures the formation of the symmetric wake.

RAE 2822		$M = .676$	$Re_\infty = 5.7 \times 10^6$	$\alpha = 1.930$	
		$C_L$	$C_D$ (Pressure)	$C_M$	Grid
Experiments (Ref. 12)		.566	-	-.082	-
Cell Centered		.566	.030	-.083	256x64 C-Mesh
Corner Point		.579	.040	-.084	256x64 C-Mesh
ARC2D Code		.596	.047	-.088	256x64 C-Mesh
Pulliam 1984 (Ref. 6)		.587	.038	-.084	251x51 O-Mesh

Table 1.  
Measured and computed force coefficients.  
Case (i)

RAE 2822		$M = .73$	$Re_\infty = 6.5 \times 10^6$	$\alpha = 2.790$	
		$C_L$	$C_D$ (Pressure)	$C_M$	Grid
Experiments (Ref. 12)		.803	-	-.099	-
Cell Centered		.835	.0122	-.096	256x64 C-Mesh
ARC2D Code		.839	.0118	-.096	256x64 C-Mesh
Pulliam 1984 (Ref. 6)		.825	.0123	-.095	251x51 O-Mesh

Table 2.  
Measured and computed force coefficients.  
Case (ii)

TABLE 3

NACA 0012		Transition fixed at .05 chords						Experiments (Ref. 68)		
CASE	M <sub>∞</sub>	α <sub>c</sub>	Re <sub>∞</sub>	C <sub>l</sub>	C <sub>d<sub>p</sub></sub>	C <sub>d<sub>f</sub></sub>	C <sub>d<sub>t</sub></sub>	α	C <sub>l</sub>	C <sub>d</sub>
1	.7	1.49	9x10 <sup>6</sup>	.2517	.0022	.0059	.0081	1.86	.241	.0079
2	.7	3.00	9x10 <sup>6</sup>	.4836	.0090	.0059	.0150			
3	.7	4.00	9x10 <sup>6</sup>	.6445	.0207	.0043	.0256			
4	.7	5.00	9x10 <sup>6</sup>	.7577	.0378	.0045	.0423			
5	.56	8.34	9x10 <sup>6</sup>	.9907	.0323	.00389	.0367	9.86	.983	.0253
RAE 2822		Transition fixed at .03 chords (.11 for case 1)						Experiments (Ref. 64)		
1	.676	1.83	5.7 10 <sup>6</sup>	.5677	.0031	.0073	.0104	2.40	.566	.0085
6	.725	2.4	6.5 10 <sup>6</sup>	.7601	.0062	.0062	.0124	2.92	.743	.0127
9	.730	2.79	6.5 10 <sup>6</sup>	.8415	.0121	.0059	.0181	3.19	.803	.0168
10	.750	2.81	6.2 10 <sup>6</sup>	.8650	.0247	.0073	.0320	3.19	.743	.0242
JONES										
1	.75	2.0	9x10 <sup>6</sup>	.5623	.0120	.0054	.0174			

*Table 3-legenda*

- M<sub>∞</sub> - Free stream Mach number
- α<sub>c</sub> - Angle of attack (degrees) used in the computation
- Re<sub>∞</sub> - Reynolds number based on chord and free stream conditions
- C<sub>l</sub> - Lift coefficient
- C<sub>d<sub>p</sub></sub> - Pressure drag coefficient
- C<sub>d<sub>f</sub></sub> - Friction drag coefficient
- C<sub>d<sub>t</sub></sub> - Total drag coefficient

TABLE 4

ACA 0012		Transition fixed at .05 chords						Computations (Ref 65)		
CASE	M <sub>∞</sub>	α <sub>c</sub>	Re <sub>∞</sub>	C <sub>l</sub>	C <sub>d<sub>p</sub></sub>	C <sub>d<sub>f</sub></sub>	C <sub>d<sub>t</sub></sub>	α	C <sub>l</sub>	C <sub>d</sub>
1	.7	1.49	9x10 <sup>6</sup>	.2517	.0022	.0059	.0081	1.49	.255	.0083
2	.7	3.00	9x10 <sup>6</sup>	.4836	.0090	.0059	.0150	3.00	.504	.0142
3	.7	4.00	9x10 <sup>6</sup>	.6445	.0207	.0043	.0256			
4	.7	5.00	9x10 <sup>6</sup>	.7577	.0378	.0045	.0423	5.00	.766	.0428
5	.55	8.34	9x10 <sup>6</sup>	.9907	.0323	.00389	.0367	8.34	.994	.0358
RAE 2822		Transition fixed at .03 chords (.11 for case 1)								
1	.676	1.83	5.7 10 <sup>6</sup>	.5677	.0031	.0073	.0104	1.93	.620	.0087
6	.725	2.4	6.5 10 <sup>6</sup>	.7601	.0062	.0062	.0124	2.40	.788	.0124
9	.730	2.79	6.5 10 <sup>6</sup>	.8415	.0121	.0059	.0181	2.80	.861	.0185
10	.750	2.81	6.2 10 <sup>6</sup>	.8650	.0247	.0073	.0320	2.80	.859	.0298
JONES										
1	.75	2.0	9x10 <sup>6</sup>	.5623	.0120	.0054	.0174	2.00	.576	.0178

Table 4-legenda

M<sub>∞</sub> - Free stream Mach number

α<sub>c</sub> - Angle of attack (degrees) used in the computation

Re<sub>∞</sub> - Reynolds number based on chord and free stream conditions

C<sub>l</sub> - Lift coefficient

C<sub>d<sub>p</sub></sub> - Pressure drag coefficient

C<sub>d<sub>f</sub></sub> - Friction drag coefficient

C<sub>d<sub>t</sub></sub> - Total drag coefficient

TABLE 5

NACA 0012		Transition fixed at .05 chords						Computations (Ref 66)		
CASE	M <sub>∞</sub>	α <sub>c</sub>	Re <sub>∞</sub>	C <sub>l</sub>	C <sub>d<sub>p</sub></sub>	C <sub>d<sub>f</sub></sub>	C <sub>d<sub>t</sub></sub>	α	C <sub>l</sub>	C <sub>d</sub>
1	.7	1.49	9x10 <sup>6</sup>	.2517	.0022	.0059	.0081			
2	.7	3.00	9x10 <sup>6</sup>	.4836	.0090	.0059	.0150	3.00	.503	.0144
3	.7	4.00	9x10 <sup>6</sup>	.6445	.0207	.0043	.0256			
4	.7	5.00	9x10 <sup>6</sup>	.7577	.0378	.0045	.0423	5.00	.763	.0431
5	.55	8.34	9x10 <sup>6</sup>	.9907	.0323	.00389	.0367	8.34	.988	.0362
RAE 2822		Transition fixed at .03 chords (.11 for case 1)								
1	.676	1.83	5.7 10 <sup>6</sup>	.5677	.0031	.0073	.0104			
6	.725	2.4	6.5 10 <sup>6</sup>	.7601	.0062	.0062	.0124			
9	.730	2.79	6.5 10 <sup>6</sup>	.8415	.0121	.0059	.0181			
10	.750	2.81	6.2 10 <sup>6</sup>	.8650	.0247	.0073	.0320	2.72	.838	.0289
JONES										
1	.75	2.0	9x10 <sup>6</sup>	.5623	.0120	.0054	.0174	2.00	.558	.0178

Table 5-legenda

M<sub>∞</sub> - Free stream Mach number

α<sub>c</sub> - Angle of attack (degrees) used in the computation

Re<sub>∞</sub> - Reynolds number based on chord and free stream conditions

C<sub>l</sub> - Lift coefficient

C<sub>d<sub>p</sub></sub> - Pressure drag coefficient

C<sub>d<sub>f</sub></sub> - Friction drag coefficient

C<sub>d<sub>t</sub></sub> - Total drag coefficient

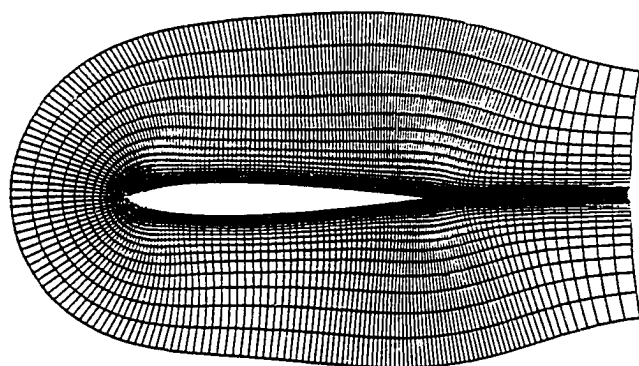


*Fig. 6.2.1*  
NACA 0012 airfoil -  
320×64 C-mesh for turbulent computations.

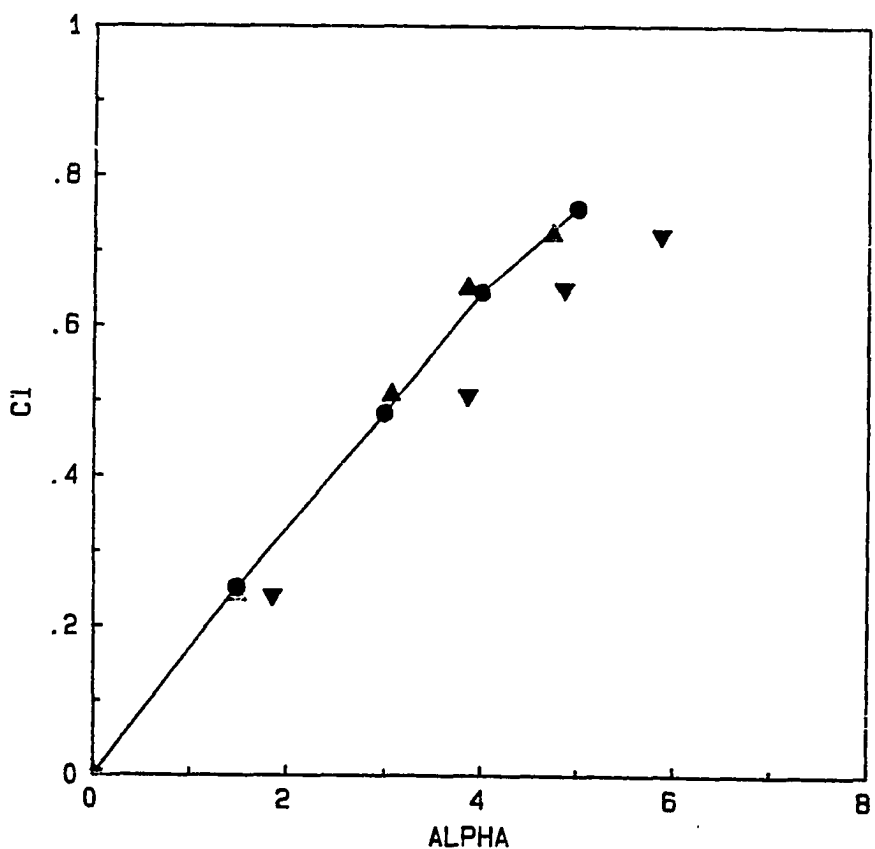


*Fig. 6.2.2*  
NACA 0012 airfoil -  $C_l-\alpha$  plot  
 $M_\infty = .7$   
 $Re_\infty = 9 \times 10^6$   
Transition fixed at .05 chords  
COMPUTED  
UNCORRECTED EXPERIMENTS (Ref. 68 )  
CORRECTED EXPERIMENTS (Ref. 68 )

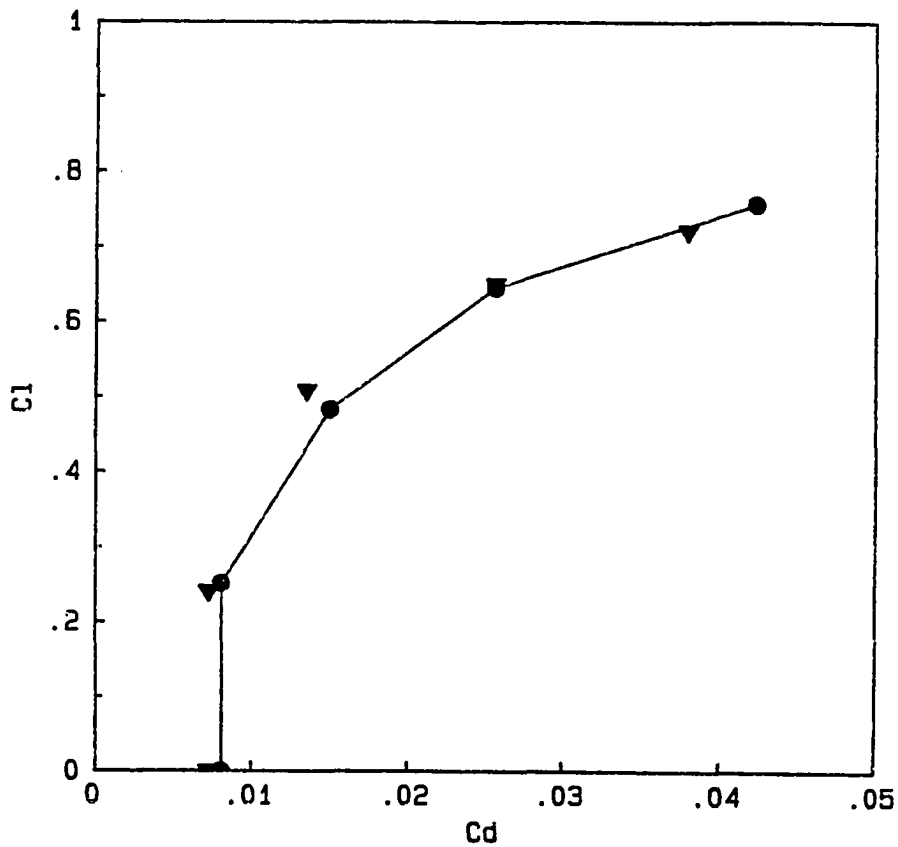


*Fig. 6.2.3*  
NACA 0012 airfoil -  $C_l$ - $C_d$  plot  
 $M_\infty = .7$   
 $Re_\infty = 9 \times 10^6$   
Transition fixed at .05 chords  
COMPUTED  
UNCORRECTED EXPERIMENTS (Ref. 68 )  
CORRECTED EXPERIMENTS (Ref. 68 )

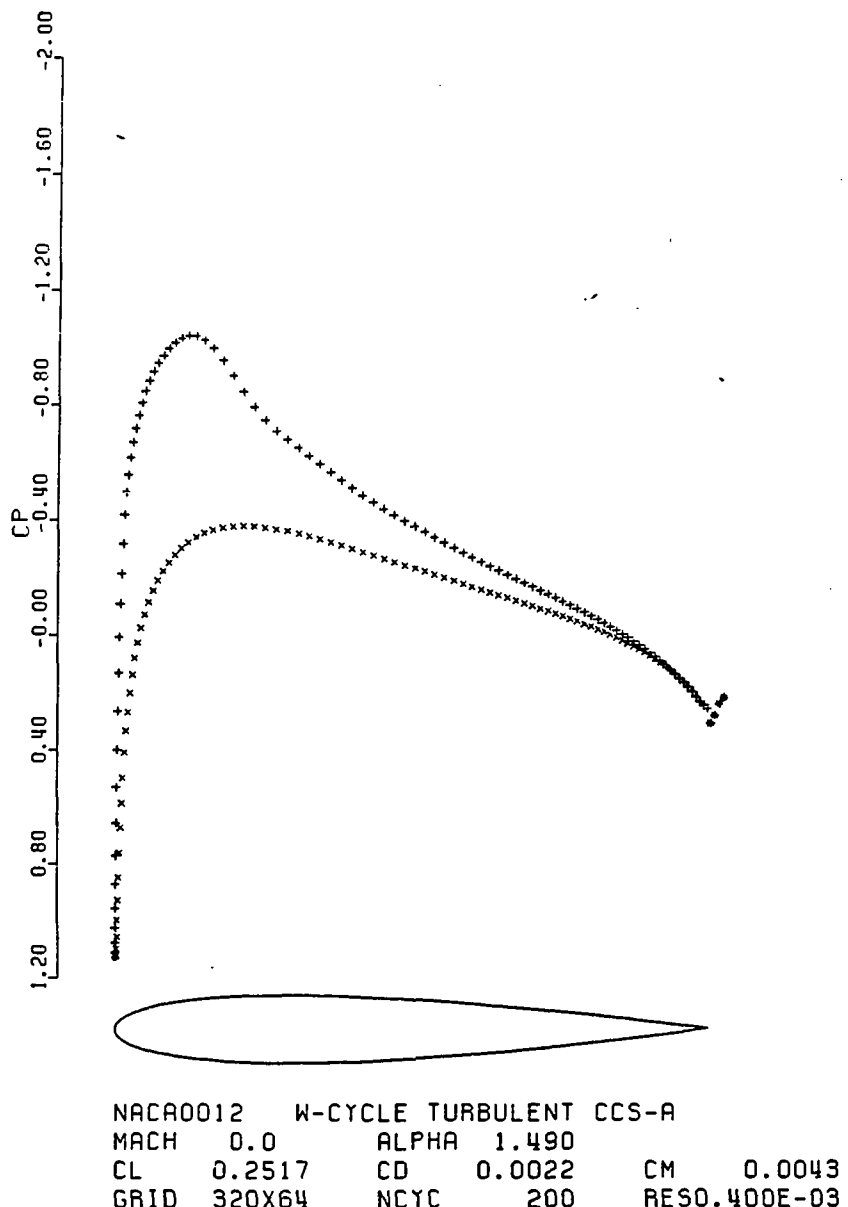


*Fig. 6.2.4a*  
NACA 0012 case (1) - CCS - A  
Pressure coefficient along the surface.

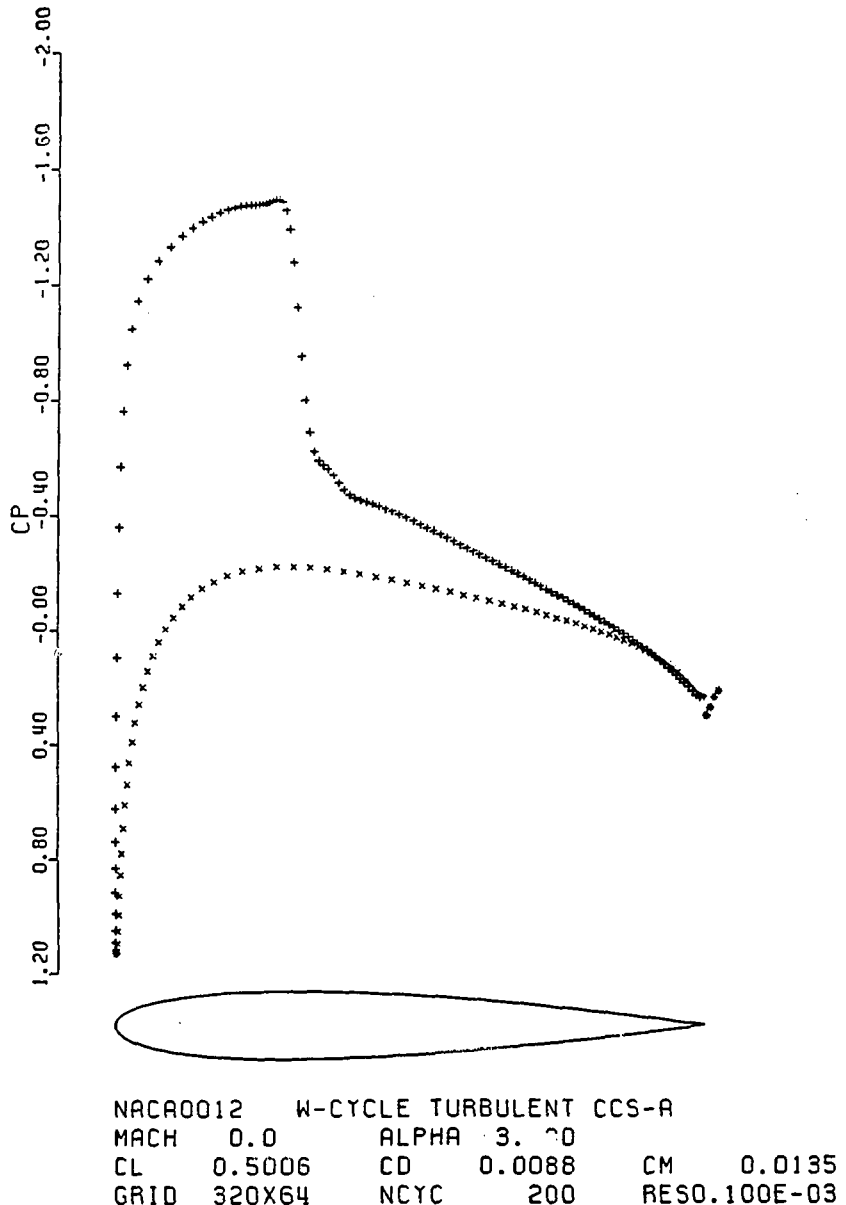
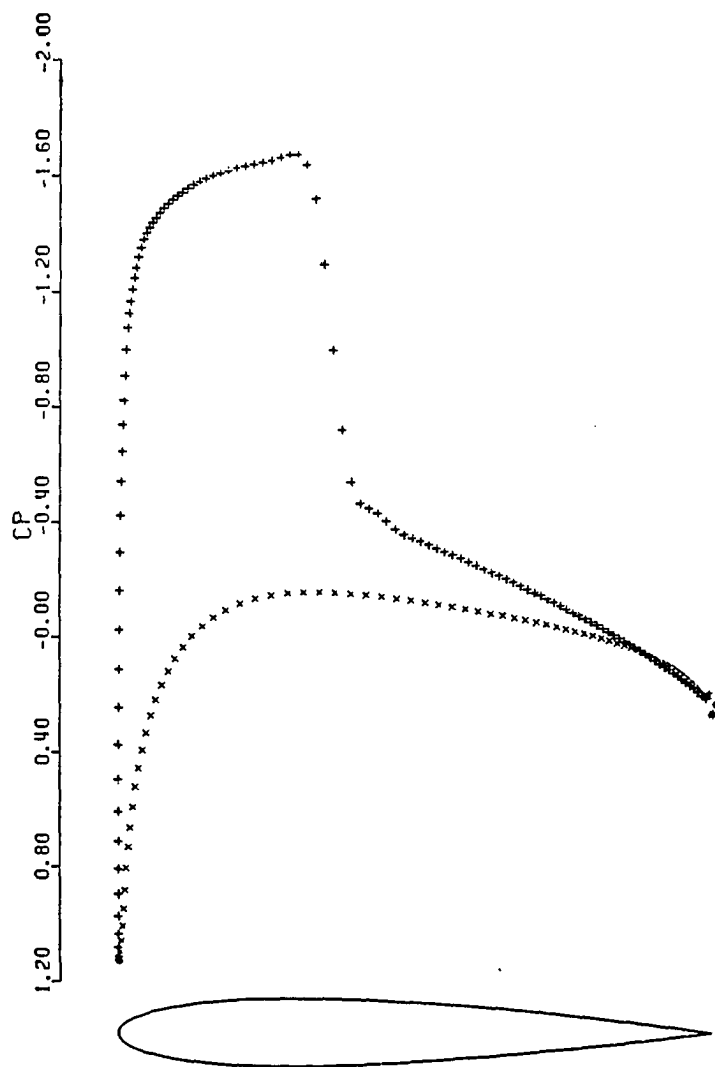
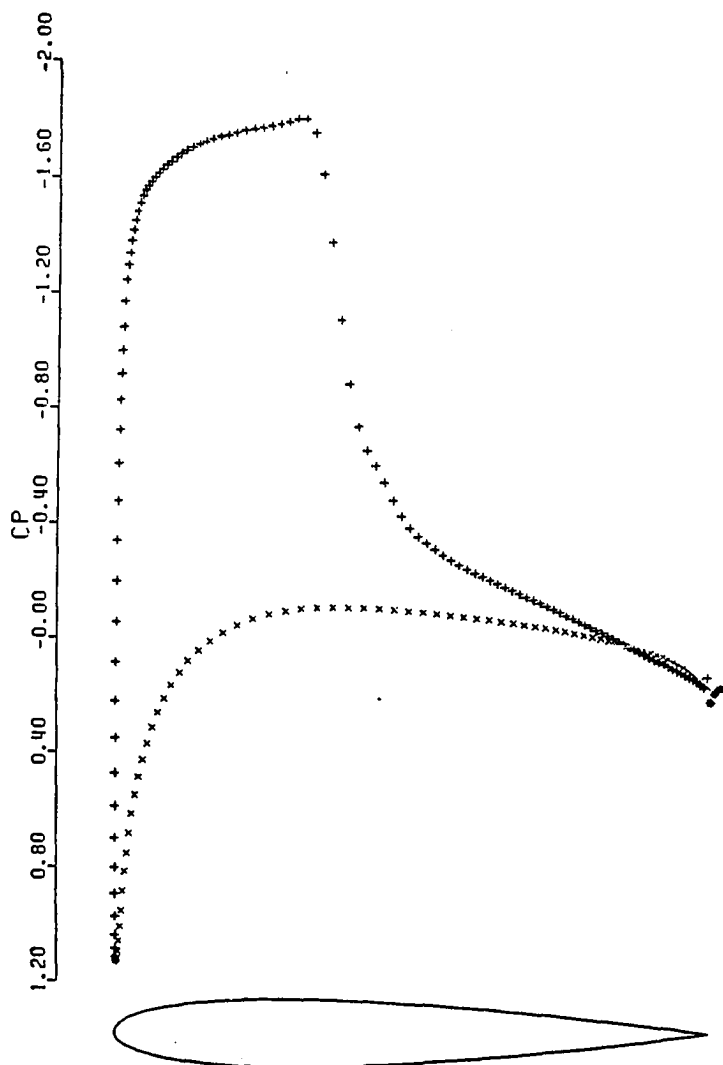


*Fig. 6.2.4b*  
NACA 0012 case (2) - CCS - A  
Pressure coefficient along the surface.



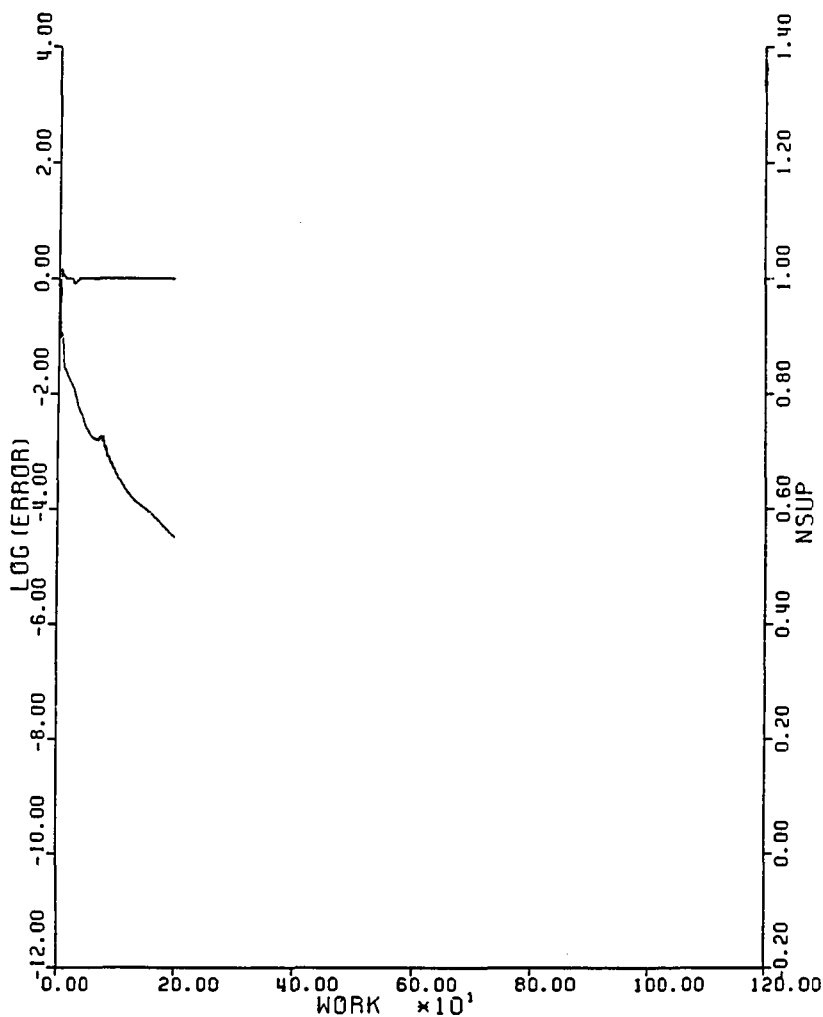
NACA0012 W-CYCLE TURBULENT CCS-A  
MACH 0.0 ALPHA 4.000  
CL 0.6445 CD 0.0207 CM 0.0176  
GRID 320X64 NCYC 125 RESO.660E-02

*Fig. 6.2.4c*  
NACA 0012 case (3) - CCS - A  
Pressure coefficient along the surface.



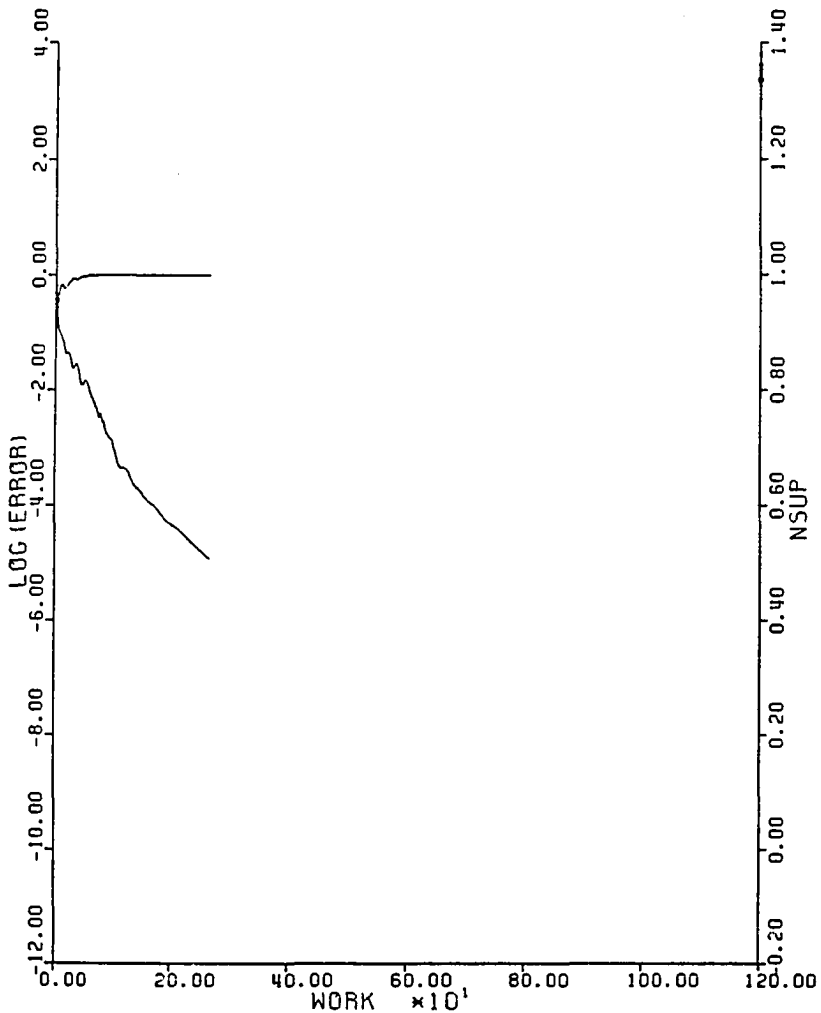
NACA0012 W-CYCLE TURBULENT CCS-A  
MACH 0.0 ALPHA 5.000  
CL 0.7581 CD 0.0378 CM 0.0183  
GRID 320X64 NCYC 300 RES0.215E-01

*Fig. 6.2.4d*  
NACA 0012 case (4) - CCS - A  
Pressure coefficient along the surface.



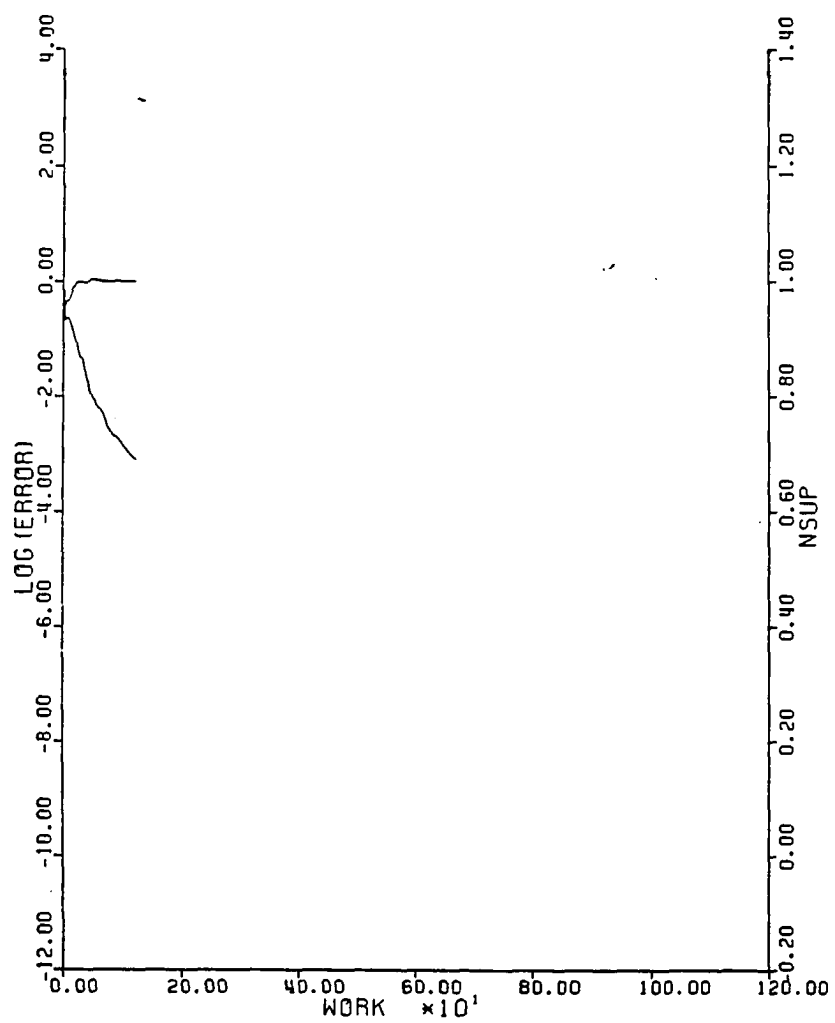
NACA0012      W-CYCLE TURBULENT CCS-A  
MACH            0.700      ALPHA        1.490  
RESID1          0.116E+02     RESID2      0.375E-03  
WORK            199.00      RATE        0.9494  
GRID            320X64

*Fig. 6.2.5a*  
NACA 0012 case (1) - CCS - A  
Convergence History.



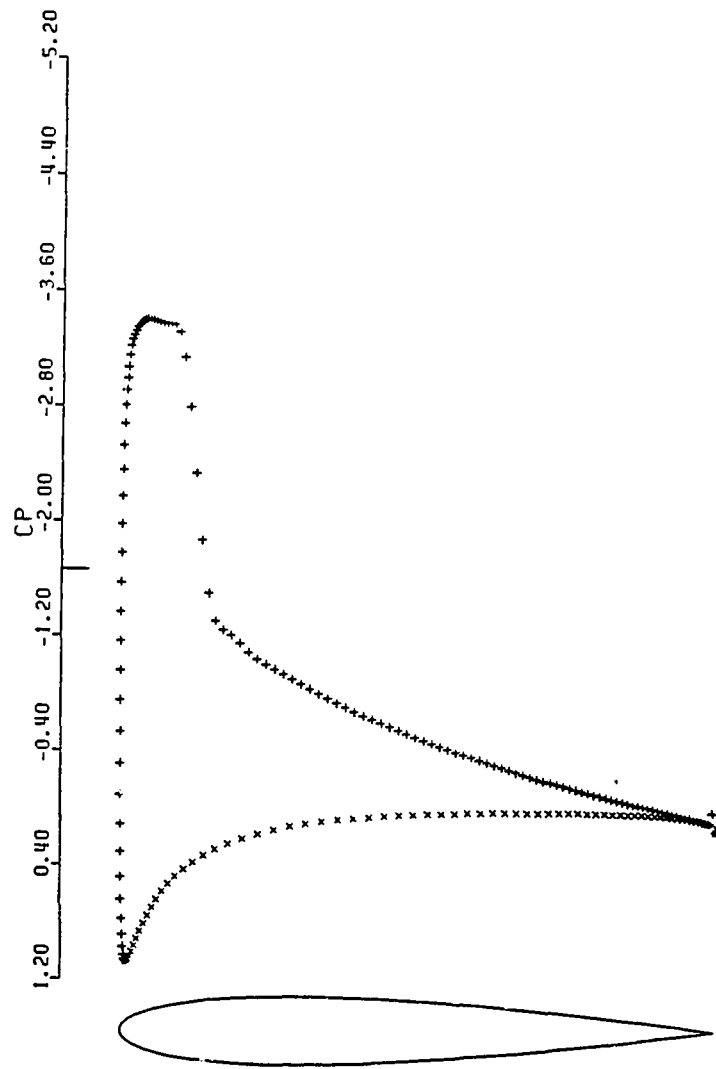
NACA0012 W-CYCLE TURBULENT CCS-A  
MACH 0.700 ALPHA 3.000  
RESID1 0.659E+01 RESID2 0.783E-04  
WORK 265.58 RATE 0.9582  
GRID 320X64

*Fig. 6.2.5b*  
NACA 0012 case (2) - CCS - A  
Convergence History.



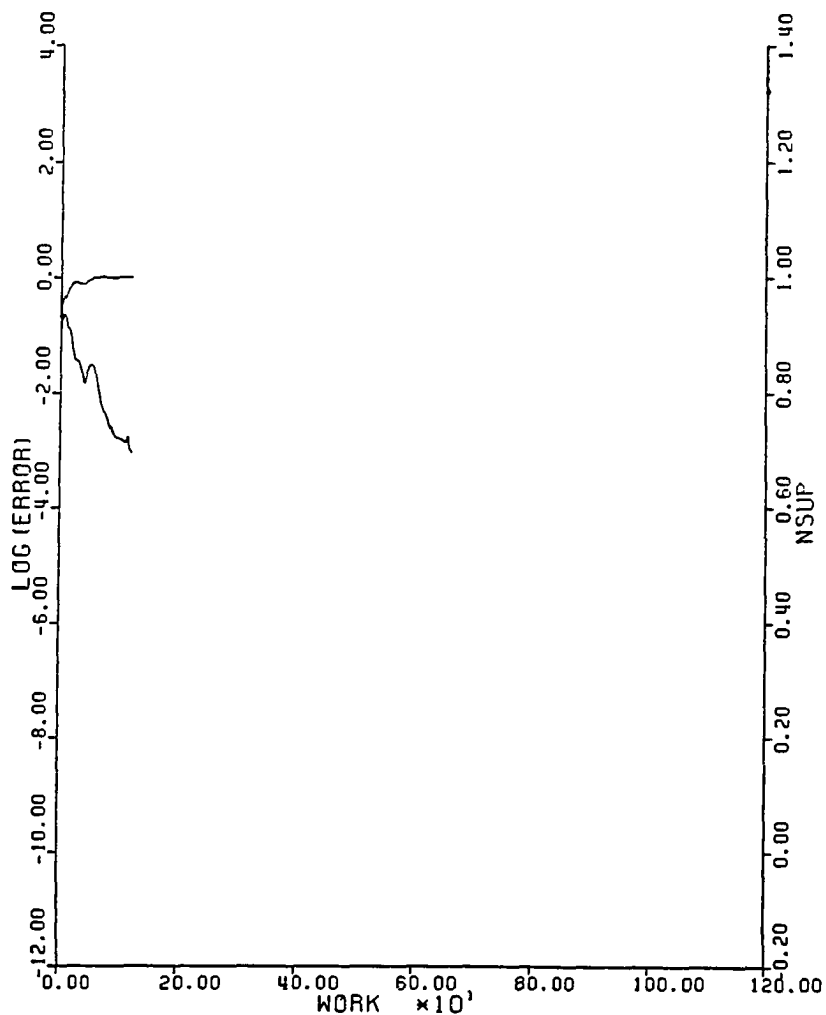
NACA0012 W-CYCLE TURBULENT CCS-A  
MACH 0.700 ALPHA 4.000  
RESID1 0.850E+01 RESID2 0.660E-02  
WORK 124.00 RATE 0.9439  
GRID 320X64

*Fig. 6.2.5c*  
NACA 0012 case (3) - CCS - A  
Convergence History.



NACA0012 W-CYCLE TURBULENT CCS-A  
MACH 0.550 ALPHA 8.340  
CL 0.9907 CD 0.0323 CM 0.0364  
GRID 320X64 NCYC 125 RESO.840E-02

**Fig. 6.2.6**  
NACA 0012 case (5) - CCS - A  
Pressure coefficient along the surface.



NACA0012 W-CYCLE TURBULENT CCS-A  
MACH 0.550 ALPHA 8.340  
RESID1 0.957E+01 RESID2 0.839E-02  
WORK 124.00 RATE 0.9448  
GRID 320X64

*Fig. 6.2.7*  
NACA 0012 case (5) - CCS - A  
Convergence History.

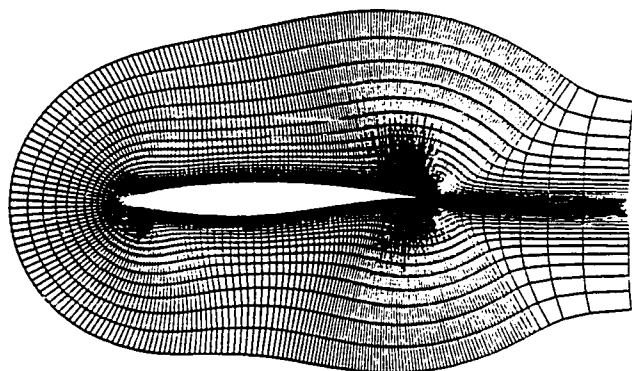


*Fig. 6.2.8*  
RAE 2822 airfoil - CCS - A  
320x64 grid for turbulent calculations.

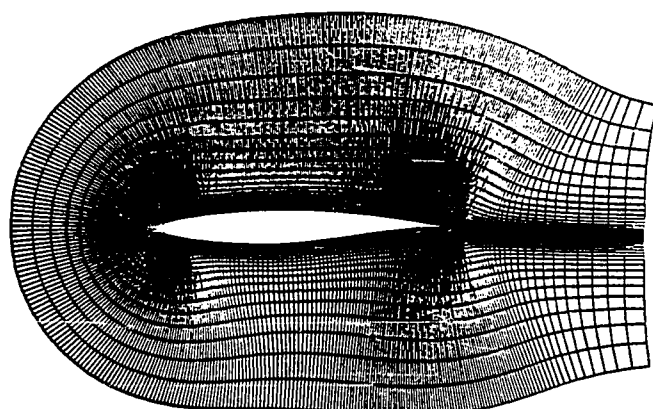
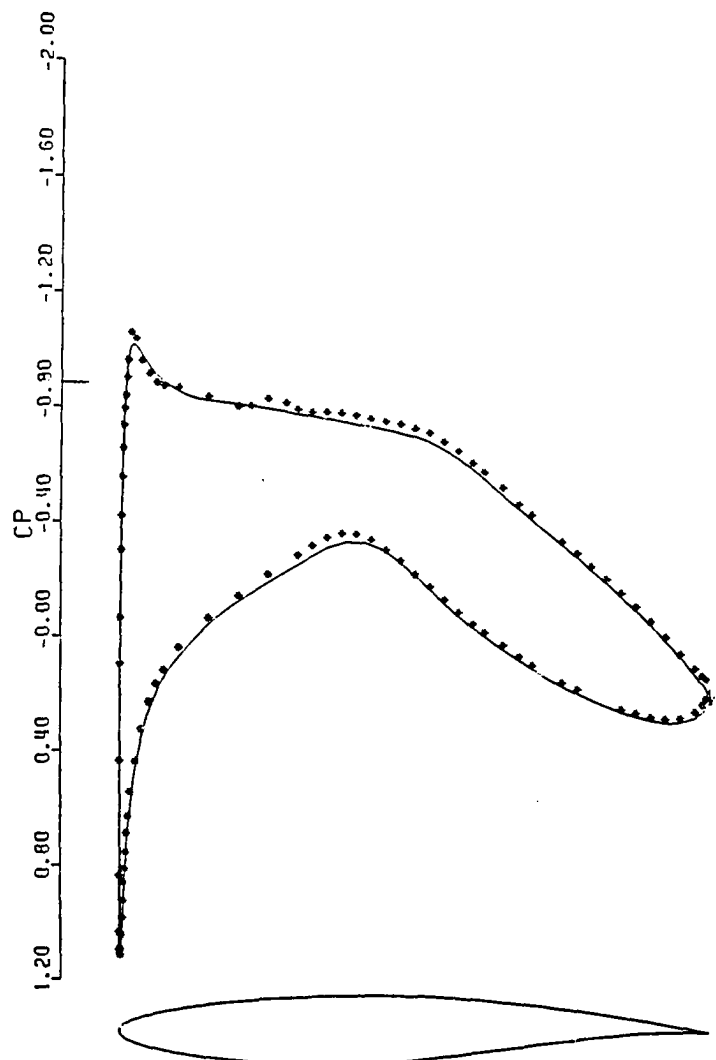
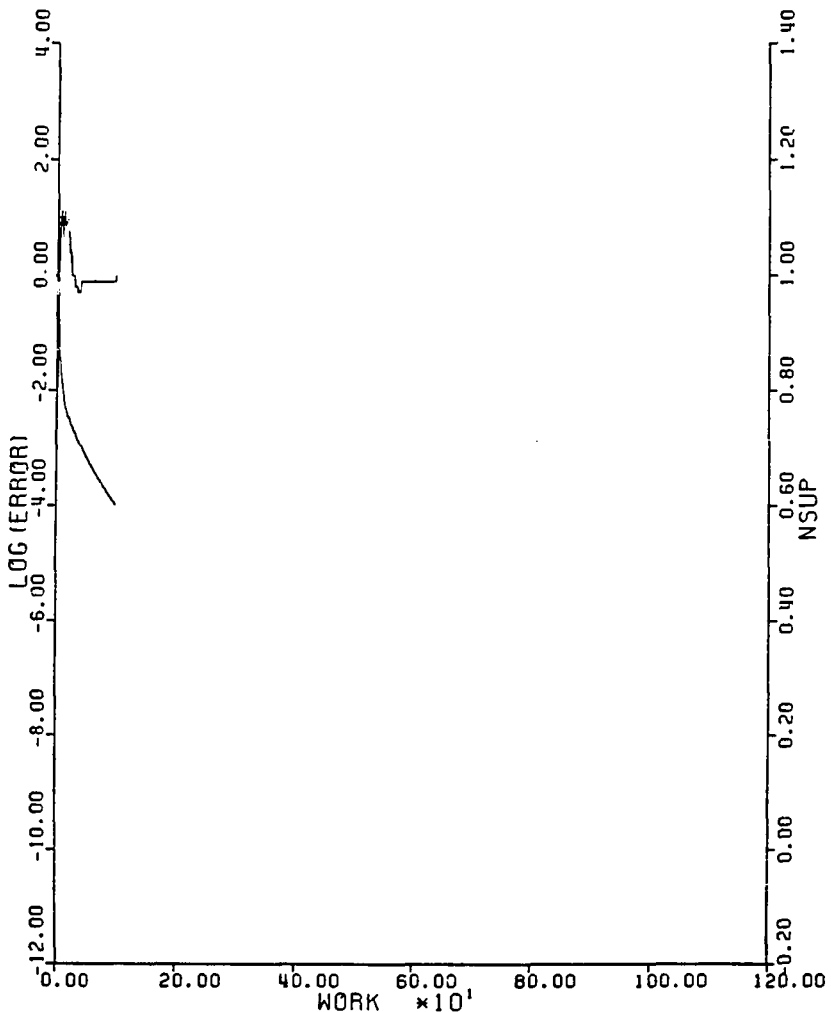


*Fig. 6.2.9*  
RAE 2822 airfoil - CCS - A  
512x64 grid for turbulent calculations.



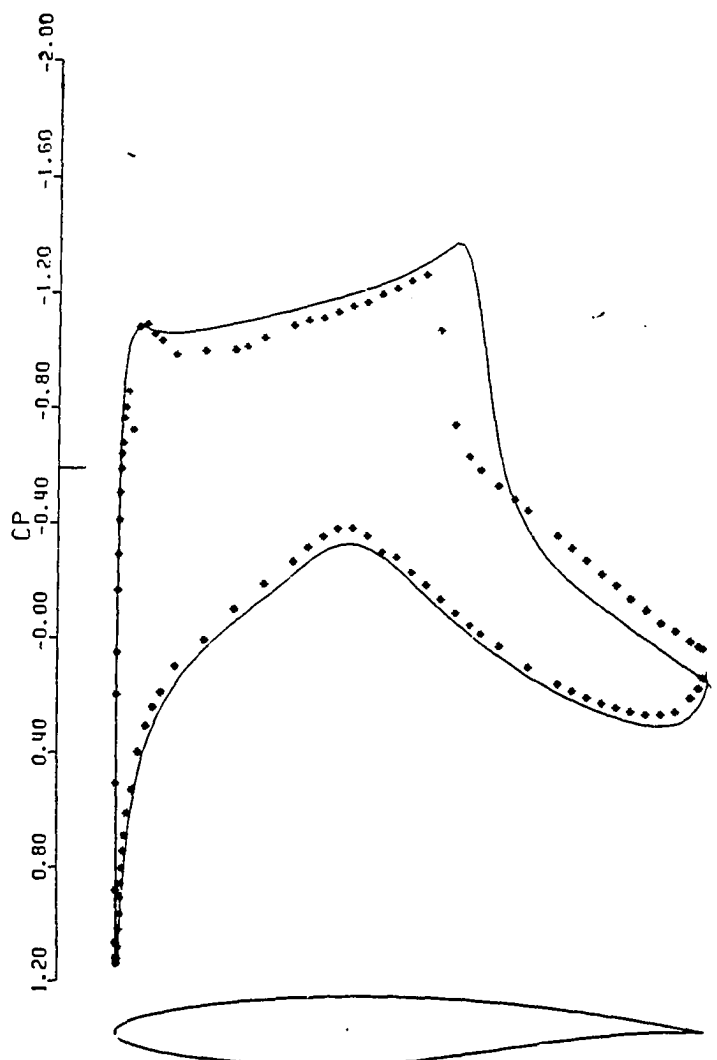
RAE2822 W-CYCLE TURBULENT = 1  
MACH 0.676 ALPHA 1.890  
CL 0.5677 CD 0.0031 CM -0.0807  
GRID 320X64 NCYC 100 RESO.700F-03

*Fig. 6.2.10*  
RAE 2822 airfoil case (1) - CCS - A  
Pressure coefficient along the surface.  
Solid line - Computed solution  
\* - Experiments (Ref. 64)



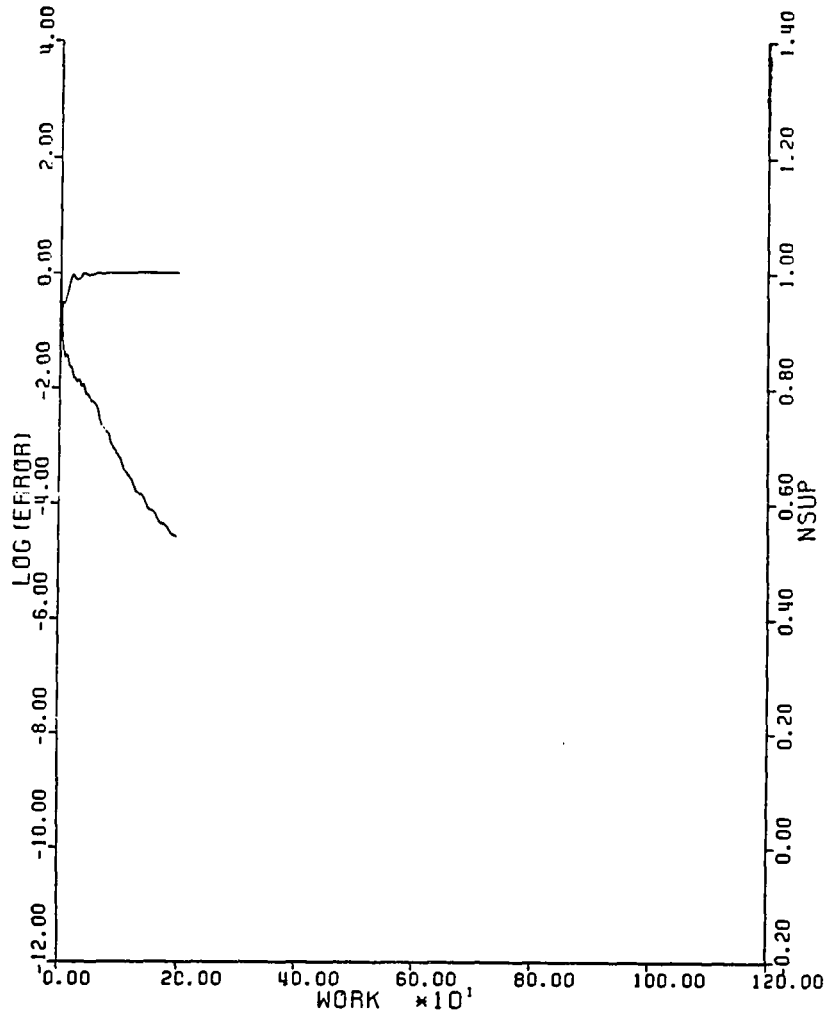
RAE2822      W-CICLE TURBULENT \* 1  
MACH            0.676      ALPHA        1.890  
RESID1 0.692E+01      RESID2 0.714E-03  
WORK            99.00      RATE         0.9114  
GRID            320X64

*Fig. 6.2.11*  
RAE 2822 airfoil case (I) - CCS - A  
Convergence History.



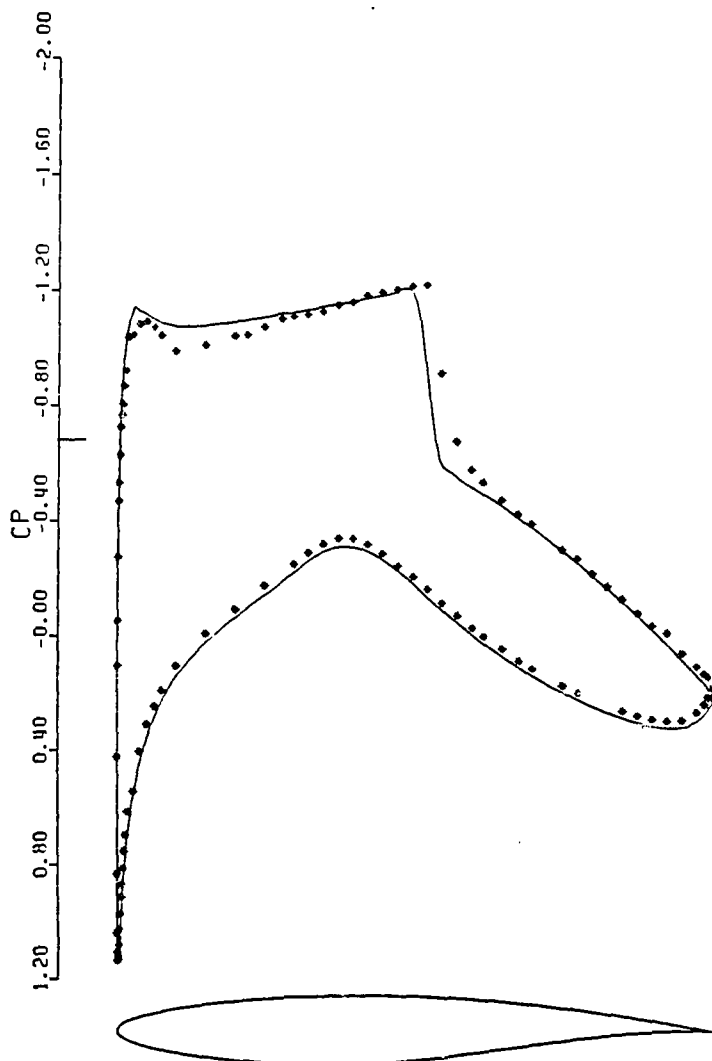
RAE2822 W-CYCLE TURBULENT \* 10  
MACH 0.750 ALPHA 2.800  
CL 0.8404 CD 0.0231 CM -0.1139  
GRID 320X64 NCYC 200 RESO.200E-03

*Fig. 6.2.12*  
RAE 2822 airfoil case (10) - CCS - A  
Pressure coefficient along the surface.  
Solid line - Computed solution  
\* - Experiments (Ref. 64 )



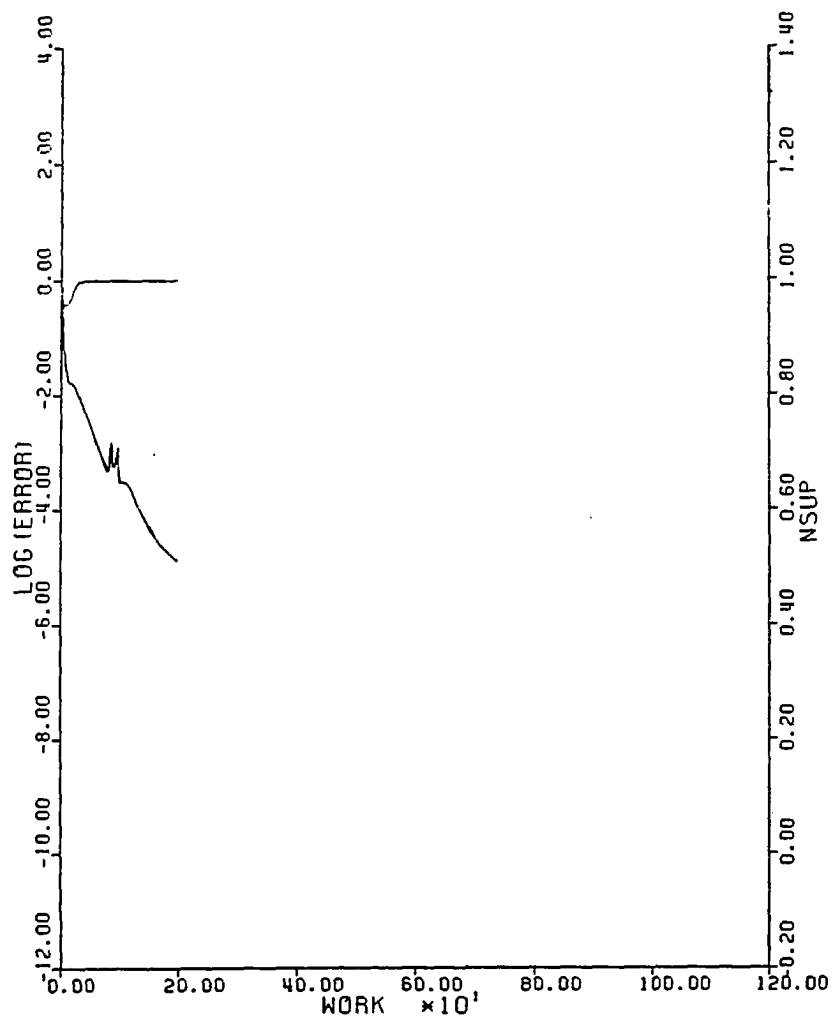
RAE2822 W-CYCLE TURBULENT = 10  
MACH 0.750 ALPHA 2.800  
RESID1 0.875E+01 RESID2 0.231E-03  
WORK 199.00 RATE 0.9484  
GRID 320X64

Fig. 6.2.13  
RAE 2822 airfoil case (10) - CCS - A  
Convergence History.



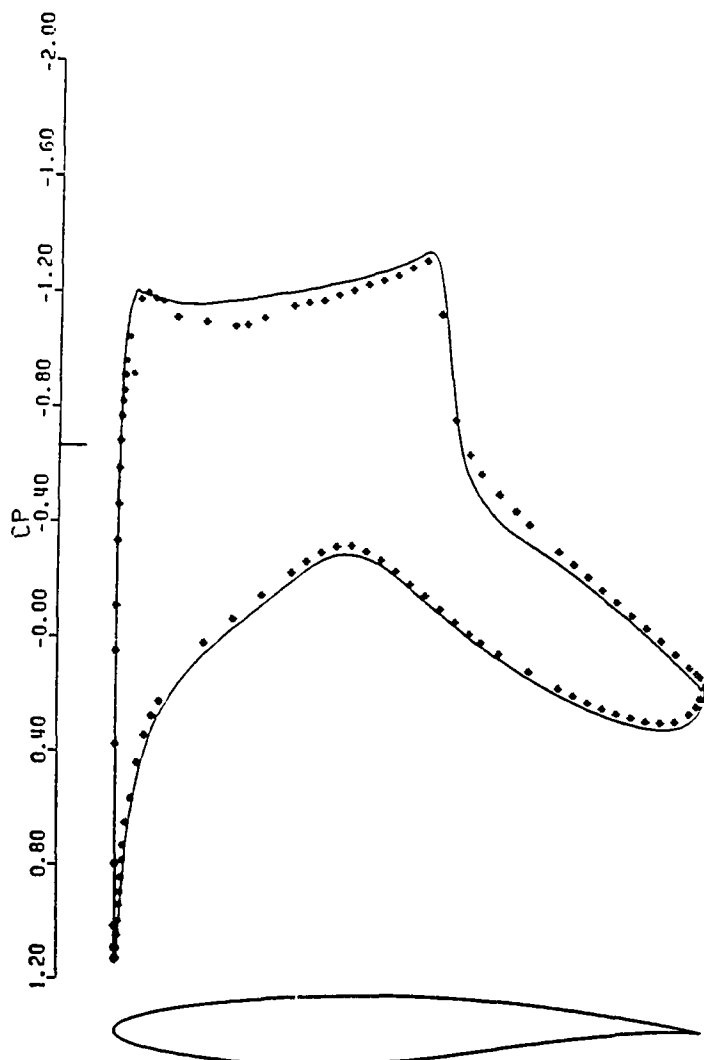
RAE2822 W-CYCLE TURBULENT # 6 BL  
MACH 0.725 ALPHA 2.400  
CL 0.7601 CD 0.0062 CM -0.0906  
GRID 512X64 NCYC 200 RESO.100E-03

*Fig. 6.2.14*  
RAE 2822 airfoil case (6) - CCS - A  
Pressure coefficient along the surface.  
Solid line - Computed solution  
\* - Experiments (Ref. 64)



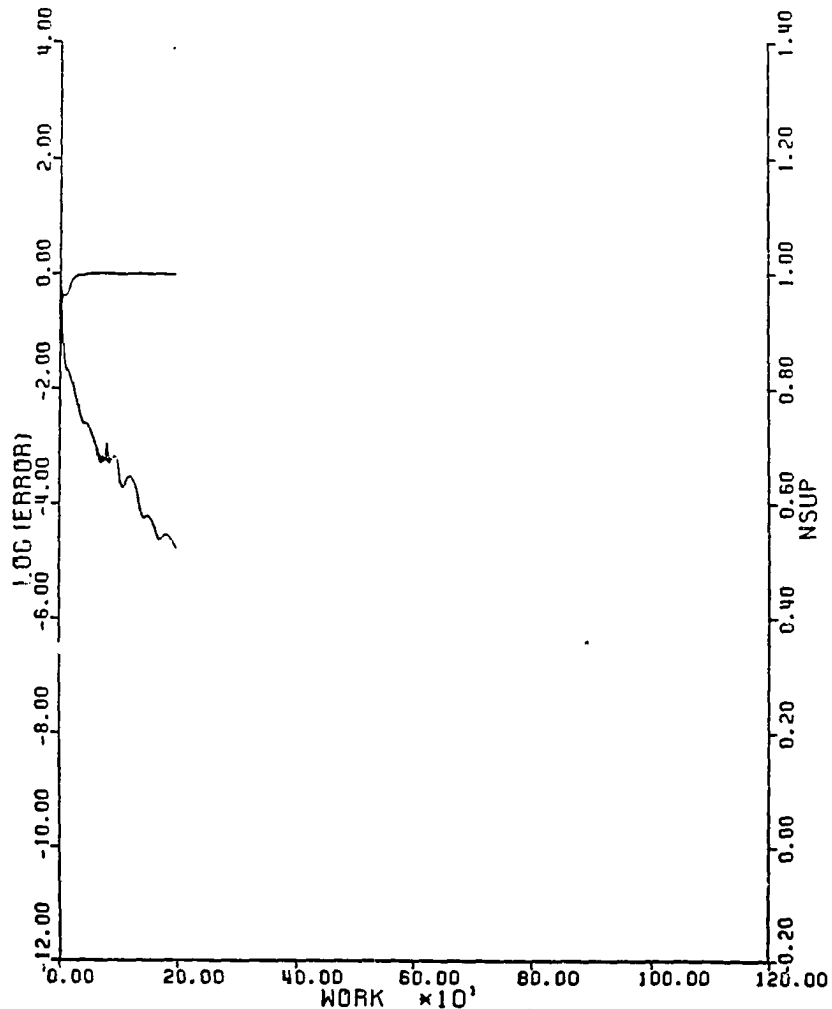
RAE2822      W-CYCLE TURBULENT # 6 BL  
MACH      0.725      RLPHA      2.400  
RESID1 0.113E+02      RESID2 0.149E-03  
WORK      199.00      RATE      0.9451  
GRID      512X64

*Fig. 6.2.15*  
RAE 2822 airfoil case (6) - CCS - A  
Convergence History.



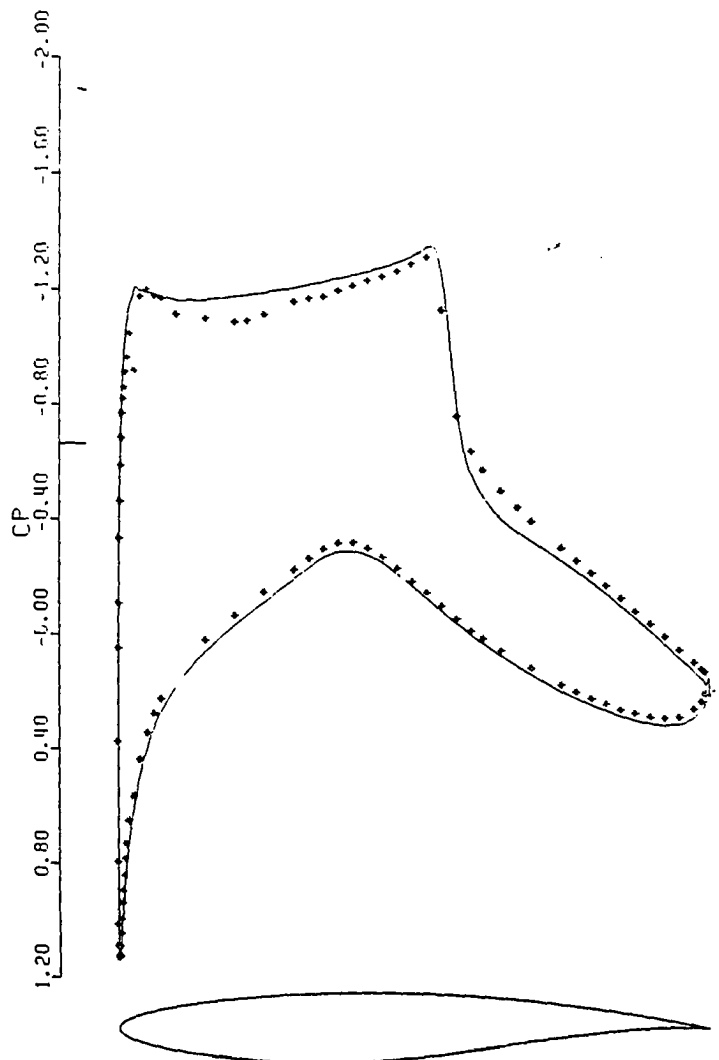
RAE2822 W-CYCLE TURBULENT \* 9 BL  
MACH 0.730 ALPHA 2.790  
CL 0.8415 CD 0.0121 CM -0.0960  
GRID 512X64 NCYC 200 RESO.200E-03

**Fig. 6.2.16**  
RAE 2822 airfoil case (9) - CCS - A  
Pressure coefficient along the surface.  
Solid line - Computed solution  
\* - Experiments (Ref. 64 )



RAE2822 W-CYCLE TURBULENT # 9 BL  
MACH 0.730 ALPHA 2.790  
RESID1 0.117E+02 RESID2 0.195E-03  
WORK 199.00 RATE 0.9462  
GRID 512X64

*Fig. 6.2.17*  
RAE 2822 airfoil case (9) - CCS - A  
Convergence History.



RAE2822 W-CYCLE TURBULENT # 9 BL VIS2 = 0.  
MACH 0.730 ALPHA 2.790  
CL 0.8424 CD 0.0122 CM -0.0962  
GRID 512X64 NCYC 200 RESO.400E-03

*Fig. 6.2.18*  
RAE 2822 airfoil case (9) - CCS - A  
Pressure coefficient along the surface.  
Solid line - Computed solution  
\* - Experiments (Ref. 64)

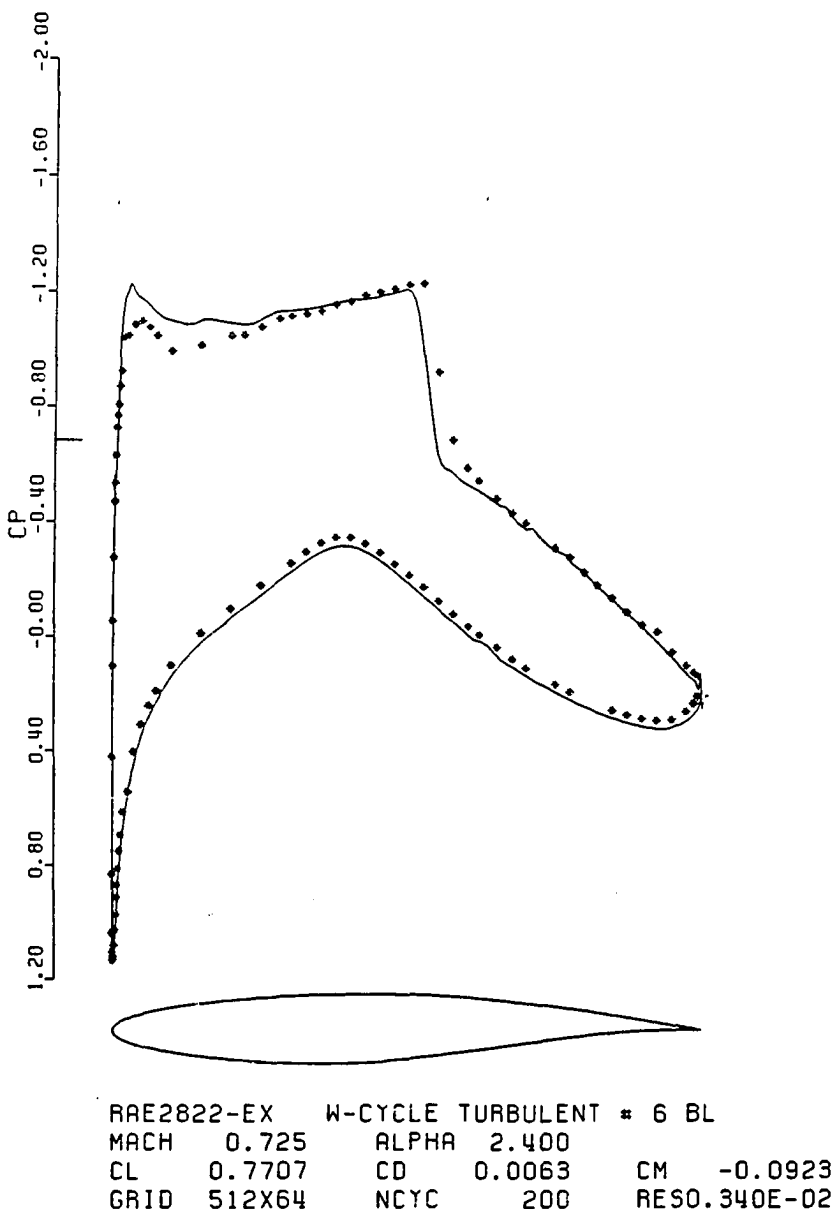


**Fig. 6.2.19**  
RAE 2822 airfoil case (6) - CCS - A  
Pressure coefficient along the surface.  
Solid line - Computed solution  
\* - Experiments (Ref. 64 )

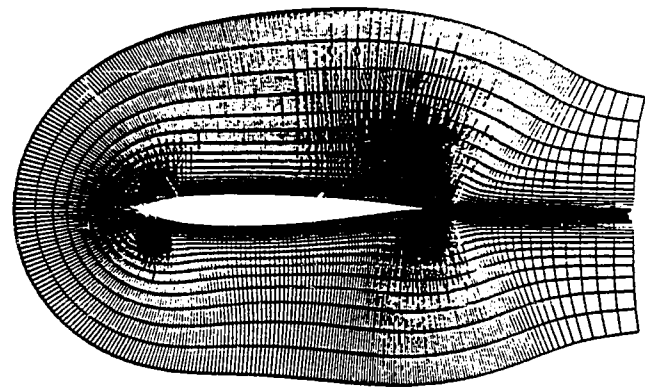
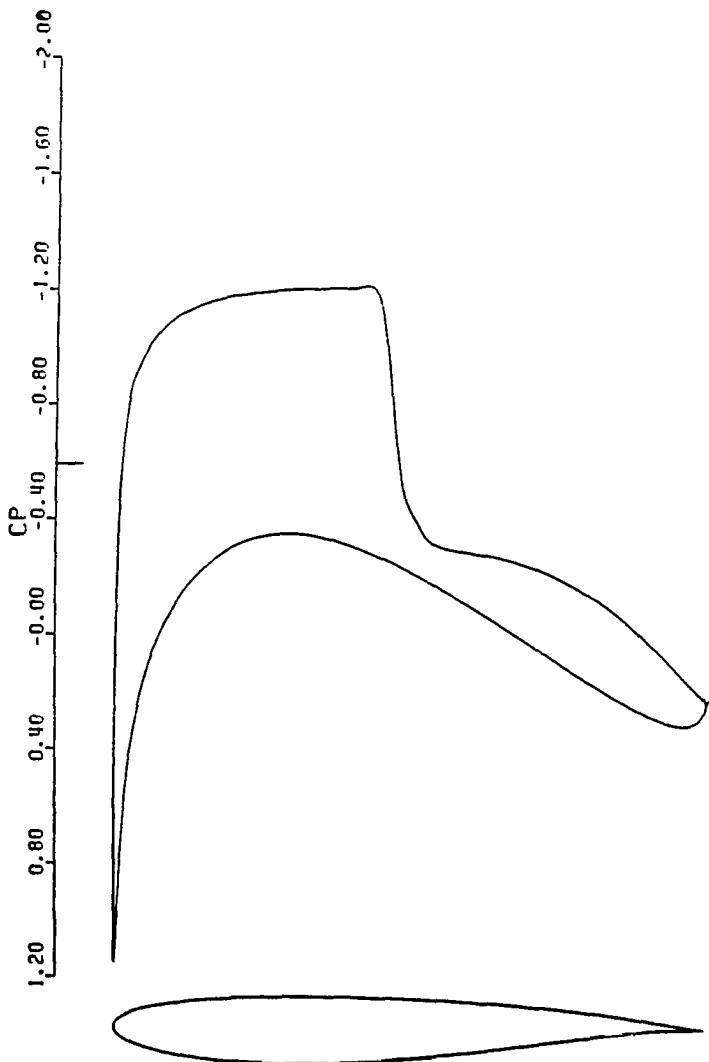
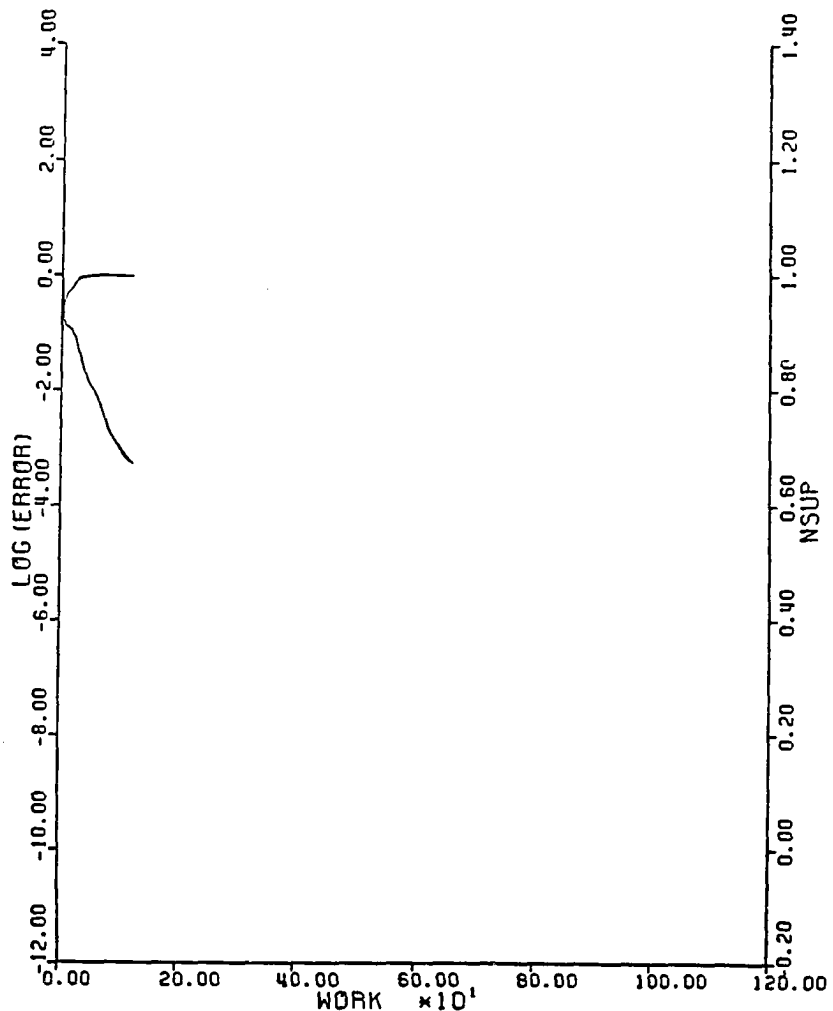


*Fig. 6.2.20*  
**JONES airfoil - CCS - A**  
**512×64 grid for turbulent calculations.**



JONES W-CYCLE TURBULENT # 1 CCS -A  
MACH 0.750 ALPHA 2.000  
CL 0.5623 CD 0.0120 CM -0.0492  
GRID 512X64 NCYC 125 RESO.230E-02

*Fig. 6.2.21*  
JONES airfoil - CCS - A  
Pressure coefficient along the surface.  
Solid line - Computed solution



JONES W-CYCLE TURBULENT = 1 CCS - A  
MACH 0.750 ALPHA 2.000  
RESID1 0.430E+01 RESID2 0.231E-02  
WORK 124.00 RATE 0.9411  
GRID 512X64

*Fig. 6.2.22*  
JONES airfoil - CCS - A  
Convergence History.

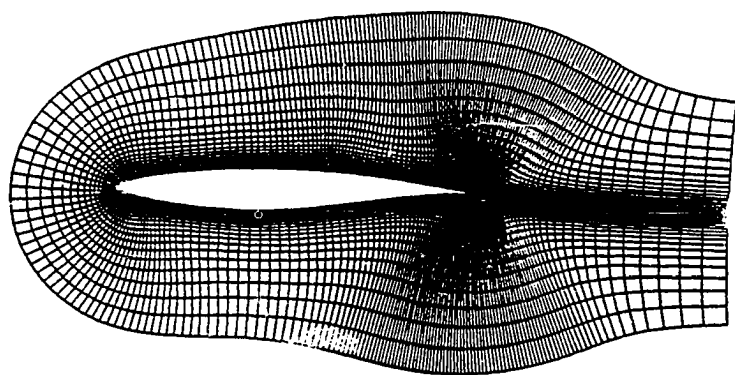


*Fig. 6.3.1*  
RAE 2822 airfoil - CCS - A  
320×64 grid for turbulent calculations.

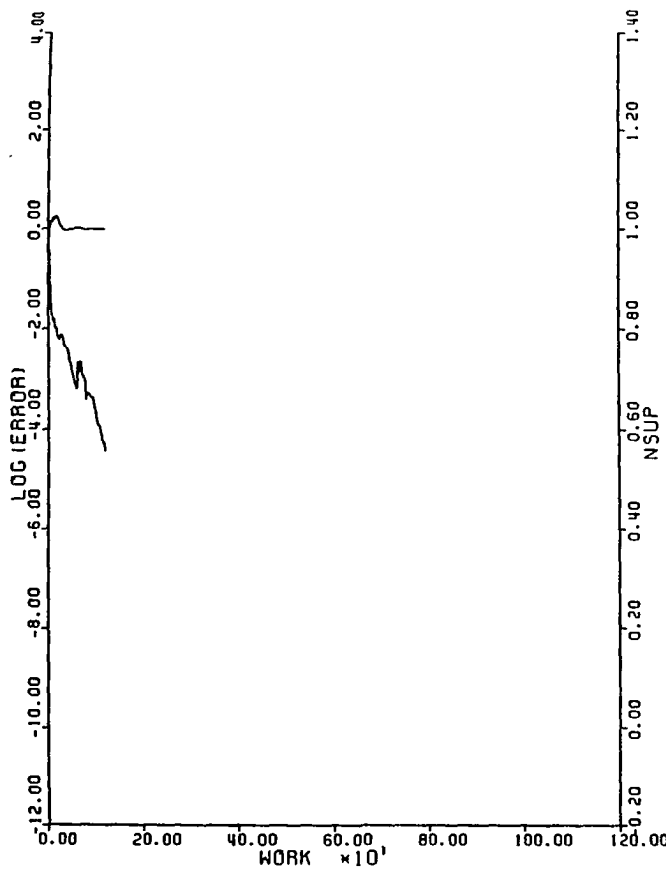


Fig. 6.3.2  
RAE 2822 airfoil case (9) - CCS - A  
Convergence History

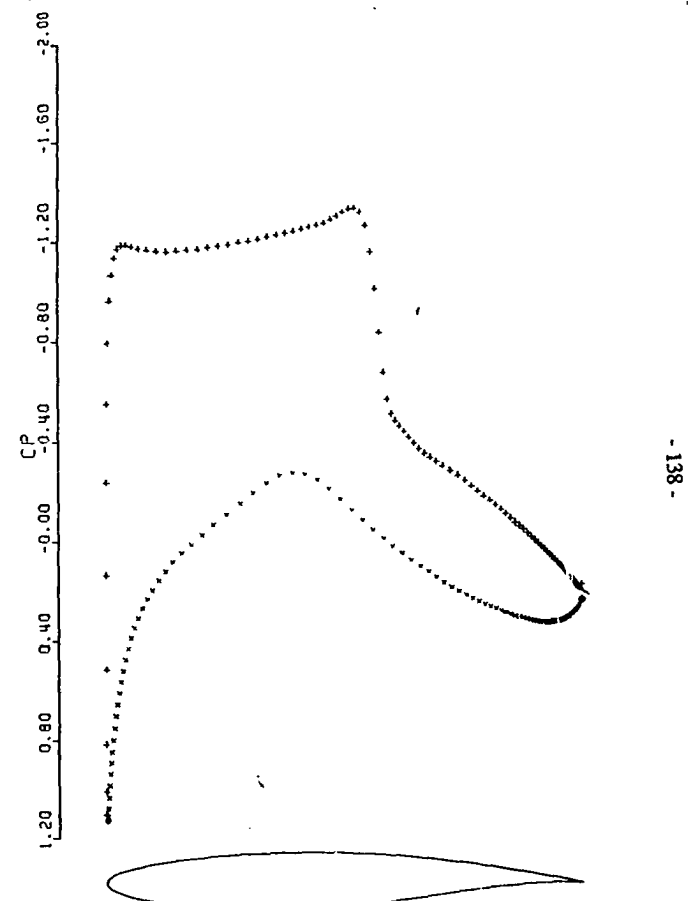
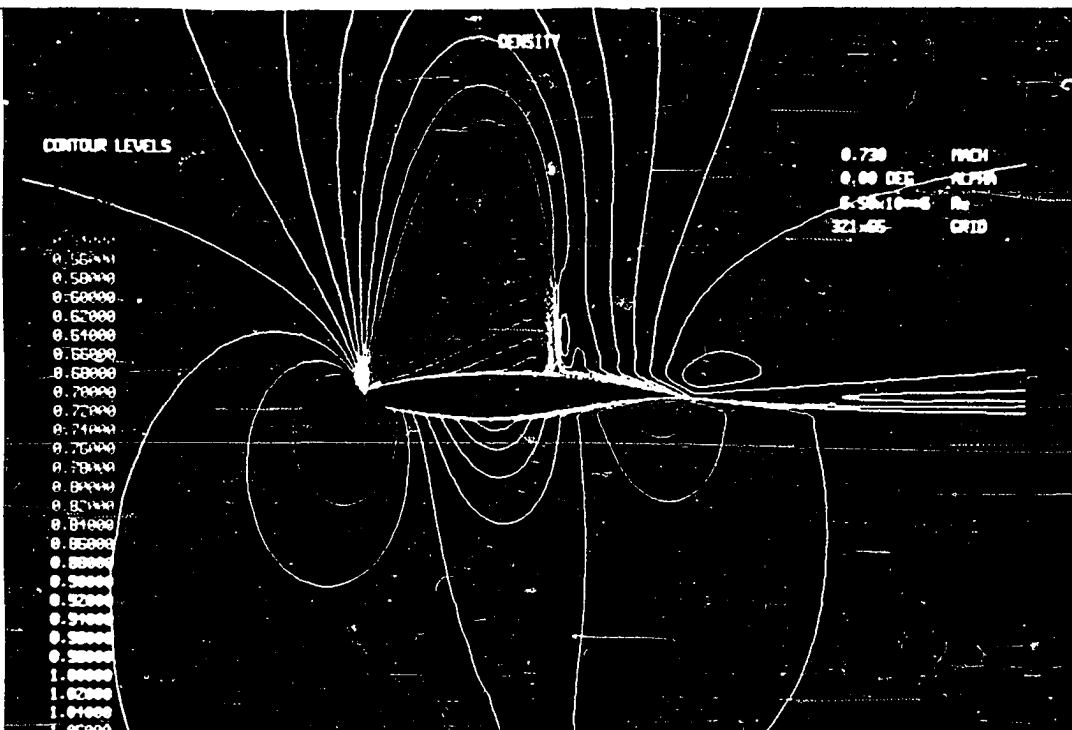
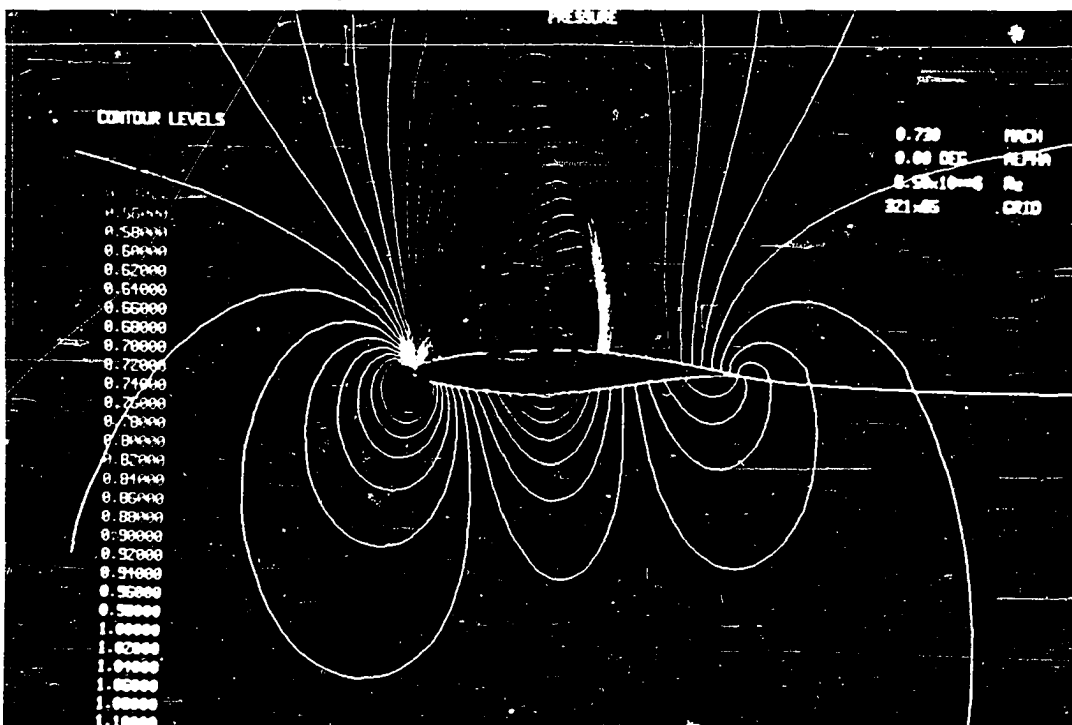


Fig. 6.3.3  
RAE 2822 airfoil case (9) - CCS - A  
Pressure coefficient along the surface.



**Fig. 6.3.4**  
RAE 2822 airfoil case (9) - CCS - A  
Density Contours



**Fig. 6.3.5**  
RAE 2822 airfoil case (9) - CCS - A  
Pressure Contours

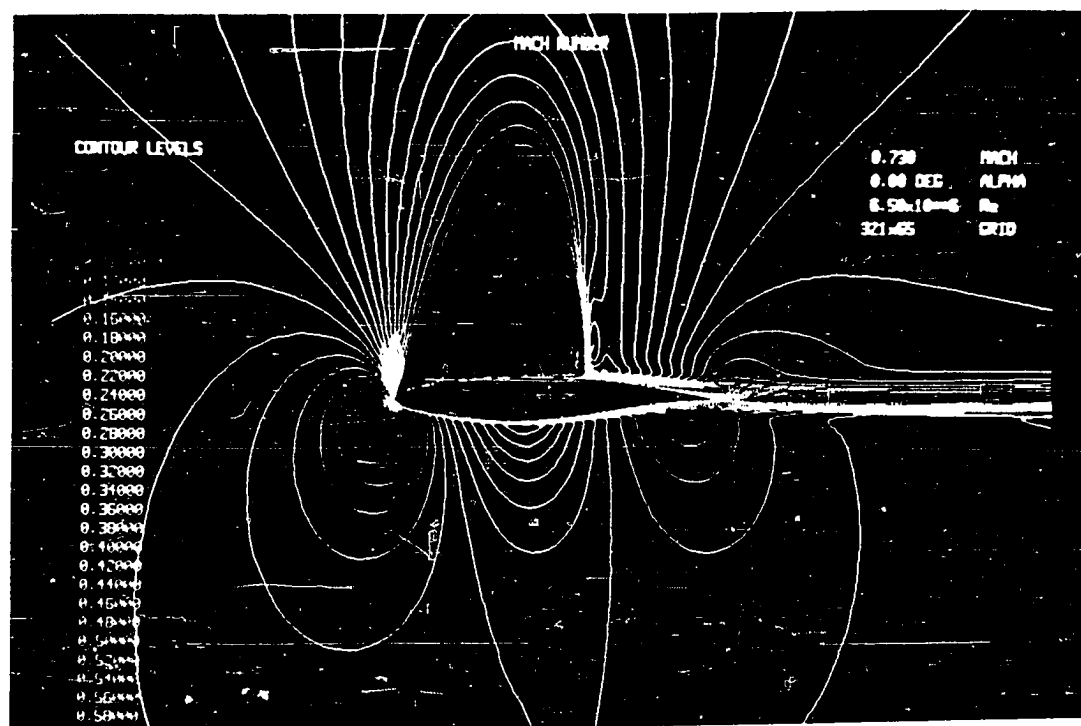


*Fig. 6.3.6*  
RAE 2822 airfoil case (9) - CCS - A  
Mach Contours

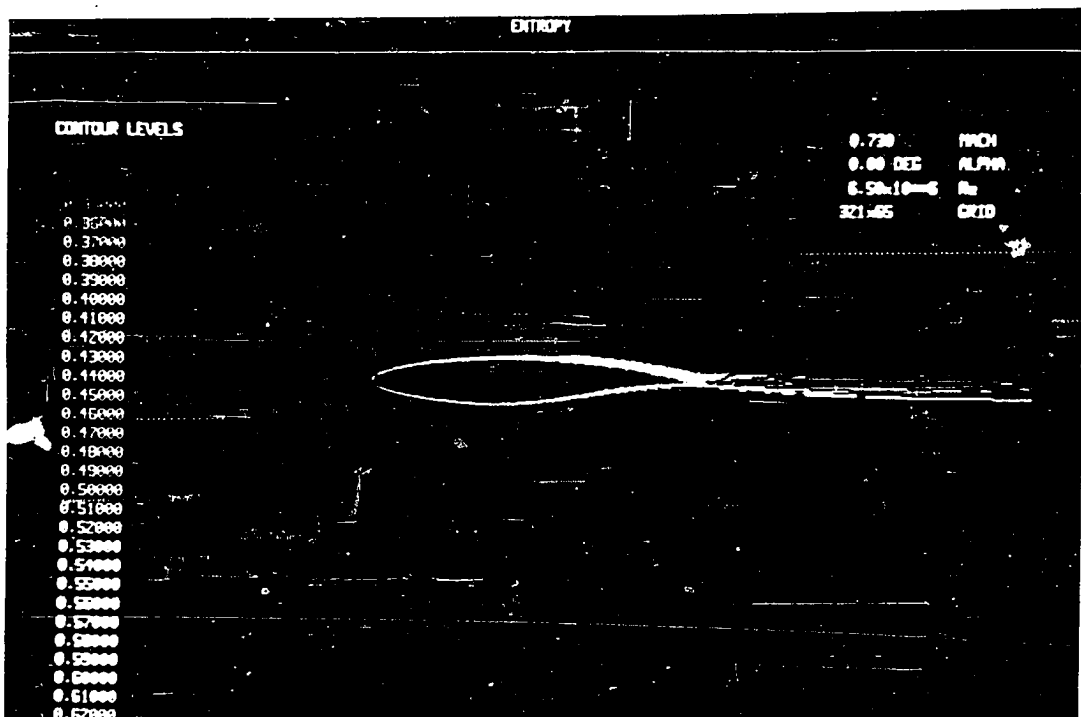


*Fig. 6.3.7*  
RAE 2822 airfoil case (9) - CCS - A  
Entropy Contours

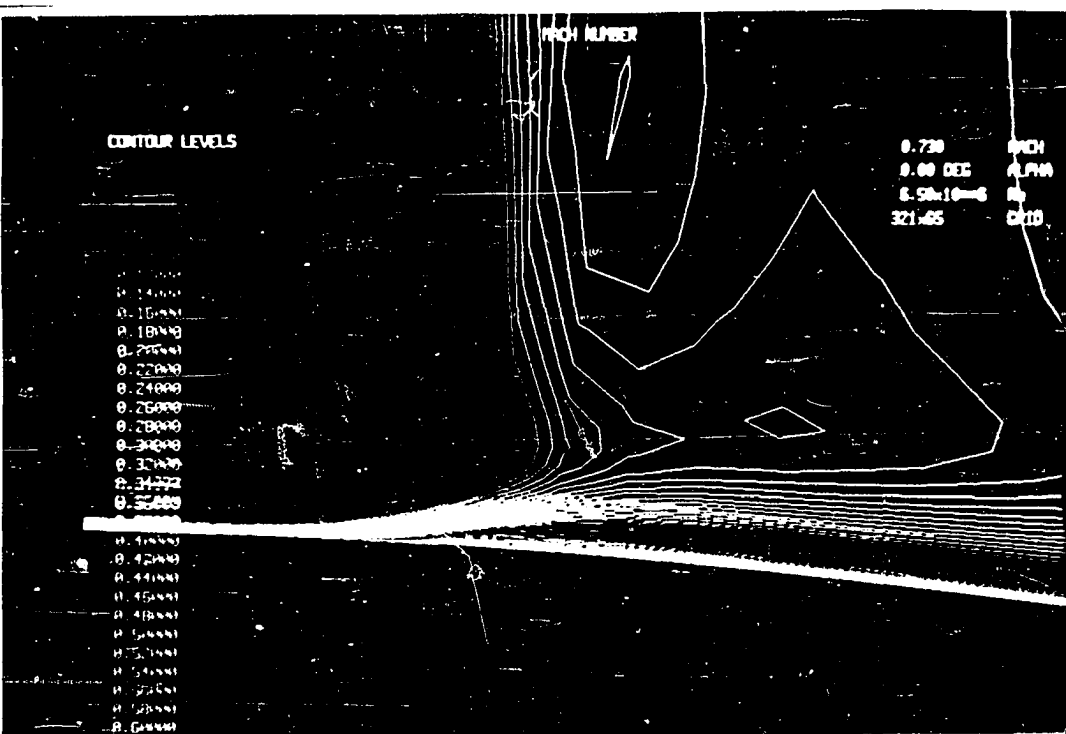


*Fig. 6.3.8  
RAE 2822 airfoil case (9) - CCS - A  
Mach Contours - close up*

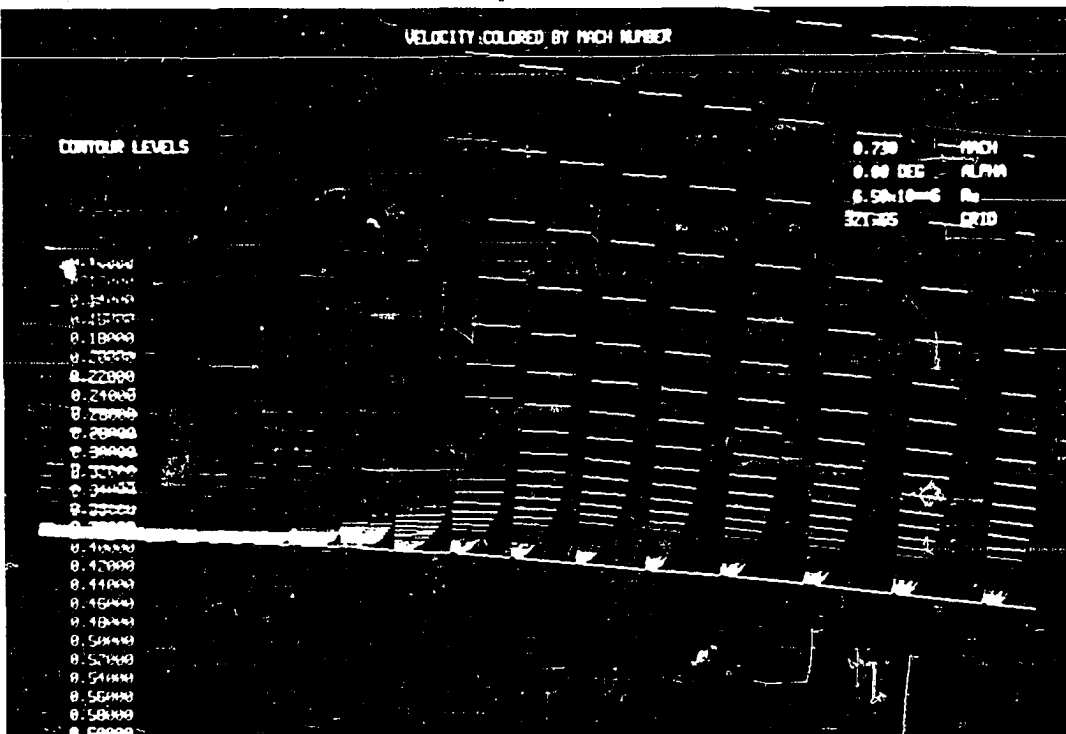


*Fig. 6.3.9  
RAE 2822 airfoil case (9) - CCS - A  
Velocity vector field - close up*

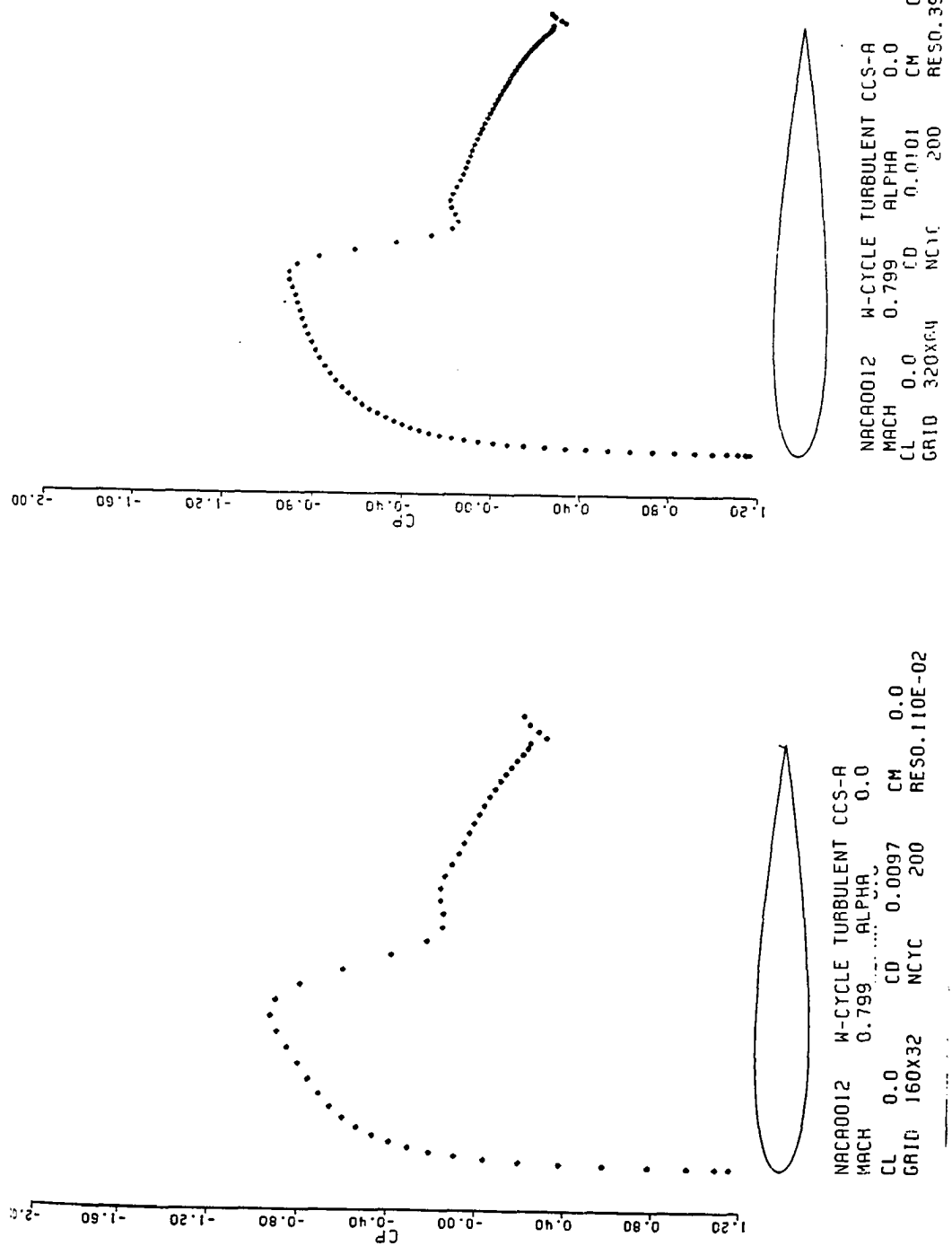
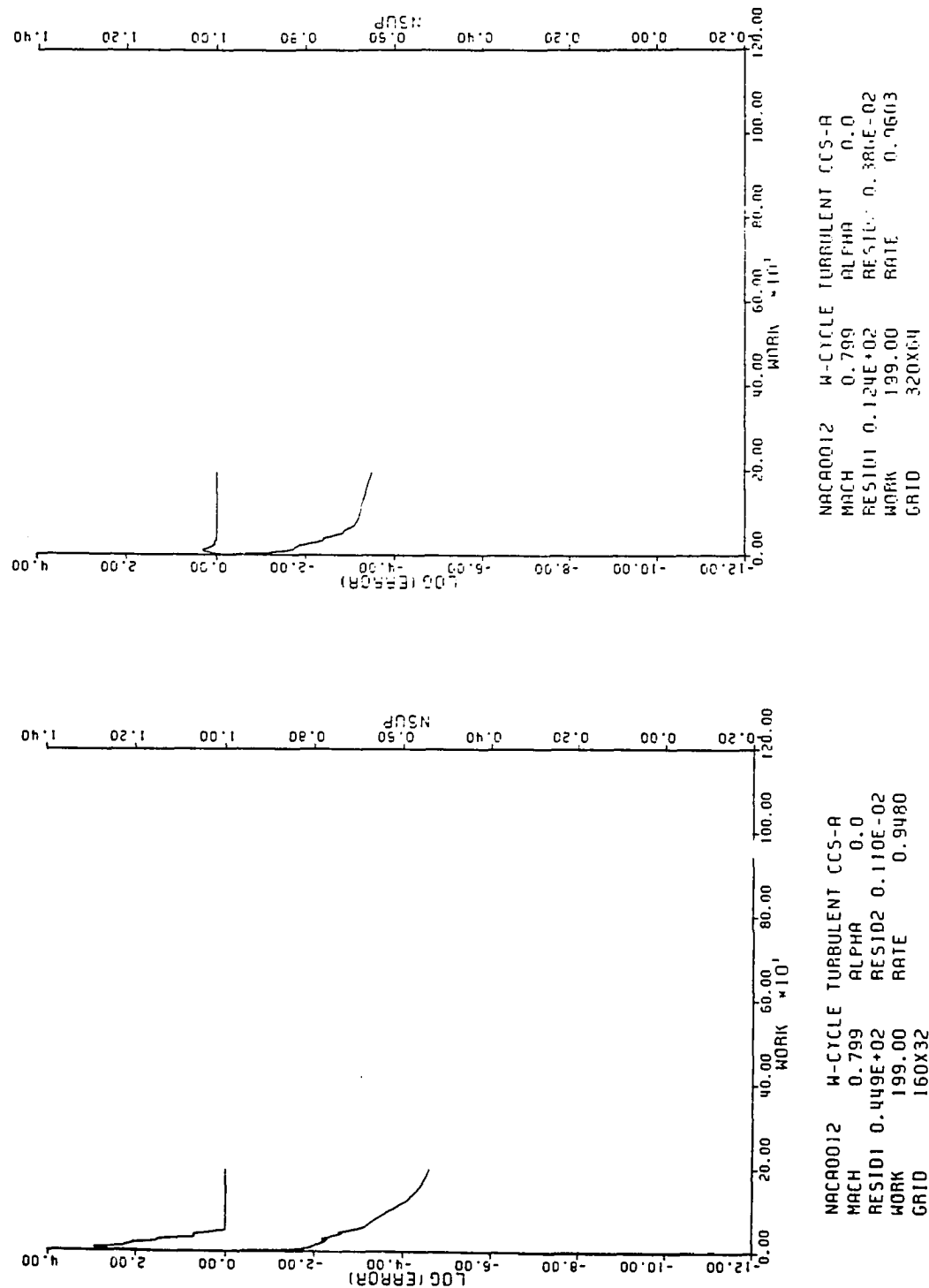
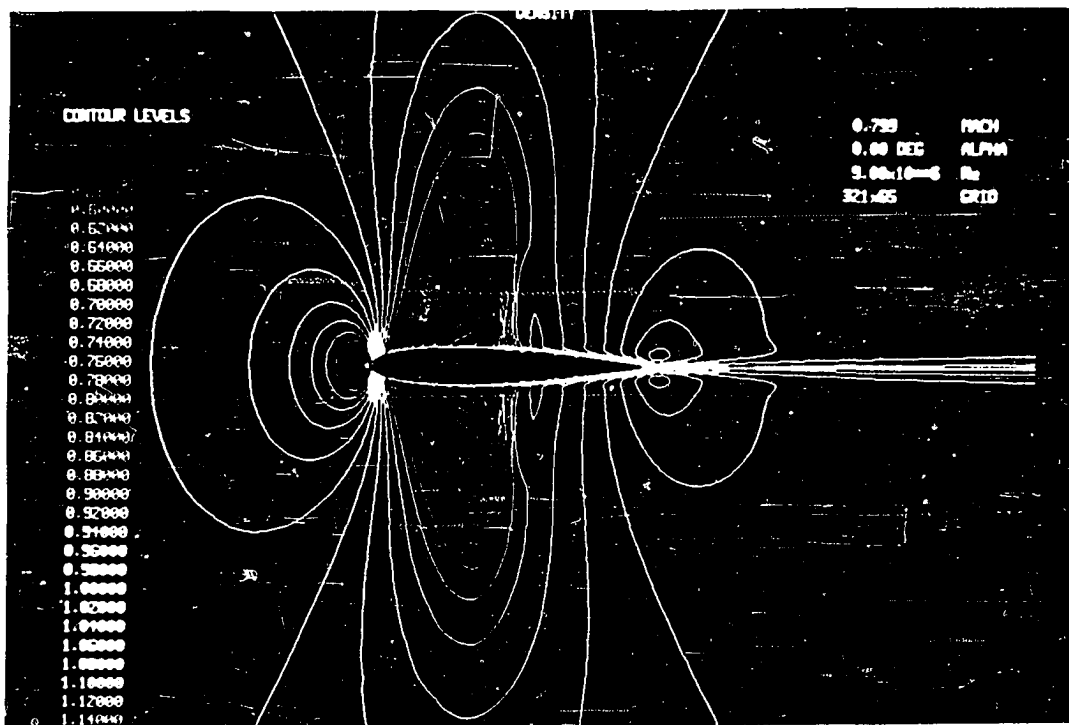
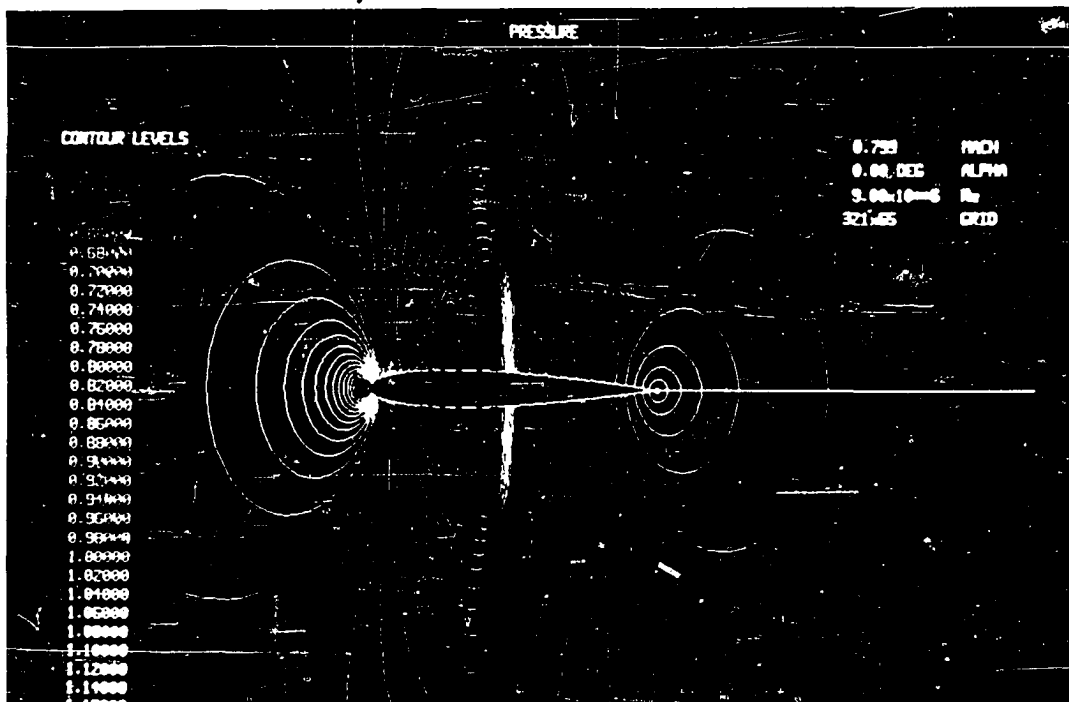


Fig. 6.3.10  
NACA 0012 airfoil - CCS-A  
Pressure coefficient along the surface.





*Fig. 6.3.12  
NACA 0012 airfoil - CCS - A  
Density Contours*



*Fig. 6.3.13  
NACA 0012 airfoil - CCS - A  
Pressure Contours*

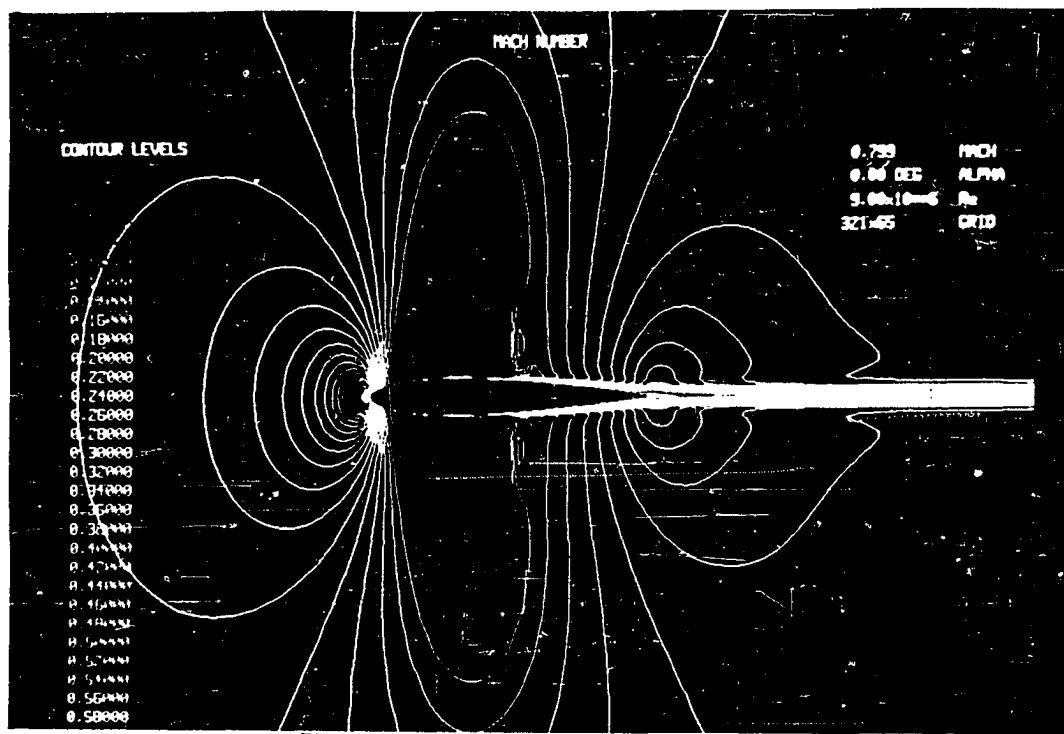


*Fig. 6.3.14  
NACA 0012 airfoil - CCS - A  
Mach Contours*

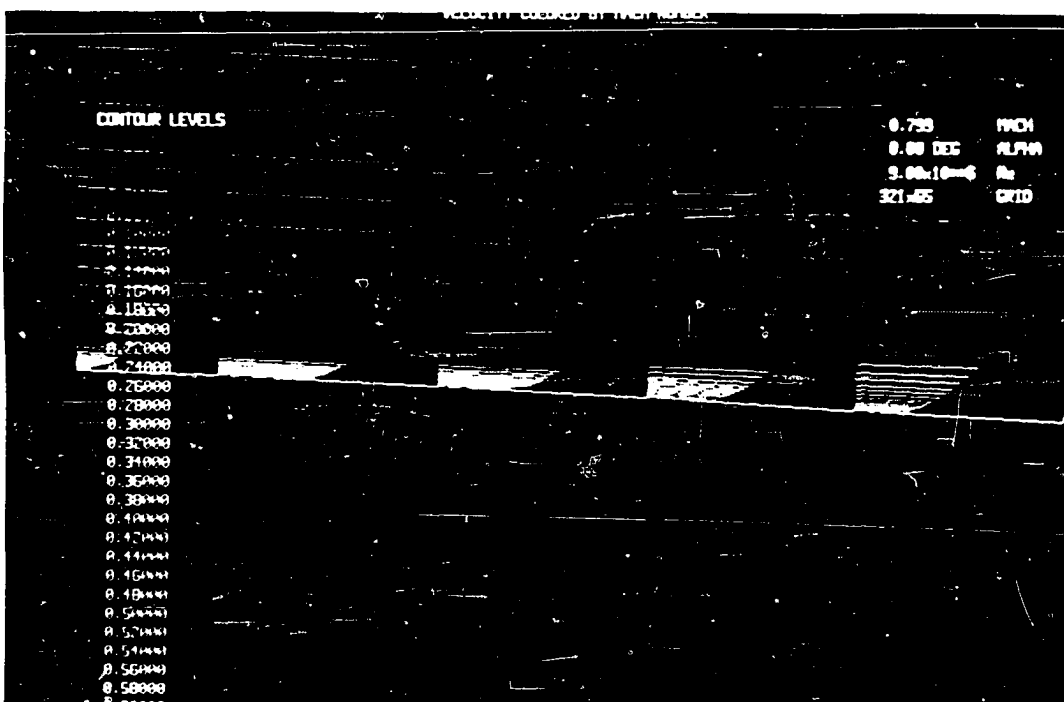


*Fig. 6.3.15  
NACA 0012 airfoil - CCS - A  
Velocity vector field - close up*

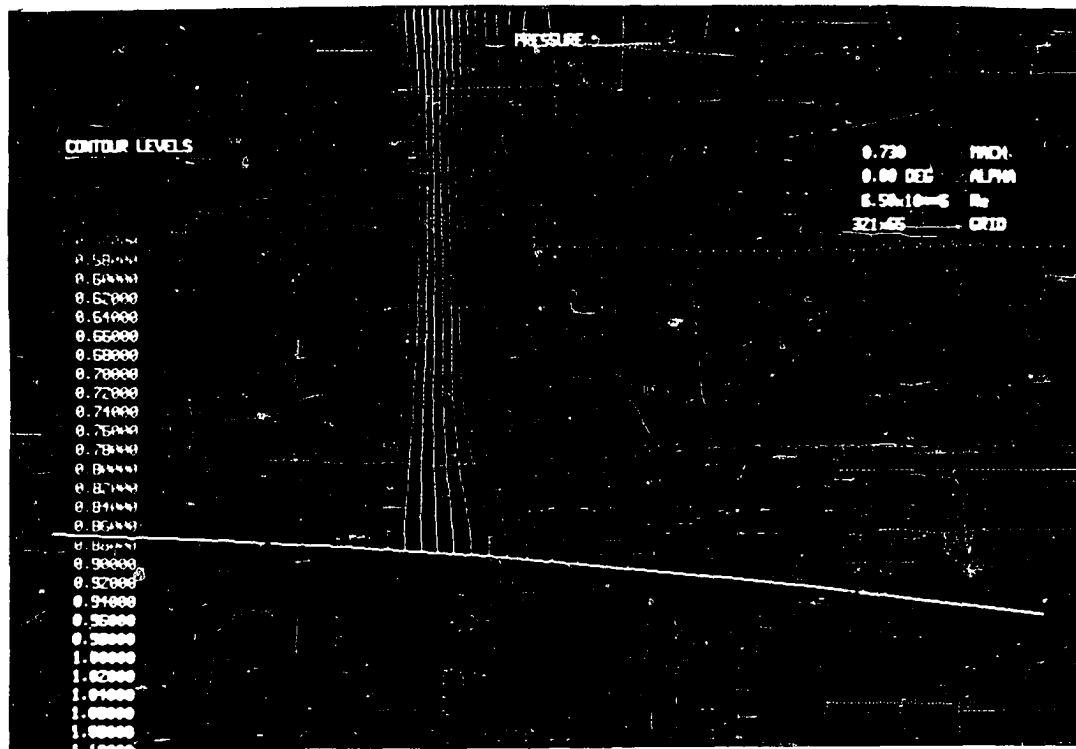


**Fig. 6.3.16**  
**NACA 0012 airfoil - CCS - A**  
**Pressure Contours - close up**

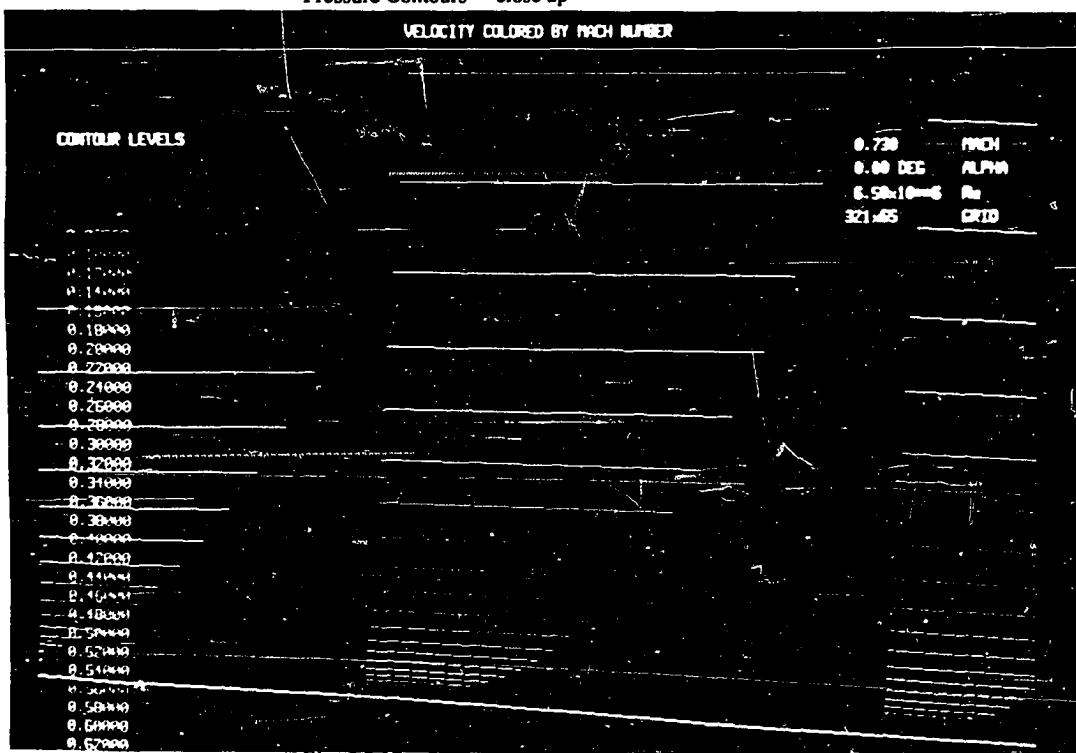


*Fig. 6.3.17*  
NACA 0012 airfoil - CCS - A  
Velocity vector field - close up

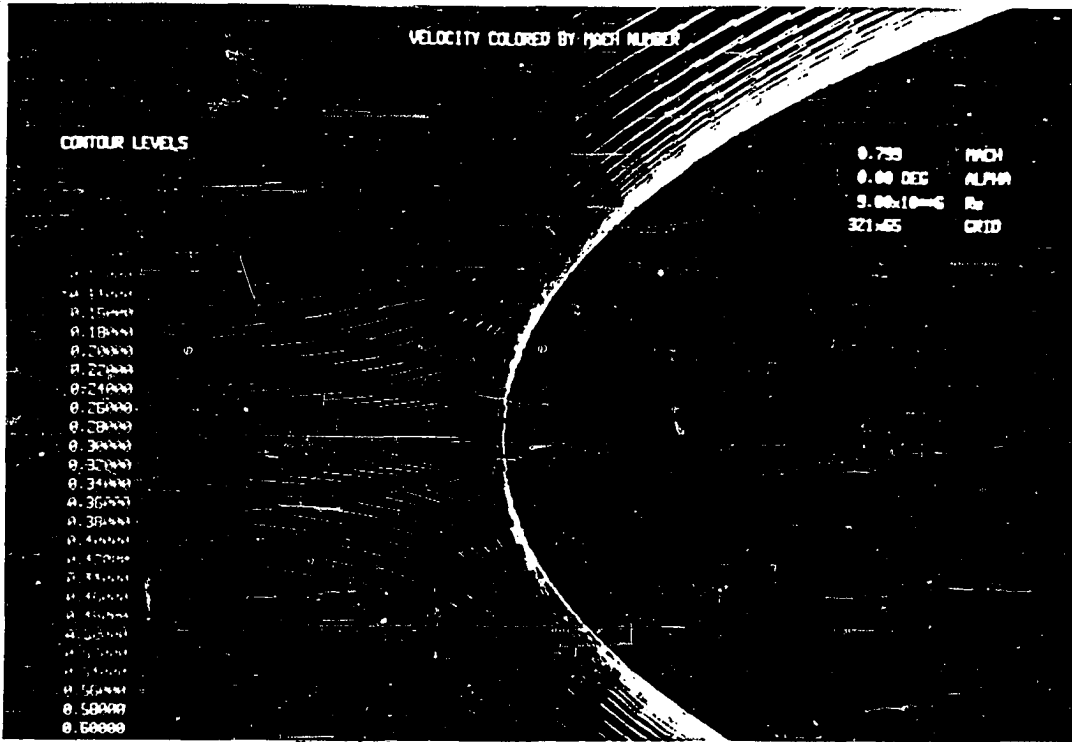


*Fig. 6.3.18*  
NACA 0012 airfoil - CCS - A  
Velocity vector field - close up

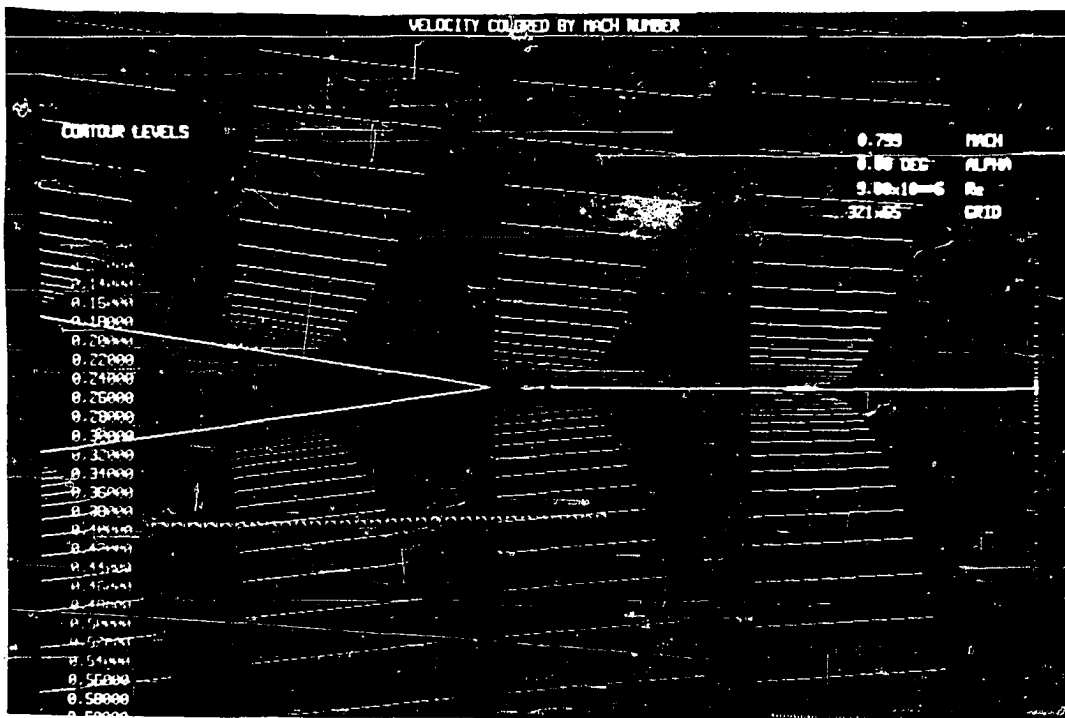


*Fig. 6.3.19*  
NACA 0012 airfoil - CCS - A  
Velocity vector field - close up

## CHAPTER 7

### CONCLUSIONS AND FUTURE WORK

In this work the finite volume formulation has been extended to the treatment of the compressible two dimensional Navier Stokes equations for both cell centered and vertex schemes on regular quadrilateral meshes. Two alternative discretization formulas for the cell centered schemes have been evaluated.

Computer codes utilizing those formulations have been written and the accuracy of the proposed discretization formula has been tested against experimental results and other computed results in the literature. Accurate solutions of the Euler equations have been obtained on grids with high aspect ratio cells. Also, satisfactory accuracy has been demonstrated by laminar flows computations in the transonic and supersonic regimes. Applications of the numerical methods to the Reynolds averaged equations have also been presented for a variety of transonic flows. These exhibit excellent agreement with the results of calculations by other numerical methods using the same turbulence model. For attached flows good agreement with experimental data is also obtained. When the shock boundary layer interaction becomes strong enough to cause significant separation the algebraic turbulence models fails to produce a good simulation, and large variations in the results can be produced by substituting alternative models. Alternative application of the cell centered method to internal flows is briefly described in Appendix C.

It has been shown that the convergence to a steady state solution can be greatly enhanced by the use of multiple grids and that results within engineering accuracy can be obtained in a relatively small number of steps.

There are , however, many areas of further research where contributions are needed. Those areas include the following:

(1) Turbulence Modeling.

This is the area that must receive the highest priority. The laminar computations have shown that the proposed algorithm can handle very well all the difficulties of a viscous calculation. In particular it can handle separated regions quite robustly. The application to the Reynolds averaged equations , however, seems to indicate that turbulence modeling in separated regions behind shock waves is very poor. It has been shown that predictions using the Baldwin and Lomax model agree fairly well with experimental data when the flow is attached or only slightly separated. When the shock wave is strong enough to separate the flow, the model tends to overpredict the extent of the separated region. This results in the prediction of a stronger shock located too far downstream. Not only is the reproduction of the physics inadequate there , but also there is an increased possibility of failure of the numerical scheme through a discontinuous prediction of the eddy diffusivity. It seems that a differential model would be desirable for both physical and numerical purposes. Since the numerical algorithm is fully vectorizable, the increase in the computational effort incurred by the introduction of a two-equation model should not exceed 30%. The possibility of extending the work of Yakhot and Orszag [69] is currently under investigation.

(2) Numerical Discretization and Accuracy.

Proper treatment of the far field boundary conditions in the wake region requires further research. Increasing accuracy could also be sought through the use of locally refined grids

following Berger and Jameson [70]. One possibility is the use of the embedded grid technique (fig. 7.1) for which the finite volume formulation of this work is particularly well suited. Another area of possible improvement is the treatment of the artificial dissipative terms using flux limited dissipation. Fig. (7.2) shows the results for case 9 of reference [64] obtained with the flux limited dissipation model on a relatively coarse  $256 \times 32$  grid. The comparison between the computed pressure distribution (solid line) and the experiments (symbols) indicate that accuracy can indeed be increased on coarser grids. This is of particular importance for three dimensional applications where currently available computers do not allow the use of superfine grids.

(3) Acceleration Techniques.

In this area an investigation of the effects of the low frequency components on the multigrid cycles would be very helpful. Another area that needs to be explored is the formulation and use of appropriate preconditioning [71]. It has been noted in this study that one of the main constraints on the time step limit of our explicit scheme for viscous computations is the limit set by the wave speed in the inner region of the boundary layer. This constraint comes about because of the 'hyperbolic' treatment of the convection operator everywhere in the flow field. However, there are large regions within the boundary layer where the flow is locally incompressible. Optimization of the scheme in these regions could be achieved by sacrificing time accuracy in favor of the introduction of an appropriate preconditioning matrix.

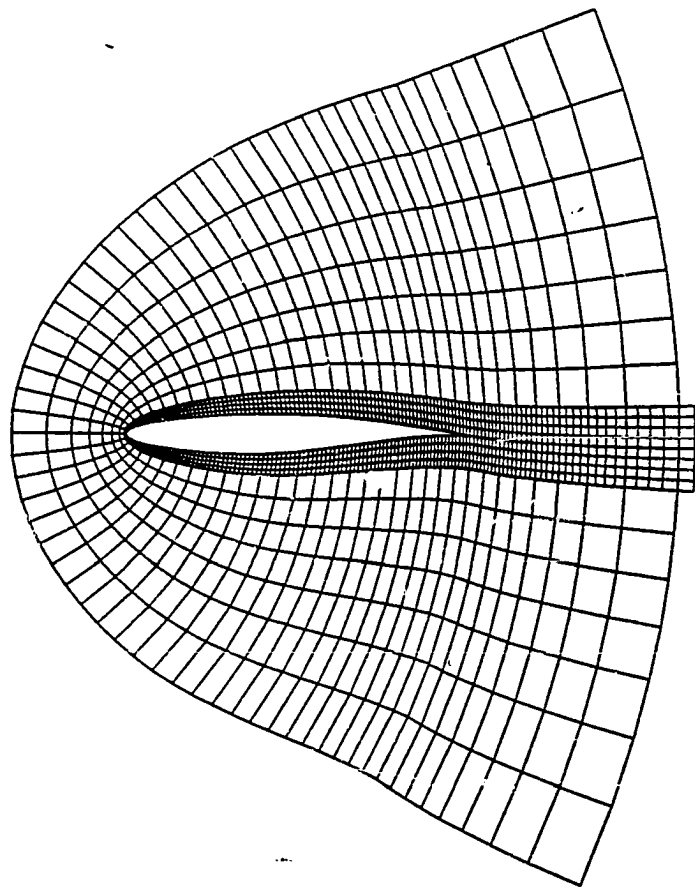
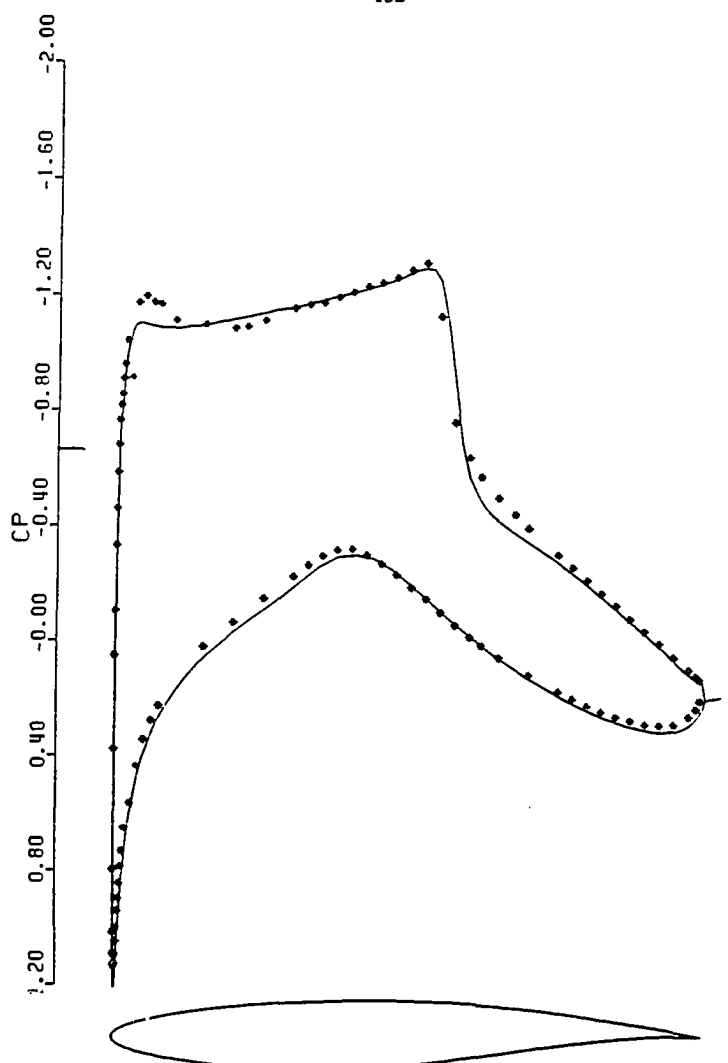


**Fig. 7.1**  
**RAE 2822**  
**Embedded Grid system.**



RAE2822 W-CYCLE TVD \* 9  
MACH 0.730 ALPHA 2.790  
CL 0.8134 CD 0.0203 CM -0.0993  
GRID 256X32 NCYC 75 RESO.152E-01

*Fig. 7.2*  
RAE 2822 airfoil case (9) - CCS - A  
Pressure coefficient along the surface.  
(Flux Limited dissipation model)  
Solid line - Computed solution  
\* - Experiments (Ref. 64)

## REFERENCES

1. Rubbert, P. E., "Design Applications of CFD at Boeing", Supercomputing in Aerospace, NASA CP 2454, March 1987.
2. Peterson, V. L., and Baillhaus, W. F. Jr, "History of the Aerodynamic Simulation Program, Supercomputing in Aerospace, NASA CP 2454, March 1987.
3. Le Balleur, J. C., "Numerical Viscid-Inviscid Interaction in Steady and Unsteady Flows", Proc. 2nd Symposium on Numerical and Physical Aspects of Aerodynamic Flows, Long Beach, CA, 1983.
4. Melnik, R. E., "Turbulent Interactions on Airfoils at Transonic Speeds - Recent Developments", Proc. AGARD Conference on Computation of Viscous-Inviscid Interactions, Colorado Springs, 1980, AGARD CP 291, Paper No. 10.
5. Metha, U., Chang, K.C., and Cebeci, T. C., "Relative Advantages of Thin-Layer Navier-Stokes and Interactive Boundary-Layer Procedure", NASA TM-86778, 1985.
6. Rubesin, M. W., "Turbulence Modeling", Supercomputing in Aerospace, NASA CP 2454, March 1987.
7. Melnik, R. E., "An Overview of Computational Fluid Dynamics Development and Application at Grumman", Supercomputing in Aerospace, NASA CP 2454, March 1987.
8. MacCormack, R. W., and Baldwin, B. S., "A Numerical Method for Solving the Navier Stokes Equations with Application to Shock Boundary Layer Interactions", AIAA Paper 75-1, 1975.
9. MacCormack, R. W., "A Numerical Method for Solving the Equations of Compressible Viscous Flows", AIAA Paper 81-110, 1981.
10. Beam, R., and Warming, R. F., "An Implicit Factored Scheme for the Compressible Navier Stokes Equations", AIAA Journal, 16, 1978, pp. 393-402.
11. Steger, J. L., "Implicit Finite Difference Simulation of Flows About Arbitrary Two Dimensional Geometries", AIAA Journal, 16, 1978.
12. Pulliam, T. H., and Steger, J. L., "Implicit Finite Difference Simulations of Three Dimensional Compressible Flow", AIAA Journal, Vol. 18, 1980.
13. Pulliam, T. H., and Steger, J. L., "Recent improvements in Efficiency, Accuracy and Convergence for Implicit Approximate Factorization Algorithms", AIAA Paper 85-0360, January 1985.
14. Pulliam, T. H., "Euler and Thin Layer Navier Stokes Codes: ARC2D, ARC3D", Note for Computational Fluid Dynamics User's Workshop, March 1984.
15. Shang, J. S., and Hankey, W. L., "Computation of Flow Past a Hypersonic Cruiser", Proc. 2nd Symposium on Numerical and Physical Aspects of Aerodynamic Flows, Long Beach, CA, 1983.
16. Peyret, R. , and Viviand, H., AGARDograph, No. 212, September 1975.

17. Metha, U. , and Lomax, H., "Reynolds Averaged Navier Stokes Computations of Transonic Flow - The State of the Art", Proc. Transonic Perspectives Symposium, Moffet Field, 1979, edited by D. Nixon, AIAA, 1981, pp. 297-375.
18. Giles, M., Drela, M., and Thompkins, W.T., "Newton Solution of Direct and Inverse Transonic Euler Equations", AIAA Paper 85-1530, Proc. AIAA 7th Computational Fluid Dynamics Conference, Cincinnati, 1985, pp.394-402.
19. Jameson, A., Schmidt, W., Turkel, E., "Numerical Solution of the Euler Equations by Finite Volume Methods Using Runge-Kutta Time Stepping Schemes", AIAA paper 81-1259, 1981.
20. Jameson, A., Baker, T. J., and Weatherill, N. P., "Calculation of Inviscid Transonic Flow over a Complete Aircraft", AIAA Paper 86-0103, January, 1986.
21. Jameson, A., "Solution of the Euler Equations by a Multigrid Method", Applied Mathematics and Computation, Vol. 13, 1983, pp. 327-356.
22. Agarwal, R., and Deese, J., "Computation of Transonic Viscous Airfoil, Inlet and Wing flow Fields", AIAA Paper 84-1551, June 1984.
23. Swanson, R. C., and Turkel, E., "A Multistage Time-Stepping Scheme for the Navier Stokes Equations", AIAA Paper 85-0035, January 1985.
24. Chima, R. V., and Johnson, G. M., "Efficient Solutions of the Euler and Navier Stokes Equations with a Vectorized Multiple-grid Algorithm".
25. Davis, R. L., Ni, R. H., and Carter, J. E., "Cascade Viscous Flow Analysis Using the Navier Stokes Equations", AIAA Paper 86-0033.
26. Ni, R. H., "A Multiple Grid Scheme for Solving the Euler Equations", AIAA Journal, Vol. 20, 1982, pp. 1565-1571. Applied Mathematics and Computation, Vol. 13, 1983, pp. 327-356.
27. Jameson, A., "Multigrid Algorithms For Compressible Flow Calculations" , MAE Report 1743, Text of Lecture given at 2nd European Conference on Multigrid Methods, Cologne, October 4, 1985.
28. Baldwin, B. S., and Lomax, H., "Thin Layer Approximation and Algebraic Model for Separated Turbulent Flows", AIAA Paper 78-275 ,1978.
29. Thompson, P. A., "Compressible Fluid Dynamics", McGraw-Hill
30. Reynolds, O. " On The Dynamical Theory of Incompressible Viscous Fluids and The Determination of The Criterion ", Phil. Trans. A, CLXXXVI, 123, 1894.
31. Rubesin, M. W., and Rose, W. C. "The Turbulent Mean-Flow, Reynolds-Stress, and Heat-Flux Equations in Mass-Averaged Dependent Variables" NASA-TM-X-62248, March 1973.
32. Cebeci, T., and Smith, A. M. O., " Analysis of Turbulent Boundary Layers" , Academic Press, 1974.
33. Jones, W. P. and Launder, B. E., " The prediction of Relaminarization with a Two-Equations Model of Turbulence ", Int. J. Heat and Mass Transfer, 15, pp. 303-314, 1972.
34. Rubesin, M. W., and Viegas, J. R., " A Critical Examination of The Use of Wall Functions as Boundary Conditions in Aerodynamic Calculations", Third Symposium on Numerical and Physical Aspect of Aerodynamics Flows, California State University, Long Beach, Calif., Jan 1985.
35. Johnson, D. A., and King, L. S., " A Mathematically Simple Turbulent Closure Model for Attached and Separated Turbulent Boundary Layers", AIAA Journal, 23, pp. 1684-1692, 1985.

36. Bradshaw, P., Ferris, D. H., and Atwell, N. P., "Calculations of Boundary Layer Development Using The Turbulent Energy Equation", *Journal of Fluid Mechanics*, 28, pp. 553-616, 1967.
37. King, L. S., and Johnson, D. A., " Separated Transonic Airfoil Calculations With a Nonequilibrium Turbulence Model", *NASA - TM 86830*, 1986.
38. Jameson, A., "Current Status and Future Directions of Computational Transonics" , ASME Symposium on future Directions of Computational Mechanics, Anaheim, December 1986.
39. Jameson, A., "Transonic Flow Calculations", Princeton University Report, MAE 1651, 1984, included in Lecture Notes in Mathematics, 1127, edited by F. Brezzi, Springer Verlag, 1985, pp. 156-242.
40. Pulliam, T. H., private Communication.
41. Jameson, A., "A Vertex Based Multigrid Algorithm for Three Dimensional Compressible Flow Calculations", ASME Symposium on Numerical Methods for Compressible Flows, Anaheim, Dec. 1986. MAE 1751, 1984.
42. Vincenti, W. G., and Kruger, C. H., "Introduction to Physical Gas Dynamics", Krieger .
43. Godunov, S. K., "A Difference Method for the Numerical Calculation of Discontinuous Solutions of Hydrodynamic Equations", *Mat. Sbornik*, 47, 1959, pp. 271-306, translated as JPRS 7225 by U.S. Dept. of Commerce, 1960.
44. Van Leer, B., "Towards the Ultimate Conservative Difference Scheme IV. A New Approach to Numerical Convection", *Journal of Computational Physics*, Vol. 23, 1977, pp. 276-299.
45. Stager, J.L., and Warming, R.F., "Flux Vector Splitting of the Inviscid Gas Dynamics Equations with Applications to Finite Difference Methods", *Journal of Computational Physics*, Vol. 40, 1981, PP.263-293.
46. Venkatakrishnan, V. "Computation of Unsteady Flows Over Moving Airfoils" Ph. D. Thesis, MAE Dept. Princeton University, Oct.1986.
47. Richtmyer, R. D., and Morton, K. W., "Difference Methods for Initial-Value Problems ", Interscience.
48. Abarbanel, S. , and Gottlieb, D. "Optimal Time Splitting for Two and Three Dimensional Navier-Stokes Equations with Mixed Derivatives", *Journal of Computational Physics*, 41, 1981, pp. 1-33.
49. Jameson A., "A Non-Oscillatory Shock Capturing Scheme Using Flux Limited Dissipation", MAE Report 1653.
50. Morawetz, C. S., "On the Non-Existence of Continuous Transonic Flows Past Profiles", *Communications in Pure and Applied Mathematics*, Vol. 9, 1956, pp.45-48.
51. Fedorenko, R. P., " The Speed of Convergence of One Iterative Process" , USSR Comp. Math. and Math. Phys., Vol. 4, 1964, pp. 227-235.
52. Brandt, A., "Multigrid Methods: 1984 Guide, With Applications to Fluid Dynamics", Lecture Notes for the Computational Fluid Dynamics Lecture Series, Von Karman Institute for Fluid Dynamics, Rhode-Saint-Genese, Belgium, March, 1984.
53. Hackbusch, W., "Multigrid Convergence Theory", Multigrid Methods, Lecture Notes in Math. 960, Springer-Verlag, 1982.
54. Yoon , S., "Numerical Solution of the Euler Equations by Implicit Schemes with Multiple Grids", Ph. D. Thesis, Mae Dept., Princeton University, September 1985.
55. Mavriplis, D., "Solution of the Two-Dimensional Euler Equations on Unstructured Triangular Meshes" , Ph. D. Thesis, Mae Dept., Princeton University, 1987.

56. Grasso, F., Martinelli, L., and Jameson, A., "A Multistage Multigrid Method for the Compressible Navier-Stokes Equations", GAMM-Workshop on Numerical Simulation of Compressible Navier Stokes Flows INRIA, Sophia Antipolis, 1985.
57. Cambier L., "Computation of Viscous Transonic Flows Using an Unsteady Type Method and a Zonal Grid Refinement Technique", GAMM-Workshop on Numerical Simulation of Compressible Navier Stokes Flows INRIA, Sophia Antipolis, 1985.
58. Hollander, H. , and Ravalason, W. , "Resolution Des Equations de Navier-Stokes en Fluid Compressible Par Methode Implicite", La Recherche Aerospacial, 1, 1986, pp. 23-43.
59. Peyret, R., and Taylor T. D., "Computational Methods for Fluid Flow", Springer-Verlag, 1983.
60. Bristeau, M. O., Glowinski, R., Dimoyer, B., Periaux, J., Perrier , P., and Pironneau, O., "Finite Element Methods for The Compressible Navier Stokes Equations", AIAA Computational Fluid Dynamics Conference, AIAA Paper 83-1890, July 1983.
61. Bernard, J. J., Allegre, J., and Raffin, M., "Champs d'Ecoulements Rarefies Compressibles Autour d'un Profil NACA 0012", Contrat D.R.E.T. 80/636, Rapport Technique.
62. Martinelli, L., Jameson, A., and Grasso, F., "A Multigrid Method for the Navier-Stokes Equations", AIAA paper 86-0208, January, 1986.
63. Coakley, T.J., "Turbulence Modeling Methods for The Compressible Navier-Stokes Equations", AIAA Paper 83-1693
64. Cook, P. H., Mc Donald, M. A., and Firmin, M. C. P., "AEROFOIL RAE 2822 Pressure Distributions , Boundary Layer and Wake Measurements", AGARD Advisory Report No. 138, 1979.
65. Coakley, T. J., "Numerical Simulation of Viscous Transonic Airfoil Flows", AIAA-87-0416,1987.
66. Maksymiuk, C. M.,and Pulliam, T.H., " Viscous Transonic Workshop Results Using Arc2d", AIAA-87-0415, 1987.
67. Rumsey, C.L., Taylor, S.L., Thomas, J.L., and Anderson, W.K., "Application of an Upwind Navier-Stokes Code to Two-Dimensional Transonic Airfoil Flow", AIAA-87-0413.
68. Harris, D. H., " Two-Dimensional Aerodynamic Characteristics of the Naca 0012 Airfoil in the Langley 8-foot Transonic Pressure Tunnel" NASA TM 81927, April 1981.
69. Yakhot, V., and Orszag, S. A., "Renormalization Group Analysis of Turbulence. I. Basic Theory", Journal of Scientific Computing, Vol. 1, 1986.
70. Berger, M. J. , and Jameson, A., "Automatic Adaptive Grid Refinement for The Euler Equations", Mae Report 1633, Princeton University, October 1983.
71. Turkel, E., "Preconditioned Methods for the Solving the Incompressible and Low Speed Compressible Equations", ICASE Report No. 86-14, 1986.
72. Finzi, B., Pastori, M., "Calcolo Tensoriale e Applicazioni", Zanichelli.
73. Visbal, M. R., "Calculation of Viscous Transonic Flows about a Supercritical Airfoil", AFWAL - TR 86-3013, July 1986.
74. Bassi F., Grasso, F., Jameson , A., Martinelli, L., and Savini, M., "Solution of the Compressible Navier-Stokes Equations for a Double Throat Nozzle", GAMM-Workshop on Numerical Simulation of Compressible Navier Stokes Flows INRIA,Sophia Antipolis, 1985.
75. Proceedings of The GAMM-Workshop on Numerical Simulation of Compressible Navier Stokes Flows INRIA,Sophia Antipolis, 1985, to be published by Vieweg.

--

## APPENDIX A

### Baldwin & Lomax Turbulence Model

The algebraic turbulence model used for closure of the Reynolds averaged equations is patterned after the formulation of Baldwin and Lomax [28]. In its original form it is a relatively simple algebraic model that make use of a two layers eddy diffusivity formulation. The effective turbulent momentum transfer coefficient  $\mu_t$  is taken as:

$$\frac{\mu_t}{\mu_\infty} = \mu^* = \begin{cases} (\mu^*)_{inner} & y^* < y^{*crossover} \\ (\mu^*)_{outer} & y^{*crossover} < y^* \end{cases} \quad (A.1)$$

where  $y^*$  is the dimensionless normal distance to the wall and  $y^{*crossover}$  is the minimum value of  $y^*$  at which the inner and outer formulations match.

The inner formulation follows the Prandtl-Van Driest formula. Consistent with the dimensionless form given in Chapter 2 the eddy viscosity coefficient is defined as

$$(\mu^*)_{inner} = \frac{Re_\infty}{\gamma^2 M_\infty} \rho^* l^*{}^2 |\omega^*| \quad (A.2)$$

where

$$l^* = k \frac{\gamma}{C} \left[ 1 - \exp(-y^*/A^*) \right] \quad (A.3)$$

is the length scale of the turbulence in the inner region,  $k$  is a model constant,  $|\omega^*|$  is the dimensionless magnitude of the vorticity vector and  $(y^*)^*$  is the dimensionless distance from the wall in walls units consistent with the scaling employed :

$$y^{*+} = \frac{\sqrt{\rho^* w^* t^*}}{\mu_w^*} y^* \sqrt{\frac{Re_\infty}{\gamma^2 M_\infty}} \quad (A.4)$$

In the outer part of the boundary layer the following formula is employed:

$$(\mu^*)_{outer} = \frac{Re_\infty}{\gamma M_\infty} K C_{cp} \rho^* F_{wake} F_{Kleb} \quad (A.5)$$

where  $K$  and  $C_{cp}$  are model constants, and the function  $F_{wake}$  is taken as

$$F_{wake} = \min \left\{ y^*_{max} F_{max}, C_{wk} y^*_{max} U^*_{max} / F_{max} \right\} \quad (A.6)$$

while the quantities  $y^*_{max}$  and  $F_{max}$  are determined by value and corresponding location of the maximum of the function:

$$F = y^* |\omega^*| \left[ 1 - \exp(-y^{*+}/A^*) \right] \quad (A.7)$$

In wake regions the exponential term in the above equation is set to be 0.  $F_{Kleb}$  which is given by the following formula:

$$F_{Kleb} = \left[ 1 + 5.5 \left( \frac{C_{kleb} y}{y_{max}} \right)^6 \right]^{-1} \quad (A.8)$$

is a correction suggested to account for intermittency effects, and  $U^*_{max}$  is the maximum difference of the magnitude of the velocity in the profile.

Also, transition to turbulence can be modeled by setting a cut off value for the computed eddy diffusivity. The suggested criterion is :

$$\mu^*_{\epsilon} = 0 \quad \text{if} \quad \mu^*_{max} < C_{max} \quad (A.9)$$

The following values for the model constant are employed :

$$A^+ = 26$$

$$C_{cp} = 1.6$$

$$C_{kleb} = .3$$

$$C_{wk} = 1.0$$

$$k = .4$$

$$K = .0168$$

$$C_{max} = 14$$

$$Pr_i = .9$$

In the implementation of the turbulence model in the flow codes the the calculation of the eddy diffusivity model was limitated to 2/3 of the total number of points in the outer direction.

Also although the full Reynolds Averaged equations were coded, the 'numerical' thin layer approximation is effectively achieved by the lack of resolution in the streamwise direction provided by the typical computational meshes employed.

Many variations of this turbulence model have been proposed and employed in the literature with the aim of improving the computed results [73] and overcoming numerical difficulties. The implementation of the turbulence model in the flow code developed in the present work has been somewhat troublesome, and it seems worthwhile to give a summary of the advantages and disadvantages of such a model based on our experience.

### **1. Advantages**

1. Algebraic models are mathematically the simplest and computationally the least intensive of all the possible closure approximations.
2. The implementation of the Baldwin and Lomax model is fairly straightforward since it does not involve the numerical determination of the edges of the boundary layer as required by similar algebraic models [5].
3. This model has been widely used by many authors and it has been implemented in many different flow codes. A data bank of computed results is therefore available in the literature and comparisons of the computed results by different numerical schemes is possible.

### **2. Disadvantages**

1. The first disadvantage is common to all the algebraic models. Namely the effects of the turbulent pressure [linear invariant of the Reynolds stress tensor] are not accounted for. This is a particularly severe weakness in regions of strong viscous-inviscid interaction where, with computers now becoming available, improvements in the streamwise resolution are possible. Moreover, the flow history is completely neglected.
2. The determination of the peak value of the function  $F$  is not an easy matter. When regions

of separation are present, a double peak arises with the first peak close to the wall. This gives erroneous evaluation of the eddy diffusivity profile.

3. During the iteration process the predicted values of  $\mu_t$  can experience a strong variation from cycle to cycle, causing a definite slowdown in the convergence rate. This effect is due to the fact that the selection of the minimum in the outer formulation (eq. A.6) may change from cycle to cycle.
4. The formulation in the wake region does an extremely poor job, and determination of the wake velocity profiles is troublesome.
5. Switching between the airfoil and wake region cause the prediction of a discontinuous distribution of the eddy viscosity. Although this can be cured, to some extent, by empirically smoothing the values of  $\mu_t$  near the trailing edge [73] , questions about the accuracy of the simulation in the trailing edge region arise.
6. The coding and the optimization of the turbulence model for a vector machine is cumbersome, and optimization can be achieved only by making use of systems routines.

## APPENDIX B

### Discrete Gauss Theorem

The numerical evaluation of the partial derivatives needed to construct an approximation to the stress tensor and heat flux vector is accomplished by making use of a discrete form of the Gauss Theorem [72]. This theorem gives an integral relation between the partial derivatives of a generic function and its values on the boundary of an arbitrary domain. In 2-D, for example, to compute the derivatives of a generic function  $f(x,y)$  one has:

$$\begin{aligned} \int_S f_x dS &= \int_S f(x,y) dy \\ \int_S f_y dS &= - \int_S f(x,y) dx \end{aligned} \quad (\text{B.1})$$

where  $S$  is a fixed domain with boundary  $\partial S$  in a cartesian reference frame  $(x,y)$ . Then, approximating the right hand side by trapezoidal rule yields:

$$\begin{aligned} (f_x)_{ij} S_{ij} &= \frac{1}{2} \left\{ \sum_{k=1}^4 (f_{k+1} + f_k)(y_{k+1} - y_k) \right\} \\ (f_y)_{ij} S_{ij} &= -\frac{1}{2} \left\{ \sum_{k=1}^4 (f_{k+1} + f_k)(x_{k+1} - x_k) \right\} \end{aligned} \quad (\text{B.2})$$

where :

$$f_1 = f_5$$

$$x_1 = x_5$$

$$y_1 = y_5.$$

The choice of the integration domains depends on the formulation employed as discussed in Chapter 3. Here the subscript  $ij$  define the location at which the derivatives are approximated while  $x_k$  and  $y_k$  are the coordinates of the vertices along the path of integration.

It is also very easy to show that summing the expressions (B.2) a discrete form of the divergence theorem that is equivalent to a flux balance for the domain  $D$  is recovered. In fact by summing eqs (B.2) and dividing and multiplying each term by the length  $l_{k+1,k}$  of the corresponding edges one gets:

$$(f_x + f_y)_{ij} S_{ij} = \frac{1}{2} \left\{ \sum_{k=1}^4 (f_{k+1} + f_k) \frac{(y_{k+1} - y_k)}{l_{k+1,k}} l_{k+1,k} - (f_{k+1} + f_k) \frac{(x_{k+1} - x_k)}{l_{k+1,k}} l_{k+1,k} \right\} \quad (\text{B.3})$$

which is a discrete form of the divergence theorem. In fact

$$\mathbf{n}_{\text{out}} = \left[ \frac{-(y_{k+1} - y_k)}{l_{k+1,k}}, \frac{(x_{k+1} - x_k)}{l_{k+1,k}} \right] \quad (\text{B.4})$$

is the outer normal to the  $k+1,k$  edge. These results support several claims made in Chapter 3:

- (a) The discretization of the convective terms for the vertex scheme accounts to trapezoidal integration.
- (b) In the CCS-b formulation a second application of the Gauss theorem to each components of the viscous stress and heat flux vector is equivalent to making a flux balance.
- (c) The formulation for the viscous terms in the vertex scheme is equivalent to a flux balance in the cell formed by joining the centers that surround each vertex.

## APPENDIX C

### Computations of Internal Laminar Flows

In a parallel effort the flow solver built on the CCS-B formulation was adapted to handle internal flows problems. The modifications to the original code involve the treatment of the boundary conditions and the interfacing of the flow solver with a different mesh generation technique [74].

With the aim of showing the accuracy, robustness and flexibility of the finite volume formulation developed in the present work, a sample of computed laminar results for 2-D planar a double throat nozzle are reported here.

The results presented correspond to the mandatory cases of the GAMM-Workshop on Numerical Solution of Compressible Navier-Stokes Flows, held at INRIA on December 1985. The mandatory problems for the Workshop require the computation of laminar flows on a fixed geometry for flow regimes characterized by the following features:

- (i) Away from the wall, the flow become supersonic as it crosses the first throat region.
- (ii) The flow remains supersonic, except near the wall, in the second divergent.

These features require the minimum exit pressure, corresponding to the maximum flow rate, for a given Reynolds number.

The fluid enters the nozzle at the inlet originating from an infinite reservoir where it is at rest with temperature  $T_0$ , pressure  $p_0$ , density  $\rho_0$ , sound speed  $a_0$ , and the evolution of the fluid

particles between the reservoir and the inlet section is assumed to be isoenergetic and isentropic. This correspond to an inviscid flow approximation between the reservoir and the inlet. Therefore the basic conditions to be imposed at the inlet section are:

- (1) total enthalpy equal to the reservoir enthalpy
- (2) entropy equal to the reservoir entropy.

An additional condition could also be specified at the inlet , but all the properties cannot be known a priori since the mass flow rate is not arbitrary. In the calculations the assumption of inviscid parallel flow is made at the inlet section. No-slip conditions, and a constant temperature (equal to the reservoir temperature) are assigned at the wall.

The mesh used in the computations is a body fitted H-mesh obtained by solving the Laplace equation for the stream function  $\psi$  on an equally spaced grid that covers the physical domain. The coordinates of the vertices are obtained by finding lines of constant velocity potential  $\phi$  and constant  $\psi$  , yielding a system of orthogonal coordinate lines. To improve the resolution of the viscous layer the grid is refined near the wall.

The calculations for the three test cases corresponding to three different Reynolds number ( based on the half length of the inlet section and reservoir conditions  $Re = \alpha_o L p_o / \mu_o$  ) have been performed on a  $152 \times 32$  mesh (fig. 1) with the nodal distribution of points shown in (fig. 2). The three stage scheme with implicit smoothing was used without multigrid.

#### 1. $Re = 100$

The flow variables have been initialized assuming uniform flow conditions corresponding to an inlet Mach number of .4. Figs 3-5 show , respectively, the computed pressure, Mach number, and entropy contours. From the plot of the dimensionless pressure ( $p/p_o$ ) and the Mach number (fig. 7) along the centerline, it can be seen that, for this Reynolds number, strong recompression regions are absent . Due to the strong influence of the viscous effects , however, an extended recirculation region between the two throats is formed as it is shown by the plot of the

dimensionless wall pressure (fig. 8) and wall skin friction coefficient  $\tau_w/(\frac{1}{2}\rho_0 a_\infty^2)$  (fig. 9). The flow separates at  $x_s = 2.98$  and reattaches at  $x_r = 4.83$ . The plot of the dimensionless mass flow rate  $Q/\rho_0 a_\infty L$  (the subscript \* refers to the sonic conditions for an isentropic flow) shows the good convergence and accuracy of the computation (fig. 10). The deviation from the constant mass flow rate solution is less than 2%. A comparison between the dimensionless wall heat flux coefficient  $C_h/(\frac{1}{2}\rho_0 a_\infty^3)$  plotted in fig. 10 and the wall skin friction (fig. 8) verifies the analogy between the two quantities.

### 2. $Re = 400$

For this case the flow variables have been initialized from the converged solution obtained at  $Re = 100$ . The isobar and isomach lines (figs. 12 - 14), as well as the plot of the surface and centerline quantities (figs. 15 - 20), show the formation of a fairly strong shock wave. The interaction of the shock with the viscous layer is responsible for the delay in the flow reattachment as observed in fig. 18. Due to the sensible reduction of the viscous layer, the dimensionless mass flow rate increases with respect to the previous computed case, as it appears from fig. 19. Also, the computed mass flow rate is nearly constant except in the shock region.

### 3. $Re = 1600$

The flow field was initialized by using the computed solution at  $Re = 400$ . For this case, apart from the viscous layer the flow is supersonic from the first throat to the outlet section. The shock wave becomes oblique and the extent of the recirculation bubble between the throats is sensibly reduced ( figs. 21 - 29 ). A second recirculation region appears just downstream of the second throat due to the interaction of the impinging shock and the viscous layer. Again, as one would expect, the mass flow rate is increased respect to the previous cases ( fig. 28 ).

As the author is not aware of the existence of experimental data for the cases presented, a final assessment of the accuracy of the computed solutions is not possible. However the computed

results are consistent with the physical expectation, and a grid refinement study [74] shows that the computed solutions are grid independent. Also, the results are in good agreement with the solutions obtained by other numerical methods [75].

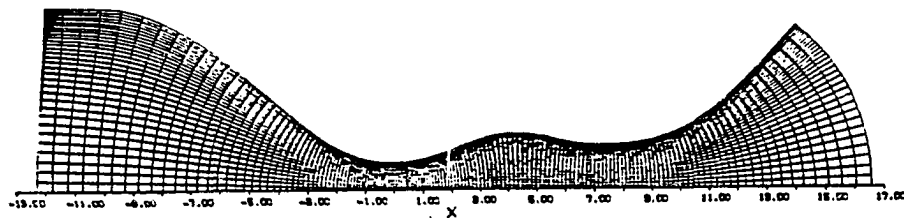


Fig. 1 - Computational Mesh (152x32)

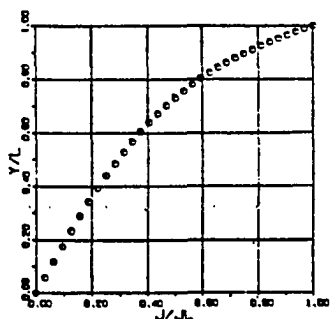


Fig. 2 - Mesh Point Distribution

Table 1 - CPU Time and Residual Values

Re	Grid	CPU	$\log \text{RMS}(\frac{du}{dt})$
100	152x32	1260	-3.9281
400	152x32	1000	-4.5302
1600	152x32	600	-4.5406

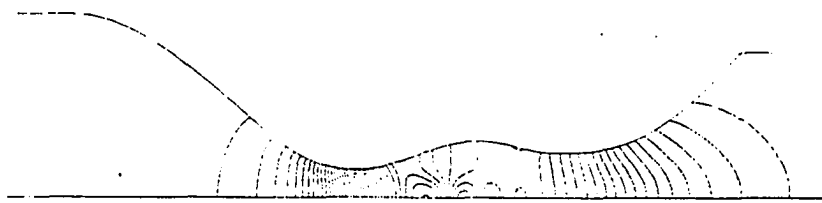


Fig. 3 - Pressure Contours (DP = .02)

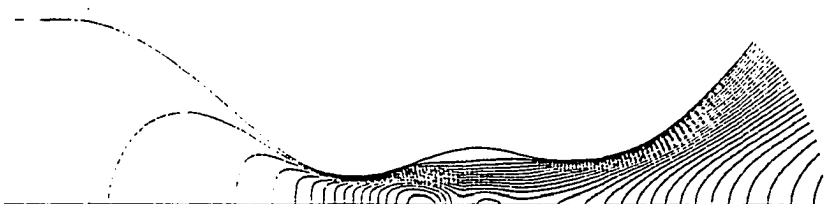


Fig. 4 - Mach Contours (DM = .1)

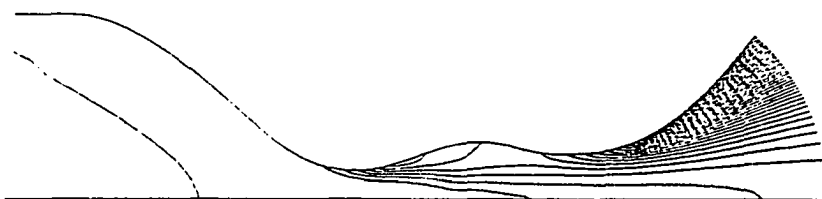


Fig. 5 - Entropy Contours (DS = .1)

Table 2 - RE = 100

	x	-10	-4	0	4	7	13
WALL VALUES	$p/p_0$	.99661	.98346	.54908	.35386	.33556	.023897
	$C_f$	.0011264	.0071064	.0095134	.0025015	.041744	.022022
SYMMETRY VALUES	$C_h$	.47032E-5	.69091E-4	.007057	.0011061	.0035174	.0037657
	$p/p_0$	.99435	.97016	.59374	.40499	.34521	.070498
AXIS VALUES	M	.091126	.20912	.90042	1.14721	1.18759	2.16658
	S	.99995	1.00008	1.00041	1.05225	1.11369	1.18381

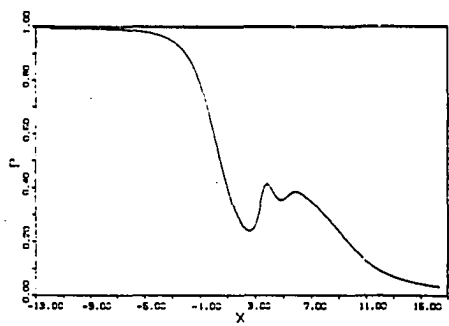


Fig. 6 - Centerline Pressure

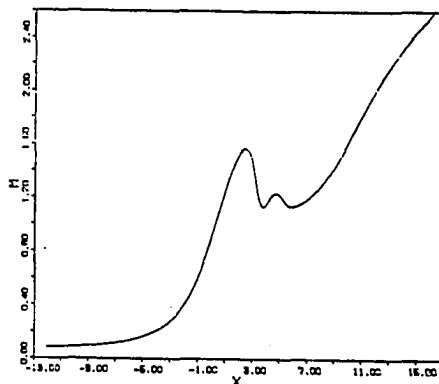


Fig. 7 - Centerline Mach Number

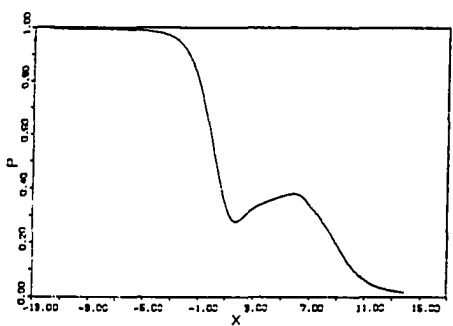


Fig. 8 - Wall Pressure

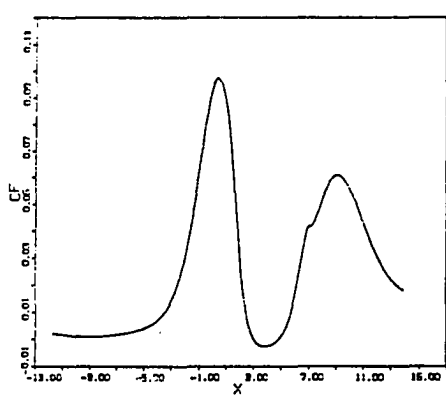


Fig. 9 - Wall Skin Friction

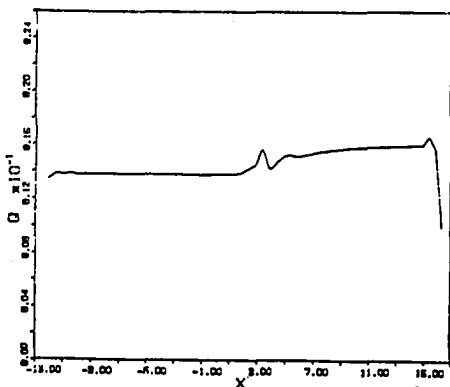


Fig. 10 - Mass Flow Rate

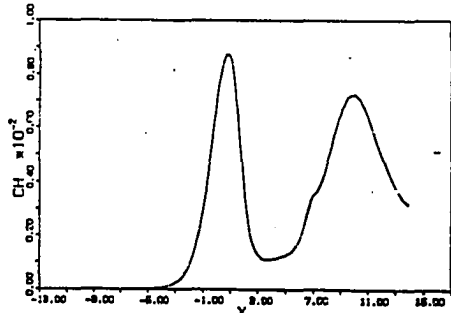


Fig. ii - Wall Heat Flux

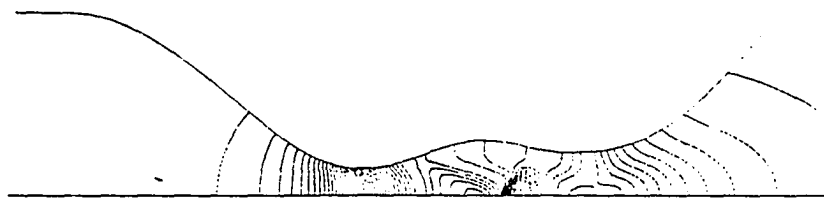


Fig. 12 - Pressure Contours (DP = .02)

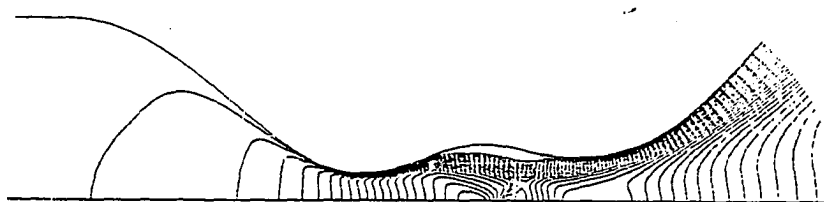


Fig. 13 - Mach Contours (DM = .1)

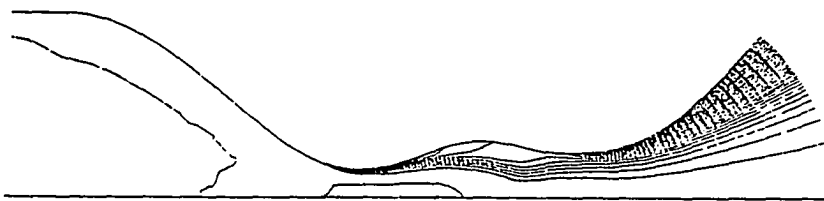


Fig. 14 - Entropy Contours (DS = .1)

Table 3 - RE = 400

	x	-10	-4	0	4	7	13
WALL VALUES	$P/P_0$	.99638	.98117	.512455	.25509	.28135	.18906
	$C_f$	.47717E-3	.0039085	.049432	.00219	.015262	.0095716
	$C_h$	.23642E-5	.45368E-4	.0036684	.48878E-3	.001548	.0015795
SYMMETRY VALUES	$P/P_0$	.99357	.96778	.57570	.11183	.22272	.06108
	$M$	.006811	.21703	.92619	2.08007	1.5906	2.42434
	$S$	.99996	1.00002	.9995	1.00341	1.027	1.0324

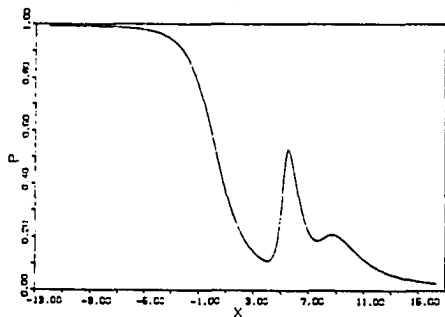


Fig. 15 - Centerline Pressure

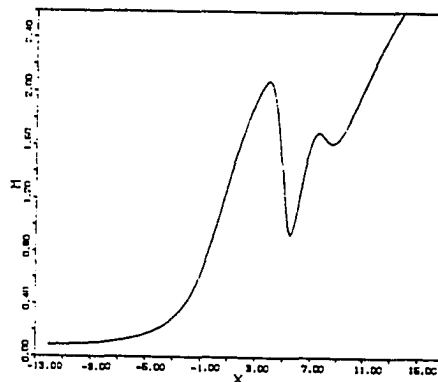


Fig. 16 - Centerline Mach Number

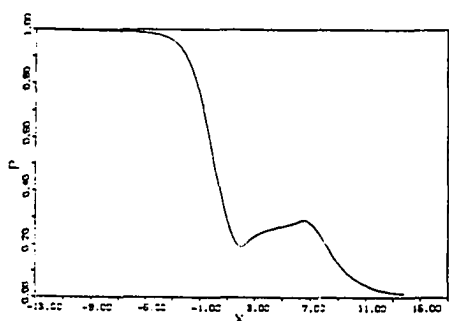


Fig. 17 - Wall Pressure

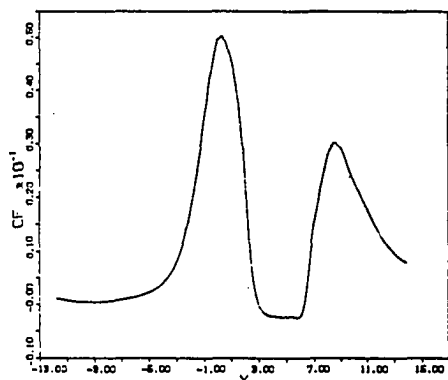


Fig. 18 - Wall Skin Friction

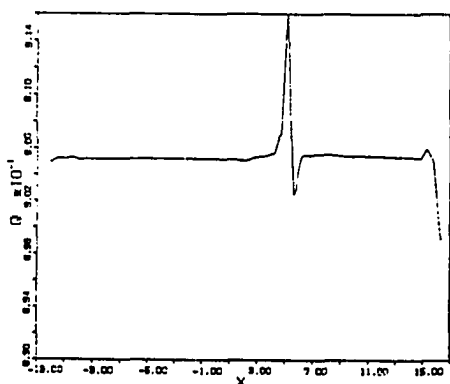


Fig. 19 - Mass Flow Rate

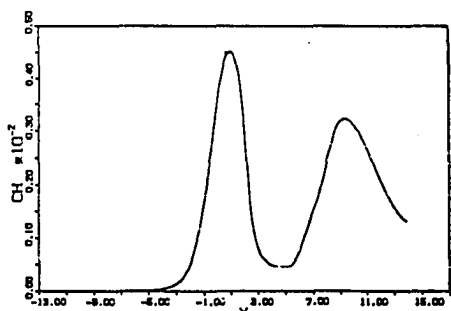


Fig. 20 - Wall Heat Flux

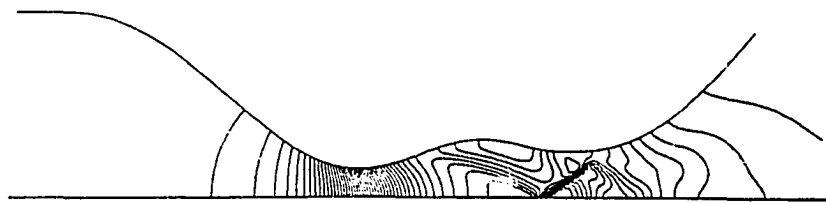


Fig. 21 - Pressure Contours (DP = .02)

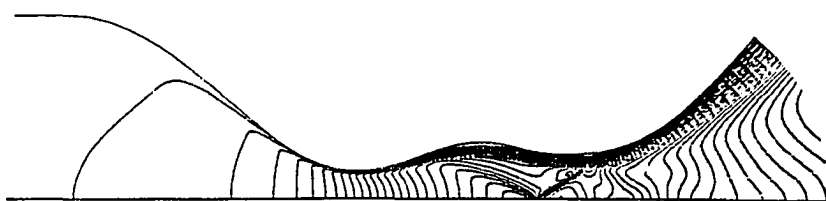


Fig. 22 - Mach Contours (DM = .1)

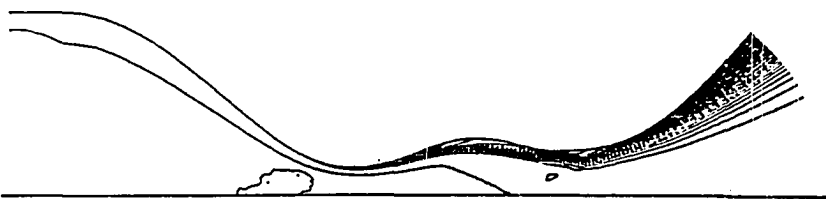


Fig. 23 - Entropy Contours (DS = .1)

Table 4 - RE = 1600

	x	-10	-4	0	4	7	13
WALL VALUES	$p/p_{\infty}$	.99625	.98005	.49071	.19565	.12673	.014435
	$c_f$	.21724E-3	.0021475	.02526	-.67258E-3	.013253	.004195
	$c_h$	.24654E-6	.25331E-4	.0019085	.35770E-3	.0014171	.68152E-3
SYMMETRY VALUES	$p/p_{\infty}$	.99317	.96640	.56657	.094517	.33586	.050162
	M	.099733	.22163	.93948	2.19385	1.30375	2.55742
<hr/>							
S	.99996	1.	.99976	.99964	1.0265	1.0254	

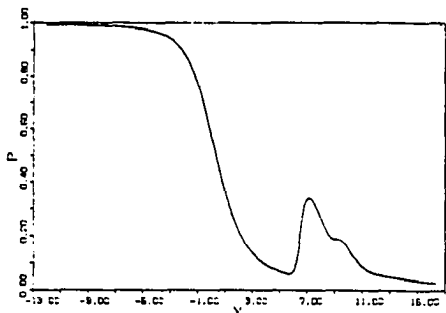


Fig. 24 - Centerline Pressure

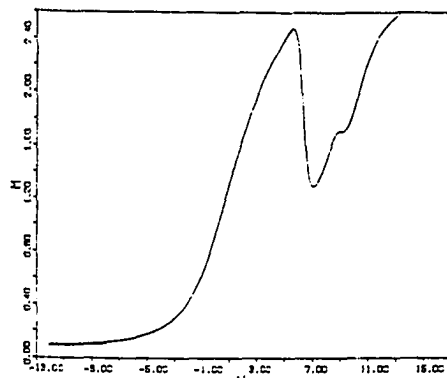


Fig. 25 - Centerline Mach Number

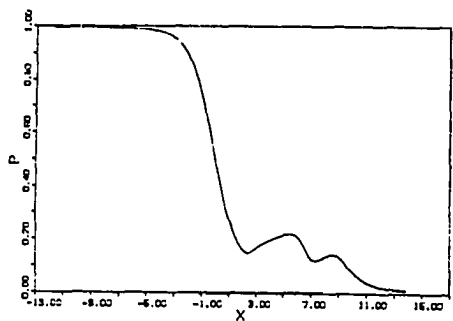


Fig. 26 - Wall Pressure

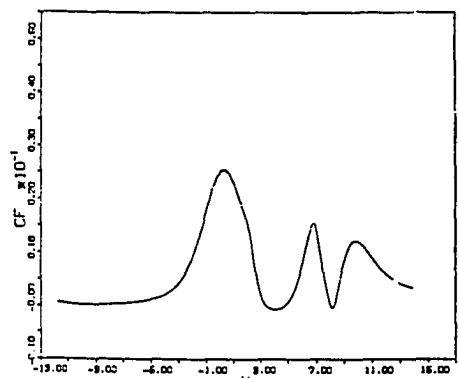


Fig. 27 - Wall Skin Friction

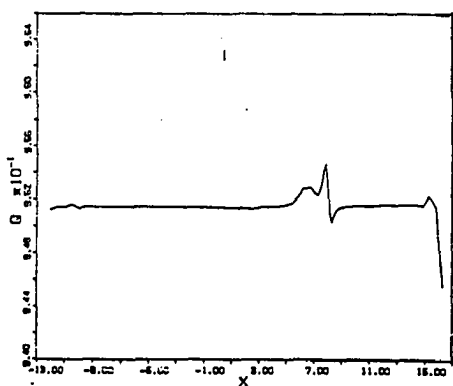


Fig. 28 - Mass Flow Rate

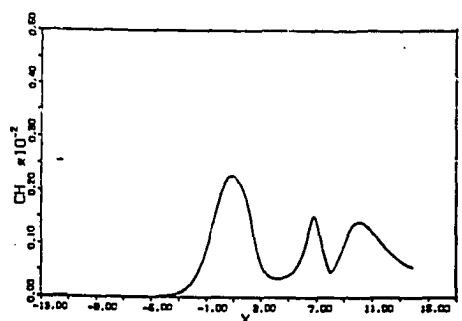


Fig. 29 - Wall Heat Flux